Legacy cross-section measurements of the $t\bar{t}Z$ production process in the trileptonic final state at $\sqrt{s} = 13\,\text{TeV}$ with the ATLAS detector

Dissertation

zur Erlangung des mathematisch-naturwissenschaftlichen Doktorgrades
„Doctor rerum naturalium“
der Georg-August-Universität Göttingen

im Promotionsprogramm ProPhys
der Georg-August University School of Science (GAUSS)

vorgelegt von

Steffen

Korn

aus Kiel

Göttingen, 2023

Betreuungsausschuss

Prof. Dr. Arnulf Quadt
Prof. Dr. Steffen Schumann
PD Dr. Ralf Bernhard

Mitglieder der Prüfungskommission:

Referent: Prof. Dr. Arnulf Quadt
II. Physikalisches Institut, Georg-August-Universität Göttingen

Koreferent: Jun.-Prof. Dr. María Moreno Llácer
Instituto de Fisica Corpuscular (IFIC), Centro Mixto Universidad de Valencia - CSIC

Weitere Mitglieder der Prüfungskommission:

PD Dr. Ralf Bernhard
II. Physikalisches Institut, Georg-August-Universität Göttingen

Prof. Dr. Karl-Henning Rehren
Institut für Theoretische Physik, Georg-August-Universität Göttingen

Prof. Dr. Ansgar Reiners
Institut für Astrophysik, Georg-August-Universität Göttingen

Prof. Dr. Steffen Schumann
Institut für Theoretische Physik, Georg-August-Universität Göttingen

Tag der mündlichen Prüfung: 23.06.2023

Referenz: II.Physik-UniGö-Diss-2023/02

Legacy cross-section measurements of the $t\bar{t}Z$ process in the trileptonic final state at 13 TeV with the ATLAS detector

Abstract

After three years of data-taking during the second run of the LHC at CERN, Geneva, Switzerland, the ATLAS detector has recorded its most extensive proton-proton collision data set to date, allowing for a wide range of Standard Model (SM) precision measurements. Through this dataset, a large number of top quark pairs in association with a Z boson ($t\bar{t}Z$) and with it key SM parameters are accessible. Several theories beyond the SM provide possible extensions to the electroweak sector of the SM, leading to deviations of the $t\bar{t}Z$ production cross-section from its SM predictions in the presence of new physics. With the large dataset recorded by ATLAS, a final $t\bar{t}Z$ analysis has gained interest to provide legacy cross-section measurements and interpretations within the SM effective field theory to provide the most cohesive picture of the $t\bar{t}Z$ production process to date.

This work mainly presents the results of the inclusive cross-section measurement obtained using the 140 fb^{-1} large Run 2 dataset collected by the ATLAS detector between 2015 and 2018 at 13 TeV centre-of-mass energy. It focuses on the measurement of the inclusive cross-section in the trileptonic channel, where exactly three leptons (electrons or muons), two originating from a Z decay and one from a leptonic top quark decay and at least three jets, one of which must be b-tagged, are selected. The obtained data is unfolded using the profile-likelihood unfolding approach, and interpretations of the inclusive and differential measurements within the framework of the SM effective field theory are presented. A deeper focus of this thesis lies in developing neural-network-based classifiers for $t\bar{t}Z$ event classification in the trileptonic channel.

Finale Wirkungsquerschnittsmessungen des $t\bar{t}Z$-Prozesses im trileptonischen Endzustand bei 13 TeV mit dem ATLAS-Detektor

Zusammenfassung

Nach drei Jahren der Datennahme während des zweiten Laufs des LHC am CERN in Genf, Schweiz, hat der ATLAS-Detektor seinen bisher umfangreichsten Proton-Proton-Kollisionsdatensatz aufgezeichnet, der eine breite Palette von präzisen Messungen des Standardmodells (SM) ermöglicht. Durch diesen Datensatz ist eine große Anzahl von Top-Quark-Paaren in Verbindung mit einem Z-Boson ($t\bar{t}Z$) und damit wichtige SM-Parameter zugänglich. Mehrere Theorien jenseits des SM bieten mögliche Erweiterungen für den elektroschwachen Sektor des SM. Abweichungen des $t\bar{t}Z$-Produktionsquerschnitts von den SM-Vorhersagen würden auf das Vorhandensein einer neuen Physik hinweisen. Mit dem großen Datensatz, der von ATLAS aufgezeichnet wurde, hat eine abschließende $t\bar{t}Z$-Analyse an Interesse gewonnen, um finale Querschnittsmessungen und Interpretationen innerhalb der effektiven SM-Feldtheorie bereitzustellen und so ein möglichst zusammenhängendes Bild des $t\bar{t}Z$-Produktionsprozesses zu erhalten.

In dieser Arbeit werden vornehmlich die Ergebnisse der Messung des inklusiven Wirkungsquerschnitts vorgestellt, die mit dem $140\,\mathrm{fb}^{-1}$ großen Run 2-Datensatz gewonnen wurden, der vom ATLAS-Detektor zwischen 2015 und 2018 bei 13 TeV Massenschwerpunktenergie gesammelt wurde. Er konzentriert sich auf die Messung des inklusiven Wirkungsquerschnitts im trileptonischen Kanal, bei dem genau drei Leptonen (Elektronen oder Myonen), von denen zwei aus einem Z-Zerfall und eines aus einem leptonischen Top-Quark-Zerfall stammen, und mindestens drei Jets, von denen einer b-tagged sein muss, ausgewählt werden. Die erhaltenen Daten werden entfaltet, und es werden Interpretationen der inklusiven und differentiellen Messungen im Rahmen der effektiven Feldtheorie des SM vorgestellt. Ein tieferer Schwerpunkt dieser Arbeit liegt in der Entwicklung von Klassifikatoren auf der Basis neuronaler Netze zur Klassifizierung von $t\bar{t}Z$-Ereignissen im trileptonischen Kanal.

Contents

Acknowledgements

If anything, particle physics is teamwork, and I was lucky enough to be part of a great team in Göttingen, the second institute and ATLAS. I am grateful to many people who have made it possible for me to write these lines now. They are meant to be a small selection, as the rest cannot be said in a nutshell. To all: Thank you very much! First of all, I would like to thank Arnulf Quadt, my PhD supervisor, for giving me the opportunity to do this PhD, for the many opportunities to broaden my horizons, to gain new experiences and for the possibility to continuously develop myself. I am grateful to Steffen Schumann and Ralf Bernhard, the members of my thesis advisary committee, who have been guiding me throughout the last three and a half years. I want to express my sincere thanks to the Konrad Adenauer Foundation, which has supported this promotion and shown me opportunities beyond it. I am deeply indebted to Elizaveta Shabalina for her daily supervision at the Second Physics Institute and CERN. Your tremendous wealth of experience, advice and guidance has contributed significantly. So many thanks! I would also like to thank Baptiste Ravina from the bottom of my heart. Your help with this work was indispensable, and I am grateful for the one or other piece of advice, the one or other beer and the many funny moments. Many thanks also to the entire ttZ analysis team; as I said, an analysis is teamwork, and I have always enjoyed being part of this team. I am grateful for my time at CERN and remember the days with pride and joy. My acknowledgement would not be complete without mentioning my friends at the second physics institute and outside. Thank you all so much! Thanks for the coffee breaks with their particular topics, the fun evenings, competing together in the pub quiz, and so many other innumerable things. In particular, I would like to thank Anton and Sven. Thank you for always having a sympathetic ear in all my situations. The last few years have been up and down, happy and unhappy and I don't know how I could have managed it all without the people who have accompanied and supported me on my way in the last few years. My greatest thanks go to you. Zuletzt möchte ich meiner Familie danken. Danke an alle Körner; Mama, Papa, Felix und Thiemo! Danke, dass ihr da seid, egal was auch ist. Danke für eure Unterstützung! Ohne euch wäre das hier nicht möglich gewesen. Liebe Oma Helga, vielen Dank für deine Weisheit und dein offenes Ohr. Danke auch an Gitta und Jürgen. Diese Arbeit ist auch für euch, auch wenn ihr sie nicht mehr lesen könnt.

Contributions by the Author

Performing an analysis on data taken by the ATLAS experiment is only the final step of a long list of technological and scientific achievements required to perform any measurement. The design and construction of the detector require decadelong efforts, which then continue through the operation phase. These efforts can only be undertaken in extensive, international collaborations. These achievements towards an experimental measurement are reflected by the fact that corresponding papers are always published in the name of the entire collaboration. The work documented in this thesis reflects the author's contributions to the measurement of the $t\bar{t}Z$ production process using proton-proton collision data taken by the ATLAS experiment between 2015 and 2018 [1]. The following paragraphs will provide a non-exhaustive list of the author's contributions to this measurement.

The $140\,\text{fb}^{-1}$ Run 2 legacy analysis of the $t\bar{t}Z$ production process in final states with two, three or four leptons utilises neural networks in all three decay channels to separate signal and background events. The author designed the necessary tools to develop these neural networks in the three channels and developed the neural network approach in the trileptonic channel. Dominic Babal performed the development of the neural network approaches in the dileptonic channel. In the tetraleptonic channel, the original neural network approach was developed by Tomke Schroer as part of her MSc. thesis under the supervision of the author and then finalised by Lucia Keszeghova in her PhD thesis.

The author furthermore produced necessary samples for the analysis using the *Worldwide LHC Computing Grid* and performed the measurement of the inclusive cross-section of the $t\bar{t}Z$ production process in the trileptonic channel. For this measurement, additional data-driven fake lepton control regions were finalised by the author and included in the measurement mentioned above. Work performed for the inclusive cross-section measurement is a prerequisite for the differential measurements (presented in Section 9.2) and the interpretation of it in the Standard Model effective field theory framework (discussed in Section 9.3). This thesis will however briefly mention these contributions to contextualise the entire $t\bar{t}Z$ measurement. However, they do not represent the focus of the author's work.

Foreword

From birth, we are imbued with a sense of wonder and curiosity, driven to explore and understand the world around us. In childlike curiosity, we splash in puddles and pluck leaves from bushes to ponder the nature of existence and the mysteries underlying our reality. Though this innate scientific curiosity may sometimes fade over time, it often remains a constant throughout our lives, propelling us forward in our quest for knowledge and understanding.

Throughout history, philosophers, scholars, and scientists have sought to unlock the universe's secrets to uncover the underlying principles that govern our world. Their discoveries have pushed the boundaries of physics and philosophy, shaping our understanding of the natural world and, among other achievements, inspiring literary works of great depth and complexity. No work captures this quest for understanding more fully than Goethe's Faust, in which the titular character makes a pact with the devil to uncover nature's inner workings. Despite his desire, Faust and his creator Goethe are ultimately denied a satisfactory answer in their lifetime. Goethe, an amateur scientist who, in addition to his literary work, was also active in botany, mineralogy, anatomy and physics, died in 1832 in Weimar, Germany.

Exactly a century after his death, Werner Heisenberg was honoured in Stockholm with the Nobel Prize in Physics, whose work once again shook up the picture of the world of nature's smallest building blocks. Modern quantum mechanics, which Heisenberg helped to develop, revolutionised human understanding of the interrelationships of the microcosm, precisely the question Faust wanted to get to the bottom of.

Today's particle physics has emerged from the continuous exploration of this microcosm, as a continuation of the story of childlike curiosity and in the spirit of Goethe's Faust. The result of the search for answers to these ancient questions culminates today in the Standard Model of Particle Physics (SM), which summarises the understanding of the elementary building blocks of nature, the elementary particles, and their interactions.

The strength of this comprehensive model of nature lies in the accurate prediction of its parameters, which can be verified by precision measurements, allowing a test of the SM's self-consistency. By scrupulously revisiting the SM and searching for physics beyond it, the opportunity arises to unhinge human understanding of nature once again.

Our task is not just a mere study of the multiplicity of elementary particles;

it is a quest to unravel the mysteries of the universe, understanding the intricate interactions between the cosmos' building blocks and uncovering their secrets. As we delve deeper into the past in our studies and look back to the beginning of time, we face an increasingly hot universe whose immense energy density enabled the simultaneous existence of a multitude of light and heavy particles. These high energy density states, which existed shortly after the Big Bang, can today be recreated in the laboratory by bringing light, stable particles into collision. The kinetic energies of these particles allow us to reproduce the conditions of the early universe, thus creating heavy particles, making it possible to understand the origin of our world and the laws that govern it.

In lockstep with the advancing technical revolution of the last century, achieving ever higher centre-of-mass energies and proving the existence of heavier particles has become possible. Based on the achievements of generations before us, we continue in the passion that drives us to seek answers to the most profound questions of existence.

The heaviest of the known elementary particles to date is the top quark, discovered independently by the D0 and CDF collaborations at the Tevatron in 1995. The discovery of the top quark marked a significant achievement in particle physics. However, it is not the journey's end but another step forward in understanding the universe. The discovery of the tau neutrino in 2004 and the Higgs boson in 2012 completed the Standard model's particle zoo, and all these particles have become the subject of intense study.

This thesis focuses on the associated production of a top quark pair and a Z boson at a centre-of-mass energy of 13 TeV in trileptonic final states. Furthermore, it highlights recent measurements performed by the ATLAS collaboration at the Large Hadron Collider (LHC) at CERN in Geneva, Switzerland.

CHAPTER 1

Introduction

A good question can make all the difference. Why behaves nature the way it does? What is everything made of? Is there an underlying mechanism to explain everything?

Answering these profound questions has been humankind's most significant endeavour for millennia. It is a quest that transcends the boundaries of science and touches upon the essence of human existence. Generations of philosophers and physicists have unravelled the mysteries of the inner workings of our universe and the laws governing it and, in doing so, have advanced collective human knowledge substantially. By diving ever deeper into the complex world of the microcosm surrounding us, we are gaining a better understanding of the physical world and delving into the fundamental nature of reality. The study of the smallest pieces of nature is not just a technical exercise but a philosophical pursuit that touches upon the very meaning of existence.

The ancient Greek philosopher Democritus, who first proposed that the universe comprises indivisible particles, understood that the microcosm study is not just about understanding the physical world but about understanding ourselves and our place in the universe. While the idea that the building blocks of nature must consist of something elementary already came up in Democritus' time, the concept of elementary particles had its advent with the discovery of the electron by J. J. Thomson in 1897 [2]. In hindsight, J. J. Thomson's discovery can be defined as the birth of particle physics. In his *plum-pudding model* [3] from 1904, Thomson attempted to explain the two then-known properties of atoms; that atoms have no net electric charge while their hypothetical constituents, the electrons, do. He explained these observed properties with a volume of electrons, the *plums*, surrounding a volume of positive charge, the *pudding*. His model assigned an inner structure to the atom for the first time.

The plum-pudding structure of the atom was then revised by E. Rutherford [4] and probed by H. Geiger and E. Marsden in dedicated scattering experiments [5, 6],

supporting the model of an atom consisting of a heavy nucleus surrounded by light electrons. The constituents of the nuclei, the protons and neutrons, were subsequently discovered and described by E. Rutherford and J. Chadwick, respectively in a series of publications [7–11].

With this simple set of three elementary particles, the crown jewel of science of the 19th century, the periodic table of elements, could finally be explained in detail. However successful these discoveries were in explaining the structure of the known elements, the simple set of elementary particles was soon overthrown with the discovery of the positron [12] and muon [13–15]. These discoveries introduced the concept of anti-particles and heavier particles with unknown properties and unknown origins. Why would nature provide additional sets of (anti-) particles with heavier masses?

While P. Dirac could explain the mathematical concept of anti-particles in a quantum theory of the electron [16], the discoveries of these new and even heavier particles were only later structured by Murray Gell-Mann's eightfold way [17, 18].

In his work, previously considered fundamental particles were replaced by smaller constituents named quarks [19]. The existence of these newly proposed elementary constituents was supported by the precise prediction of the Ω^- particle, which was discovered in 1964 [20]. Furthermore, scattering electrons off protons in so-called deep inelastic scattering experiments performed at the *Deutsches Elektronen-Synchrotron* (DESY) [21] and the *Stanford Linear Accelerator Center* (SLAC) [22, 23] supported the model of point-like constituents, the quarks, within the proton.

Today the Standard Model of Particle Physics (SM) describes the set of elementary particles in modern particle physics. It comprises 12 fermions, 6 quarks and 6 leptons, 4 force-carrying particles, the bosons, and the Higgs boson. The SM will be explained in detail in Section 1.1.

While the list of fermions was completed in 2000 with the discovery of the tau neutrino by the DONUT collaboration [24], the list of bosons was only completed in 2012 with the discovery of the Higgs boson by the ATLAS and CMS collaborations [25, 26]. The discovery of this remaining piece of the SM puzzle established the Higgs mechanism in the SM as the process that leads to electroweak symmetry breaking and thus to the fermions and bosons becoming massive. The most massive of the known elementary particles is the top quark. Its importance within the framework of the SM and production and decay mechanisms are described in Section 1.2. A relevant property of each fermion is its interaction with the individual gauge bosons of the SM. Particularly relevant for this work is the interaction of the top quark with the Z boson, providing insights into the properties of the top quark and the inner workings of the neutral current weak interaction which will also be highlighted in Section 1.2

1.1 The Standard Model of Particle Physics

The Standard Model of particle physics (SM) [27–38] summarises the description of the microcosm, the elementary particles, and their mutual interactions in a unified theory. It comprises 12 elementary spin-½ fermions and 5 bosons with integer spin, acting as exchange particles of the 3 fundamental interactions described by the SM: The strong interaction mediated by the gluon (g), the electromagnetic interaction mediated by the photon (γ), and the weak interaction mediated by $W^{\pm}$ bosons and the Z^0 boson[1].

The electromagnetic and weak interactions are combined in the electroweak unification [27–30] based on work performed by Glashow, Salam, and Weinberg in the 1970s, forming a combined description of the electroweak processes within a local $SU(2) \otimes U(1)$ gauge symmetry. Together with the $SU(3)$ subgroup describing the interaction with the gluon fields of the strong interaction (Quantum Chromodynamics, QCD), the mathematical formalism of the SM is a renormalisable quantum field theory based on a local $SU(3) \otimes SU(2) \otimes U(1)$ gauge symmetry.

The electroweak Lagrangian density $\mathcal{L}_{\text{EW}}$ before electroweak symmetry breaking of the SM is then given by

$$
\begin{aligned}
\mathcal{L}_{\text{EW}} &= \mathcal{L}_{\text{fermions}} + \mathcal{L}_{\text{gauge}} + \mathcal{L}_{\text{coupling}} + \mathcal{L}_{\text{Higgs}} + \mathcal{L}_{\text{Yukawa}} \\
&= \sum_f \bar{\psi}_f i\gamma^\mu \partial \psi_f \\
&- \frac{1}{4} B_{\mu\nu} B^{\mu\nu} - \frac{1}{2}\text{tr}(W_{\mu\nu} W^{\mu\nu}) - \frac{1}{2}\text{tr}(G_{\mu\nu} G^{\mu\nu}) \\
&+ \sum_f \bar{\psi}_f \gamma^\mu \left(-g' \frac{1}{2} Y_W B_\mu - g \frac{1}{2} \tau \mathbf{W}_\mu \right) \psi_f \\
&+ \left| \left(\partial_\mu - i g W_\mu^a t^a - i g' Y_\phi B_\mu \right) \phi \right|^2 + \mu^2 \phi^\dagger \phi - \lambda (\phi^\dagger \phi)^2 \\
&- \sum_{f_d} g_{f_d} (\bar{L} \phi R + \bar{R} \phi^\dagger L) - \sum_{f_u} g_{f_u} (\bar{L} \phi_c R + \bar{R} \phi_c^\dagger L),
\end{aligned}
$$

where the first term, $\mathcal{L}_{\text{fermion}}$, describes the kinetic term for a Dirac fermion, represented by ψ_f. The sum goes over all fermions.

The second term, $\mathcal{L}_{\text{gauge}}$, describes the interactions between the gauge bosons (photons, gluons, W and Z bosons) and the gauge fields (electromagnetic, strong, and weak). The $B_{\mu\nu}$, $W_{\mu\nu}$ and $G_{\mu\nu}$ terms are the field strength tensors, where $B_{\mu\nu}$ is the gauge field tensor for the $U(1)$ group, $W_{\mu\nu}$ the field tensor for the $SU(2)$ group and $G_{\mu\nu}$ is the gluon field tensor. The field strength tensor for a given field, $F^a_{\mu\nu}$, is defined as:

$$
F^a_{\mu\nu} = \partial_\mu \mathcal{A}^a_\nu - \partial_\nu \mathcal{A}^a_\mu + g_i f^{abc} \mathcal{A}^b_\mu \mathcal{A}^c_\nu,
$$

[1] In the following the charges of the Z^0 boson and $W^{\pm}$ bosons will be omitted for simplicity wherever possible.

where $\mathcal{A}_\mu^a$ describes the given gauge field, g_i is the respective gauge coupling constant and f^{abc} is the structure constants of the corresponding gauge group.

The third term, $\mathcal{L}_{\text{coupling}}$, introduces couplings between fermions and the electroweak gauge fields. Within the electroweak sector left-handed fermions interact within the framework of the $U(1) \otimes SU(2)$ symmetry group. The weak hypercharge is denoted by Y_W. B_μ is the $U(1)$ gauge field, W_μ is the three component $SU(2)$ gauge field and τ represents the Pauli matrices. Through the electroweak unification the electric charge Q, the third component of the weak isospin $I_W^{(3)}$ and Y_W are related through $Q = I_W^{(3)} + 1/2Y_W$.

The $\mathcal{L}_{\text{Higgs}}$ term introduces quadratic terms in the gauge fields W_μ and B_μ which give mass to the $W^\pm$ and Z bosons. Their mass scales are *fine-tuned* by the non-zero vacuum expectation value, v, which arises in the unitary gauge. In the Higgs mechanism[2] [39, 40] ϕ consists of two complex scalar fields placed in a weak isospin doublet:

$$\phi = \begin{pmatrix} \phi^+ \\ \phi^0 \end{pmatrix} = \frac{1}{\sqrt{2}} \begin{pmatrix} \phi_1 + i\phi_2 \\ \phi_3 + i\phi_4 \end{pmatrix}.$$

One of the scalar fields is neutral, written as ϕ^0 and the other is charged such that ϕ^+ and $(\phi^+)^* = \phi^-$ provide the longitudinal degrees of freedom of the $W^\pm$ bosons.

Finally, the last term describes the Yukawa interaction terms where g_{f_u} and g_{f_d} are Yukawa couplings of the up and down type particles respectively. The SM fermions are placed in left-handed $SU(2)$ doublets, L, and right-handed $SU(2)$ singlets, R. The sums run over the up and down type particles, respectively. The elementary particles acquire finite masses by coupling to the Higgs field after the process of *spontaneous symmetry breaking* through the Higgs mechanism, which also gives rise to the Higgs boson. After spontaneous symmetry breaking, the Higgs doublet in the unitary gauge is

$$\phi(x) = \frac{1}{\sqrt{2}} \begin{pmatrix} 0 \\ v + h(x) \end{pmatrix},$$

where $h(x)$ is the physical Higgs field. The masses of the charged leptons and quarks in the SM can then be expressed in terms of v and their respective Yukawa coupling, $m_f = \frac{g_f v}{\sqrt{2}}$, leading to following terms in the Lagrangian after symmetry breaking:

$$\mathcal{L}_u = -m_u \bar{u}u - \frac{m_u}{v} \bar{u}uh,$$
$$\mathcal{L}_d = -m_d \bar{d}d - \frac{m_d}{v} \bar{d}dh,$$

where the first term gives rise to the mass of the up and down-type fermions and the second represents the coupling to the Higgs boson itself.

[2]The mechanism was developed simultaneously by several independent groups and is hence also known as Englert–Brout–Higgs–Guralnik–Hagen–Kibble mechanism, Anderson–Higgs mechanism or Anderson–Higgs–Kibble mechanism. Hereafter, *Higgs mechanism* is used.

The fermions are grouped into 6 leptons and 6 quarks, respectively, which are arranged in weak isospin doublets, with the electrically neutral, massless neutrinos comprising the up-type leptons and the up (u), charm (c) and top quark (t) with an electrical charge of $\frac{2}{3}e$ being the up-type quarks. While the down-type electron (e), muon (μ) and tau (τ) complete the lepton doublets, the quark doublets are completed with the down, strange and bottom quark, carrying an electrical charge of $-\frac{1}{3}e$. These doublets arise from the parity-violating nature of the weak interaction, the prefered coupling to fermions with negative chirality (left-handed), which is mathematically described by the left-handed representation in the Poincaré group of special relativity [41].

The arrangement into two families of left-handed fermion doublets carrying the isospin as mentioned above and right-handed isospinless singlets reflects the underlying parity-violating nature of the electroweak charged-current interactions as well as the different couplings of these fermions to the strong force. While the electrically neutral Z boson, mediating the neutral-current weak interaction, couples to all fermions, the strong interaction only couples to the colour charge-bearing quarks. Since the leptons are colour-neutral, they only interact via the electroweak force. A summary of the particles of the SM and their interactions is given in Figure 1.1. In the following, the interactions within the SM and its shortcomings are described in detail.

Strong Interaction

The strong interaction, known as *Quantum Chromodynamics* (QCD), is based on a non-Abelian $SU(3)$ gauge symmetry and acts on all particles carrying colour charge, often denoted as *red*, *green* and *blue* (r, g, b) [43–46]. It was only partially mentioned above in the $\mathcal{L}_{EW}$ term and shall now be discussed in more detail. The complete Lagrangian of QCD is given by

$$\mathcal{L} = \sum_q \bar{\psi}_{q,a}(i\gamma^\mu \partial_\mu \delta_{ab} - \frac{g_s}{2}\gamma^\mu \lambda^c_{ab} G^c_\mu - m_q \delta_{ab})\psi_{q,b} - \frac{1}{4}\mathrm{tr}(G_{\mu\nu}G^{\mu\nu}), \tag{1.1}$$

Latin and Greek indices run from 1 to 3 and 1 to 4, respectively, using Einstein's convention for the sums.

The interaction between quarks and gluons is described using the Dirac matrices γ^μ and quark-field spinors $\psi_{q,a}$ where $q = (u, d, c, s, t, b)$ describes the quark flavour and the index a is the colour index running over the three colours. The quark's colour is rotated in $SU(3)$ space through the interaction of the Dirac spinors with the physical gluon fields, G^c_μ, originating from the eight 3×3 Gell-Mann λ-matrices of the $SU(3)$ group. The fundamental interaction factors are the strong coupling constant, g_s, and the quark masses originating from the Higgs mechanism.

As a consequence of the $SU(3)$ gauge group being non-Abelian and colour conservation in strong interactions, the gluon carries a combination of colour and anti-colour and hence is subject to self-interaction[3].

[3]It should be noted here that if nature had chosen a $U(3)$ gauge symmetry instead, a ninth,

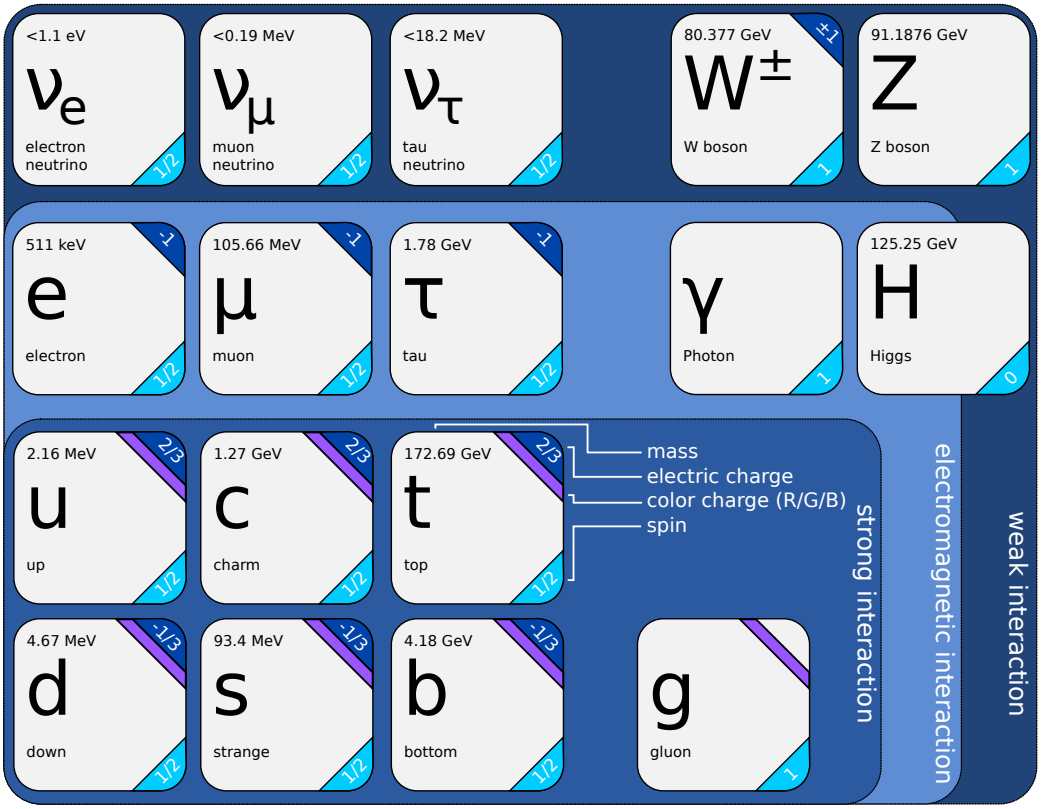

Figure 1.1: Summary of the particles of the Standard Model. The six leptons and six quarks are shown on the left-hand side, vertically split by their third component of the weak isospin. Horizontally they are arranged into three generations. The gauge bosons and the Higgs boson are depicted on the right. The coloured areas imply with which bosons the individual particles interact. Particle masses are taken from Ref. [42].

No colourless states are observed in nature, implying confinement to colour-neutral states, known as *colour confinement*. It has the consequence that, in practice, only colour-neutral states like mesons (qq or $\bar{q}\bar{q}$) and baryons (qqq or $\bar{q}\bar{q}\bar{q}$) are observed. Recently, tetraquarks ($q\bar{q}q\bar{q}$) and pentaquarks ($qqqq\bar{q}$) have also been observed [47–50], agreeing with the hypothesis of colour confinement.

Although QCD is known as the strong interaction, the interaction is by no means strong at all energy scales since the actual strength of the coupling depends on the process of interest's energy scale. Of particular relevance for hadron collider physics is QCD at high momentum transfer, Q^2, a regime probed by the LHC. At these scales, QCD becomes perturbative, and statements about observables are expressed

colourless gluon would exist. This gluon could then propagate infinite distances, giving the strong interaction an infinite range and providing us with a significantly different universe.

in terms of a renormalised coupling $\alpha_s(Q^2, \mu_R^2)$ as a function of the energy scale and an unphysical renormalisation scale μ_R which obeys the *renormalisation group equation*

$$\mu_R^2 \frac{\mathrm{d}\alpha_s}{\mathrm{d}\mu_R^2} = \beta(\alpha_s) = -(b_0\alpha_s^2 + b_1\alpha_s^2 + b_2\alpha_s^4 + \dots). \tag{1.2}$$

Here b_i refers to the i-loop β-function coefficient. For energy regimes where $m_q \ll \mu_R$ Equation 1.2 can be evaluated to

$$\alpha_s(Q^2, \Lambda_{\mathrm{QCD}}) = \frac{12\pi}{(11n_c - 2n_f)\log(Q^2/\Lambda_{\mathrm{QCD}}^2)}, \tag{1.3}$$

where Λ_{QCD} denotes a cut-off scale beyond which perturbation theory does not hold. The number of quark flavours and colours is described by n_f and n_c, respectively. A key element of Equation 1.2 is its minus sign which leads to an ever-decreasing strength of α_s at higher energy scales, a process known as *asymptotic freedom*. The two particularities of QCD, i.e. its increasing strength with distance and its decreasing strength at larger energy scales, have been thoroughly probed through measurements of α_s. A summary of measurements performed at H1, ZEUS, DØ, CDF and more recently at ATLAS and CMS is shown in Figure 1.2 [51–67].

The fact that QCD is asymptotically free simplifies the calculation of QCD processes at hadron colliders like the LHC, allowing for precise determination of QCD-based cross-sections.

The initial state for calculating these processes depends on the *hard interaction* between gluons or quarks. However, at the LHC beams of protons, extended objects comprised of gluons and quarks, the partons, are brought into collision. This results in the challenge that perturbative QCD can not describe this underlying dynamic state as the interactions between the partons do not happen across short distances. Instead, this dynamic state of an ensemble of partons, each carrying a fraction of the proton's momentum, $0 < x < 1$, is described through *parton distribution functions* (PDFs), $f_i(x, \mu_F^2)$, where μ_F describes an energy scale beyond which QCD again becomes perturbative.

The Dokshitzer-Gribov-Lipatov-Altarelli-Parisi (DGLAP) evolution equations describe the dependency of the PDFs on this energy scale [68–70]. The PDF set relevant for calculations at the LHC is the NNPDF3.0NLO PDF set [71] computed from a global dataset using multiple results, among which are new experimental data from ATLAS, CMS, HERA, and HERA-II[4]. Collectively, the entire process $p + p \to f + \bar{f}$, i.e. the creation of a fermion-antifermion pair in the final state, can be described using the *factorisation theorem* [72]

$$\sigma(pp \to f\bar{f}) = \sum_{i,j} \int \mathrm{d}x_i \mathrm{d}x_j f_i(x_i, \mu_F^2) f_j(x_j, \mu_F^2) \tag{1.4}$$

$$\times \hat{\sigma}(ij \to f\bar{f})(\hat{s}, x_i, x_j, m_f, \mu_F^2, \mu_R^2), \tag{1.5}$$

[4]For the complete set of experimental data see Ref. [71] and references therein.

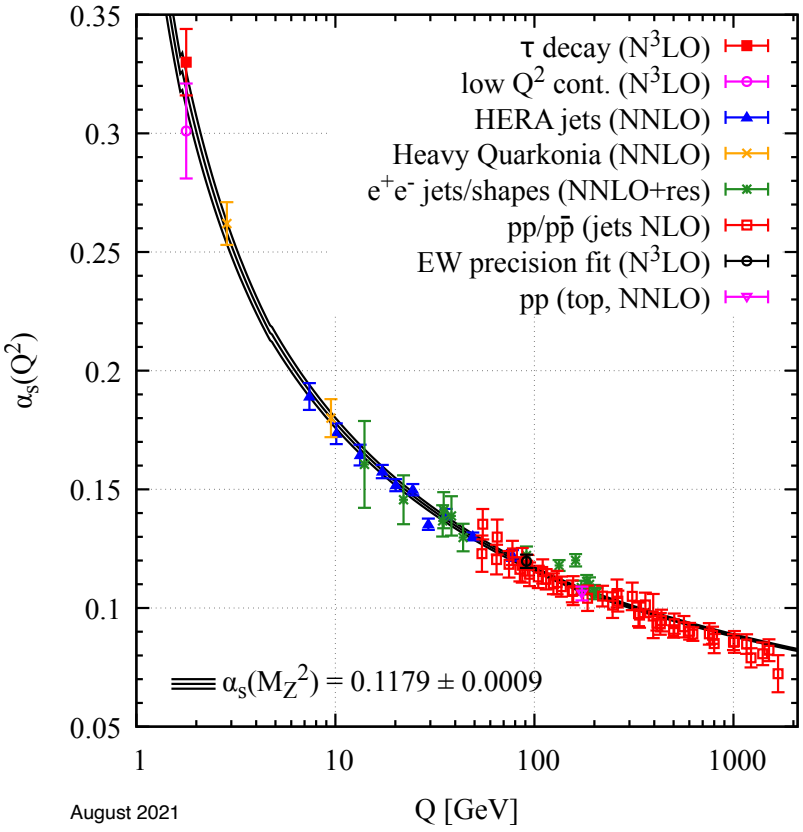

Figure 1.2: Summary of measurements of α_s highlighting its dependency on the energy scale Q taken from Ref. [51–67]. The degree of perturbation theory used in extracting α_s for each measurement is indicated in brackets (NLO:next-to-leading order; NNLO: next-to-next-to-leading order; NNLO+res.: NNLO matched to a resummed calculation; N3LO: next-to-NNLO).

where i and j label the parton types, i.e. gluons and (anti)quark flavours, and $\hat{\sigma}(ij \to f\bar{f})$ denotes the hard scattering cross-section of the underlying process computed using perturbative QCD. This cross-section depends on the renormalisation, factorisation scales, and the effective centre-of-mass energy of the parton-parton collision, $\hat{s}$, and the fermions mass m_f.

The factorisation theorem separates the proton-proton collision process into two parts: the PDFs (Equation 1.4) and the cross-section of the hard scattering (Equation 1.5). The PDFs, denoted by $f_i(x_i, \mu_F^2)$ and $f_j(x_j, \mu_F^2)$, describe the probability density of finding a parton with a certain fraction of the parent proton's momentum, x_i and x_j, depending on the factorisation scale μ_F^2. The hard scattering cross-section, $\hat{\sigma}(ij \to f\bar{f})$, denotes the underlying process of creating a fermion-antifermion pair in the final state, computed using perturbative QCD, depending on the renormalisation scale μ_R^2, the factorisation scale μ_F^2, the effective centre-of-mass energy of the parton-

parton collision, $\hat{s}$, and the fermion mass, m_f. This separation allows calculating the total cross-section of the process $p+p \to f+\bar{f}$ by convolving the PDFs and the hard scattering cross-section. The sum in the equation goes over all possible parton types i, j that can participate in the process, for example, quarks, antiquarks and gluons.

Similarly, the calculation of the cross-section of a process such as $\sigma(pp \to t\bar{t}Z)$, i.e. the associated production of a top quark pair and a Z boson at the LHC at a given centre-of-mass energy can be calculated knowing the necessary PDFs and the underlying theoretical cross-section of the hard interaction.

The Electroweak Interaction

The electroweak unification combines the electromagnetic and weak theory, described by quantum electrodynamics (QED) and quantum flavour dynamics (QFD).

QED is the field theory describing the interaction of electrically charged particles and photons in the SM. It is based on an Abelian gauge theory with the $U(1)$ symmetry group, resulting in a corresponding electromagnetic gauge field, A_μ. Due to the Abelian nature of QED, no photon-photon couplings exist. The great success of QED originates from the complete agreement of QED with special relativity [5]. Among these accurate predictions are the predictions of the anomalous magnetic dipole moment of the electron and the fine structure constant, α, which nowadays can be tested with outstanding accuracy [74, 75].

On the other hand, the weak interaction consists of the charged and neutral current weak interaction named after the electric charge of the respective mediator, namely the $W^\pm$ and Z bosons. The charged current weak interaction acts solely on left-handed weak eigenstates (d', s', b') placed in weak isospin doublets. While the weak eigenstates of the leptons are identical to their mass eigenstates, the weak quark eigenstates are comprised of linear combinations of their mass eigenstates (d, s, b) as defined via the CKM matrix[6] [76, 77]:

$$\begin{pmatrix} u' \\ s' \\ b' \end{pmatrix} = \begin{pmatrix} V_{ud} & V_{us} & V_{ub} \\ V_{cd} & V_{cs} & V_{cb} \\ V_{td} & V_{ts} & V_{tb} \end{pmatrix} \begin{pmatrix} u \\ s \\ b \end{pmatrix}.$$

The diagonal elements of the CKM matrix are close to unity, highlighting the preferred intra-generation flavour exchange. Off-diagonal elements are strongly suppressed, especially the corner elements V_{td} and V_{ub}. The left-handed weak isospin doublets of the first generation and the right-handed isospin singlets, which do not interact via

[5] R. Feynman is quoted calling QED "the jewel of physics" for its highly accurate predictions [73].

[6] The work of the authors of [76], M. Kobayashi and T. Maskawa, expanded the matrix formalism to three generations from the two generations initially described by N. Cabbibo in [77].

the charged current interaction, are then expressed as

$$\text{Leptons} : \begin{pmatrix} \nu_L \\ e_L \end{pmatrix},\ \nu_R,\ e_R,$$
$$\text{Quarks} : \begin{pmatrix} u_L \\ d'_L \end{pmatrix},\ u_R,\ d'_R$$

The indices L and R denote the left-handed and right-handed components. The second and third-generation doublets and singlets are defined analogously. This experimentally observed parity-violating nature of the weak interaction [78], i.e. the exclusive interaction via left-handed doublets, is reflected by the *vector-axialvector* structure of its coupling

$$W^{\pm} : \frac{-ig_W}{2\sqrt{2}}\gamma^{\mu}(1-\gamma^5)V_{ij}$$
$$Z : \frac{-ig_Z}{2}\gamma^{\mu}(C_V - C_A\gamma^5)$$

where γ^{μ} ($\mu \in [1,5]$), represent the Dirac matrices, $g_{W/Z}$ the weak coupling constants of the charged and neutral currents, $C_V = T_W^{(3)} - 2Q\sin(\theta_W)$ the vector and $C_A = T_W^{(3)}$ the axial vector components of the coupling with the weak mixing angle θ_W and V_{ij} the CKM matrix elements. While the charged current weak interaction via the exchange of $W^{\pm}$ bosons is maximally parity-violating, the neutral current weak interaction favours left-handed weak eigenstates but also couples to right-handed eigenstates. The strength and structure of the neutral current interaction and its parity violation depend on the magnitude of the experimentally measured C_V and C_A parameters. These parameters are hence of great importance for the top-Z coupling. In the SM, flavour-changing neutral currents (FCNC) only exist at higher orders by exchanging two $W^{\pm}$ bosons. However, these FCNCs are heavily suppressed by the GIM mechanism[7] [30].

Initially treated as disjoint theories, the weak interaction and electromagnetic interaction were unified by the electroweak unification into a joint description as a single Yang-Mills field by Glashow, Weinberg, and Salam [27–30]. The two underlying Lie groups, namely $SU(2) \otimes U(1)$, introduce the weak isospin gauge fields $W_{\mu}^{(i)}$ with $i \in [1,2,3]$ and the weak hypercharge gauge field B_{μ}, giving rise to the weak isospin and the weak hypercharge, Y_W, respectively. To conserve the invariance under $SU(2) \otimes U(1)$ gauge transformations, the weak hypercharge of a particle can be written as $Y_W = 2(Q - I_W^{(3)})$, where Q is the electrical charge of the particle and $I_W^{(3)}$ the third component of its weak isospin.

These fields further give rise to three massless W bosons (W_1, W_2, W_3) and the massless B boson. The Higgs field is added as a complex scalar $SU(2)$ doublet $(\phi^+, \phi^0)^T$ with a potential

$$V(\phi) = m^2\phi^{\dagger}\phi + \lambda(\phi^{\dagger}\phi)^2,$$

[7] Named after S.L. Glashow, J. Iliopoulos and L. Maiani.

In the case of a $\lambda < 0$, the neutral component of the doublet acquires a non-zero vacuum expectation value,

$$\langle\phi\rangle = \frac{1}{\sqrt{2}}\begin{pmatrix}0\\v\end{pmatrix}$$

inducing the breaking of the SM $SU(3)_C \otimes SU(2)_L \otimes U(1)_Y$ symmetry. The Z and W bosons acquire mass, $m_W^2 = I_W^2 v^2/4$ and $m_Z = (Y^2 + I_W^2)v^2/4$.

The Higgs acquires its mass through the vacuum expectation value and the coupling constant λ, given by $m_H = \lambda v$. The physical fields $W_\mu^\pm$, Z_μ and A_μ emerge after spontaneous symmetry breaking of the electroweak symmetry as linear combinations of the unphysical fields

$$\begin{aligned} W_\mu^\pm &= \frac{1}{\sqrt{2}}(W_\mu^{(1)} \mp iW_\mu^{(2)}) \\ Z_\mu &= +B_\mu \cos(\theta_W) + W_\mu^{(3)} \sin(\theta_W) \\ A_\mu &= -B_\mu \sin(\theta_W) + W_\mu^{(3)} \cos(\theta_W), \end{aligned}$$

where θ_W denotes the weak mixing angle. It relates the electric charge, the weak isospin and the weak hypercharge through $e = I_W \sin(\theta_W) = Y_W \cos(\theta_W)$ and also provides the relationship between the mass of the Z and W boson through $m_W = \cos(\theta_W)m_Z$. The photon and the gluon remain massless.

The coupling of the Higgs to other particles is characterised by the particle's mass, leading to a weak coupling for light particles and a strong for heavy particles like the electroweak bosons and the top quark.

1.1.1 Limitations of the Standard Model

The Standard Model of particle physics is a highly successful theory that has been able to accurately explain a wide range of phenomena in nature. Despite its success, the SM fails to explain several experimental observations, highlighting the need to expand it.

An example of such a shortcoming are astrophysical observations of rotation curves[8] [79], and velocity dispersions of galaxies [80, 81] showing significant discrepancies between the expected rotation curves and mass density and the observations, indicating the presence of significant contributions of invisible matter, namely *dark matter*. Furthermore, precise measurements of galaxy clusters indicate that dark matter's presence outweighs visible matter's presence. The SM does not explain this existence and the universe's apparent abundance of dark matter.

Additionally, cosmological measurements indicate the presence of a significant *dark energy* contribution making up the total energy of the known universe [82–85]. The SM does not include any candidates for dark matter particles, and it remains an open question of how dark matter and dark energy fit into our current understanding of the universe.

[8] Assuming Kepler's laws of motion.

While these astrophysical observations show that the SM is incomplete, others, such as the observation of neutrino oscillations [86], are only possible if at least two neutrino generations are massive and therefore disagree with the corresponding SM predictions. The SM is hence not only incomplete, but it also partially mispredicts nature's properties, making the need for a more complete theory apparent.

A popular example of an extension of the SM is *Super Symmetry* (SUSY). As its name implies, SUSY introduces a new feature, a symmetry between fermions and bosons. This symmetry introduces new (*supersymmetric*) particles, the so-called *sparticles*, which differ from their SM partners by half a unit of spin. The supersymmetric partners of SM fermions are spin-0 scaler *sfermions* and the supersymmetric partners of SM bosons represented by the spin-half *gauginos*. Through SUSY, a unification of particle physics and gravity [87] is provided at the Planck energy scale, $M_P \sim 10^{19}\,\text{GeV}$. At this scale, the strength of the gauge interactions known from the SM and the strength of gravity become comparable, making SUSY a seemingly exciting candidate for a *grand unified theory*.

1.2 The Top Quark

The existence of a third generation of quarks was first postulated through the introduction of the CKM mechanism in 1973 [76]. With this mechanism, Kobayashi and Maskawa proposed a solution to the previously observed CP violation in kaon decays [88]. Their expansion of the quark sector using three left-handed $SU(2)$ quark doublets not only predicted the existence of two other particles, but its formalism also agrees with experimental observations since. The discovery of the τ-lepton [89] in 1975, and the first particle of this new hypothetical third quark generation, the bottom quark, in 1977 by the E288 experiment team [90], strongly suggested the existence of a third neutrino in the lepton sector and the missing third generation up-type quarks in the quark sector.

Even though a $SU(2) \times U(1)$ gauge symmetry involving six quarks seemed to be preferred by the physics community of the 1970s and 80s due to its ability to describe the observed weak phenomena, including CP violation, alternative topless models were developed too [91, 92]. These models, strengthened by the failure to discover the top quark at PETRA, broke the understanding of quarks and leptons in terms of families and introduced the bottom quark in their simplest forms as a $SU(2)$ singlet. Just like models without a strange quark would introduce strangeness-changing neutral currents, models without a top quark would introduce flavour-changing neutral currents. By analysing B-meson decays using experimental data taken by the CLEO collaboration, the possibilities of such models with a $SU(2)$ singlet were ruled out [93–95].

Measurements proposed in the late 1970s and early 1980s to determine the number of low mass neutrinos in radiative Z^0 production processes ($e^+e^- \to \gamma\nu\bar{\nu}$) [96–98] were conducted by experiments at the LEP collider in the early 1990s [99–101]. The results of these measurements favoured the hypothesis of three light neutrino generations, further supporting the hypothesis of the existence of a third up-type quark.

A SM candidate for this particle, now known as the top quark, was discovered in 1995 by the CDF [102] and DØ collaborations [103] at the TEVATRON collider, completing the SM quark sector. A primary goal of the experiments at the TEVATRON and LHC was to measure this quark's properties to probe the SM's electroweak sector further. The combined mass of the top quark, m_t, based on published direct measurements from TEVATRON Run 1 and Run 2 and LHC data taken at $\sqrt{s} = 7\,\text{TeV}$ results in an exceptional mass of $m_t = 172.69 \pm 0.30\,\text{GeV}$ [42][9], making the top quark the heaviest known quark in the SM[10].

This exceptionally high mass leads to a Yukawa coupling close to unity, leading to a seemingly intimate relationship of the top quark and the Higgs and assigning the top quark a central role in the electroweak symmetry breaking in the SM.

[9] A discussion of the definition of the top quark mass can be found in the review *The Top Quark* in Ref. [42].

[10] For comparison, a gold atom ($m_{AU} = 196.9665\,\text{u} \approx 183\,\text{GeV}$) is often used to highlight the large mass of the top quark; however, the mass of the top quark is closer to that of a (less popular) rhenium atom ($m_{Re} = 186.207\,\text{u} \approx 173\,\text{GeV}$).

Owing to $|V_{tb}| \gg |V_{td}|, |V_{ts}|$ the decay width of the top quark is dominated by the two-body decay into W bosons and b quarks, resulting in a predicted decay width in the SM at NLO[11] of $\Gamma_t = 1.35\,\text{GeV}$ [104]. CMS performed a precise measurement of the top quark decay width by combining measurements of the ratio $\mathcal{B}(t \to Wb)/\mathcal{B}(t \to Wq)$, with $q \in [b\,, s\,, d]$, and previously performed cross-section measurements [105], resulting in $\Gamma_t = 1.36 \pm 0.02(\text{stat.})^{+0.14}_{-0.11}(\text{syst.})$ [106], agreeing with the SM prediction. This decay width can be converted into a lifetime of about $0.5 \times 10^{-24}\,\text{s}$, which lies below the typical QCD hadronisation time scale by about one order of magnitude. As a result, the top quark decays before top-flavoured hadrons or $t\bar{t}$-quarkonium-bound states can form [107], thereby passing on its properties to its decay products. A reconstruction of these decay products allows for reconstructing the top quark and its properties.

The property studied in the most remarkable detail is the top quark's mass, as this value significantly impacts many SM predictions. Among these predictions is the electroweak stability of the SM where small changes in the Higgs and top quark mass can significantly impact the conclusions on vacuum stability, i.e. whether additional minima in the Higgs potential exist [108, 109].

While the charges of all other quarks could be determined through production at the threshold in e^+e^- collisions, no e^+e^--collider with sufficient centre-of-mass energy was yet constructed to produce $t\bar{t}$ pairs. Results of the top quark charge measurement by CDF, DØ, ATLAS and CMS excluded exotic top quark models [110, 111] with top quark charges of $q_t = 4/3e$ and indicate that the observed particles charge is consistent with the SM charge prediction for the top quark [112–115]. The third component of the top quark's weak isospin, defining the quark as an up-type quark, has yet to be measured. This relevant electroweak coupling parameter can be probed through measurements of the associated production of top quarks and Z bosons or photons. Of particular interest for this thesis is the top-Z coupling, where the coupling is probed through effective field theory (EFT) fits based on inclusive and differential cross-section measurements of processes involving top-Z couplings. The following section introduces the single-top-quark and top-quark pair production. Afterwards, the associated production with a Z boson is discussed, and means of probing the top-Z coupling are presented.

Top Quark Production

Two families of top quark production processes exist at hadron colliders: $t\bar{t}$ pair and single-top-quark (single-top) production. Tree-level Feynman diagrams of these processes are shown in Figure 1.3 with the top quark highlighted in red in the $t\bar{t}$ production processes and blue in the single-top production processes. The dominant production mode at the LHC is top-antitop pair production ($t\bar{t}$ production). This QCD-based $t\bar{t}$ production process can be split into two different production processes: gluon-gluon fusion ($gg \to t\bar{t}$) and quark-antiquark annihilation ($q\bar{q} \to t\bar{t}$). At the

[11] Assuming $m_t = 173.3\,\text{GeV}$.

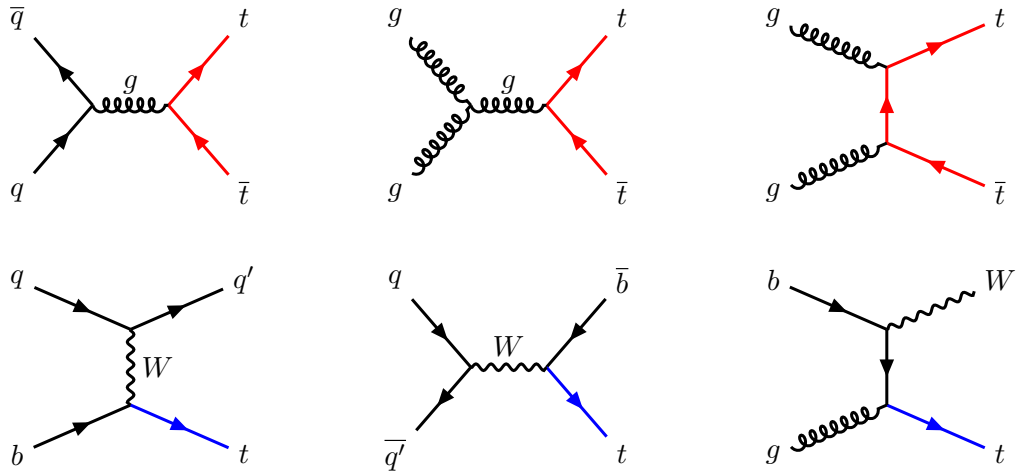

Figure 1.3: Tree level Feynman diagrams of the $t\bar{t}$ production process (top row) and the single-top-quark production process (bottom row). From left to right, the quark-antiquark annihilation and gluon-gluon fusion processes are shown for the $t\bar{t}$ production process and the s-channel, t-channel, and associated for the single-top-quark production process. The produced single top quarks and top quark pairs are marked in blue and red, respectively.

LHC, gluon-gluon fusion makes up about 90 % of the total production cross-section, with the remainder from quark-antiquark annihilation.

The $t\bar{t}$ production cross-section has been measured at the TEVATRON ($p\bar{p}$ at $\sqrt{s} = 1.96\,\text{TeV}$) by CDF and D∅ [116–119] and at the LHC (pp at $\sqrt{s} = 5,\ 7,\ 8,\ 13$, and $13.6\,\text{TeV}$) by ATLAS and CMS [120–133]. These measurements at the two colliders agree with NNLO + NNLL calculations [134–136]. A summary is given in Figure 1.4. New ATLAS and CMS measurements of the $t\bar{t}$ cross-section recently performed at a centre-of-mass energy of the LHC of $13.6\,\text{TeV}$ are also in agreement with the SM prediction [133, 137]. These measurements highlight the predictive power of the SM and the associated extensive top quark physics program at the LHC and TEVATRON.

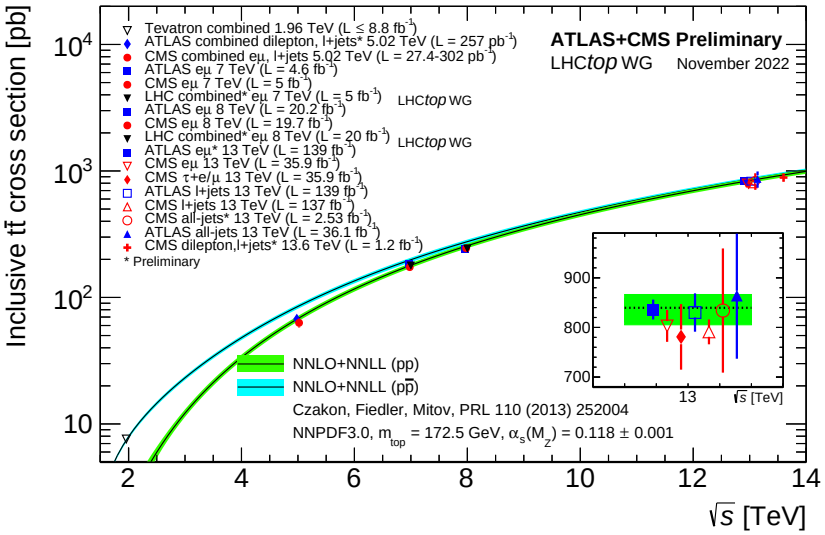

Figure 1.4: Summary of the $t\bar{t}$ cross-section measurements performed at the TEVATRON and the LHC as a function of the centre-of-mass energy, covering a range from $\sqrt{s} = 1.96\,\text{GeV}$ up to $\sqrt{s} = 13.6\,\text{GeV}$. The measurements are compared to the NNLO QCD calculation completed with NNLL resummation. Measurements at identical centre-of-mass energy are displayed next to one another for clarity. The summary is provided by the LHCTOPWG [138].

Top Quark Decay

Due to the heavy suppression of the off-diagonal elements of the CKM matrix reflected by $|V_{tb}| \gg |V_{td}|, |V_{ts}|$, top quarks predominantly decay into a pair of W and b quarks. The W can subsequently decay into a quark-antiquark pair ($q\bar{q}'$) or into a charged lepton and the corresponding (anti-)neutrino ($\ell\bar{\nu}_\ell$) leading to three possible final states for $t\bar{t}$ pair production

$$t\bar{t} \to W^+bW^-\bar{b} \to q\bar{q}'b + q''\bar{q}'''\bar{b}, \qquad (45.7\,\%)$$
$$t\bar{t} \to W^+bW^-\bar{b} \to q\bar{q}'b + \ell^-\nu_{\ell^-}\bar{b}, \qquad (43.8\,\%)$$
$$t\bar{t} \to W^+bW^-\bar{b} \to \ell^+\nu_\ell b + \ell'^-\bar{\nu}_{\ell'^-}\bar{b}. \qquad (10.5\,\%)$$

where the three decay modes are defined as the all-hadronic, lepton+jets (ℓ+jets) and dilepton ($\ell\ell$) decay channels, respectively. A further split of the lepton+jets (dilepton) channel based on lepton flavour leads to further sub-channels contributing approximately 15 % (1 to 2 % each)[12]. Each of these channels comes with particular experimental challenges. The all-hadronic decay channel has the largest branching

[12]It should be noted here those decay modes involving τ leptons are often not considered when lepton+jets or dileptonic final states are probed. In these cases, *leptons* only refers to electrons and muons.

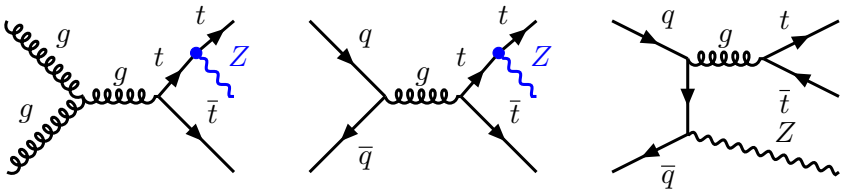

Figure 1.5: Examples of Feynman diagrams showing the top-Z coupling in the $t\bar{t}Z$ production process with the Z marked in blue in gluon-gluon fusion (left) and quark-antiquark annihilation (middle). In the associated production process (right), no top-Z coupling is present.

ratio but comes with large background contributions from other QCD processes, which are experimentally difficult to suppress. For measuring top quark properties and the couplings to the gauge bosons, the lepton+jets and dilepton channels are favoured as they significantly reduce the impact of QCD-driven background processes and provide a relatively clean environment to perform precision measurements. With an increasing number of neutrinos in the final state, new reconstruction challenges arise because the neutrinos can not be fully reconstructed in the ATLAS detector.

1.3 Top Quarks in Association with Z Bosons

The study of the properties of the top quark can be grouped into two areas of study: The study of the top quark's properties and its coupling to the bosons of the SM. The second area corresponds to processes where top quarks are produced in association with SM gauge bosons, denoted as $t + X$ or $t\bar{t} + X$ where X represents either the Higgs boson ($t + H$, $t\bar{t} + H$), Z boson ($t + Z$, $t\bar{t} + Z$), photon ($t + \gamma$, $t\bar{t} + \gamma$) or W boson ($t + W$[13]).

These processes are particularly relevant for all BSM theories, which modify the coupling of the top quark to SM bosons or introduce new couplings.

This work is mainly concerned with measuring the inclusive cross-section of the $t\bar{t}Z$ production process in final states with three leptons and the subsequent interpretation of the measurements completed by further measurements of differential cross-sections in the framework of the SM EFT. Example Feynman diagrams of the underlying SM process are shown in Figure 1.5 with the Z-top vertex highlighted as a blue dot.

In particular, this Z-fermion vertex can be described by:

$$\Gamma_{\mu}^{Z\,f\bar{f}} = \frac{g}{2\cos\theta_W}\gamma^{\mu}\left(g_V^f - g_A^f\gamma^5\right), \tag{1.6}$$

where g_V^f and g_A^f are the vector and axial vector couplings of the Z boson to the fermion, respectively. In the case of the SM-like top-Z coupling, these constants are

[13]For simplicity, the "+" is omitted hereafter. The W in the $t\bar{t}W$ process is expected to originate from the initial state, making the process insensitive to the top-W coupling.

given by

$$g_V^t = I_W^{(3),t} - 2Q_i^t \sin_W^\theta = \frac{1}{2} - \frac{4}{3}\sin^2\theta_W, \tag{1.7}$$

$$g_A^t = I_W^{(3),t} = \frac{1}{2}, \tag{1.8}$$

assuming the weak isospin of the top quark is $I_W^{(3),t} = \frac{1}{2}$, and its charge is $Q_i^t = \frac{2}{3}e$ in units of the elementary charge.

1.3.1 Theory calculations

While the top-Z-coupling appears almost trivial at first glance, dedicated theory calculations of the $pp \to t\bar{t}Z$ production process are far from it. Today, the cross-section of the process $pp \to t\bar{t}Z$ can be typically calculated at NLO as shown, for example, in Refs. [139, 140] which are typically matched to parton shower algorithms. Even though complete NNLO calculations are not yet available, at least parts of higher-order perturbative corrections can be taken into account already today through resummation techniques regarding corrections originating from the emission of soft gluons. These contributions arise from the fact that any particle detector has a finite resolution implying that measured cross-sections always include arbitrarily soft particles. The following paragraphs summarise such dedicated theory calculations of the $t\bar{t}Z$ production process from Refs. [141] and [142].

The first set of the theoretical predictions performs threshold resummation of soft gluon corrections to the total associated production of a top quark pair with a Z boson, $t\bar{t}Z$. The authors provide resummation results at NNLL accuracy using the direct QCD Mellin space technique in the three-particle invariant mass kinematics. The calculations follow the procedures in the authors' related work for the $pp \to t\bar{t}H$ production process, described in Ref. [143].

The NLO cross-section is calculated using the MadGraph5_aMC@NLO generator for the differential distributions, and PowHel [144–146] for the NLO total cross-section and the PDF4LHC15_30 PDF set.

The input parameters of the calculations are

$$m_t = 172.5\,\text{GeV}, \qquad m_Z = 91.188\,\text{GeV},$$
$$m_W = 80.385\,\text{GeV}, \qquad m_H = 125\,\text{GeV}.$$

The fermi constant is taken to be $G_F = 1.1663787 \times 10^{-5}\,\text{GeV}^{-2}$. Three scale choices are evaluated:

$$\begin{aligned} m_{t\bar{t}Z}\text{-based}: &\quad \mu_F = \mu_R = m_{t\bar{t}Z} = \sqrt{(p_t + p_{\bar{t}} + p_Z)}^2 \\ \frac{m_{t\bar{t}Z}}{2}\text{-based}: &\quad \mu_F = \mu_R = \frac{m_{t\bar{t}Z}}{2} \\ M\text{-based}: &\quad \mu_F = \mu_R = M = m_t + \frac{m_Z}{2}, \end{aligned}$$

where p_t, $p_{\bar{t}}$, and p_Z are the four momenta of the top, anti-top and the Z boson, respectively.

While the first choice represents the natural choice for the threshold and kinematics in the resummation, the second choice is often used in fixed-order calculations. Scale uncertainties are evaluated by independently varying the central scale values up and down by a factor of 2. The calculations also include PDF + α_s uncertainties. For a detailed description of the calculation and the treatment of uncertainties, see the original Ref. [141] and references therein. The authors combine the predictions of the three scale choices to

$$\sigma^{\text{NLO+NNLL}}_{t\bar{t}Z,\,\text{Kulesza et al.}} = 863^{+8.5\,\%}_{+9.9\,\%}(\text{scale}) \pm 3.2\,\%(\text{PDF} + \alpha_s), \tag{1.9}$$

which serves as the primary reference $t\bar{t}Z$ cross-section for this analysis. The authors also provide the bare NLO results for the three scales choices, which range between $\sigma^{\text{NLO}}_{t\bar{t}Z}(m_{t\bar{t}Z}) = 659^{+14.1\,\%}_{-12.7\,\%}$ for the $m_{t\bar{t}Z}$-based scale choice to $\sigma^{\text{NLO}}_{t\bar{t}Z}(M) = 843^{+9.7\,\%}_{-11.3\,\%}$ for the M-based scale choice. From these results, two conclusions can be drawn: Firstly, a measured cross-section with uncertainties less than 10 % will rival the precision achieved in theoretical calculations, a performance that was already achieved by the recent measurements of the process by ATLAS and CMS [147, 148]. The inclusive measurement results presented here surpassed this threshold. Secondly, it can be seen that precise measurements of the cross-section in the order of less than 10 % uncertainty provide sensitivity to NLO versus NLO+NNLL calculations.

The second set of theoretical calculations of the associated production of a top quark pair with a Z boson, $t\bar{t}Z$, include the complete set NLO electroweak and QCD contributions of $\mathcal{O}(\alpha_s^i \alpha^{j+1})$ with $i+j = 2$, 3 [142]. The authors make predictions for the $pp \to t\bar{t}Z(+X)$ final state at a centre of mass energy of $\sqrt{s} = 13\,\text{TeV}$, where $+X$ indicates that the process is modelled inclusively, including extra QCD and QED radiation. Broggio et al. too use the MadGraph5_aMC@NLO generator to obtain NLO corrections for the $t\bar{t}Z$ production process and perform soft gluon emissions corrections resummed to NNLL accuracy based on the work in the original references of the authors [149–152]. The used PDF set is the `LUXqed17_plus_PDF4LHC15_nnlo_100` PDF set [153, 154] which is based on the PDF4LHC PDF set. For the calculations, the following set of values for SM parameters is used:

$$\begin{aligned} m_t &= 173.34\ (172.5)\,\text{GeV}, & m_Z &= 91.1876\ (91.188)\,\text{GeV}, \\ m_W &= 80.385\ (80.385)\,\text{GeV}, & m_H &= 125\ (125)\,\text{GeV}, \end{aligned}$$

where the numbers in brackets describe the constants used in the calculations by Kulesza et al. presented above, with the only notable difference being the slightly different top mass used in the two calculations. Two choices for the central values for the factorisation and renormalisation scale are adopted. The first scale choice is based on

$$H_\text{T} = \sqrt{m_t^2 + p_{\text{T},t}^2} + \sqrt{m_t^2 + p_{\text{T},\bar{t}}^2} + \sqrt{m_Z + p_{\text{T},Z}^2}, \tag{1.10}$$

with the masses of the top quark (m_t), and the transverse momenta of the top ($p_{\mathrm{T},t}$) and anti-top quark ($p_{\mathrm{T},\bar{t}}$) and the Z boson ($p_{\mathrm{T},Z}$).

Again, the second scale choice is the $m_{t\bar{t}Z}$-based scale choice already presented above. Uncertainties originating from higher-order scale corrections are again estimated by varying scales up and down by a factor of 2.

PDF uncertainties are evaluated following the procedure described in Ref. [155]. The calculated cross-section resulting from the combined scales choices is

$$\sigma^{\mathrm{NLO+NNLL}}_{t\bar{t}Z,\,\mathrm{Broggio\ et\ al.}} = 810.9 \pm 0.3\,\%(\mathrm{MC\,stat.})^{+11.1\,\%}_{-9.6\,\%}(\mathrm{scale}) \pm 2.5\,\%(\mathrm{PDF})\,\mathrm{fb}, \qquad (1.11)$$

agreeing with the calculation by Kulesza et al. within uncertainties. Comparing these two calculations provides sensitivity to the small differences in the two calculations, such as the slightly different scale choices or the used top-quark mass.

Figure 1.6 shows distributions of the invariant mass of the $t\bar{t}Z$ system, $m_{t\bar{t}Z}$, and the transverse momentum of the Z boson, $p_{\mathrm{T},Z}$, comparing the $\mathrm{NLO_{QCD}}$+NNLL calculations with NLO +NNLL calculations. In addition to the differential cross-section different a study on resummation effects (NLO vs. NLO +NNLL), the difference between the additive and multiplicative approach (NLO+NNLL vs. NLO $\times$ NNLL) including only scale uncertainties and the impact of electroweak corrections ($\mathrm{NLO_{QCD}}$+NNLL vs NLO+NNLL) is provided through the panels in the figure which is discussed in detail in the author's main work in Ref. [142].

While the calculations of the SM cross-section at NLO+NNLL is a well-established concept today, the question remains whether the SM adequately describes the $pp \to t\bar{t}Z$-process realised in nature or whether other yet hidden contributions play a role too. The following section will address this question and give a brief insight into possible extensions of the SM.

1.3.2 Extensions to the SM

Today various extensions to the SM exist that could affect the Z-top vertex, such as introducing new neutral gauge bosons, like the Z' boson, which would introduce a $pp \to Z' \to f\bar{f}$ production process and hence also impact the $t\bar{t}Z$ production rate.

Precision measurements of observables sensitive to these changes, such as inclusive and differential cross-sections, can probe the top quark sector for new physics and set constraints on such possible BSM theories.

While the above example represents a dedicated search for new particles, in general, physics beyond the SM, specifically modifications of the coupling of the top quark and the Z boson, can, in practice, be studied in the context of an effective field theory (EFT), namely the *Standard Model Effective Field Theory*, SMEFT [156–158], in a model-independent way.

In this approach to extend the SM beyond its dimension-4 terms in the Lagrangian, additional degrees of freedom are introduced. The SM is considered a low-energy approximation of a BSM model valid at higher energies outside the energy phase space currently accessible at the LHC. New effects from BSM theories can

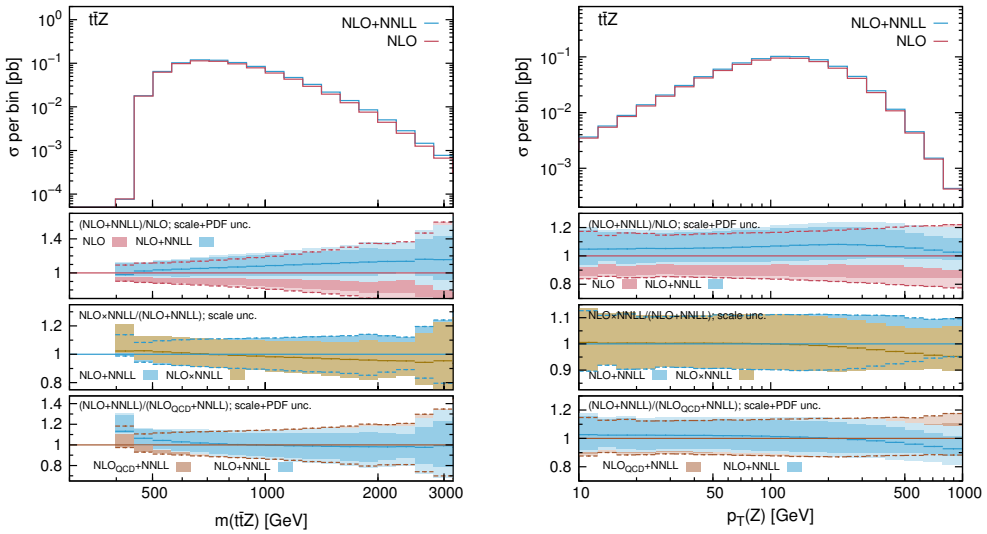

Figure 1.6: Distributions of the invariant mass of the $t\bar{t}Z$ system, $m_{t\bar{t}Z}$, and the transverse momentum of the Z boson, $p_{\mathrm{T},Z}$. The top ratio focuses on resummation effects (NLO vs. NLO +NNLL). The second ratio addresses the difference between the additive and multiplicative approach (NLO+NNLL vs. NLO × NNLL), including only scale uncertainties. The last third ratio describes the impact of electroweak corrections ($\mathrm{NLO_{QCD}}$+NNLL vs NLO+NNLL). Figures are taken from Ref. [142].

then be characterised through a set of operators, $\{\mathcal{O}^{(2)}\}$, and corresponding Wilson coefficients, $\{\mathcal{C}^{(d)}\}$:

$$\mathcal{L}_{\mathrm{SMEFT}} = \mathcal{L}_{\mathrm{SM}} + \sum_{d>4} \mathcal{L}^{(d)}, \quad \mathcal{L}^{(d)} = \sum_{i=1}^{n_d} \frac{\mathcal{C}_i^{(d)}}{\Lambda^{d-4}} \mathcal{O}_i^{(d)}, \tag{1.12}$$

where Λ denotes a suitable cutoff scale which is conventially set to $\Lambda = 1\,\mathrm{TeV}$. While the number of the operators $\mathcal{O}^{(d)}$ is known up to $d = 8$, current computation tools only allow the study of potential SMEFT effects up to $d = 6$. In the analysis addressed in this thesis, the focus lies on $\mathcal{L}^{(6)}$ as it can be shown that this order is the lowest relevant order for the top quark sector. Higher order operators are suppressed accordingly by higher orders of Λ.

The dependence of an observable $\mathcal{O}$ on EFT effects described by set of Wilson coefficients, $\{\mathcal{C}^{(d)}\}$, can be parametrised as

$$\mathcal{O} = \mathcal{O}_{\mathrm{SM}} + \sum_i \mathcal{C}_i A_i + \sum_{i,j} \mathcal{C}_i \mathcal{C}_j B_{ij}, \tag{1.13}$$

where A_i and B_{ij} are parameters for probing individual Wilson coefficients and pairs of coefficients through a simple quadratic fit. The linear term, A_i, can hence be understood as the interference between the SM and the SMEFT effects. The quadratic

term, B_{ij}, then denotes a purely SMEFT-based contribution, where B_{ii} represents a *purely* quadratic term and B_{ij} with $i \neq j$ refers to a *cross* term.

Since the SM term, $\mathcal{O}_{\text{SM}}$, is calculated at LO in QCD, discrepancies between MC and $t\bar{t}Z$ data can arise, which relies on modelling at NLO in QCD. These potential discrepancies are removed following a scaling approach:

$$\mathcal{O} \to \mathcal{O}' = \frac{\mathcal{O}_{\text{SM}}^{\text{NLO}}}{\mathcal{O}_{\text{SM}}^{\text{LO}}} \times \left(\mathcal{O}_{\text{SM}}^{\text{LO}} + \sum_i \mathcal{C}_i A_i + \sum_{i,j} \mathcal{C}_i \mathcal{C}_j B_{ij} \right). \tag{1.14}$$

Any deviations of observables sensitive to the effects induced by the operators can then be expressed in terms of $\{\mathcal{C}^{(d)}\}$, which in the absence of new physics, turn into constraints on these coefficients.

The set of operators considered here consists of 29 dimension-6 SMEFT operators, corresponding to 42 Wilson coefficients[14].

Given the above description of the $t\bar{t}Z$ production process, the question arises of the state of the most recent measurements and whether these measurements prefer the SM prediction. A summary of such $t\bar{t}Z$ measurements and indications for previously performed EFT interpretations is shown in Figure 1.7. The figure shows the ratio between the measured and theoretical cross-sections for each measurement of the process performed by the ATLAS and CMS collaboration.

First evidence for the $t\bar{t}Z$ process was found by CMS and ATLAS at $\sqrt{s} = 7\,\text{TeV}$ [159] and 8 TeV [160], respectively. The process was later observed by CMS at $\sqrt{s} = 8\,\text{TeV}$ [161] and firmly established with more precise measurements at $\sqrt{s} = 13\,\text{TeV}$ by the two experiments [147, 148, 162, 163]. Currently, the most in-depth measurement of the top-Z coupling is performed by CMS in a 13 TeV measurement using a partial Run 2 dataset consisting of $77.5\,\text{fb}^{-1}$. The measurements utilise final states with three (3ℓ) or four (4ℓ) leptons where the Z is reconstructed through the decay into a pair of leptons with the same flavour and opposite charge. CMS provides an interpretation of this measurement in the context of SMEFT in the Warsaw basis [167] in the form of constraints for four relevant Wilson coefficients: c_{tZ}, $c_{tZ}^{[I]}$, $c_{\phi t}$, and $c_{\phi Q}^{-}$, where the former two induce electroweak dipole moments, and the later two induce anomalous neutral-current interactions. The measurements performed by the two experiments are consistent with the SM predictions.

The current status of the $t\bar{t}Z$ process can hence be summarised into a set of precise inclusive and differential measurements by both ATLAS and CMS and first probes of the top-Z interaction. Recent experimental measurements have reached the same level of precision as the corresponding theoretical predictions, which are today available at NLO+NNLL precision. All of the recent measurements agree with the SM prediction, with slightly higher cross-sections favoured by the measurements than predicted by the dedicated theory calculations.

This thesis presents the results of the most recent ATLAS measurement of the $t\bar{t}Z$ production process, emphasising the author's contributions.

[14] A detailed description of these operators and their effects is provided in Section 7.4.

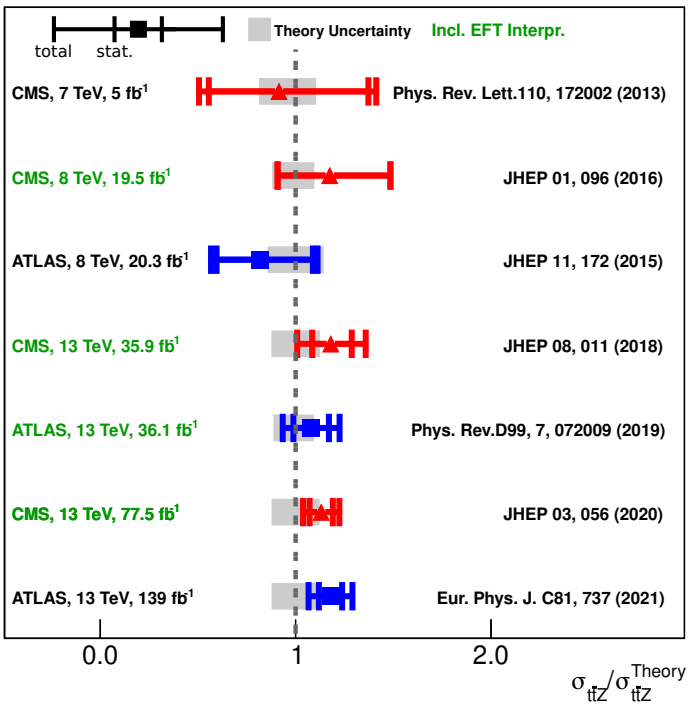

Figure 1.7: Previous measurements of the $t\bar{t}Z$ production at the LHC [147, 148, 159–163]. The measurements are presented as the ratio of the measured cross-section with respect to the theory predictions. The inner and outer error bars represent the statistical and combined statistical and systematic uncertainty. Different markers indicate the collaborations. Measurements with a corresponding EFT interpretation are marked in green. The grey blocks represent the theory uncertainties [142, 145, 164–166]. The published measurement by CMS at $\sqrt{s} = 8\,\text{TeV}$ only provides total uncertainties.

CHAPTER 2

Experimental Methods

The relevant physical quantity of the measurements described in this work relies on a setup delivering proton-proton collisions to study the properties of the underlying interactions. These collisions are provided by the Large Hadron Collider (LHC), the largest particle-physics accelerator ever built, and recorded using the ATLAS experiment. Both are located at the largest particle physics laboratory of the world, the *European Organization for Nuclear Research*, CERN (French: *Conseil Européen pour la Recherche Nucléaire)*.

CERN was founded in 1954, initially devoted to the peaceful study of atomic nuclei after the second world war. Shortly after, the research focus was shifted towards high-energy physics (HEP) and the study of elementary particles and their interactions. CERN currently has 23 member states with hundreds of institutes and universities across the globe contributing to research efforts making it the largest and most complex research organisation to date. Today CERN's primary role is to provide the infrastructure for the hosted experiments. These experiments are run by large international collaborations comprised of national research organisations and institutes throughout the pool of member and associated member states.

The CERN accelerator complex and the LHC, which provide the proton-proton collision data relevant to this thesis, are introduced in the following sections. The ATLAS experiment and its subdetectors are introduced in section Section 2.2. Section 2.3 then discusses the processing of the signals recorded by the subdetectors into relevant physical properties of particles within the reconstruction and identification process.

2.1 The Large Hadron Collider (LHC)

The Large Hadron Collider (LHC) [168] at CERN is currently the most powerful particle accelerator in the world. The 27 km circular accelerator is located in an underground tunnel at CERN on the Swiss-French border near Geneva. It completes a series of pre-accelerators in which protons are gradually accelerated to energies of 6.8 TeV, and finally brought to collision in opposite orbits, leading to collision energies of currently 13.6 TeV[1].

The LHC was first proposed in the 1980s as a way to probe the fundamental nature of the universe at energies that were not accessible with previous generations of accelerators. Construction of the LHC began in 1998, and the first beams were circulated in the accelerator in 2008. Since then, data taken at the LHC has been used to make several groundbreaking discoveries, including the Higgs boson discovery in 2012.

Since the first beams were circulated, LHC has operated at the cutting edge of technology, with its powerful magnets and complex detectors pushing the limits of what is currently possible in high-energy physics research. While LHC can accelerate both heavy ions and protons, the operation mode relevant for this work is that of proton-proton collisions.

As of 2020, the source of the highly energetic proton beams is the new Linear accelerator 4 (LINAC4), which accelerates negative hydrogen ions to 160 MeV using radiofrequency (RF) cavities. Upon injection into the Proton Synchrotron (PS) Booster, the H^- ions are stripped off their 2 electrons, leaving only protons. For Run 1 and Run 2, the primary injection of protons into the PS BOOSTER was performed directly by LINAC4's predecessor, LINAC2[2], from a bottle of hydrogen gas.

In the PS BOOSTER, the protons are accelerated in four superimposed synchrotron rings up to 2 GeV and then injected into PS, thereby greatly enhancing the initial energy and number of protons entering the PS compared to directly injecting into PS. In the PS, the protons are accelerated using conventional dipole magnets in a synchrotron with a circumference of 628 m up to 26 GeV. The Super Proton Synchrotron (SPS), a synchrotron with a circumference of approximately 7 km and hence the second largest machine in CERN's accelerator complex after the LHC, accelerates the protons up to 450 GeV. Finally, the protons are injected into the LHC. In the LHC, they are accelerated by a factor of approximately 14 using 16 RF cavities, each driven by a high-power klystron, bringing the protons from 450 GeV to beam energies of 6.8 TeV.

Colloquially, particle physics refer to particle beams when considering collisions. However, at the LHC these beams consist of particle packages or bunches of approximately 10^{11} protons. The number of bunches varies with the filling scheme of the LHC. These bunches are arranged in sets, so-called bunch trains. They are

[1] The relevant centre of mass energy (CME) for this work is 13 TeV, which was achieved during the second run of data taking (Run 2). The quoted 13.6 TeV represent the current CME.

[2] Note that the predecessor is not LINAC3. LINAC3 is the starting point for ions, providing the lead ions for the LHC.

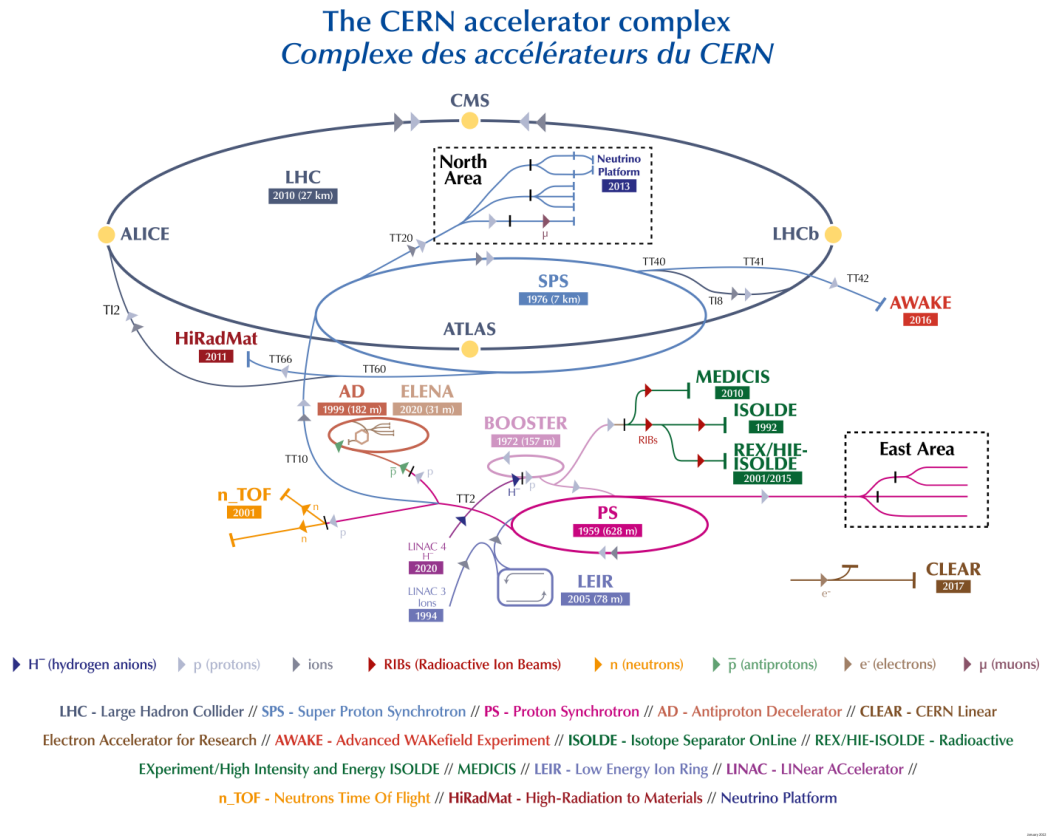

Figure 2.1: Overview of the CERN accelerator complex supplying accelerated particles to several different experiments across the CERN site. The current LHC accelerator chain consists of the pre-accelerators LINAC 4, the booster, the Proton-Synchrotron (PS), the Super Proton Synchrotron (SPS) and finally, the LHC itself. ©CERN

crossed and brought into a collision every 25 ns at the heart of the four LHC experiments, corresponding to a collision frequency of 40 MHz. The high energy proton beam is steered and focused around the ring using 1232 superconducting dipole and 474 quadrupole magnets with additional octupole magnets providing higher order focussing corrections. An overview of the CERN accelerator complex is shown in Figure 2.1.

The LHC hosts four main experiments. The two large multi-purpose detectors ATLAS and CMS [169, 170], located at tunnel entry point 1 and 5, respectively, perform precision measurements in the high-energy environment provided by the LHC. The ALICE experiment [171], situated at point 2, is a specialised detector focussing on heavy-ion collisions and the study of strongly interacting matter. The LHCb experiment [172], located at point 8, is an asymmetrical forward detector specialised to study the physics of B mesons.

The LHC has been operating since 2010 following a magnet quench accident and subsequent repair time shortly after its commissioning in 2008. In March 2010, the physics program of the LHC and the four experiments commenced to carefully test the predictions of the SM and search for new physics beyond it. Of particular interest in 2010 was the search for the Higgs boson. Earlier experiments at LEP [173] and TEVATRON [174] had already ruled out a wide range of possible Higgs masses, which lead to two possible outcomes for the experiments at the LHC: either the Higgs boson would be found or it would not be found, with either outcome being groundbreaking for particle physics.

During the data-taking period from 2010 until the end of 2011 (Run 1), the LHC delivered about $5.5\,\text{fb}^{-1}$ of integrated luminosity at $\sqrt{s} = 7\,\text{TeV}$. In 2012 the beam energies were increased to 4 TeV and data corresponding to about $23\,\text{fb}^{-1}$ was taken, eventually leading to the discovery of the Higgs boson in 2012[3].

After 2012 a scheduled two-year shutdown followed to allow for repairs and upgrades of the accelerator infrastructure and the LHC experiments. In 2015, the LHC restarted with an increased centre of mass energy of 13 TeV with a peak luminosity, $\mathcal{L}_{\text{peak}} = 5 \times 10^{33}\,\text{cm}^{-2}\text{s}^{-1}$. The peak luminosity was subsequently improved to $19 \times 10^{33}\,\text{cm}^{-2}\text{s}^{-1}$ by the end of Run 2. It delivered about $156\,\text{fb}^{-1}$ between 2015 and the end of Run 2 in 2018, of which ATLAS recorded $147\,\text{fb}^{-1}$. For $140\,\text{fb}^{-1}$ of recorded data, stable data-taking conditions were achieved, deeming this data "Good for Physics".

Figure 2.2 summarises the data taking of Run 2, highlighting the improved performance of the LHC towards the end of the run with a significant portion of the data recorded in 2018 alone, owing to an improved understanding and operation of the LHC accelerator complex. After 2018 the LHC entered its second long-term shutdown to undergo additional maintenance and upgrades after it was restarted in July 2022. In the currently ongoing Run 3, the centre of mass energy is increased to 13.6 TeV, and the peak luminosity to $25.3 \times 10^{33}\,\text{cm}^{-2}\text{s}^{-1}$ with an indicative integrated luminosity target of $250\,\text{fb}^{-1}$ across four planned years of data-taking. After Run 3, the LHC will be shut down again to upgrade it further to the *High Luminosity LHC* (HL-LHC) with the start of the next data-taking period foreseen for 2029.

During the running period of Run 2, the collision profiles, the average number of interactions per bunch crossing (pileup), $\langle\mu\rangle$, changed between 2015 and 2018. While $\langle\mu\rangle = 13.4$ was achieved at the beginning of Run 2, towards the end of Run 2, $\langle\mu\rangle = 37.8$ was achieved. The average $\langle\mu\rangle$ was 33.7 throughout Run 2.

A run under special low pileup conditions amounting to approximately $340\,\text{pb}^{-1}$ was performed in 2017 and 2018 to allow for dedicated electroweak precision measurements. The double peak structure in the 2017 pileup profile originates from running the LHC with fewer but higher intensity bunches during that year.

The mean number of interactions per bunch crossing during Run 2 is summarised in Figure 2.3.

[3]Both ATLAS and CMS used the entire 2010/2011 dataset and parts of the 2012 dataset since the particle was discovered before the end of the data taking period.

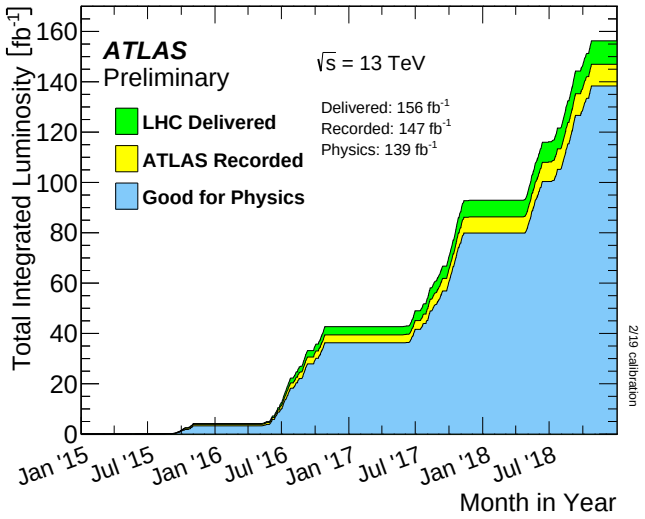

Figure 2.2: Overview of the cumulative luminosity of proton-proton collisions at $\sqrt{s} = 13\,\text{TeV}$ delivered to ATLAS by the LHC (green), the luminosity recorded by ATLAS (yellow) and the amount of data certified to be good quality data (blue) taken during stable beam conditions. This dataset corresponds to $139\,\text{fb}^{-1}$ of proton-proton collision data. The figure is taken from Ref. [175]. It reflects the previous luminosity results. The updated luminosity result is $140\,\text{fb}^{-1}$.

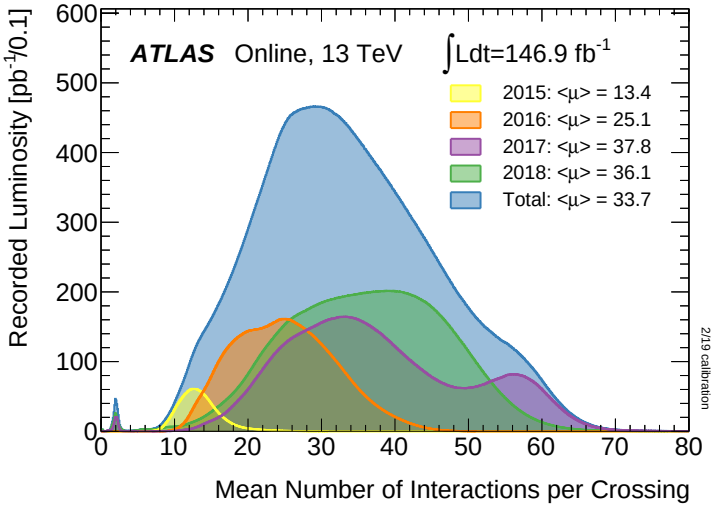

Figure 2.3: Summary of the average number of interactions per bunch crossing during Run 2. Data recorded by ATLAS during stable beam conditions are shown. The small peak at $\langle\mu\rangle \approx 2$ corresponds to a brief run under special low pileup conditions dedicated to electroweak precision measurements. Figure is taken from Ref. [175].

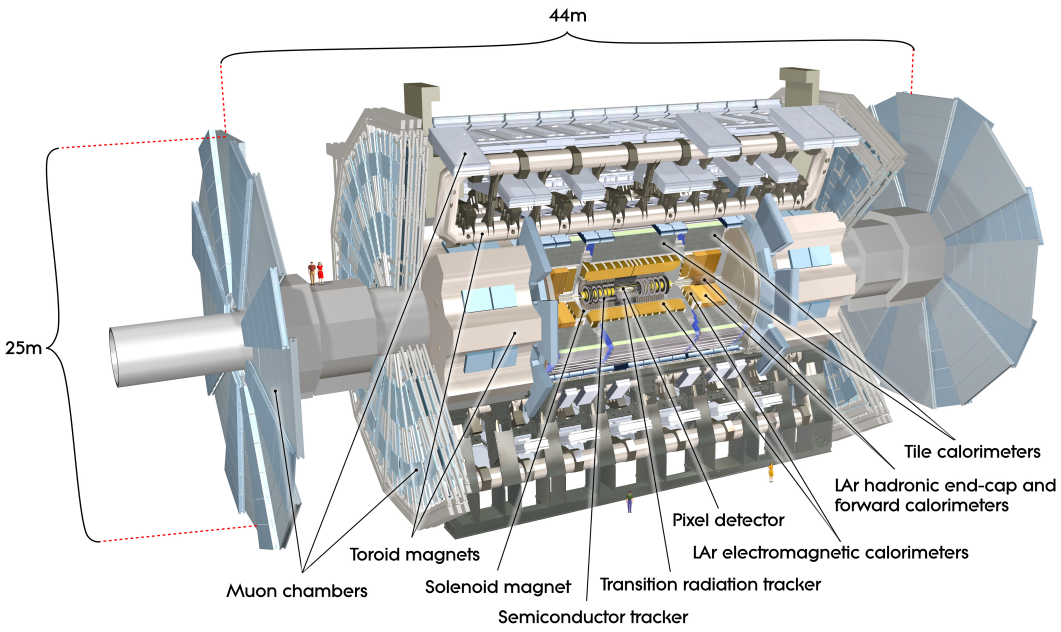

Figure 2.4: Schematic overview of the ATLAS detector at the LHC at CERN. The specialised sub-detectors are arranged in an onion-style fashion around the interaction point, covering almost the full 4π solid angle. ©CERN

2.2 The ATLAS Experiment

The ATLAS (*A Toroidal* LHC *ApparatuS*) experiment represents one of the four experiments at the LHC. It is a cylindrical general-purpose detector with a length of 46 m, a diameter of 25 m and a weight of 7000 t, a weight that is comparable to the 10,000 t of the Eiffel Tower in Paris, underling the remarkable (civil) engineering effort of the detector's construction. These dimensions make it the largest particle detector ever used at an accelerator. A key feature of ATLAS is the octagonal arrangement of the toroidal magnet system, placed in a cylindrical shape around the beam pipe. This magnet system gives ATLAS not only its size but also its characteristic shape.

The ATLAS detector is positioned at one of four collision points of the LHC. Clockwise along the LHC, ATLAS is placed between LHCb and ALICE. On the opposite side of the LHC is its sister experiment, the second general-purpose detector at the LHC, CMS.

The detector consists of several specialised sub-detectors arranged in an onion-style layout. An overview of the layout is shown in Figure 2.4.

In the following, the sub-detectors are introduced in detail: The Inner Detector detector measures tracks of charged particles and reconstructs vertices of hard and secondary interactions, the calorimeters measure the deposited energies of particles, and the Muon Spectrometer measures the transverse momenta of muons.

The origin of the ATLAS coordinate system is located at the nominal interaction point, i.e. a theoretical point in the beam pipe where the proton beams are brought into collision within the experiment.

Here, the Z-axis runs along the beam, and the x-y plane corresponds to the plane perpendicular to the beam axis, with the x- and y-axes pointing in the direction of the centre of the LHC and the Earth's surface, respectively. This Cartesian coordinate system is transformed in ATLAS into a z-η-ϕ coordinate system, which uses the azimuthal angle ϕ and the polar angle θ. In practice, the polar angle is replaced by the rapidity, which is defined as:

$$y \equiv \frac{1}{2} \log \left(\frac{|\vec{p}| - p_L}{|\vec{p}| + p_L} \right),$$

where $\vec{p}$ is the momentum vector of the particle and p_L is the longitudinal component of the momentum. This choice of the coordinate system is motivated by the Lorentz-invariant nature of rapidity differences for Lorentz boosts along the beam axis.

Throughout the ATLAS experiment, a closely related quantity, pseudorapidity, denoted by η, is generally used. It is defined as $\eta = -\log \tan(\theta/2)$, where θ is the polar angle of the particle. The use of pseudorapidity emerges from the relativistic limit, where particle masses can be neglected.

In order to compare the relative positions of two particles in the detector, the ATLAS experiment uses the quantity $\Delta R = \sqrt{\Delta\phi^2 + \Delta\eta^2}$, the quadratic sum of the differences in pseudorapidity ($\Delta\eta$) and azimuthal angle ($\Delta\phi$) between the two particles. The following paragraphs present the sub-detectors from the inside to the outside.

The Inner Detector

The Inner Detector (ID) [176,177] is a cylindrical detector at the heart of ATLAS. It is 6.2 m long and measures 2.1 m in diameter, making it the most compact subdetector in ATLAS. The ID consists of three subsystems: The Pixel Detector (PIXEL), the Semiconductor Tracker (SCT), and the Transition Radiation Tracker (TRT). All three subsystems consist of a central multi-layer barrel structure and endcaps in the form of disks. Figure 2.5 provides an overview of the ID.

In conjunction, the three subsystems measure electrically charged particles' momentum, direction and charge by fitting *tracks* to hits. These tracks are bent by the magnetic field of the thin central solenoid [178], which encloses the Inner Detector and provides a magnetic field of about 2T using indirectly-cooled aluminium-stabilised superconductors. In ATLAS, the position of the solenoid was chosen to be in front of the electromagnetic calorimeter, which requires minimal use of materials to not interfere with the energy measurements in the calorimeters. In contrast, the sister experiment CMS solenoid is located outside the calorimeters.

The track reconstruction provides vital elements of the particles' momenta measurement and the identification of primary and secondary vertices, i.e. the reconstruction of the origin of tracks coming from the hard interaction itself and from

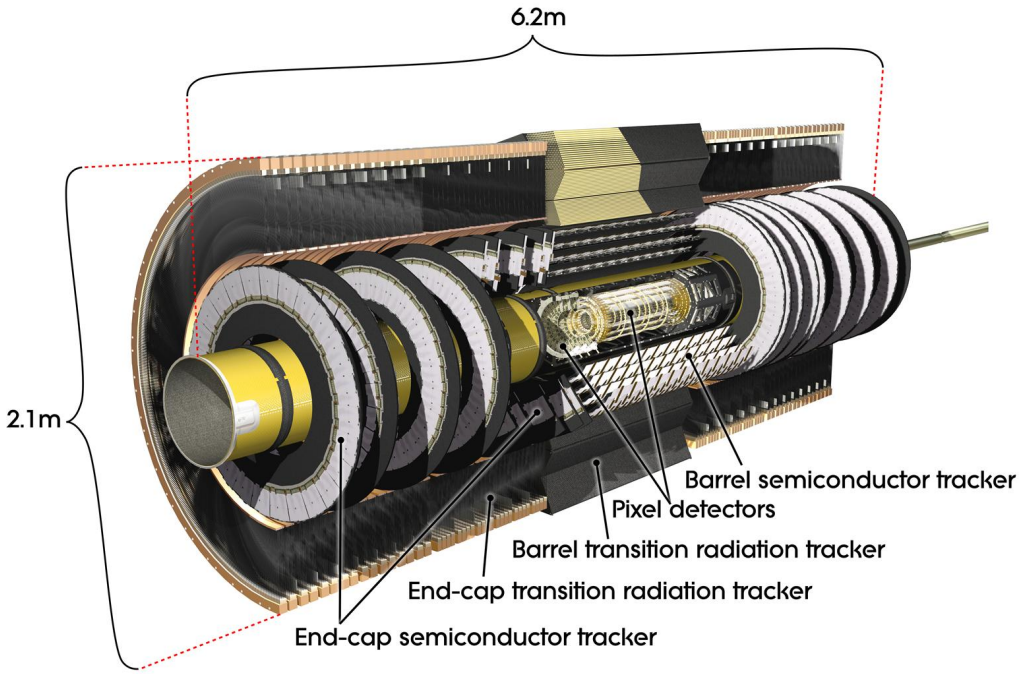

Figure 2.5: Overview of the ATLAS Inner Detector (ID) and its three subsystems: The Pixel detector, the Semiconductor Tracker (SCT), and the Transition Radiation Tracker (TRT), arranged in central multi-layer barrels with endcaps in the form of disks. ©CERN

the subsequent decays of short-lived particles. For the HL-LHC, the entire Inner Detector will be replaced by the radiation hard fully silicon-based Inner Tracker (ITK) [179, 180], which is designed to operate at the peak luminosity of the LHC of $7.5 \times 10^{34}\,\mathrm{cm}^{-2}\mathrm{s}^{-1}$, corresponding to about 200 inelastic proton-proton collisions.

The innermost component of the ID, the pixel detector, encloses the beam pipe at a distance of 3.3 cm. It consists of four cylindrical layers of silicon pixels arranged in 1736 modules with a coverage of $|\eta| < 2.5$ and three symmetrical end caps with 288 pixel modules. The total number of individual pixels is 92 million, with a pixel size of $50 \times 250\,\mu\mathrm{m}^2$ in the innermost layer (IBL) and $50 \times 400\,\mu\mathrm{m}^2$ in the external layers.

The silicon microstrip-based SCT radially surrounds the pixel detector and extends the tracking volume to distances of $299 < r < 560\,\mathrm{mm}$. It consists of four layers of silicon-strip sensors in the barrel region and two endcaps of nine disks each. The majority of modules is comprised of 2×2 rectangular 285-µm-thick p-on-n silicon sensors strips [181] with a pitch of 70 µm, a length of 6 cm and a stero angle between the back-to-back doublets of 40 mrad. In total, there are 2112 barrel modules and 2×988 endcap modules

The TRT enveloping the pixel detector and SCT again consists of a barrel and two

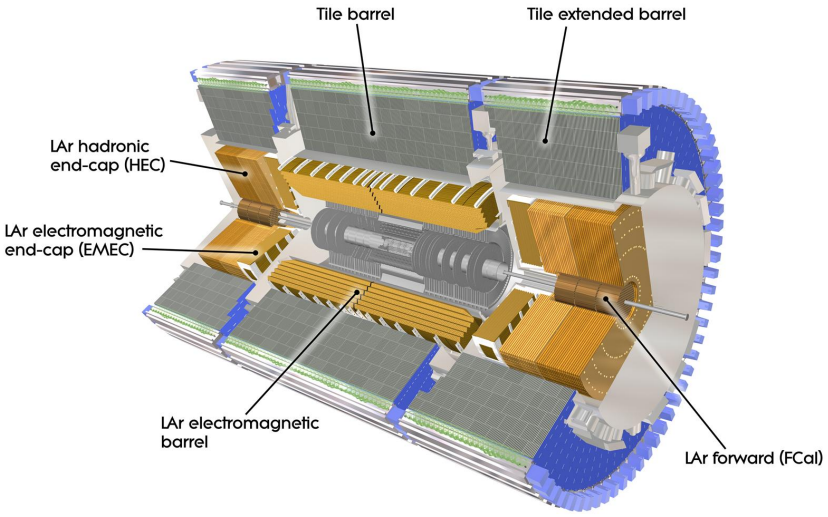

Figure 2.6: Schematic view of the ATLAS calorimeter system comprised of the Liquid Argon calorimeter (LAr), ECAL, and the Tile Hadronic calorimeter, HCAL. Like the ID system shown in Figure 2.5, the calorimeters are arranged into a central barrel component and endcap components in the forward regions. ©CERN

endcaps filled with thin-walled proportional drift tubes. The subdetector utilises the relativistic γ-dependent probability of transition radiation, allowing it to discriminate lighter particles from heavier particles.

A critical task of the ID is to aid in identifying b-jets, i.e. jets that are likely to have originated from bottom quarks. One way to identify b-jets is by searching for the presence of a displaced secondary vertex in the event. This secondary vertex likely originates from long-lived B mesons, which have a significantly longer average lifetime than light mesons and travel a detectable distance in the detector before decaying into lighter particles. The presence of these B mesons indicates the presence of a b-jet, which is relevant information for any top quark analysis.

The Calorimeters

The energy of stable particles and long-lived particles, as well as decay products of short-lived particles, is measured in ATLAS using a two-stage calorimeter system consisting of the *Liquid Argon Calorimeter* (LAr) [182] and the *Tile Hadronic Calorimeter* [183]. In the following, the names of the calorimeters are omitted, and their purpose refers to them: *Electromagnetic Calorimeter* (ECAL) for LAr and *Hadronic Calorimeter* (HCAL) for the Tile Hadronic calorimeter. While the ECAL mainly measures the energy of electrons and photons, the HCAL is designed to measure the energy of particles interacting strongly with heavy nuclei, i.e. hadrons. Figure 2.6 provides an overview of the entire ATLAS calorimeter system.

The ECAL is a sampling calorimeter with accordion geometry surrounding the ID, segmented into three main layers at increasing ECAL depth for $|\eta| < 2.5$ and two coarser main layers in the forward regions. The showering particles, triggered by the absorber plates, ionise the liquid Argon. The applied high voltage in the LAr medium induces a drift of the ions and electrons towards the absorber and electrode, thereby inducing an electrical current. This induced current is then converted into an electrical signal.

Similar to the ID, it is divided into a central barrel region, covering a pseudorapidity $|\eta| < 1.475$, and two endcaps covering $1.35 < |\eta| < 3.2$. The ECAL's first barrel layer, corresponding to 4-5 radiation lengths, finely segmented in the η direction, provides photon direction information and separation between photons and π^0 particles based on electromagnetic shower shapes. The remaining two barrel layers and endcap layers provide the main shower energy measurements and mean for correcting leakage behind the first layer(s). In addition, a thin pre-sampling layer, covering the region $|\eta| < 1.8$, is situated between the solenoid cryostat and the ECAL to correct energy losses from inert solenoid material upstream to the ECAL of 3-6 radiation lengths. The amount of inert material is most considerable towards higher $|\eta|$ values. The thickness of the ECAL itself corresponds to 22 radiation lengths.

Like the ECAL, the HCAL is a sampling calorimeter comprised of alternating layers of passive steel absorber plates and scintillating plastic tiles as active material. It is divided into three cylinders. In the central region, the *Long-Barrel* (LB) covers a pseudorapidity range of $|\eta| < 1.0$. It is flanked on both sides by movable *Extended Barrel* (EB) covering $0.8 < |\eta| < 1.7$. Within the EB, the LAr-based hadronic calorimeter endcaps are situated, consisting of 2 segments in-depth and covering $1.5 < |\eta| < 3.2$. Within the endcaps surrounding the beampipe, an additional LAr-based forward calorimeter provides η coverage for $3.1 < |\eta| < 4.9$ using three layers consisting of copper (1st layer) and tungsten (second and third layer) as absorber materials. In the core of the HCAL, electrical signals are generated by photomultiplier tubes that receive scintillation light via wavelength-shifting fibres connected to the individual calorimeter cells. In the endcaps, the generation of electrical signals follows the procedure described for the ECAL. The width of the HCAL core is 7.4 effective nuclear interaction lengths, λ (9.7 when including the ECAL).

The Muon Spectrometer

Due to their minimal-ionising nature, muons only deposit a small fraction of their energy in the calorimeters; hence an additional detector system is necessary to measure their energy and momenta. The Muon Spectrometer (MS) is the outermost *onion-shell* in ATLAS and comprised of 4 subsystems: *Thin Gap Chambers* (TGC), *Resistive Plate Chambers* (RPC), *Monitored Drift Tubes* (MDT), and *Cathode Strip Chambers* (CSC), amounting to about 4,000 individual muon chambers. The goal of the MS is to measure the momentum, charge, and direction of muons with high precision.

Eight large air-core toroidal magnets surrounding the barrel region [184] and

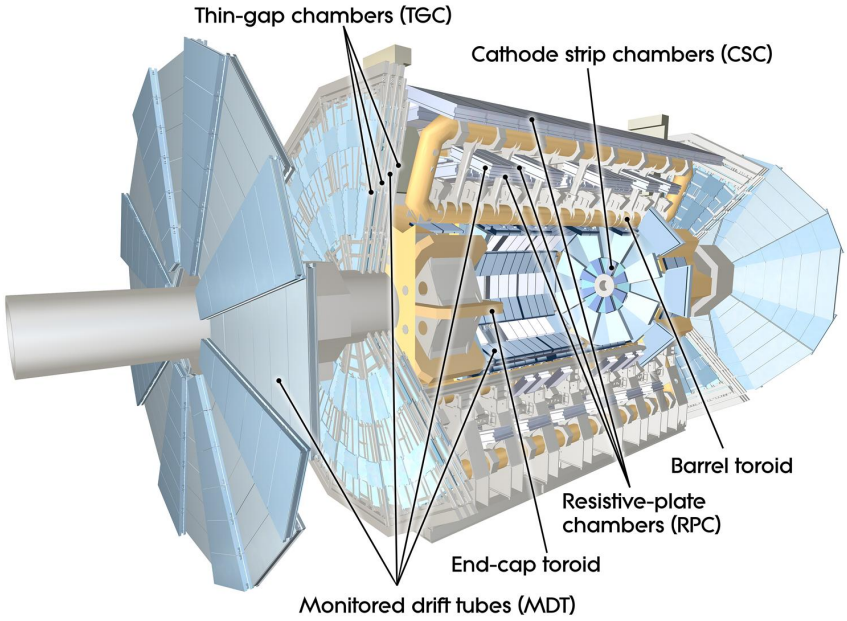

Figure 2.7: Illustration of the ATLAS Muons subsystem and the magnet system consisting of the central toroid magnet coils and the endcap toroid. ©CERN

two toroidal endcaps [185] provide a magnetic field of about 4 T. The unique 25 m barrel toroid coils represent the largest toroid magnet ever constructed and give ATLAS its name and iconic appearance. This magnet system results in a magnetic field approximately orthogonal to the muon tracks deflecting them according to the Lorentz force. An overview of the MS is shown in Figure 2.7. The subcomponents of the MS measure muon tracks in a region of $|\eta| < 2.7$. Precise measurements of the muons momenta are performed by MDT and CSC where the MDT covers a range of $|\eta| < 2.0$ with the CSC covering the remaining range up to $\eta = 2.7$. Information from the fast RPC and TGC is not used for the full momenta measurements but for fast trigger decisions, which will be explained in the following section.

Trigger and Data Acquisition

While detecting particles in ATLAS is an instrumentational challenge, the online processing, selecting and storing of events is a data acquisition and management challenge. The goal of the ATLAS *trigger and data acquisition* (TDAQ) system is to meet these requirements and maximise the data suitable for physics analysis. The design parameters of ATLAS and the LHC allow the detector to observe about 2 billion proton-proton collisions per second technically.

Such a stream of data taken by the sub-detectors would correspond to approximately 60 million megabytes per second. The instantaneous storage of such amounts of data is beyond what is technically feasible today, both in terms of the required

storage bandwidth and space. Due to these limitations, a compromise must be found between the technically possible storage rate and the capture of relevant events that could lead to discoveries. As it is unclear which events may lead to discoveries, it is necessary to select potentially interesting events based on simple criteria. These criteria are defined to be quickly evaluated at the electronic level, thus allowing a rough pre-selection. This pre-selection, i.e. the triggering of a writing process for an individual event, is done in ATLAS within the framework of a two-stage *trigger system*.

The *Level-1* (L1) trigger is a hardware trigger [186]. It consists of customised electronics in the detector, triggering on reduced-granularity information collected by the calorimeters and the Muon spectrometer. Its main components are the L1 calorimeter trigger (L1CALO) and the L1 muon trigger (L1MUON), which identify electron, photon, τ-lepton, muon and jet candidates alongside a global sum of the missing transverse energy of the event. The processing time for an event is 2.5 µs, during which the event is held in on-detector memory buffers. The L1 trigger selects events based on event-level properties such as the total energy of the calorimeter, the missing transverse energy or the multiplicity of objects above a given threshold (e.g. the transverse momentum of an electron). The performance of the muon and electron triggers during Run 2 is explained in detail in Ref. [187, 188].

After the event has passed the L1 trigger, the *Front-End* detector electronics of all sub-detectors are read out, and the event data is passed on to *ReadOut Drivers* and subsequently to the *ReadOut System*. While the former performs the initial data processing, the latter buffers it. Afterwards, the data is sent to the second trigger stage, the *High-Level Trigger* (HLT). The HLT is a software trigger where the trigger decision is based on the complete event information from all subdetectors. Within 200 µs, a detailed analysis of the event is performed, during which a more detailed examination of the collision data recorded by the sub-detectors occurs. Finally, the HLT selects approximately 1000 events per second. These events are passed on to the relevant storage systems and are available for further analysis.

At a later stage during the offline event reconstruction, a process referred to as *trigger matching* is performed. It is used to identify the relationship between particles detected in the trigger system and the reconstructed objects using more precise offline reconstruction algorithms. As the L1 trigger only has limited time and resources to process the data, its reconstruction may differ from the complete reconstruction of the object it selects. The matching is designed to determine the relationship between objects generated by offline reconstruction and objects generated by the trigger algorithms. Thus, mapping these two allows to answer questions like, did this reconstructed offline object cause this trigger chain to fire?

Of interest to the analysis addressed in this thesis are electron and muon triggers, targeting $t\bar{t}Z$ final states with this charged leptons[4].

At the HLT stage, the initial electron and muon reconstruction is conducted in all

[4]Since the reconstruction of τ leptons is challenging, dedicated τ lepton triggers are only used in analyses specifically aiming at τ-based final states.

regions of interest, defined by regions with calorimeter clusters with high transverse energy or muon tracks in the muon chambers provided by the L1 trigger system. If candidate particles pass criteria defined for a fast selection based on calorimeter and ID information, more precise algorithms reconstruct the objects, considering information outside the region of interest. A detailed description of the HLT reconstruction of electrons and muons is given in Refs. [187, 188].

Luminosity measurements

To compare the predicted cross-section of a process to the number of observed events, the luminosity of the dataset is required. The absolute luminosity scale at the LHC is determined via van der Meer beam separation scans in a dedicated running period in each year of data taking. These dedicated running periods differ from the standard physics conditions because a reduced number of bunches is used to avoid parasitic encounters between incoming and outgoing bunches that would be present during nominal data-taking conditions. The van der Meer scan measurements are combined with complementary measurements from individual experiment luminosity measurements. The results of this measurement set are then used to determine the instantaneous luminosity at the data-taking regime.

The ATLAS luminosity measurement is based on two redundant luminosity detectors and other algorithms that contribute different capabilities and systematic uncertainties to the luminosity measurement. In Run-II, the primary luminosity measurement was provided by the LUCID 2 Cherenkov detector [189]. Measurements performed by the *Beam Condition Monitor*, BCM, and offline measurements of the multiplicity of charged particle tracks complement the measurements performed by LUCID 2. In addition, LAr contributes *gap current* measurements from EMEC and FCal and photomultiplier current measurements from TILE, which are proportional to the instantaneous luminosity.

The integrated luminosity delivered to ATLAS by the LHC grouped into years and summed up is shown in Table 2.1. The *luminosity blocks* (LB), time intervals of about one minute of data-taking, certified to be taken during good data-taking conditions, are part of the so-called *good-run list* (GRL). Whenever analyses refer to the *full* Run 2 dataset, the usage of the GRL containing $140.07 \pm 1.17\,\text{fb}^{-1}$ is implied [190]. Analyses that do not require a fully operational detector or allow for looser operational conditions can use larger portions of the delivered luminosity.

Table 2.1: Integrated luminosity delivered by the LHC during Run 2 and integrated luminosity deemed good for physics analyses in ATLAS (*good run list* - GRL) [190]. The usage of the *full* Run 2 dataset implies the usage of the GRL containing $140.07 \pm 1.17\,\text{fb}^{-1}$. Analyses that do not require a fully operational detector or allow for looser operational conditions can use larger portions of the delivered luminosity.

Year	Delivered Luminosity [fb^{-1}]	GRL [fb^{-1}]
2015	4.0	3.24 ± 0.04
2016	39.0	33.40 ± 0.30
2017	50.6	44.63 ± 0.50
2018	63.8	58.79 ± 0.64
Total	157.4	140.07 ± 1.17

2.3 Particle Identification and Reconstruction

In a typical proton-proton collision, a multitude of particles is created. The vast majority of these particles decay into lighter, more stable particles before even reaching the wall of the beam pipe. Out of the large number of particles produced in collisions at the LHC, only 14 types of particles with $\tau c > 500\,\mu\text{m}$ have a prospect to interact with the first point of detection in the ID. The relevant detectable particles with sufficiently large lifetimes are $e^{\pm}$, $\mu^{\pm}$, γ, $\pi^{\pm}$, $K^{\pm}$, $p^{\pm}$, K^0_L and n of which only the electrons, muons and photons are elementary. The others are bound through the colour confinement imposed by QCD. Any coloured particles will produce sprays of colour-neutral particles through hadronisation, referred to as *jets*. The interaction of these objects, the elementary ones and the jets, with the detector, vastly differ from object to object. The purpose of the ATLAS detector described in Section 2.2 is to measure the properties of these objects and the properties of the particles they represent precisely.

While the actual detector measurements, for example, represent a set of hits in the ID or deposited energy in the calorimeters, the actual physics objects are more complex objects used as proxy objects of the actual particle properties.

In a proton-proton collision in ATLAS, several different types of *physics objects* are distinguished. The objects originating from the underlying hard interaction or scattering at parton level are defined as the *parton level* or *truth level* objects. This object level includes all particles typically drawn in a Feynman diagram to describe the underlying process. Hence also, photons and leptons are considered parton-level objects. In the next stage, the coloured parton-level objects emit other particles via QCD and QED radiation and form bound states through hadronisation. The family of these objects is referred to as *particle level objects*. The signature of these particles measured by the detector is then defined as the *detector level* or *reconstruction level* object. From an experimental point of view, only the reconstruction-level objects are directly accessible through measurements. The parton and particle level information is only accessible through simulation.

The reconstructed objects relevant for this analysis: electrons, muons, jets, b-jets, and missing transverse energy are discussed in the following.

Electrons

Electrons leave a track in the ID through ionisation and interact with the ECAL, where they deposit most of their energy. The reconstruction algorithm is based on a matching of topologically connected energy clusters [191] (so-called *topo-clusters*) in the calorimeters[5] to tracks in the ID.

Track candidates are seeded based on *hits* in the SCT and PIXEL detector. A pattern recognition algorithm is applied using the pion hypothesis for the model of the energy loss through the interaction of the particle with the ID material. If the pattern recognition algorithm fails to reconstruct a track with $p_T > 1\,\text{GeV}$ looser

[5]Information from the HCAL is also used here.

conditions on the Bremsstrahlung of the particle are applied, allowing up to 30 % energy loss at each ID intersection point.

Track candidates with $p_T > 400\,\text{MeV}$ are fit using the *Global χ^2 Track Fitter* [192] and subsequently using Gaussian-sum filters [193] taking radiative losses and non-linear effects due to Bremsstrahlung into account.

Calorimeter clusters are seeded using a grid of 200×256 cells in $\eta \times \phi$ space of the ECAL, dividing the ECAL into cells of size $\Delta\eta \times \Delta\phi = 0.025 \times 0.025$. Each cell defines an energy *tower* consisting of the energy depositions of the first, second and third layer in the ECAL and the pre-sampler where available. These cells are used to build calorimeter clusters using a sliding window algorithm [194]. Reconstructed clusters are formed from these clusters by symmetrically expanding the cluster size in $\eta \times \phi$ and calibrating the clusters energy [195,196]. Combining these clusters with the track candidates mentioned above leads to electron candidates. For each reconstructed *electron candidate*, a multivariate likelihood discriminant is calculated to discriminate between electrons originating from the hard interaction (so-called prompt electrons) and non-prompt electrons such as electrons originating from photon conversion[6], the misidentification of hadrons or heavy flavour decays. The ATLAS *prompt lepton tagging algorithm*, initially developed in the context of an ATLAS $t\bar{t}H$ multilepton analysis [189], is used to define isolated leptons. The algorithm is trained to separate leptons from prompt sources such as W, or τ decays from leptons from semileptonic B-hadron decays. Based on this approach, two boosted decision trees provide a *prompt lepton veto* (PLV) score and a dedicated PLV score for low p_T leptons (*Low-p_T* PLV), respectively. Working points are defined through cuts on these scores:

$$\text{Low}\,p_\text{T}\text{PLV} < a' p_\text{T}^3 + b' p_\text{T}^2 + c' p_\text{T} + d' \qquad (p_\text{T} < p_{\text{T}0}), \tag{2.1}$$

$$\text{PLV} < a p_\text{T}^3 + b p_\text{T}^2 + c' p_\text{T} + d \qquad (p_\text{T} < p_{\text{T}0}), \tag{2.2}$$

$$\text{PLV} < \max(-0.88, A + B\exp(-p_\text{T}/C)). \tag{2.3}$$

For electrons used in this analysis, the *loose* PLV working point is used for defining isolated electrons based on a set of electron-specific and working-point-specific parameters for the cut parameters listed in Table 2.2.

Muons

Muons stand out in ATLAS as they are minimum-ionising particles and only interact weakly with the detector material.

The correct identification and reconstruction of muons in this analysis are essential for reconstructing Z bosons. The reconstruction of muons in ATLAS primarily relies on track information from the MS and ID. To account for energy losses affecting track parameters, information from the calorimeters is also used to aid muon reconstruction and provide MS-independent tagging of ID-based muon candidates.

[6] An electron candidate originating from a converted photon corresponds to an energy cluster matched to a conversion vertex. An electron candidate originating from an unconverted photon corresponds to an energy cluster matched to neither a track nor a conversion vertex.

Table 2.2: Working-point-specific parameters of the prompt lepton tagging tool for the cut parameters in Equation 2.1. Parameters are listed separately for muons and electrons. The tool was initially developed in the context of an ATLAS $t\bar{t}H$ multilepton analysis [189].

		a'	b'	c'	d'
PLV Loose (e)		0.000345	-0.016259	0.243588	-1.133747
PLV Loose (μ)		0.000335	-0.014904	0.215737	-0.730525
	$p_{\mathrm{T},0}$ [GeV]	a	b	c	d
PLV Loose (e)	12	0	-0.000106967	-0.0160896	0.960105
PLV Loose (μ)	12	-0.000186	0.0058481	-0.0788936	1.05942
	$p_{\mathrm{T},1}$ [GeV]	A	B	C	
PLV Loose (e)	18.457	-0.94386	3.03257	28.0508	
PLV Loose (μ)	18.452	-0.958651	3.54785	19.6155	

The reconstruction of muons falls into five different muon types: *Combined muons* (CB muons) originate from a track fit of MS and ID hits, considering calorimeter-based energy losses.

Inside-out combined muons are reconstructed through the extrapolation of ID-based track fits towards a minimum of three loosely-aligned hits in the MS, removing the need for a MS track.

Muon-spectrometer extrapolated muons are reconstructed from MS tracks, which can not be matched to ID tracks in a complementary fashion to inside-out combined muons.

Segment-tagged muons are reconstructed by requiring extrapolated ID tracks to satisfy tight angular matching requirements to at least one MS segment.

Lastly, *calorimeter-tagged* muons are identified by extrapolating ID-based tracks into the calorimeters and identifying corresponding energy deposits.

In the ATLAS experiment, muon identification is achieved by applying a series of quality requirements based on the unique characteristics of each reconstructed muon type. These requirements are designed to reject fake and non-prompt muons, particularly those resulting from pion or kaon decays (e.g. $\pi^{\pm} \to \mu^{\pm}\nu$ or $K^{\pm} \to \mu^{\pm}\nu$), while still providing accurate momentum measurements.

There are five working points for muon identification in ATLAS: *Tight*, *Medium*, *Loose*, *HighPt*, and *LowPt*. For this analysis, the *Medium* working point is employed, as it minimises the systematic uncertainties related to muon reconstruction and calibration and is currently the default criteria used by ATLAS. The *Loose*, *Tight*, and the two p_{T}-based working points are designed to reconstruct the $H \to ZZ \to \mu^{+}\mu^{-}\mu^{+}\mu^{-}$ decays, analyses that are limited by backgrounds from non-prompt muons, and extreme phase spaces, respectively.

The Medium working point utilises three types of muons: muon-spectrometer-

only extrapolated, Silicon-associated Forward, and combined. These three types of muons overlap and supplement each other based on various requirements, such as the number and quality of hits needed and the η regions in which they are used. A loose selection on the compatibility between ID and MS momentum measurements is also applied. In order to account for mismodeling in the simulation, Monte Carlo (MC) scale factors are calculated.

Similar to the electron case, the prompt lepton tagging algorithm is used to define isolated muons. Again several isolation WPs are defined, balancing prompt-muon acceptance, rejection of non-prompt muons, and performance close to other objects. Here again, the *loose* working point and Equation 2.1 are used using the muon-related parameters in Table 2.2. These isolation criteria reject most muons from heavy-flavour hadron decays.

Jets

The confinement of QCD binds colour charge-carrying gluons and quarks to colourless bound states. The particles coming out of the hadronisation process result in a collimated stream of particles traversing the detector, depositing energy in the calorimeters. These energy depositions within the calorimeters form *jets*, which serve as proxy objects of the particles originating from the hard scattering process or secondary vertices. Based on the lateral and longitudinal segmentation of the calorimeters, three-dimensional topo-clusters are seeded with cells with energies $E_{\text{cell}} > 4\sigma^{\text{Calo}}_{\text{noise}}$, where E_{cell} is the energy of the seed cell and $\sigma^{\text{Calo}}_{\text{noise}}$ the standard deviation of the expected noise. The clusters are laterally and longitudinally expanded to include adjacent cells with $E_{\text{cell}} > 2\sigma^{\text{Calo}}_{\text{noise}}$ and subsequently their neighbouring cells. The calorimeter response throughout ATLAS is calibrated to the electromagnetic scale, resulting in an identical response to electromagnetic showers from electrons or photons. The lower response of hadronic interactions in the HCAL is compensated by extrapolating from measurements of the mean energy deposition of particles with given momentum. The topo-clusters are combined using a sequential jet clustering algorithm, the anti-k_t algorithm [197], as implemented in the FASTJET package [198]. In the anti-k_t algorithm, well separated particles with large momenta $p_{\text{T},1}$, $p_{\text{T},2}$, ... (so-called *hard particles*) are clustered together with low transverse momenta (so-called *soft particles*) through a distance metric

$$d_{i,j} = \min(1/p^2_{\text{T},i}, 1/p^2_{\text{T},j})\Delta R^2_{ij}/R^2, \tag{2.4}$$

where i runs over the hard and j over the soft particles, and R describes the radius parameter of the algorithm. ΔR gives the distance in the η-ϕ-plane. In this procedure, hard particles accumulate soft particles into a conical jet of radius R. Hard particles with neighbouring hard particles within $R < \Delta R_{ij} < 2R$ will result in the harder jet being conical and the softer jet missing the overlap with the harder jet.

In ATLAS, jet objects are defined using the *particle flow algorithm* [199] using a list of tracks and topo-clusters as input where the energy of the former is subtracted

from the latter cell by cell. Additionally, hadronic recoil activity below the jet reconstruction threshold is considered, providing a more precise missing transverse energy estimate [200]. In the algorithm, the tracks are matched to single topo clusters. Additional topo-clusters are added based on the expected energy of the particles taking the topo-clusters position and the momentum of the track measurement into account. A detailed description of the steps performed to form particle flow jets (*PFlow jets*) can be found in Ref. [199].

Due to the complex nature of jets, their energies have to be calibrated. The calibration occurs in several steps. First, the jet's four-momentum is corrected to originate from the reconstructed primary vertex while keeping its energy constant. The p_{T} of the jet is first corrected by subtracting the per-event pile-up contribution to its p_{T} using the jet ghost-area subtraction method [201, 202], based on a median p_{T} density ρ of jets in the η-ϕ plane. Since the ρ distribution is derived from the calorimeter's central, low occupancy region, a residual pile-up dependence remains for jets in the forward, high occupancy calorimeter region. This residual correction is derived from MC simulations as the difference between the reconstructed jet p_{T} and the truth jet p_{T} and depends on the number of primary vertices, N_{PV}, and the mean number of pp-interactions, μ. The corrected jet p_{T}, $p_{\mathrm{T}}^{\mathrm{corr}}$, is then calculated to be

$$p_{\mathrm{T}}^{\mathrm{corr}} = p_{\mathrm{T}}^{\mathrm{reco}} - \rho \times A - \alpha \times (N_{PV} - 1) - \beta \times \mu, \tag{2.5}$$

where α and β are derived from linear fits to the truth jet p_{T} distribution in bins of $p_{\mathrm{T}}^{\mathrm{truth}}$ and $|\eta|$.

Afterwards, the *absolute* jet energy scale (JES) corrects the jet's four-momentum to the particle-level energy scale, accounting for η-based reconstruction dependencies through the η calibration. Subsequently, a sequential correction of residual dependencies of the JES on longitudinal and transverse jet features is applied, considering differences between quark and gluon-initiated jets. For this correction, sensitive observables are used in a *global sequential calibration* [203]. At the end of the calibration procedure, well-measured reference objects are used to apply a final *in situ* calibration on residual differences. A detailed overview of the entire calibration procedure is given in Ref. [204].

To suppress pile-up events from *in-time* and *out-of-time*, pile-up mimicking jet signatures, a multivariate tagging tool based on the k-nearest neighbour algorithm, the *jet-vertex-tagger* (JVT) [205] is used. The tagging decision score of this tool is employed to reject reconstructed jets with a high probability of originating from pile-up interactions.

b-Jets

As top quarks predominantly decay into a W boson and a b-quark, identifying jets containing b-hadrons, b-jets, is essential for any top quark analysis. The long lifetime, high mass, and decay multiplicity of these b-hadrons can be utilised to allow

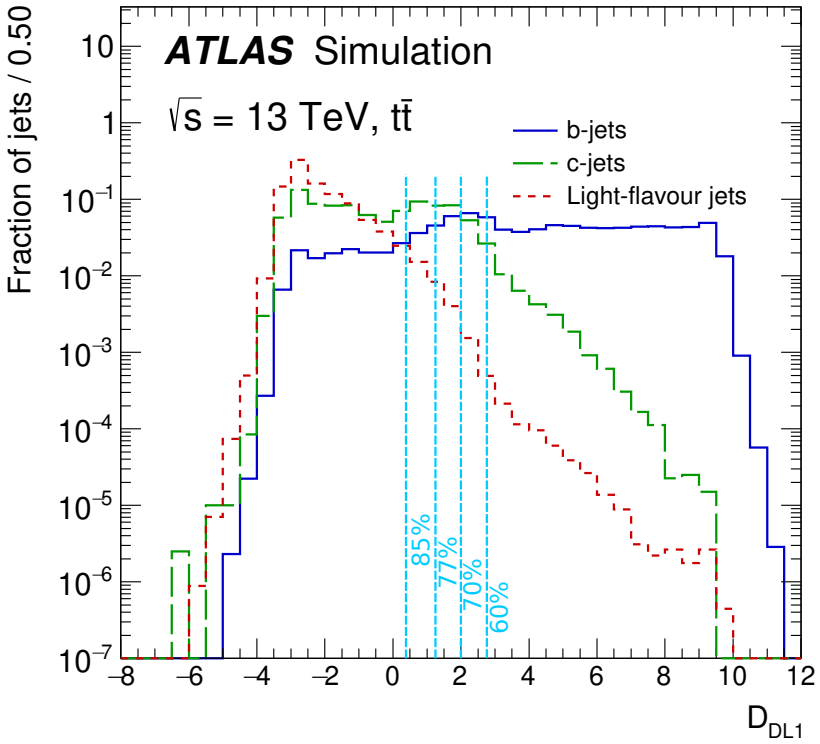

Figure 2.8: DL1 b-tagging distribution for b-jets, c-jets and light-flavour jets shown in blue, green, and red, respectively. The b-tagging working points are shown in light blue. The figure is adapted from [206].

for tagging of b-jets. In ATLAS, two categories of algorithms[7] for b-jet tagging exist: Inclusive algorithms that exploit large *impact parameters* of tracks, i.e. tracks displaced from the nominal interaction point, originating from b-hadron decays (IP2D and IP3D), and approaches where the secondary vertex is explicitly reconstructed (SV1, JETFITTER) [207]. For the b-tagging algorithms used in this analysis, DL1, several low-level tagging algorithms are combined through a deep feed-forward neural network [208]. The algorithm provides a three-dimensional output corresponding to the probabilities for a jet to be a b-jet (p_b), c-jet (p_c), or light-flavour jet (p_{light}). The three output probabilities are combined into a final b-tagging discriminant,

$$D_{DL1} = \log\left(\frac{p_b}{f_c \cdot p_c + (1 - f_c) \cdot p_{\text{light}}}\right), \tag{2.6}$$

where f_c describes the effective c-jet fraction in the training sample, allowing for an a posteriori optimisation of the algorithm's performance.

[7] Primarily used in Run 1.

Four cuts on the discriminants distribution are imposed to evaluate and calibrate the performance of the algorithms using $t\bar{t}$ events [206] at 60 %, 70 %, 77 %, and 85 % b-jet tagging efficiency, respectively. These cuts are referred to as working points (WP) and form a *pseudo-continuous* distribution of five bins where the fifth bin originates from the case where a jet does not pass any WP. The distribution is bounded by the trivial 100 % and 0 % efficiency cases. The distribution of the discriminant is shown in Figure 2.8 with the different WPs highlighted in light blue. The lines represent the cut value of the respective WP at $D_{DL1}(WP) = (0.46, 1.45, 2.02, 2.74)$ for WP $\in$ (85 %, 77 %, 70 %, 60 %), respectively. The c-jet (light-flavour jet) rejection at the WP chosen for the preselection of this analysis (85 %) is 27 (1300).

Missing Transverse Energy

In a central pp-collision, the momentum within the transverse plane with respect to the beam axis is conserved. By summing the momenta of all observed particles belonging to one interaction, the *missing transverse momentum*, colloquially referred to as *missing transverse energy*, $E_{\mathrm{T}}^{\mathrm{miss}}$, can be calculated. The primary source of $E_{\mathrm{T}}^{\mathrm{miss}}$ are neutrinos undetectable in ATLAS. Their transverse momentum does not enter the sum of transverse momenta leading to a deficit of observed transverse momenta. To a smaller extent, the loss of objects in the beam pipe, in non-active detector material or through inaccurate reconstruction also contributes to this deficit. The calculated value of $E_{\mathrm{T}}^{\mathrm{miss}}$ is often associated with the neutrino or other invisible BSM particles. However, this one-to-one association breaks down in case multiple invisible particles are present as only the sum of invisible momenta is accessible.

The missing transverse energy reconstruction in ATLAS takes the previously defined, calibrated objects with high p_{T} into account. The sequence of treatment of the objects is based on the average reconstruction quality of the objects taking tracks and topo-clusters associated with the respective objects into account and avoiding double-counting signals in the reconstruction process. In addition to the high p_{T} objects, unused tracks and calorimeter topo-clusters are considered in a so-called *soft-term*, describing the residual *soft* interactions (as opposed to the underlying *hard* interaction) within an event. These soft objects must be isolated, associated with the primary vertex and fulfil $p_{\mathrm{T}}^{\mathrm{soft}} < 400\,\mathrm{MeV}$. The $E_{\mathrm{T}}^{\mathrm{miss}}$ of the event is then calculated as the negative sum of the transverse momenta of the hard-terms and the soft-term objects,

$$E_{\mathrm{T}}^{\mathrm{miss}} = \underbrace{\sum_{\mathrm{Object}} \left(-\sum_{\mathrm{j}} p_{\mathrm{T}}^{j} \right)}_{\text{hard-terms}} - \underbrace{\sum_{\mathrm{Soft}} p_{\mathrm{T}}^{\mathrm{soft}}}_{\text{soft-term}}, \tag{2.7}$$

where the outer sum of the hard terms runs over the type of reconstructed object and the inner sum over the reconstructed objects themselves.

The $E_{\mathrm{T}}^{\mathrm{miss}}$ contributions with and without genuine missing transverse energy are probed in $W \to e\nu$, $W \to \mu\nu$, $t\bar{t}$, and $Z \to \mu\mu$ final states [209].

Fake leptons

Non-prompt leptons are colloquially referred to as *fake* leptons. While non-prompt leptons are leptons predominantly originating from meson decays, decays of heavy-flavour hadrons, or photon conversion, fake leptons are mostly light jets that create lepton-like detector signatures. In this analysis, all objects not originating from the underlying hard interaction are considered *fake* leptons or *fakes*. In MC, these objects are identified using lepton-based truth information. In this analysis, fake leptons predominantly originate from the semileptonic decay of heavy-flavour hadrons. Four distinct categories of fakes are defined: electrons from heavy-flavour sources (F-e-HF), muons from heavy-flavour sources (F-μ-HF), electrons from other sources (F-e-Other), and any other fake electrons from other sources (F-Other).

Overlap-Removal

As explained in the previous section, identifying physical objects in the detector is ambiguous because several objects can usually be reconstructed from the same detector signals. This ambiguity is removed by only considering one object based on a set of operations on all objects. These overlap removal procedures consider shared quantities between objects, such as a shared track or shared energy depositions in the calorimeter. Additionally, distances measured in differences of rapidity, Δy, and ΔR are considered to quantify the distances between individual objects and remove spatially overlapping objects.

Reconstruction of top quarks

Top quarks can be reconstructed by correctly assigning the four-momenta of their decay products. In the trileptonic channel, the challenge lies in reconstructing the $t\bar{t}$ system. The reconstruction procedure is split into two subsequent parts: the reconstruction of the leptonically decaying top quark (the leptonic-side top) and the reconstruction of the hadronically decaying top quark (the hadronic-side top). In the analysis, the order of reconstructing the leptonic-side top quark first puts the leptonic reconstruction in a privileged position as the b-jet determined to originate from the leptonically decaying top quark is not considered anymore for the hadronic-side top quark reconstruction.

For the leptonic-side top reconstruction, it is assumed that the $E_{\mathrm{T}}^{\mathrm{miss}}$ of the event predominantly originates from the neutrino from the leptonically decaying W boson, and the impact of other sources is negligible. A W boson mass constraint is applied on the four-vector-sum of the four-momenta of the neutrino and the lepton not associated with the Z boson (non-Z lepton), leading to a quadratic equation to determine the momentum of the neutrino in the z direction, $p_{\nu z}$:

$$Ap_{\nu z}^2 + Bp_{\nu z} + C = 0, \tag{2.8}$$

where A, B, and C depend solely on the neutrinos p_{T} and ϕ, the W boson mass constraint, and the kinematics of the non-Z lepton. If $B^2 > 4AC$, two solutions for

$p_{\nu z}$ are possible, corresponding to two possible neutrino candidates. If $B^2 < 4AC$, no real solutions are possible, and $E_{\mathrm{T}}^{\mathrm{miss}}$ is decreased in steps of 100 MeV until real solutions can be obtained (i.e. $B^2 = 4AC$).

The neutrino candidates are combined with a b-tagged jet to form the leptonically decaying top quark. For each neutrino candidate, the jet minimising $\Delta R(b\text{-jet}, \nu\ell\text{-system})$ is considered, which in the case of two neutrino candidates might be two different jets. The top quark candidate mass, $m_{b\ell\nu}$, is compared to the mass distribution of correctly reconstructed top quarks in $t\bar{t}Z$ events, built from parton-level neutrinos, a detector-level lepton and a jet matched to the corresponding parton-level object. Compared with this idealised distribution, representing a perfect reconstruction, an output weight for each top quark candidate is calculated, and the candidate most consistent with a leptonically decaying top quark is selected.

The hadronic-side top quark is reconstructed by reconstructing top quarks from sets of jets compatible with the decay of a W boson and a b-jet. All remaining b-jets ordered by their pseudo-continuous b-tagging score are considered for this reconstruction. From all untagged jets, the pair with an invariant mass, m_{jj}, most consistent with the measured W boson mass, $m_W = 80.377 \pm 0.012\,\mathrm{GeV}$ [42], is assigned to the W boson. Trileptonic events with only three jets, of which one is b-tagged are not fully reconstructable. If the event has two b-tagged jets, the remaining untagged jet is used in place of the W boson, assuming the second untagged jet lies outside the detector's acceptance. If the event has only one b-tagged jet[8], only the hadronically decaying W boson is reconstructed, assuming the second b-jet is out of the acceptance of the detector. In this case, the hadronically decaying top quark can only be reconstructed incompletely.

Reconstruction of Z Boson Candidates

In this analysis, Z bosons are reconstructed by considering the reconstructed prompt leptons in an event. Each lepton is reconstructed as either a muon or an electron, with τ-leptons not being reconstructed in this analysis. From all leptons, lepton pairs with opposite electric charge and the same lepton flavour are defined, so-called *opposite-sign-same-flavour lepton pairs* (OSSF). These OSSF pairs form up to two Z boson candidates. Each Z candidate's mass is defined through the invariant mass of the two corresponding leptons, $m_{\ell\ell}^{\mathrm{OSSF}}$. For multiple Z candidates, the OSSF pair with an invariant mass closest to the Z pole mass, m_Z^{pole}, is considered to originate from the Z boson.

This analysis focuses on events with on-shell Z bosons, which are reconstructed when $|m_Z^{\mathrm{reco}} - m_Z^{\mathrm{pole}}| < 10$,GeV, while all other candidates are considered off-shell. The efficiency of the reconstruction technique is evaluated using truth-level information and found to be 95.76 % for $Z \to e^-e^+$ and 95.53 % for $Z \to \mu^-\mu^+$ in $t\bar{t}Z$ signal events. The efficiencies are determined by matching reco-level leptons passing the preselection to truth-level leptons within a ΔR-cone of $\Delta R < 0.1$. The recon-

[8] which at this point was already used for the leptonic-side top reconstruction

Table 2.3: Reconstruction efficiencies of the Z boson reconstruction algorithm.

Channel	Correct [%]	Partially correct [%]	Z out of acceptance [%]
$t\bar{t}(Z \to e^+e^-)$	95.76	2.26	1.97
$t\bar{t}(Z \to \mu^+\mu^-)$	95.53	2.81	1.66

struction efficiencies, percentages of partially correctly reconstructed Z bosons, and those falling out of acceptance are given in Table 2.3.

CHAPTER 3

Signal and background modelling

The underlying quantum-mechanical nature of collision events prevents event-based statements on the true nature of the event. Instead, data taken by ATLAS must be compared to a set of simulated events from Monte Carlo (MC) generators. By comparing the predicted number of the MC events with the total amount of the data[1], conclusions about the processes under investigation can be drawn, and their cross-sections can be measured.

The generated MC events, describing the theoretical nature of the proton-proton collisions at a collision rate of 25 ns, are interfaced to a simulation of the ATLAS detector [210] utilising GEANT4 [211], simulating the passage of the generated particles through ATLAS.

The object reconstruction for these MC events is identical to that of data events described in Section 2.3. To reduce the computational costs, detector simulations based on the ATLSFAST-II package, (AFII) [210] are used for some subdominant processes, in which the complexity of the modelling of the hadronisation process in the calorimeters, i.e. the showering process, is reduced.

The parton shower and hadronisation process are simulated using dedicated software packages and explained in detail below. The modelling of the processes also includes the simulation of additional *pp* interactions from the same (in-time pileup) or adjacent bunch crossings (out-of-time pileup). For the description of the pileup, minimum-bias interactions generated with PYTHIA 8 [212–214] are superimposed. Furthermore, the MC are reweighted to match the simulated pileup distribution to that observed in the data as previously highlighted in Figure 2.3.

All MC events are split into three statistically independent MC *production campaigns*, namely *mc16a*, *mc16d*, and *mc16e*. The production campaigns are simulated using the respective pileup profile at the LHC for 2015-2016 (mc16a), 2017 (mc16d) and 2018 (mc16e). All three campaigns are combined to form the full Run 2 MC pre-

[1] The term *data* is exclusively used for actual events taken by the detector. In the case of simulated events, the term MC *events* is used.

diction. The appendix provides a complete list of all used MC samples in Chapter A.

3.1 Simulation of the $t\bar{t}Z$ Signal Process

The $t\bar{t}Z$ signal process is modelled at next-to-leading order (NLO) in the strong coupling constant α_s using the MadGraph5_aMC@NLO 2.8.1 generator [215] and the NNPDF3.0NLO PDF set [71]. The renormalisation and the factorisation scales are set to $0.5 \times \sum_i \sqrt{m_i^2 + p_{T,i}^2}$, where the sum includes all particles on the matrix element level. The theoretical cross-section of the $t\bar{t}Z$ process is calculated at NLO +electroweak accuracies using MadGraph5_aMC@NLO. It is taken from Ref. [165] and includes off-shell corrections calculated in Ref. [216]. Contributions due to $t\bar{t}\gamma^*$ are taken into account. The calculated cross-section amounts to

$$\sigma_{t\bar{t}Z}^{NLO} = 0.86^{+0.09}_{-0.10}\,\text{pb}, \tag{3.1}$$

with the uncertainties arising from the factorisation and renormalisation scale variations, PDF uncertainties and α_s variations. This calculation is used as a reference for this analysis and highlighted in detail in Section 1.3.1.

The simulations' top quark mass is 172.5 GeV. The decay of the individual top quarks is simulated using MadSpin [217, 218] at LO, preserving spin correlations. The parton shower and hadronisation process are simulated using Pythia 8.244 [214] with the NNPDF2.3LO PDF set [219], and the ATLAS A14 tune [220]. Unless stated otherwise, this parton shower setup with varying versions of Pythia is used for all samples. Modelling uncertainties are estimated through the up and down variation of the VAR3C parameter of the A14 tune. The EvtGen 1.7.0 program [221] is used to simulate the decay of bottom and charm hadrons.

For the differential measurements and the estimation of generator-driven uncertainties, alternative MC generator choices are considered for the $t\bar{t}Z$ signal prediction. As an alternative showering algorithm, Herwig 7.2.1 [222, 223] is interfaced to the nominal MadGraph5_aMC@NLO prediction to estimate the modelling uncertainty originating from the parton shower and hadronisation process.

In addition, alternative $t\bar{t}l\bar{l}$ samples are produced using the Sherpa 2.2.1 generator [224] at NLO precision, also including off-shell effects down to $m_{\ell\ell} = 5$ GeV. As the parton shower, the default Sherpa 2.2.1 parton shower and the NNPDF3.0NLO PDF set are used.

3.2 Simulation of Background Processes

Events representing the pair production of top quarks associated with a Higgs boson ($t\bar{t}H$) are simulated at NLO using MadGraph5_aMC@NLO 2.6.0 with the NNPDF3.0NLO PDF set and interfaced to Pythia 8.230 using the A14 tune. Background processes with $t\bar{t}$ pairs and additional W bosons ($t\bar{t}W$) are generated using Sherpa 2.2.10 [224] at NLO accuracy in QCD with the multi-leg merging of up to 1

(2) additional parton at NLO (LO). Electroweak corrections to $t\bar{t}W$ productions are described by a dedicated LO QCD $t\bar{t}W + j$ sample generated with SHERPA 2.2.10.

Single top quarks associated with a Z boson (tZq) are simulated at NLO in the four-flavour scheme, including a second b-quark in the final state, using MADGRAPH5_aMC@NLO 2.9.5 and the NNPDF3.0NLO PDF set. Again contributions due to $t\gamma^*q$ are taken into account. A filter selects trileptonic final states, namely $t \to Wb \to \ell\nu_\ell b, Z \to \ell\ell$. The events are interfaced to PYTHIA 8.245 for the parton shower and hadronisation process. Modelling uncertainties are estimated through the up and down variation of the VAR3C parameter of the A14 tune and by replacing PYTHIA with Herwig 7.2.1 as a parton shower model.

Processes with singly resonant top quarks associated with a Z boson and a W boson (tWZ) are modelled at NLO using MADGRAPH5_aMC@NLO 2.2.2 and NNPDF3.0NLO PDF set. Here $t \to Wb$ decay is inclusive, and the Z boson exclusively decays to leptons ($Z \to \ell^+\ell^-$). The parton shower and hadronisation process of tWZ events is simulated using PYTHIA 8.212. To evaluate the tWZ modelling uncertainties, a comparison with a MC sample produced with the same generator but an alternative treatment of the $t\bar{t}Z$-tWZ interference through the diagram removal scheme is performed.

Events with top quark pairs ($t\bar{t}$) are modelled at NLO accuracy using the POWHEG-BOX 2 generator [225] using the NNPDF3.0NLO PDF set. The damping factor h_{damp} is set to $h_{\text{damp}} = 1.5m_t$. Top quark decays are simulated at LO using MADSPIN. Decays of bottom and charm hadrons are modelled using the EVTGEN 1.2.0 program. The parton shower is simulated using PYTHIA 8.230. These events are particularly relevant for $t\bar{t}Z$ final states with two leptons and constitute a significant background in this case.

Events with two vector bosons (W, Z), namely WZ+jets and ZZ+jets, are simulated through SHERPA 2.2.2 using the NNPDF3.0NLO PDF set and a dedicated set of tuned parameters developed by the SHERPA authors. While events with one additional parton are simulated at NLO, events with two or three additional partons are simulated at LO accuracy. Sets of multiple matrix elements are merged and matched to the SHERPA parton shower based on the Catani-Seymour dipole factorisation scheme using the MEPS@NLO prescription [226–229]. The OPENLOOPS library [230, 231] provides virtual QCD corrections for matrix elements at NLO. In the analysis, WZ+jets and ZZ+jets events are categorised based on the heaviest flavour of any accompanying jet, namely WZ+b, WZ+c, WZ+l for WZ+jets and ZZ+b, ZZ+c, and ZZ+l for ZZ+jets. In trileptonic final states, all but the WZ+b contribution are estimated from MC. The WZ+b contribution is instead estimated from data[2]. While WZ+jets events generally contribute significantly to final states with three leptons, ZZ+jets events specifically mainly contribute to final states with four leptons.

[2]This decision is motivated by the fact that the previous ATLAS measurement of the $t\bar{t}Z$ production process was only able to assign significant uncertainties to the WZ+b contribution as WZ+jets processes were estimated in a dedicated control region mainly enriched in WZ+c and WZ+l. This analysis aims at estimating the WZ+b contribution directly.

Single boson events (W+jets and Z+jets) are generated using SHERPA 2.2.1 at NLO accuracy for up to two jets and LO accuracy for up to four jets. The NNPDF3.0NLO PDF set is used, and the samples are normalised to next-to-next-to-leading order NNLO predictions. The matching to the parton shower is again performed following the MEPS@NLO prescription. While these processes are of subdominant importance in $t\bar{t}Z$ final states with three leptons, they represent significant background contributions in $t\bar{t}Z$ final states with two leptons.

Further, rarer processes are considered. The rare production of Higgs bosons associated with a W or Z boson is modelled via PYTHIA 8.186 using the A14 tune and the NNPDF2.3LO PDF set. The simultaneous production of three top quarks ($tt\bar{t}$) and a $t\bar{t}$ pair in association with a pair of W bosons is simulated at LO using MADGRAPH5_aMC@NLO 2.2.2. interfaced to PYTHIA 8.186. Events with four top quarks ($t\bar{t}t\bar{t}$) are modelled using MADGRAPH5_aMC@NLO 2.3.3. interfaced to PYTHIA 8.230 with the A14 tune at NLO precision using the NNPDF3.1NLO PDF set. Alternative $t\bar{t}t\bar{t}$ samples using Herwig 7.0.4 as the parton shower algorithm are also used. The production of events with three heavy gauge bosons (WWW, WWZ, WZZ, ZZZ), including events with up to six leptons, are simulated using SHERPA 2.2.2 and the NNPDF3.0NLO PDF set at NLO accuracy for final states with no additional partons and at LO accuracy for final states with up to three additional partons. A list of the processes and their respective contributions are given in Table 3.1.

[3]The processes listed here are processes which in trileptonic final states exclusively occur with fake leptons. In dileptonic final states, these samples contribute as prompt background processes. All other processes are also considered fakes in the analysis if they contain fake leptons.

[4]The estimation of fakes is based on a fake-factor-approach which is explained in Chapter 6.

Table 3.1: List of processes with relevant contributions to the event yields in the analysis. The used generator and parton shower are provided alongside the cross-section of the individual processes. The cross-sections are rounded for display purposes. In addition, the NLO k factor is given.

Process	Generator	Shower Algorithm	Cross-section [pb]	k-factor
$t\bar{t}Z$	MadGraph5_aMC@NLO 2.8.1	Pythia 8.244	0.876	-
- $t\bar{t}(Z \to e^+e^-)$	*	*	0.037	1.12
- $t\bar{t}(Z \to \mu^+\mu^-)$	*	*	0.037	1.12
- $t\bar{t}(Z \to \tau^+\tau^-)$	*	*	0.037	1.12
- $t\bar{t}(Z \to \nu\bar{\nu})$	*	*	0.155	1.10
- $t\bar{t}(Z \to q\bar{q})$	*	*	0.529	1.10
$t\bar{t}H$	MadGraph5_aMC@NLO 2.6.0	Pythia 8.230	0.51	-
- $t\bar{t}H(1\ell)$	*	*	0.205	1.10
- $t\bar{t}H(2\ell)$	*	*	0.051	1.10
- $t\bar{t}H$(full hadronic)	*	*	0.205	1.10
$t\bar{t}W$	Sherpa 2.2.10	-	0.639	-
- $t\bar{t}W$	*	*	0.597	1.17
- $t\bar{t}W$(EWK)	*	*	0.042	1.13
tZq	MadGraph5_aMC@NLO 2.9.5	Pythia 8.245	0.03	1.11
tWZ	MadGraph5_aMC@NLO 2.2.2	Pythia 8.212	0.02	1.00
- $WZ \to \ell\ell\ell\nu$	*	*	4.583	1.00
- $WZ \to \ell\ell\ell\nu jj$	*	*	0.046	1.00
ZZ+jets	Sherpa 2.2.2	-	0.88	
- $ZZ(gg \to h \to \ell\ell\ell\ell$ incl., $m_{4\ell} < 130\,\text{GeV})$	*	*	0.010	1.00
- $ZZ(gg \to h \to \ell\ell\ell\ell$ incl., $m_{4\ell} > 130\,\text{GeV})$	*	*	0.010	1.00
- $ZZ \to \ell\ell\ell\ell$	*	*	1.252	1.00
- $ZZ \to \ell\ell\ell\ell$(low $m_{\ell\ell}$ p_T complement)	*	*	1.432	1.00
Other processes with other non-prompt leptons[3]	varying	varying	DD-approach[4]	
$t\bar{t}$	Powheg-Box 2	Pythia 8.230	87.71	
W+jets ($Z \to \ell\ell$)	Sherpa 2.2.1	-	52.88	1.0
Z+jets ($Z \to \ell\ell$)	Sherpa 2.2.1	-	6414	1.0

CHAPTER 4

Event Selection

An event selection isolates desired signal events while simultaneously rejecting background events. Typically, selection regions are defined based on criteria such as expected signal event signatures or detector performance, allowing for efficient and precise measurements of the desired process. All events considered for measuring the inclusive cross-section of the $t\bar{t}Z$ production process are selected from proton-proton collision data recorded by the ATLAS detector between 2015 and 2018 during Run 2 of the LHC. On this dataset, selection criteria are imposed targeting the trileptonic $t\bar{t}Z$ final states. Generally, two selections are applied: *preselection* and the actual *event selection*. While the event selection in an ATLAS analysis focuses on reconstructed objects and imposing topological or kinematic cuts on them, the preselection defines a more straightforward set of selection criteria allowing for a rough selection of events. The preselection and the actual event selection are equally applied to data and MC events.

Additionally, preselected data events considered for the analysis must have been recorded during stable data-taking conditions [232] as explained in Section 2.1. They need to be part of the so-called *good run list*, which summarises all runs of the LHC where ATLAS achieved stable data-taking conditions, i.e. where all parts of the ATLAS detector were operational.

Preselected events must have at least one reconstructed primary vertex with at least two associated tracks with a minimum p_{T} of 500 MeV. This selection assures a high likelihood of a hard interaction between two partons. Furthermore, selected events in this analysis must coincide with the firing of a single electron or single muon trigger in the ATLAS HLT system, indicating the presence of at least one electron or muon, respectively. These triggers consist of a chain of varying criteria connected through a logical `OR` as presented in Table 4.1. The individual triggers follow the convention

`HLT_<type><pT>_<ID>_<iso>`, (4.1)

Table 4.1: Summary of the single electron and single muon triggers. The trigger chain is split into individual trigger decisions. Selected events must coincide with at least one of these triggers being fired. Next to the trigger string, the trigger decision is split into the identification, isolation and p_{T} criteria.

Trigger	Trigger string	Identification	Isolation	p_{T} cut [GeV]
Trigger string convention	HLT_<type><pT>_<ID>_<ISO>			
Single electron trigger (≥ 1 electron)	HLT_e24_lhmedium_L1EM20VH[1]	Medium	EM[2]	> 24
	HLT_e26_lhtight_nod0_ivarloose[3]	Tight	Loose	> 26
	HLT_e60_lhmedium_nod0	Medium	None	> 60
	HLT_e140_lhloose_nod0	Loose	None	> 140
Single muon trigger (≥ 1 CB muon)	HLT_mu20_iloose_L1MU15[4]	None	Loose	> 20
	HLT_mu26_ivarmedium	None	Loose	> 26
	HLT_mu50	None	None	> 50

where <type> describes the trigger type and <pT> describes the minimum p_{T} the object coinciding with a positive trigger decision has to have. The identification and isolation requirements are described by the <ID> and <iso> strings, respectively. Events passing the trigger selection are required to pass a set of *jet-cleaning* requirements which aim at separating jets originating from hard interactions from non-collision background processes as explained in Ref. [233]. To remove muons with insufficient momentum resolution, so-called *bad muons*, a bad muon veto is used, rejecting events with at least one muon with $\sigma(q/p)/|q/p| > 0.2$, where q describes the reconstructed charge and p the momentum of the muon, respectively.

The selection of events of this analysis aims at analysis regions with significant contributions of $t\bar{t}Z$ final states with 2 (dilepton channel), 3 (trileptonic channel) or four leptons (tetraleptonic channel)[5]. The inclusive and differential cross-section measurements of the $t\bar{t}Z$ final state are performed independently in these three channels. Afterwards, the individual measurements are combined. The following terminology will focus on the 3ℓ-channel unless stated otherwise.

In the 3ℓ-channel, which is the focus of this thesis, events must have exactly three leptons (electrons or muons), including one Z-candidate following the description in Section 2.3. In addition, all OSSF candidates are required to fulfil $m_{\ell\ell} > 10\,\mathrm{GeV}$ to suppress the contamination of events with lepton pairs originating from the decay of heavy quarkonia states. The three leptons must have a p_{T} of at least 27, 20, and 15 GeV for the leading, sub-leading and trailing lepton.

[1] Only used for 2015 data.

[2] Isolation requirement specific to 2015, candidate electrons are rejected if the sum of transverse energies in the 12 towers surrounding the 2×2 central region in the EM layer is at least 2 GeV and exceeds $E_{\mathrm{T}}/8.0 - 1.8\,\mathrm{GeV}$

[3] The *nod0* suffix indicates that the trigger ignores information from the transverse impact parameter relative to the beamline.

[4] Only used for 2015 data.

[5] Hereafter the lepton multiplicity refers to the channels: 2ℓ-channel, 3ℓ-channel, and 4ℓ-channel.

Table 4.2: Event yields in the 3ℓ-channel. Selected events must have three leptons (electrons or muons) and one Z-candidate. All OSSF candidates are required to fulfil $m_{\ell\ell} > 10\,\text{GeV}$. The three leptons must have a p_T of at least 27, 20, and 15 GeV, respectively. All events must have at least three jets, and at least one must be tagged using the DL1r b-tagging algorithm at the 85 % efficiency working point.

	Process	preselected events
	$t\bar{t}Z$	702±22
$t\bar{t}X$	$t\bar{t}W$	13±7
	$t\bar{t}H$	22±2
Diboson	WZ+b	140±40
	WZ+c	250±100
	WZ+l	180±80
	ZZ+b	26±15
	ZZ+c	22±9
	ZZ+l	37±12
	tZq	145±32
	tWZ	96±18
	$t\bar{t}t\bar{t}$	2±1
	Other	7±4
Fakes	F-e-HF	35±8
	F-e-Other	42±9
	F-μ-HF	48±6
	F-Other	21±11
	Total	1790±160

All events must have at least three jets. Of these jets, at least one must be tagged using the DL1r b-tagging algorithm at the 85 % efficiency working point.

The number of selected events per process based on the above selection is displayed in Table 4.2, separated into categories such as $t\bar{t}Z$, $t\bar{t}X$, diboson (WZ+jets, ZZ+jets), tZq, fake leptons (F-e-HF, F-e-Other, F-μ-HF, F-Other), and other processes (tWZ, $t\bar{t}t\bar{t}$, and others). The primary contribution is from $t\bar{t}Z$ events, followed by WZ+jets contributions, specifically WZ+l, WZ+c, and WZ+b. Additionally, tZq events significantly contribute, while the contributions of events with fake leptons and other processes are minor.

Two options exist to enhance background event rejection further while maintaining a substantial amount of signal events. These are: setting cuts on kinematic variable distributions to differentiate the $t\bar{t}Z$ signal process from other background processes or using multi-variate techniques such as neural networks (discussed in de-

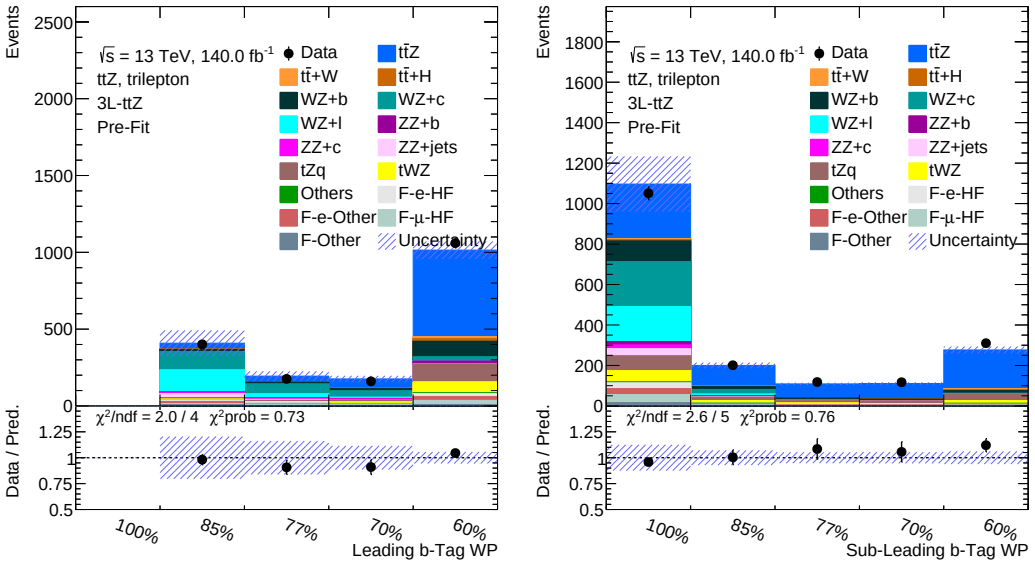

Figure 4.1: Distributions of the highest b-tagging working point in the event, second-highest b-tagging working point in the event. The data is shown using black dots. The blue uncertainty band includes statistical and systematic uncertainties. Events outside the histogram range are merged into the corresponding first or last bin. A χ^2 test evaluates the agreement between data and the MC simulation. The corresponding p-values are drawn in the lower pads of the distributions.

tail below). The former method can be seen in Figure 4.1, which displays the highest and second-highest b-tagging working point for events selected via the above criteria. The data is represented by black dots, with the blue uncertainty band encompassing statistical and systematic uncertainties. Events beyond the histogram range are merged into the nearest bin. A χ^2 test determines the agreement between data and the MC simulation, with corresponding p-values presented in the lower pads of the distributions.

The distributions exhibit significant differences in shape for $t\bar{t}Z$ and WZ+jets events. This difference originates from the fact that, on average, jets in WZ+l and WZ+c events are tagged with lower b-tagging working points than jets in $t\bar{t}Z$ final states, which are expected to produce two genuine b-jets tagged by the DL1r b-tagging algorithm. Applying cuts on these distributions at specified b-tagging working point thresholds would result in regions with high yields of either $t\bar{t}Z$ or WZ+jets events. This method, known as a *cut-and-count* analysis, was employed by ATLAS in the previous measurement of the $t\bar{t}Z$ production process [147], producing independent signal and control regions. In contrast, the latter approach involves using additional kinematic distributions and b-tagging working points as input to a neural network that outputs values used in a process called *event classification*. These kinematic distributions are displayed in Figures 4.2 and 4.3.

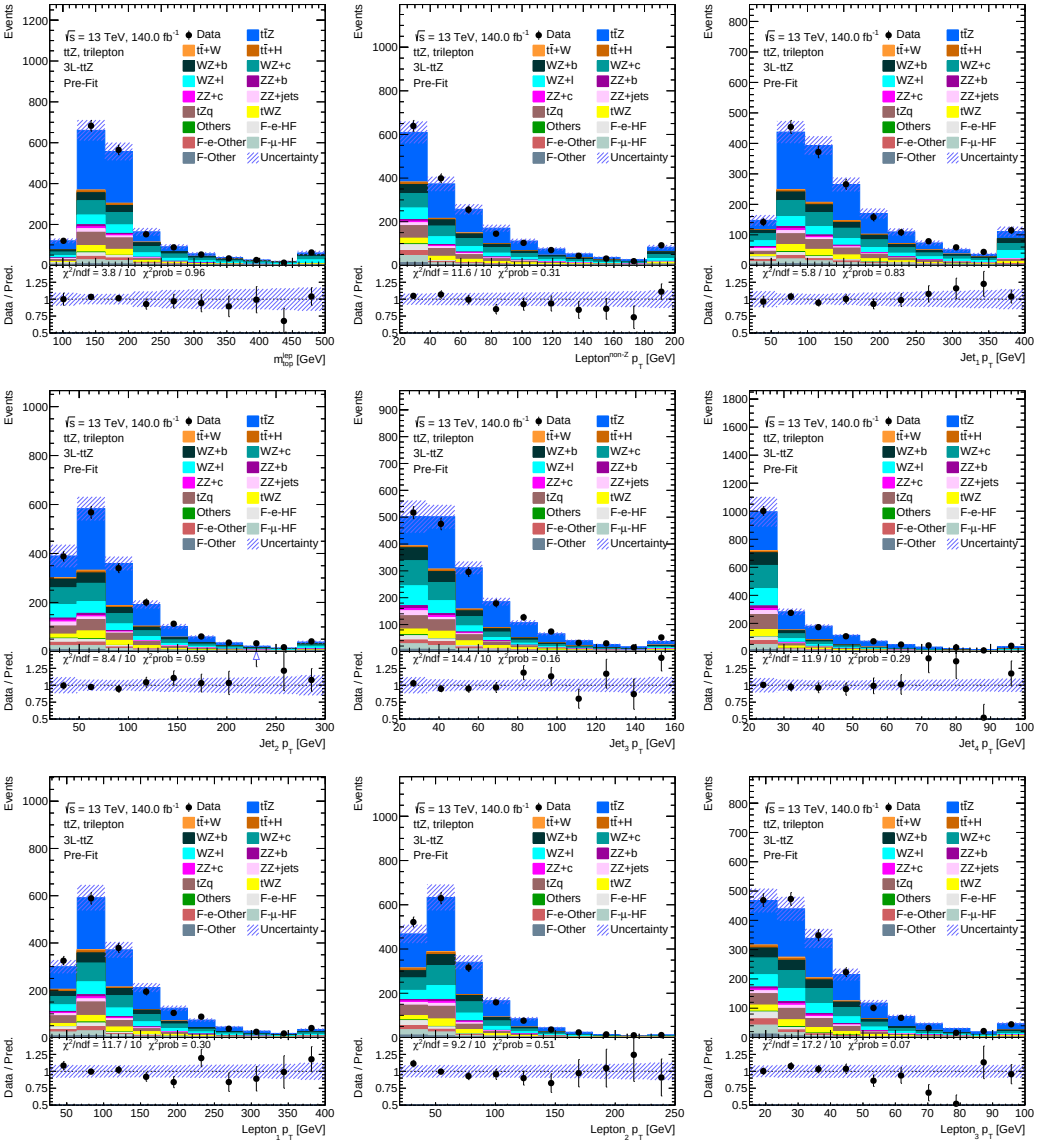

Figure 4.2: Distributions of the reconstructed mass of the leptonically decaying top quark, the p_{T} of the lepton not originating from the reconstructed Z boson, second-highest b-tagging working point in the event, the highest jet p_{T}, the 2$^{\mathrm{nd}}$-highest jet p_{T}, the 3$^{\mathrm{rd}}$-highest jet p_{T}, the 4$^{\mathrm{th}}$-highest jet p_{T}, the highest lepton p_{T}, the 2$^{\mathrm{nd}}$-highest lepton p_{T}, and the 3$^{\mathrm{rd}}$-highest lepton p_{T}. The data is shown using black dots. The blue uncertainty band includes statistical and systematic uncertainties. Events outside the histogram range are merged into the corresponding first or last bin. A χ^2 test evaluates the agreement between data and the MC simulation. The corresponding p-values are drawn in the lower pads of the distributions.

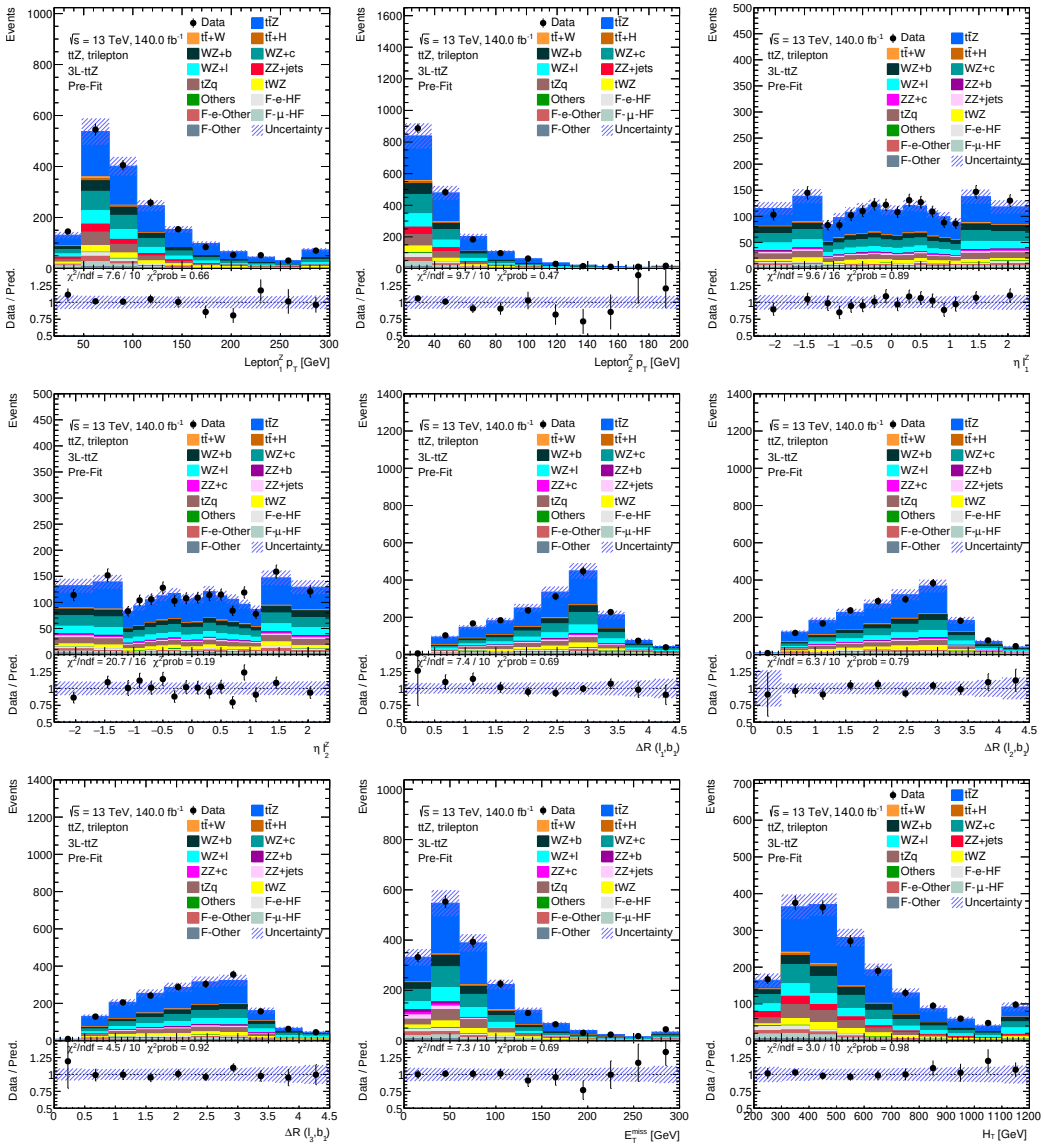

Figure 4.3: Distributions of the p_{T} of the first and second lepton originating from the reconstructed Z boson, the ΔR-distance between the first, second and third lepton and the leading b-jet, $E_{\mathrm{T}}^{\mathrm{miss}}$, and H_{T}. The data is shown using black dots. The blue uncertainty band includes statistical and systematic uncertainties. Events outside the histogram range are merged into the corresponding first or last bin. A χ^2 test evaluates the agreement between data and the MC simulation. The corresponding p-values are drawn in the lower pads of the distributions.

Similar to Figure 4.1, Figure 4.2 shows the reconstructed mass of the leptonically decaying top quark, the p_{T} of the lepton not originating from the reconstructed Z boson, second-highest b-tagging working point in the event, the highest jet p_{T}, the 2^{nd}-highest jet p_{T}, the 3^{rd}-highest jet p_{T}, the 4^{th}-highest jet p_{T}, the highest lepton p_{T}, the 2^{nd}-highest lepton p_{T}, and the 3^{rd}-highest lepton p_{T} is shown. Finally, Figure 4.3 shows distributions of the p_{T} of the first and second lepton originating from the reconstructed Z boson, the ΔR-distance between the first, second and third lepton and the leading b-jet, $E_{\mathrm{T}}^{\mathrm{miss}}$, and H_{T}. A reasonable agreement between data and the simulation is observed for all distributions.

In the following chapter the classification of events using these input distributions will be highlighted in more detail.

CHAPTER 5

Event Classification

The previous chapter discussed the preselection of events based on simple criteria such as trigger information and *cleaning requirements* like jet-cleaning and removing bad muons, followed by selecting events with $t\bar{t}Z$-like final states. While this selection chain already produces a relatively pure selection of $t\bar{t}Z$ events, many background processes remain. To further improve the separation of signal and background events, an additional event classification is performed based on *high-level* output distributions built from neural network output scores, which in turn are based on *lower-level* inputs of kinematic distributions.

If powerful classification algorithms are available, an initially large acceptance can be chosen to increase the number of $t\bar{t}Z$ events while the classification algorithms recover the signal purity through efficient background rejection. For the classification of $t\bar{t}Z$ events, an approach based on *neural networks* is followed.

In a three-year-long effort, the author developed the necessary framework to efficiently design and train neural networks in the three analysis channels (2ℓ, 3ℓ, 4ℓ) of the $t\bar{t}Z$ analysis. These tools provide a common ground for all neural networks developed in the three channels (2ℓ, 3ℓ, 4ℓ) for the analysis.

The following paragraphs will briefly explain the concept of neural networks. Afterwards, the neural network approach utilised in the trileptonic channel is presented in detail, and the procedure of classifying events is explained. Similar approaches are undertaken in the other two analysis channels, the 2ℓ and 4ℓ channels.

As this is one of the author's main contributions to the measurement of the $t\bar{t}Z$ inclusive cross-section, a detailed overview of the results and methods is provided.

5.1 The neural network approach

Neural networks are machine learning algorithms inspired by the structure and function of the human brain. They are designed to recognise patterns and make decisions or predictions based on input data.

The famous work by Alan Turing about an abstract machine designed to solve any mathematical problem [234], providing a mathematical replica of the *states of mind*, can undoubtedly be seen as a milestone in the history of computing. In his work, Turing focuses on a remaining open question about mathematics posed by the Göttinger mathematician David Hilbert at the beginning of the 20th century [235], specifically the *Entscheidungsproblem*, i.e. whether mathematics is *decidable*. In this context, questioning whether mathematics is *decidable* deals with the existence of a (mechanical) procedure which can guarantee a correct decision about whether a mathematical assertion is true[1].

In a way, Turing connects Hilbert's mathematical question with a conceptual mechanical process, i.e. a machine taking decisions. Naturally, in 1943 McCulloch and Pitts continued on Turing's work and first introduced the concept of an artificial neuron, the *McCulloch-Pitts neuron*, i.e. the first mathematical model of a neural network employing propositional logic [236]. They aimed at describing brain functions abstractly, showing that a simple mathematical description could yield immense computational capabilities.

The earliest computing model based on this inspiration, the *perceptron*, was designed by Rosenblatt in 1957 [237]. In Ref. [238], Rosenblatt develops the perceptron model further in the context of a *probabilistic model for information storage and organisation in the brain*. His work revolves around developing a machine capable of conceptualising information directly from the physical environment in the information encoded in light, sound, temperature, and others, thereby staying close to the original inspiration, the human brain. Applying such a machine would remove humans from decision-making procedures, digesting and coding the essential information, thereby automating previously human-driven processes.

However, due to the need for more affordable computing power, neural networks only gained widespread attention with the advent of the digital age in the 1980s. In 1986, the concept of *backpropagation* to train artificial neural networks was introduced [239]. Among other work performed at the time, these newly introduced concepts made it possible to develop and train neural networks to perform real-life tasks, finally getting closer to a real machine capable of performing decision tasks like a human being.

Modern neural networks

Even though the intricate structure of the human brain acted as the initial inspiration for neural networks, their modern-day design is often straightforward: A modern neural network consists of consecutive layers of interconnected *neurons*, also commonly referred to as *nodes*, which process and transfer information. Each neuron receives inputs from other neurons, processes those inputs using an activation function wrapped around trivial linear algebra, and dispatches the output to other neurons in the subsequent layer. The *feeding* of information through the network

[1] In his work, Turing was able to show that no such process exists.

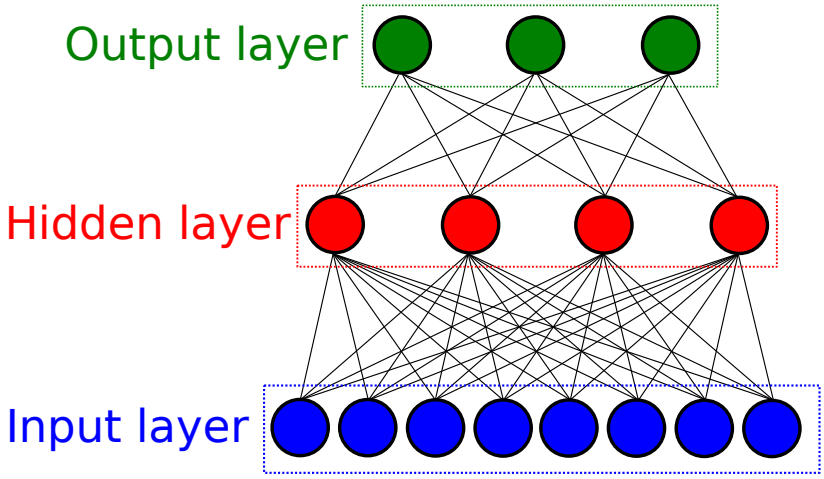

Figure 5.1: Representative overview of a feed-forward neural network. The information *flows* through the input layers towards the output layer and one or multiple hidden layers. Each layer is densely connected to the previous layer.

leads to the name of these networks: feed-forward networks. In the following, the prefix is omitted for simplicity.

The layers of such a neural network are arranged into an input layer, one or more hidden layers, and an output layer. The input layer receives the raw input data, and the output layer produces the neural network's final output. The output of each node, x', is defined through

$$x' = f(\vec{x} \cdot \vec{w} + b), \tag{5.1}$$

where $\vec{x}$ denotes the input vector, $\vec{w}$ the previous layers weights vector, and b the bias term. The activation function of the current layer is represented by f. The hidden layers process the input and pass it on to the output layer, allowing the network to learn and assemble more complex decisions. A representative overview of such a network is given in Figure 5.1

The learning procedure, typically referred to as *training*, is based on the back-propagation algorithm mentioned above, an iterative training algorithm that uses gradient descent to adjust the weights, $\vec{w}$, and biases, b, of the connections between nodes. This gradient is calculated for a *loss function*, $\mathcal{C}(y, \hat{y})$, which represents the *goodness of fit* of the model by measuring the distance between the predicted values, $\hat{y}$, and the actual values, y. The training goal is to adjust the parameters of the network, θ, such that $\mathcal{C}(y, \hat{y})$ is minimised. For a neural network with L layers, where the output of the l-th layer is given by $f_l(x)$, the output of the neural network is given by

$$y(\vec{x}) = f_L(f_{L-1}(\dots f_1(\vec{x}))), \tag{5.2}$$

where $\vec{x}$ is the input vector to the neural network. Computationally, the gradient of the loss function with respect to the network parameters, $\partial\mathcal{C}/\partial\theta$, is calculated using the chain rule of calculus. The model parameters, θ, are updated using versions of the stochastic gradient descent (SGD) algorithm. In this work, the *Adam* algorithm [240], an improved version of the classical SGD algorithm, is used implemented using the following pseudo-code:

$$
\begin{aligned}
t &\leftarrow t+1 \\
g_t &\leftarrow \nabla_\theta \mathcal{C}(\theta_{t-1}) && \text{(Calculate gradients with respect to } \theta) \\
m_t &\leftarrow \beta_1 m_{t-1} + (1-\beta_1) g_t && \text{(Biased } 1^{\text{st}} \text{ moment estimate)} \\
v_t &\leftarrow \beta_2 v_{t-1} + (1-\beta_2) g_t^2 && \text{(Biased } 2^{\text{nd}} \text{ raw moment estimate)} \\
\hat{m}_t &\leftarrow m_t/(1-\beta_1^t) && \text{(Bias-corrected } 1^{\text{st}} \text{ moment estimate)} \\
\hat{v}_t &\leftarrow v_t/(1-\beta_2^t) && \text{(Bias-corrected } 2^{\text{nd}} \text{ raw moment estimate)} \\
\theta_t &\leftarrow \theta_{t-1} - \eta \cdot \hat{m}_t/(\sqrt{\hat{v}_t}+\epsilon) && \text{(Update parameters)}
\end{aligned}
$$

Here $\beta_1 = 0.9$ and $\beta_2 = 0.999$ represent exponential decay rates for the moment estimates, and t is the timestep. The elementwise square is indicated by g_t^2. For computational stability $\epsilon = 10^{-8}$ is used. All operations on vectors are element-wise, with β_i^t denoting β_i to the power of t. The learning rate is denoted by η, determining the step size of a single update. The first and second-moment vectors and the timestep are initialised with zero. This update process is repeated for multiple epochs until the model's loss is minimal.

During training, the distributions passed from one layer to the next can vary, inducing a shift in the layer's activations. *Batch normalisation* layers apply a normalisation that aims at returning a mean output close to 0 with a standard deviation close to 1. To achieve this, a batch normalisation layer returns

$$y_i = \frac{a_i - \mu_{\text{Batch},i}}{\sqrt{\sigma^2_{\text{Batch},i} + \epsilon}} \cdot \gamma + \beta \tag{5.3}$$

during training, where a_i is the return value of the activation function of a given node in the layer, and $\mu_{i,\text{Batch}}$ ($\sigma_{i,\text{Batch}}$) the mean (standard deviation) of the outputs of node i across a batch. The parameters β and γ represent trainable offset and scaling factors, respectively. For computational stability, $\epsilon = 10^{-3}$ is used. During inference, that is, the evaluation of the model on hitherto unseen data, the layer normalises its output by applying a moving average of the mean and standard deviation computed based on all batches seen during training instead. As a result, the normalising effect only occurs for data with similar statistics as the training data.

Regularisation techniques

Model regularisation refers to a technique to prevent *overfitting*, a process which occurs when the complexity of the model allows it to become sensitive to statistical

fluctuations in the training data. Such sensitivity then leads to poor performance on unseen data. Regularisation attempts to mitigate this by adding additional constraints or penalties to the model's loss function during training, favouring more general solutions. The following four ways of regularisation are discussed: *L1 regularisation*, *L2 regularisation*, *dropout*, and *early stopping*.

L1 regularisation, introduced in 1996 [241] and commonly known as *Lasso regularisation*, describes a technique that adds a penalty term to the loss function proportional to the absolute value of the weights. This penalty favours model configurations with smaller weights, which can help reduce overfitting and improve generalisation.

L2 regularisation, also known as *Ridge regularisation* [242], adds a penalty term to the loss function proportional to the square of the weights. Similar to L1 regularisation, this favours models with smaller weights.

Dropout describes a technique where a set of the inputs of a given layer is randomly set to 0 during training, reducing the dependency of the output on any particular node [243]. This technique favours more robust models, leading to improved generalisation performance.

Lastly, early stopping defines a procedure where the model's performance on a validation set is monitored during training. The training process is stopped early if the model's performance starts to degrade. I.e., given a validation set with loss function values $l_1, l_2, \ldots, l_n$, the training process is terminated when the loss function value stops decreasing, such as when

$$v_l \leq l_{i-p} - \Delta_{\min} \quad |\forall p \in [0, P];\ i \in \mathbb{Z};\ i - p > 0, \tag{5.4}$$

where P describes a positive integer number of epochs to be monitored, denoted *patience*, and $\Delta_{\min}$ the minimum amount of change of the loss value that qualifies as an improvement. Afterwards, the model configuration with minimal loss is restored. For the development of the neural networks discussed here, dropout and early stopping were tested as regularisation methods and found to yield sufficient generalisation performance.

Model evaluation

Evaluating the performance of a model is the last essential step in any machine-learning-driven pipeline. Various metrics and techniques are available to assess a model's performance. Here three specific metrics are considered: receiver operating characteristic (ROC) curves, permutation importance, and the comparison of training and testing set performances.

ROC curves are typically used to evaluate the performance of binary classifiers, which are models that predict the class label of an input sample as either 0 or 1. The ROC curve can be calculated for multi-class classification problems by breaking the problem down into multiple binary classification scenarios. A ROC curve is generated by sketching the true positive rate (TPR) against the false positive rate (FPR) at different classification thresholds. An ideal classifier will have a ROC curve with an area under the curve (AUC) value of 1.0, while a classifier that is no better

than random guessing will have an AUC of 0.5. The AUC can be interpreted as the probability that the classifier will rank a randomly chosen positive sample higher than a randomly chosen negative sample. It is approximated using the *trapezoidal rule*, that is the sum of the areas of the trapezoids formed by the TPR and FPR values for each bin:

$$\text{AUC} = \sum_{i=1}^{n_{\text{bins}}^{\text{AUC}}-1} \frac{(\text{TPR}_i + \text{TPR}_{i+1})(\text{FPR}_{i+1} - \text{FPR}_i)}{2}, \tag{5.5}$$

where $n_{\text{bins}}^{\text{AUC}}$ is the number of bins. In the follwowing, $n_{\text{bins}}^{\text{AUC}} = 100$ is used.

Permutation importance defines a technique used to evaluate the impact of individual input variables on the model's performance. It involves randomly permutating an input variable and measuring the resulting performance degradation

$$\Delta\text{AUC} = \text{AUC}(\vec{x}, \vec{y}) - \text{AUC}(\vec{\tilde{x}}, \vec{y}), \tag{5.6}$$

where $\vec{\tilde{x}}$ represents the set of input vectors where one input feature is randomly shuffled. If the input variable is essential, there should be a significant decrease in performance after shuffling as the relation between the input feature and the output is broken. The permutation importance is then calculated as the relative change in the difference between the model's AUC using the original input data, $\vec{x}$, and the shuffled input data, $\vec{\tilde{x}}$.

In addition to these metrics, the model's performance on the training and testing sets is compared to assess the model's ability to generalise to new, unseen data. Through the Kolmogorov-Smirnov test, the empirical cumulative distribution functions (ECDFs) of the two output distributions can be compared, and their distance can be quantified [244]. The ECDF of a sample is a function describing the proportion of the sample that is less than or equal to a given value:

$$F_n(x) = \frac{1}{n} \sum_{i=1}^{n} 1_{(-\infty,x]}(X_i), \tag{5.7}$$

where $1_{(-\inf,x]}$ is indicator function which is equal to 1 if $X_i \leq x$ and 0 otherwise. The term n is the sample size. The test determines the maximum difference between the two ECDFs, commonly referred to as the KS statistic

$$D_{n,m} = \sup_x |F_{1,n}(x) - F_{2,m}(x)|. \tag{5.8}$$

Here $F_{1,n}$ and $F_{2,m}$ are the ECDFs of the two samples, and sup is the supremum function.

If the distributions originate from the same underlying probability distribution, the KS statistic is small; otherwise, it is not. The null hypothesis of the KS test is that the two samples come from the same underlying distribution, and the alternative hypothesis is that they originate from different distributions. The p-value, i.e. the probability of obtaining a KS statistic greater than or equal to the observed value

under the null hypothesis, is used to evaluate the strength of the evidence against the null hypothesis. It should be noted here that the KS is designed to be applied on continuous distributions. For binned distributions, the calculated probabilities will be higher than for comparable continuous distributions. However, as the bin width is chosen to be smaller than any physical effect of interest, the impact of this effect can be neglected, and the calculated probability is taken as a reasonable approximation of the actual probability.

In summary the aforementioned ROC curves and the AUC are used as metrics to evaluate the permutation importance of all variables. The overall performance is estimated by overlaying training and testing output distributions. The following section highlights the developed classifier approach and its performance for classifying $t\bar{t}Z$ events in the trilepton channel.

5.2 Neural networks for event classification

To reduce the influence of leading backgrounds, neural networks (NN) are used for event discrimination. A 3-class neural network is developed to discriminate between $t\bar{t}Z$, tZq and diboson events (WZ+l, WZ+c,WZ+b, ZZ+l, ZZ+c, ZZ+b). The goal of the neural network is to assign a $t\bar{t}Z$-, tZq and VV-probability to each event, where VV includes all diboson event signatures. No individual jet flavour is favoured for the classification into WZ+jets and ZZ+jets events. This choice emphasises the event's underlying WZ- and ZZ-nature instead of the jet-dependent flavour.

To utilise the entire dataset, allowing for the evaluation of all events, a k-fold cross-validation strategy is employed using $k = 4$ folds, comprising 25% of all events, respectively. Events are split into statistically independent subsets by applying the modulo operation on the event number of each event, resulting in, namely, 0,1,2 and 3 uniquely defining the subset each event enters. From these subsets, *folds* are constructed by splitting the four subsets at a ratio of 1 : 3. This procedure is performed for all MC and data samples. The yields for MC and data are checked for each sample and found to be comparable to the intended 25 % in all cases, resulting in sets with matching statistical significance.

For the training, 25% of the training data is randomly drawn from the *training set* and used as a *validation set*. Each training set, therefore, comprises $75\% \cdot 75\% = 56.25\,\%$ and each validation set 18.75 % of all events in the entire fold. The remaining 25 % of events in a fold are the *testing set*. Between folds, only the testing sets are statistically independent.

Figure 5.2 provides a schematic overview of the k-folding procedure as well as the composition of the MC dataset, split into different processes. Varying colours indicate the different folds and different processes. The $t\bar{t}Z$ signal process dominates with 39.13 %. Sub-dominant are WZ+jets processes with 10.04 % (WZ+l), 13.89 % (WZ+c), and 8.06 % (WZ+b). The tZq process makes up 8.08 %. The remaining processes comprise each less than 6.0 %. The training set (dark blue), validation set

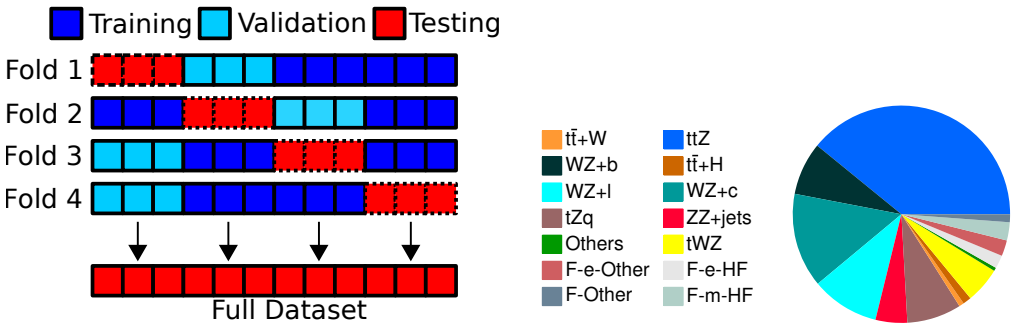

Figure 5.2: Schematic overview of the used k-folding procedure (left) and composition of the entire MC dataset (right). The dataset is split into four folds holding 25 % of the dataset each. During training, each fold is taken to split the complete dataset into a testing set (red), a training (dark blue), and a validation set (light blue). At the end of the training of all four networks, the complete dataset can be obtained through a combination of the four independent testing sets. The training and validation sets are not statistically independent. The sizes of the individual boxes are not to scale. The $t\bar{t}Z$ signal process dominates with 39.13 %. Sub-dominant are WZ+jets processes with 10.04 % (WZ+l), 13.89 % (WZ+c), and 8.06 % (WZ+b). The tZq process makes up 8.08 %. The remaining processes comprise each less than 6.0 %.

(light blue) and testing set (red) are highlighted. For the testing sets, T_i,

$$\bigcup_{i\in[1,2,3,4]} T_i = \text{Full dataset}, \tag{5.9}$$

$$T_i \cap T_j = \emptyset \quad |i,j \in [1,2,3,4], i \neq j. \tag{5.10}$$

holds. In the following, the terminology focuses on a single network. The other folds are treated identically.

In the training of the classifiers, only $t\bar{t}Z$, tZq and diboson events are considered in the training process. This decision accentuates the differences between these primary backgrounds in training.

As training weights, the MC weights are utilised. The per-batch loss, $\mathcal{L}_{\text{batch}}$, is computed as the weighted average of the product of the per-event loss, $\mathcal{L}_{\text{event}}$, and training weight, w_i. The training weights of all target classes are reweighted to avoid biases towards one target class or another, such that

$$\sum_i^N w_i^{C_j} = \sum_i^N w_i^{C_k}, \quad C_j, C_k \in t\bar{t}Z, tZq, \text{Diboson}, \tag{5.11}$$

where $w_i^{C_j}$ describes the i'th event weight of the j'th class. As a result, correct and incorrect classifications of all three target classes have an equal impact on the loss and the training.

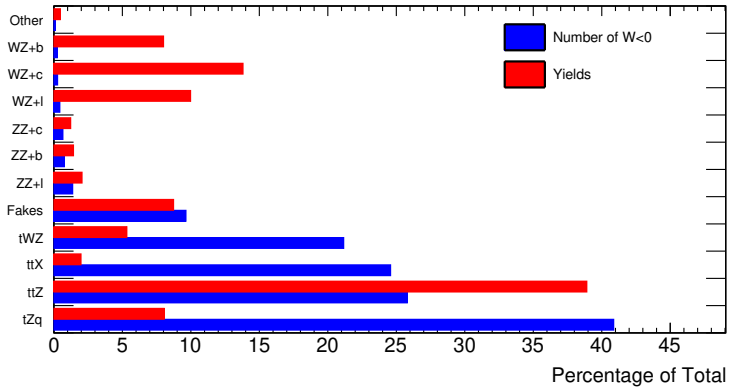

Figure 5.3: Bar chart summarising the percentage of negative event weights per sample (blue) and the percentage with respect to the total yield of the dataset. A significant number of negative event weights is observed for the $t\bar{t}Z$ and tZq process.

The impact of negative MC weights, originating from a generator-level-based reduction of the event density in some regions of phase space, is studied for the training. From a physics stance, the entire set of events, including those with negative weights, describes the complete SM prediction of nature. Hence all weights should be taken into account when training a neural network. The percentage of events with negative weights compared to the contribution to the total yield is given in Figure 5.3. The $t\bar{t}Z$ and tZq processes contribute a significant number of events with negative weights, approximately 25 and 40 %, respectively. Additionally, tWZ and $t\bar{t}X$ ($t\bar{t}H$, $t\bar{t}W$) events show large percentages of negative weights, but they are not used directly in training. Since the yields are reweighted for the training, cases can occur where the summed-up weights per batch are negative. As a result, the weighted average loss per batch can become negative. Since the training minimises the gradient of the loss with respect to the model's parameters, the minimisation breaks down as the loss diverges towards negative infinity. An alternative treatment of negative weights has to be used to preclude this breakdown of the training. Three possible options can be considered to achieve a converging loss during the training.

The first option is to set all negative event weights to zero, preventing the loss from becoming negative. Even though this option guarantees numerical stability, it ignores the effect of these events and the theory input these negative weights represent. Therefore, it is discarded.

The second option is to use the absolute value of the weights. In this case, a former reduction of event density in a given region of phase space is inverted. Since this option does not correctly reflect the generator-based event densities, it is also discarded.

In the following paragraphs, the used third option is discussed in detail. The positive weights are reweighted to account for the normalisation impact of negative weights and prevent training collapse. A scale factor, $w_{\mathrm{SF,Sample}}$, is calculated per

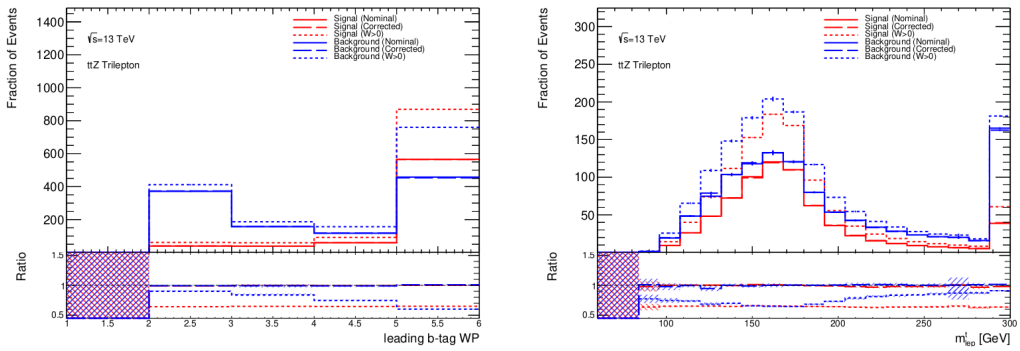

Figure 5.4: comparison of the distributions obtained using all MC weights (solid), using only positive event weights (dotted), and using the corrected MC weights (dashed). Shape differences are observed when negative event weights are dropped. The distributions show the leading b-tagging working point in the event (left) and the reconstructed mass of the leptonically decaying top quark, m^t_{lep} (right). The ratio is with respect to the unchanged distributions. After applying sample-wise scale factors which take negative event weights into account, the distributions show reasonable agreement. The shaded error bands reflect the statistical uncertainties.

sample, accounting for the difference in normalisation originating from not using negative event weights. These sample-wise scale factors are then applied to the event weights prior to the training:

$$w_{i,\text{Sample}} = w_i \cdot w_{\text{SF,Sample}}. \tag{5.12}$$

The impact of this decision on the input distributions is studied by comparing the resulting distributions using all weights to distributions using only non-negative event weights and scaled weights, here denoted *corrected*. The comparison is performed separately for signal and background events. The most notable deviations of the ratio between the distributions using all weights and only positive weights are observed for the highest b-jet working point and the reconstructed mass of the leptonically decaying top quark shown in Figure 5.4. After applying the sample-wise scale factors, the distributions show reasonable agreement. In addition to the shape of the individual distributions, the change in the correlations between distributions is checked. For this, the differences in the Pearson correlation coefficients are calculated based on the nominal and reweighted distribution. Since relative changes for uncorrelated distributions can be large, the absolute differences, ΔCorrelation, of the Pearson correlation coefficients are shown in Figure 5.5. The correlation difference is negligible for all variables, with the largest differences being observed between the sum of the transverse momenta of all reconstructed objects in the event, HT, and the jet multiplicity and the transverse momenta of the jets in the event. As a result of these studies, option three is applied for the training as it provides a reasonable theoretical description of the underlying shape of the variables and a numerically

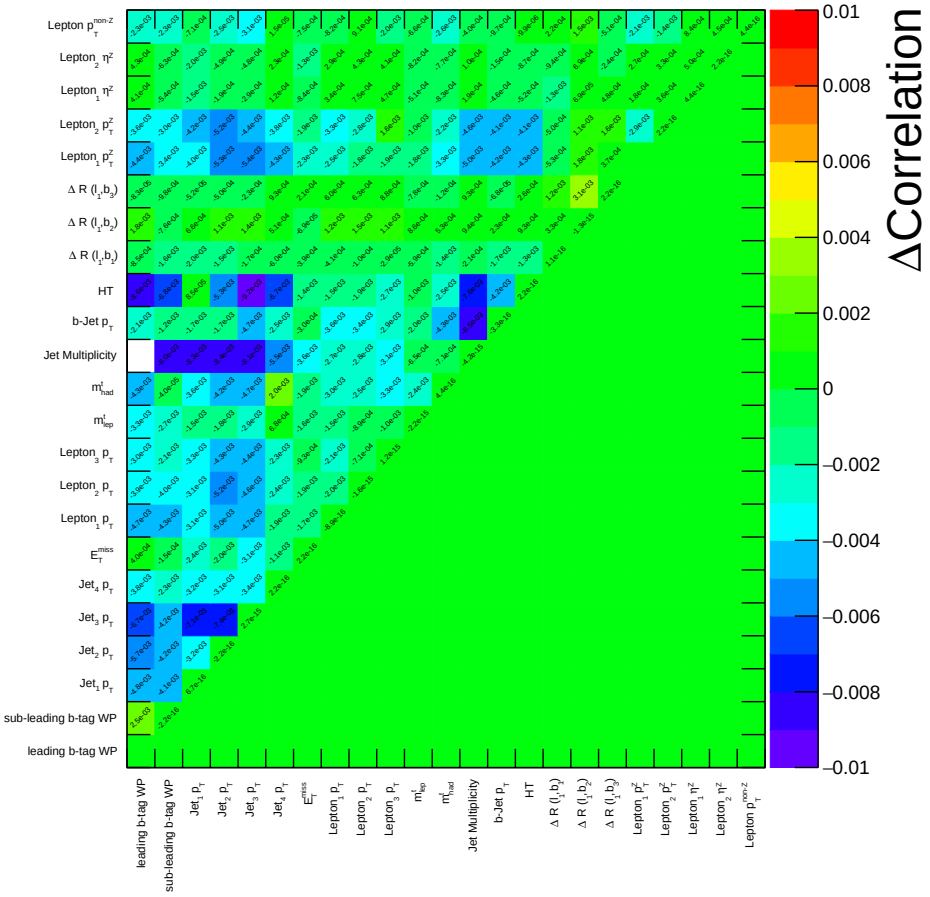

Figure 5.5: Absolute differences between the Pearson correlation coefficients calculated using the nominal and corrected distributions, ΔCorrelation. The calculated differences are negligible for all input variables.

stable training.

Before training, all events are preprocessed by scaling the input values into a range between 0 and 1 to minimise the variance of neural network weights. The necessary scale factor is determined per input variable using the entire dataset. All variables of any unseen events are scaled using the same scale factors.

Neural network architecture and training

The used NN architecture is a densely connected feed-forward network consisting of 5 hidden layers with 70, 70, 40, 50 and 70 nodes, respectively. It is based on the Keras [245] functional API within TensorFlow [246].

The activation functions for these layers are `tanh`, `ELU`, `sigmoid`, `tanh` and again `sigmoid`. The network weights are initialised by randomly drawing samples from a uniform distribution between $-L$ and L where $L = \sqrt{6/(\text{fan}_{\text{in}} + \text{fan}_{\text{out}})}$. Here fan_{in} describes the number of input units in the weight tensor and fan_{out} the number of output units in the weight tensor [247]. This initialisation method aims to set the initial weights of the neural network in a way that preserves the mean and variance of the input and output of each layer. The output layer consists of three nodes and uses the `Softmax` activation function; it is used to assign a single class label to an input sample among several possible classes. It transforms a vector of real-valued predicted values, $\hat{y}$ into a vector, interpreted as a set of mutually exclusive probabilities, $\hat{y}'$:

$$\hat{y}'_i = \text{softmax}(\hat{y}_i) = \frac{\exp(\hat{y}_i)}{\sum_{j=1}^{3} \exp(\hat{y}_j)}, \quad i = 1, 2, 3, \tag{5.13}$$

In this case, the sum of the outputs is unity. In the three-dimensional output case, the function maps the scores onto a triangular two-dimensional plane, where the probabilities lie on the surface within a triangle with legs of unit length. Section 5.2 sketches the result given two pseudo-classes. Lines of constant probabilities of the remaining third class are described by isolines parallel to the base of the triangle. Additionally, the figure indicates the isoline with the lowest probability of the third class with a blue dot.

Prior to the first and after the first and fourth hidden layers, batch normalisation layers are used.

The number of nodes per layer, the number of layers, the activation function used in each layer, and the layers where dropout or batch normalisation layers are added were optimised using a grid scan. 500 networks with randomly set parameters were trained and evaluated for this grid scan. The network with the minimum mean loss between all four folds was chosen.

This grid search did not test additional parameters like the batch size, the type of weight initialisation, the learning rate and different levels of regularisation, such as a different dropout probability or additional L1 or L2 regularisation.

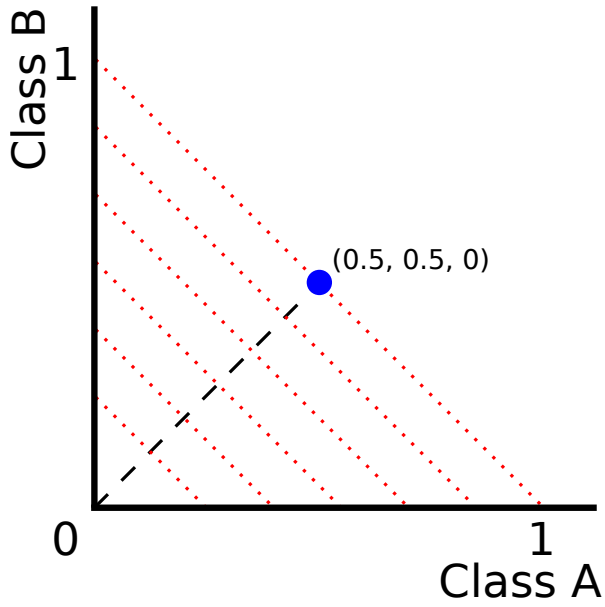

Figure 5.6: Sketch of the effect of a `Softmax` output activation function on the resulting mutually exclusive probabilities given two pseudo-classes, *class A* and *class B*. Lines of constant probabilities of the remaining third class are described by isolines parallel to the base of the triangle. The isoline with the lowest probability of the third class is indicated with a blue dot.

During the training, the categorical cross-entropy,

$$\mathrm{CE} = -\sum_{i}^{C} y_i \log(y(\vec{x})_i) \tag{5.14}$$

is minimised using the Adam optimiser with Nesterov momentum [240, 248]. Here y_i describes the target label of class i and $y(\vec{x})_i$ the prediction of the classifier for an event with inputs $\vec{x}$. The used batch size is $5 \cdot 10^3$, and the learning rate is $5 \cdot 10^{-4}$. Once no improvement better than $\Delta_{\mathrm{min}} = 10^{-4}$ concerning the validation loss is observed throughout 30 consecutive epochs, the training is stopped.

Several variables providing separation power between the three classes are considered for building the NN discriminants. Choosing input variables is based on a physics-centred *top-down* approach. In this approach, the impact of relevant observables is investigated by calculating the per-sample *separation power*,

$$\mathcal{S} = \frac{1}{2}\sum_{i}^{N} \frac{(S_i - B_i)^2}{(S_i + B_i)}, \tag{5.15}$$

where S_i is the number of signal events and B_i is the number of background events in bin i. Potential candidate variables providing separation power are kinematic

Table 5.1: Summary of the variables used as input parameters for the $t\bar{t}Z$ event classification. The first column denotes the variable's name. The second column describes the variable. In addition, the calculated separation power S between the $t\bar{t}Z$ signal events and WZ+b background events, as well as between $t\bar{t}Z$ and tZq events, is shown.

Variable	Description	$S(t\bar{t}Z$ vs WZ+$b)$ [%]	$S(t\bar{t}Z$ vs $tZq)$ [%]
b-tag WP_1	The highest b-tagging working point of all jets in the event.	1.45	0.03
b-tag WP_2	The second highest b-tagging working point of all jets in the event.	11.58	1.51
Jet $p_{\mathrm{T},i}$	p_{T} of the i'th jet, $i \in [1,4]$.	[2.9, 3.75, 4.22, 2.25]	[1.13, 2.26, 4.45, 5.56]
$E_{\mathrm{T}}^{\mathrm{miss}}$	Missing transverse energy of the event.	0.6	0.4
Lepton $p_{\mathrm{T},i}$	p_{T} of the i'th lepton, $i \in [1,3]$	[0.10, 0.06, 0.12]	[3.17, 3.17, 1.76]
m_t^{lep}	Reconstructed mass of the leptonically decaying top quark.	5.66	0.39
m_t^{had}	Reconstructed mass of the hadronically decaying top quark.	4.72	7.14
$nJets$	The jet multiplicity.	4.78	14.73
Leading b-Jet $\mathrm{p_T}$	p_{T} of the b-jet tagged with the highest working point.	8.07	0.84
ht	The sum of the transverse momentum of all jets of the event.	2.05	4.46
$\Delta R(l_i, b_1)$	ΔR between the i'th lepton and the b-jet tagged with the highest working point of the event where $i \in [1,3]$.	[2.47, 2.53, 2.22]	[1.4, 0.71, 0.48]
$p_{\mathrm{T},i}^{\mathrm{Z}}$	p_{T} of the leptons assigned to the Z	[0.26, 0.82]	[2.07, 2.87]
$\eta_{\mathrm{T},i}^{\mathrm{Z}}$	η of the leptons assigned to the Z	[1.46, 0.77]	[0.93, 0.49]
$p_{\mathrm{T}}^{\mathrm{non-Z}}$	The transverse momentum of the remaining lepton not assigned to the Z boson.	0.48	0.83

disttributions of the jets and leptons as well as variables with high-level information such as reconstructed masses or angles between objects. A summary of the selected variables and their separation power S between the $t\bar{t}Z$ signal events and WZ+b background events and between $t\bar{t}Z$ and tZq events is given in Table 5.1.

In particular b-tagging information is used to separate $t\bar{t}Z$ and tZq events from WZ+l, WZ+c, ZZ+c, and ZZ+l events. Specifically the leading and sub-leading b-tagging scores within the pseudo-continuous distribution are used. The transverse momentum of the leading b-jet provides further discrimination power as b-jets in WZ+b and ZZ+b events have to originate from QCD radiation which is on average softer than b-jets priginating from top quark decays. To discriminate between tZq and $t\bar{t}Z$ events the transverse momenta of the leading four jets is used as tZq on average has a lower jet multiplicity with softer jets. In addition, the reconstructed top mass of the leptonically and hadronically decaying top quark is used as tZq events only contain one top quark while $t\bar{t}Z$ events contain two. Furthermore, the transverse momenta of the three selected leptons as well as the information which of these is assigned to the Z boson provides discriminating power between tZq events and $t\bar{t}Z$ events.

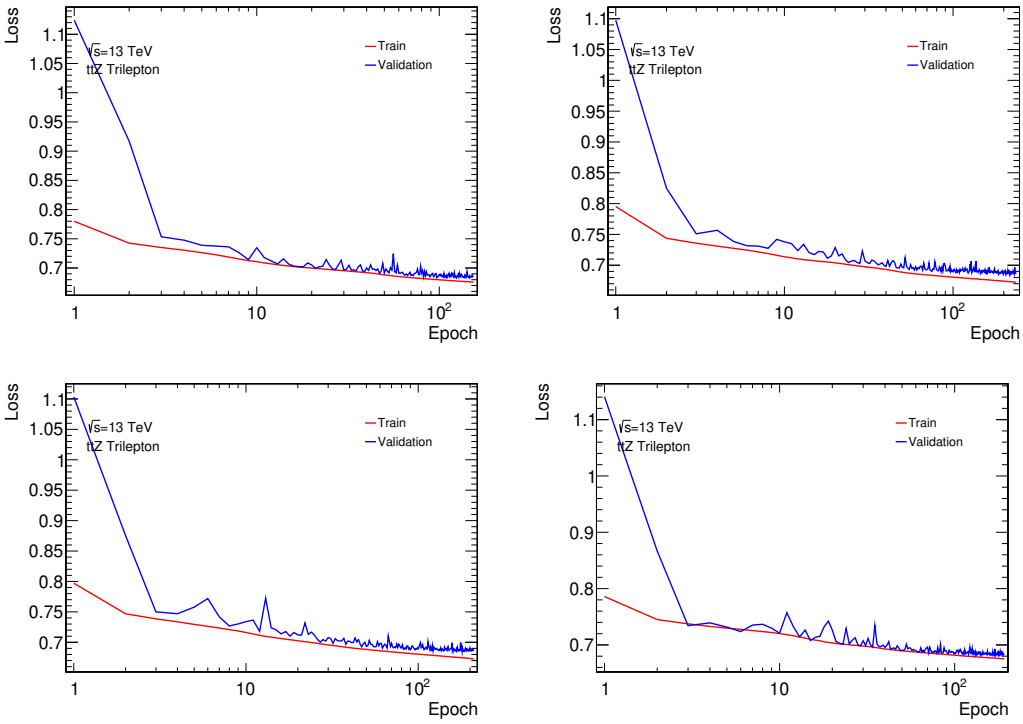

Figure 5.7: Resulting loss curves for both the training (red) and validation set (blue) for all four folds. A convergence towards a stable common loss value is observed. The convergence indicates that no overtraining occurred.

The training convergence is evaluated by comparing the achieved loss values on the training and validation set per fold. The resulting *loss curves* are shown in Figure 5.7. Small statistical fluctuations in the blue validation curves originate from the smaller sizes of these sets. In all four cases, the loss values of the training and validation set converge towards a stable common value, indicating that no overtraining occurred.

Classification of events

For a precise measurement of the $t\bar{t}Z$ inclusive and differential cross-section, events likely to originate from $t\bar{t}Z$ final states must be separated from background events. This procedure of separating signal events from background events is accomplished through the neural network-based classification of events.

For this classification, the preselection highlighted in Chapter 4 and the three-dimensional output of the model described in the previous sections are used to define three probabilities, one each for $t\bar{t}Z$ ($P(t\bar{t}Z)$), tZq ($P(tZq)$), and WZ (P(Diboson)) and assign it to each event.

Since all three outputs of the classifier sum up to unity, all three output distribu-

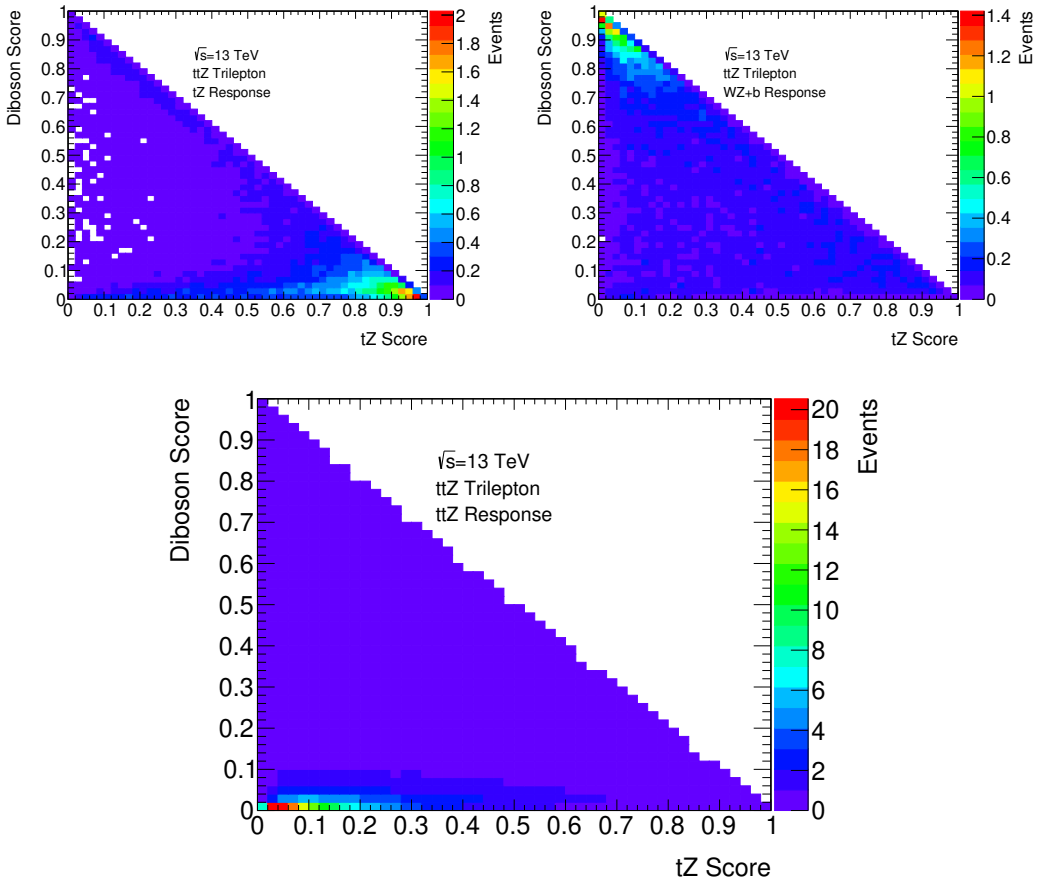

Figure 5.8: Two-dimensional output distributions for tZq (left), WZ+b (right), and $t\bar{t}Z$ (center, large) using the diboson and tZq output values, here referred to by *Diboson Score* and *tZ Score*. The distribution is constrained into a triangular shape through the `Softmax` activation function.

tions can be broken down into a two-dimensional plane, as explained above, where the x and y coordinates correspond to the background probabilities, i.e. $P(tZq)$ and P(Diboson), allowing for a visual representation of the entire output. Figure 5.8 provides a two-dimensional representation of the neural network's response to $t\bar{t}Z$, tZq and WZ+b events, where red colours indicate high event densities while blue colours indicate low densities.

A clear separation is observed, where the $t\bar{t}Z$ events accumulate in the lower left-hand corner of the diagram, the tZq events in the lower right-hand corner, and the WZ+b events in the upper left-hand corner of the distribution. From all pre-selected events in this two-dimensional distribution, three orthogonal candidate regions, specifically $R_{t\bar{t}Z}$, R_{tZq}, and R_{WZ}, are drawn considering possible square cuts on the two background probabilities, $P(tZq)$ and P(Diboson), at a step size of 0.01

Table 5.2: Definition of the trilepton signal and regions and the $CR\text{-}3\ell\text{-}WZ\text{-}LF$ control region. Events for all regions must pass the preselection. They are subsequently grouped into the three signal regions ($SR\text{-}3\ell\text{-}t\bar{t}Z$, $SR\text{-}3\ell\text{-}tZq$, and $SR\text{-}3\ell\text{-}WZ$) based on the prong output of the DNN classifier score. $CR\text{-}3\ell\text{-}WZ\text{-}LF$, mainly enriched in $WZ{+}l$ and $WZ{+}c$, is defined orthogonally to $SR\text{-}3\ell\text{-}WZ$.

Variable	**Event Selection**			
N_ℓ $(\ell = e, \mu)$	$= 3$			
	≥ 1 OSSF lepton pair with $\lvert m_{\ell\ell}^{Z} - m_Z \rvert < 10$ GeV			
	for all OSSF combinations: $m_{\text{OSSF}} > 10$ GeV			
p_{T} (ℓ_1, ℓ_2, ℓ_3)	$> 27,\ 20,\ 15$ GeV			
N_{jets} $(p_{\text{T}} > 25$ GeV)	≥ 3			
$N_{b-\text{jets}}$ (85 %)	≥ 1			
	Event Classification			
	$SR\text{-}3\ell\text{-}t\bar{t}Z$	$SR\text{-}3\ell\text{-}tZq$	$SR\text{-}3\ell\text{-}WZ$	$CR\text{-}3\ell\text{-}WZ\text{-}LF$
DNN-tZ output	< 0.43	≥ 0.43	—	—
DNN-diboson output	< 0.27	< 0.27	≥ 0.27	≥ 0.27
$N_{b-\text{jets}}$ (60 %)	—	—	≥ 1	0

in each axis starting in the origin of the distribution. The resulting target region represents a box-shaped region that expands along the x and y axes. The final cuts on the background probabilities ($P(tZq)$ and P(Diboson) are chosen by maximising the S/B and $S/\sqrt{B}$ ratios in the $t\bar{t}Z$ enriched region where S describes the number of all $t\bar{t}Z$ events given a cut combination and B all backgrounds). The remaining phase-space of the two-dimensional plain is split to form a tZq and WZ enriched region by extending the cut on the diboson output along the x-axis. Consequently, the preselected events are split into one of the three candidate regions covering the whole space of selected events.

Tighter b-tagging criteria are applied in the diboson-enriched region, requiring at least one b-jet tagged at 60 % b-tagging efficiency allowing for a good separation of $WZ{+}b$ events from $WZ{+}c$ and $WZ{+}l$ events. Events not fulfilling these cuts are grouped into a separate region denoted $CR\text{-}3\ell\text{-}WZ\text{-}LF$.

The resulting three regions separating $t\bar{t}Z$ processes from tZq and WZ processes, namely $SR\text{-}3\ell\text{-}t\bar{t}Z$, $SR\text{-}3\ell\text{-}tZq$, and $SR\text{-}3\ell\text{-}WZ$, are drawn from these candidate regions, including the additional b-tagging requirements for R_{WZ}[2]. All regions are summarised in Table 5.2.

The number of selected events split into the four regions is shown in Table 5.3 for both MC simulations and observed data events.

The purest $t\bar{t}Z$ event region is $SR\text{-}3\ell\text{-}t\bar{t}Z$ ($S/B \approx 3.12$), followed by $SR\text{-}3\ell\text{-}tZq$ ($S/B \approx 0.66$) and $SR\text{-}3\ell\text{-}WZ$ ($S/B \approx 0.37$), all treated as signal regions despite containing some tZq and $WZ{+}b$ events. The impact of $CR\text{-}3\ell\text{-}WZ\text{-}LF$ on the

[2]Note that $R_{t\bar{t}Z}$ and R_{tZq} are identical to $SR\text{-}3\ell\text{-}t\bar{t}Z$ and $SR\text{-}3\ell\text{-}tZq$, respectively.

Table 5.3: Observed and expected event yields in the trilepton signal regions and CR-3ℓ-WZ-LF obtained for an integrated luminosity of $140\,\mathrm{fb}^{-1}$. The indicated errors include the Monte Carlo statistical uncertainty and all other systematic uncertainties discussed in Chapter 8.

	SR-3ℓ-$t\bar{t}Z$	SR-3ℓ-WZ	SR-3ℓ-tZq	CR-3ℓ-WZ-LF
$t\bar{t}Z$	428.0±19.0	46.2±2.2	140.0±9.0	36.6±2.7
$t\bar{t}W$	4.3±2.2	2.2±1.1	5.2±2.7	0.5±0.3
$t\bar{t}H$	11.8±1.2	1.4±0.2	6.5±0.6	1.0±0.2
WZ+b	23.0±6.0	52.0±14.0	30.0±8.0	14.0±4.0
WZ+c	9.0±4.0	13.0±5.0	12.0±5.0	120.0±50.0
WZ+l	1.2±0.6	1.7±0.8	1.8±0.8	140.0±60.0
ZZ+b	4.5±2.6	7.0±4.0	7.0±4.0	2.5±1.4
ZZ+c	1.0±0.5	0.9±0.4	1.3±0.6	10.0±4
ZZ+l	0.4±0.2	0.3±0.2	0.5±0.2	28.0±9
tZq	20.0±4.0	12.2±3.0	91.0±22.0	8.6±1.9
tWZ	37.0±8.0	16.0±4.0	22.9±3.0	7.8±1.0
$t\bar{t}t\bar{t}$	1.6±0.8	0.1±0.1	0.3±0.2	0.1±0.1
Other	1.2±0.7	1.3±0.9	0.4±0.2	2.6±1.9
F-e-HF	5.0±1.1	4.3±1.0	13.1±2.8	6.4±2.6
F-e-Other	6.4±1.4	6.0±1.7	12.3±2.7	10.6±3.3
F-μ-HF	6.8±0.8	5.1±1.4	17.6±2.1	8.5±2.3
F-Other	2.5±1.3	2.4±1.3	3.9±2.0	7.0±4.0
Total	565 ±28	172 ±17	366 ±28	400 ±80
Data	569	175	388	397

measurement of inclusive $t\bar{t}Z$ in the 3ℓ channel is negligible. The focus is on SR-3ℓ-$t\bar{t}Z$, SR-3ℓ-tZq, and SR-3ℓ-WZ, while CR-3ℓ-WZ-LF is briefly discussed for the classifier's ability to remove WZ+l and WZ+c. In SR-3ℓ-$t\bar{t}Z$, WZ+c and WZ+l contribute $1.6,\%$ and $0.2,\%$ respectively to the total event yields.

Control histograms displaying kinematic distributions in the three signal regions are shown in Figure 5.9. They show the p_{T} and η of the leading jet, i.e. the jet with the highest p_{T} and the jet multiplicity. Good agreement between the data and the MC simulation is observed within the uncertainties.

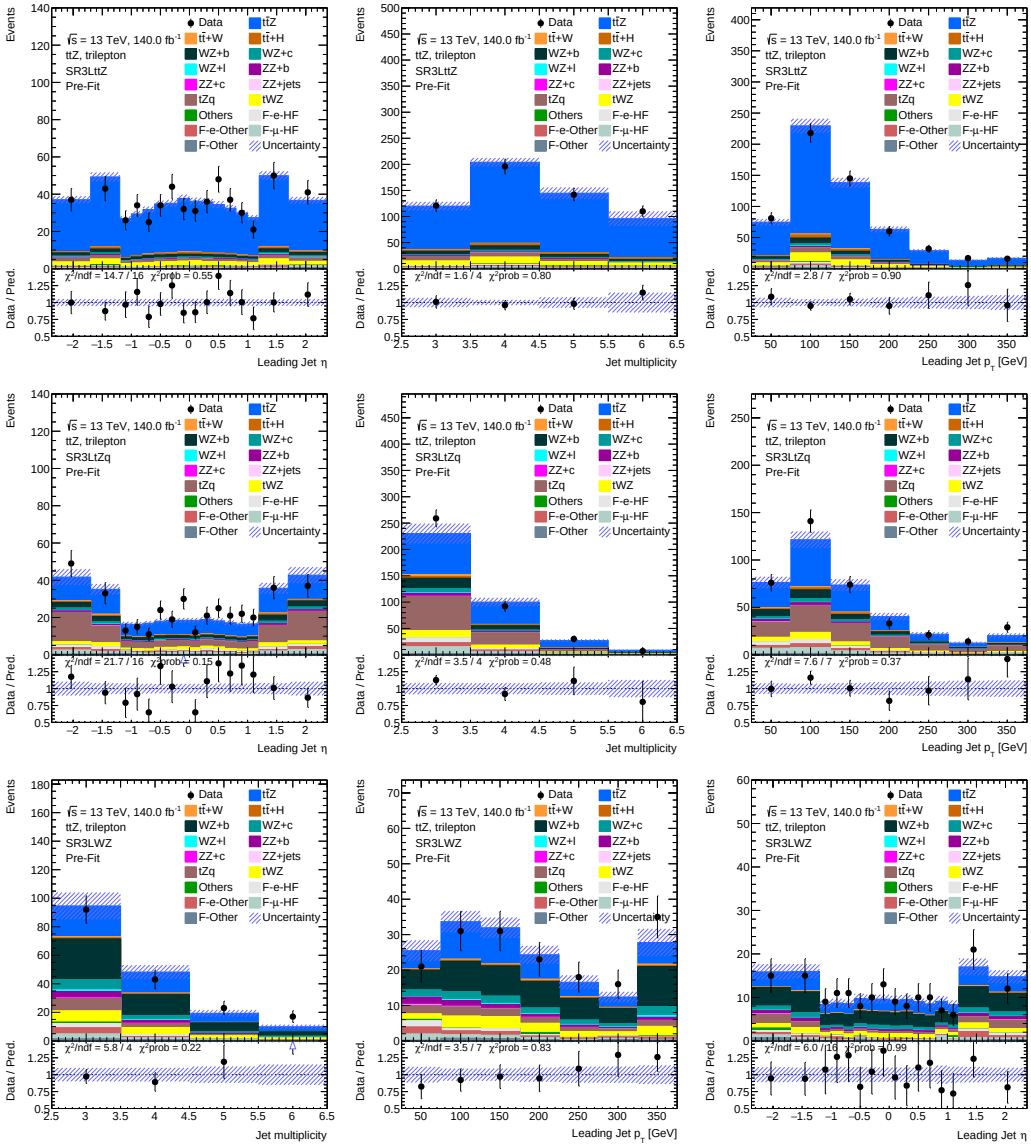

Figure 5.9: Data/MC comparison for basic kinematic variables in the SR-3ℓ-$t\bar{t}Z$ and SR-3ℓ-tZq signal regions with events passing the event selection criteria. The blue uncertainty band includes statistical and systematic uncertainties. Events outside the histogram range are merged into the corresponding first or last bin.

Performance evaluation of the classifier

To evaluate the overall performance of the classifier, ROC curves are calculated by breaking the multi-class classification down into three binary classification scenarios, namely $t\bar{t}Z$ versus rest, tZq versus rest and diboson versus rest.

A ROC curve is then generated by sketching the true positive rate (TPR) against the false positive rate (FPR) at different classification thresholds as highlighted above. The AUC is calculated using the trapezoidal rule. Additionally, to validate the model's generalisation performance, the model's output using training data is compared to the output using unseen testing data for all three output nodes. In all cases the training and testing sets are compared using 5-fold cross validation as follows:

Model 1 : train on folds 2-5, test on fold 1,
Model 2 : train on folds 1, 3-5, test on fold 2,
Model 3 : train on folds 1-2, 4-5, test on fold 3,
Model 4 : train on folds 1-3, 5, test on fold 4,
Model 5 : train on folds 1-4, test on fold 5.

The samples are further split into signal-like samples (i.e. $t\bar{t}Z$ for the $t\bar{t}Z$ output node, tZq for the tZq output node and diboson for the diboson output node) and the respective background samples. The distributions are superimposed and normalised. Afterwards, the Kolmogorov-Smirnov probability is calculated separately for the signal-like and background processes, following the description above. The resulting ROC curves and superimposed distributions are shown in Figure 5.10 for the $t\bar{t}Z$, tZq, and diboson output nodes for the first fold. The distributions for the remaining folds are shown in Figure D.1 in the appendix. No significant deviation between training and testing distribution is observed, indicating good generalisation performance of the models. The mean AUC values, $\overline{\text{AUC}}$, for the individual are

$$\overline{\text{AUC}}^{\text{Train}}_{t\bar{t}Z} = 0.770 \pm 0.003, \quad \overline{\text{AUC}}^{\text{Train}}_{tZq} = 0.819 \pm 0.001, \quad \overline{\text{AUC}}^{\text{Train}}_{\text{Diboson}} = 0.799 \pm 0.004,$$
$$\overline{\text{AUC}}^{\text{Test}}_{t\bar{t}Z} = 0.767 \pm 0.009, \quad \overline{\text{AUC}}^{\text{Test}}_{tZq} = 0.815 \pm 0.006, \quad \overline{\text{AUC}}^{\text{Test}}_{\text{Diboson}} = 0.794 \pm 0.009,$$

where the uncertainties represent the standard deviation between the four folds. Good agreeement between the individual folds and the training and testing folds in particular is observed which is reflected by a small standard deviation which also covers the difference between the individual training and testing folds.

The calculated p-values support the null hypothesis of a common underlying distribution for the testing and training output distributions.

The impact of each input variable is evaluated following the permutation importance approach discussed above. All other variables from the full set remain unchanged in this step. The AUC corresponding to the shuffled set is compared to AUC of the nominal (unshuffled) set, $\text{AUC}_{\text{nom.}}$. Its relative change,

$$\Delta\text{AUC} = \frac{\text{AUC}_{\text{nom.}} - \text{AUC}}{\text{AUC}_{\text{nom.}}}, \tag{5.16}$$

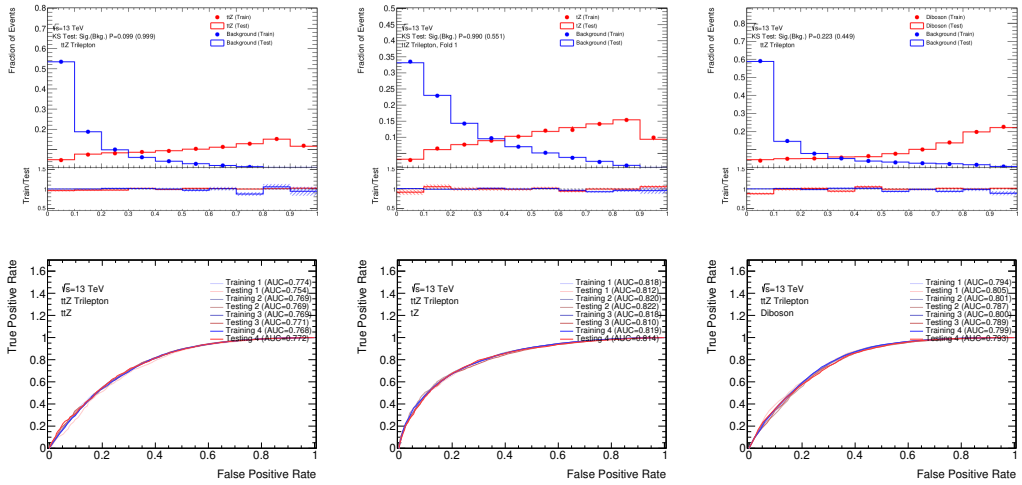

Figure 5.10: Kolmogorov-Smirnov test for the $t\bar{t}Z$, tZq, and diboson output nodes (left) for the first fold and corresponding ROC curves (right). No significant deviation between training and testing distribution is observed, indicating good generalisation performance of the model. The shaded error bands represent the statistical uncertainties.

is considered the metric for the variable's importance. It should be noted that this performance metric is sensitive to the individual performance of the input variables. However, it cannot differentiate whether a single variable is important on its own, or whether it is the correlation of that variable with another that is important. Therefore, these two cases are not further differentiated in the following and input variables are considered important in both cases. The permutation importances, evaluated for all three output nodes, are shown in Figure 5.11.

The most important variables impacting the $t\bar{t}Z$ output node are the transverse momentum of the leading jet, $\text{jet}_1\, p_\text{T}$, the sum of the momenta of all objects in the event except E_T^miss, HT, and the reconstructed mass of the hadronically decaying top quark, m_had^t. The importance of these variables originates from the separation with respect to the tZq process, which on average has less jets with smaller transverse momentum. This is also reflected by the fourth most important variable, the transverse momentum of the fourth jet in an event, which is more likely to exist for a $t\bar{t}Z$ event than a tZq event.

The most important input variables for the diboson classifier are the leading and sub-leading b-tagging working points of the event and the transverse momentum of the leading jet. The high ranking of these variables mainly originates from WZ+c and WZ+l events with no b-jets. For the tZq classifiers, again HT and the reconstructed mass of the hadronically decaying top quark are highly ranked. Additionally, the highest b-tagging working point is ranked high. The significance of these variables can be again attributed to the differentiation from $t\bar{t}Z$ events, which have more jets with larger transverse momentum on average. Additionally, leptons

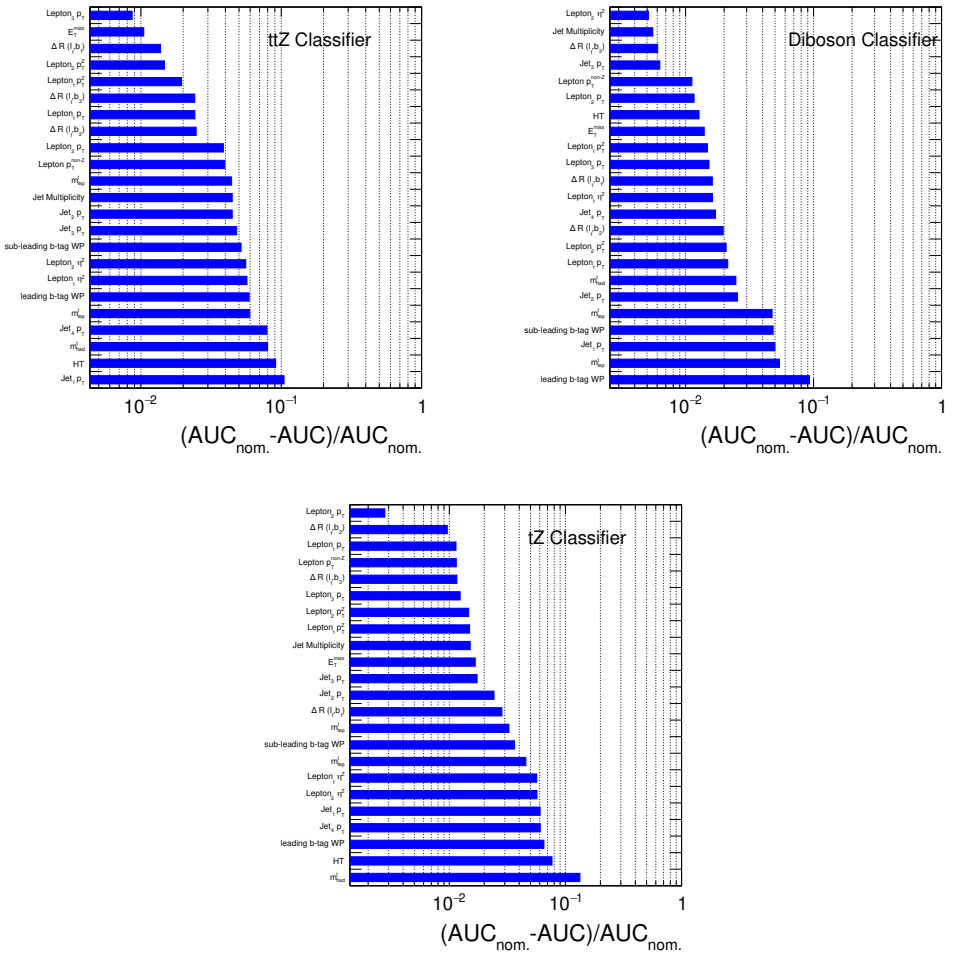

Figure 5.11: Ranked permutation importance for the $t\bar{t}Z$ (top left), the diboson (top left), and the tZq classifier outputs.

originating from the Z boson in a tZq event tend to have higher $|\eta|$ values than leptons originating from a $t\bar{t}Z$-initiated Z boson, leading to the relatively high ranking of $\eta^{\mathrm{Z}}_{\mathrm{T},1}$ and $\eta^{\mathrm{Z}}_{\mathrm{T},2}$.

CHAPTER 6

Non-prompt lepton background estimation

As highlighted in Section 2.3, fake leptons are misidentified lepton-like detector signatures originating from different sources: from heavy-flavour hadron decays, photon conversions, or light jets creating lepton-like signatures in the detector. Up to this point, events with fake leptons were taken directly from the MC prediction.

The rates at which fake leptons are generated in proton-proton collisions at the LHC is challenging to model accurately using MC simulation as the modelling of these event signatures heavily depends on the physics and detector simulation details such as the modelling and response of the detector. Because of this, for measuring the inclusive cross-section of the $t\bar{t}Z$ production process, the fake lepton background is estimated using a semi-data-driven technique, effectively replacing the MC prediction for these events.

Three fake-enriched control regions are defined for estimating events with non-prompt leptons. These regions are designed to be kinematically close $t\bar{t}Z$ final states with three prompt leptons. All events are required to pass the preselection criteria presented in Chapter 4. Three leptons are required with a p_{T} of 27, 20, and 15 GeV, respectively. Trailing leptons are allowed to fail *tight* identification and isolation requirements and pass looser ones with respect to the tight requirements imposed on leptons in the three signal regions. In the following, this lepton is referred to as *loose non-tight*. The other leptons are referred to as *tight*. The number of selected fake lepton events in these regions is significantly increased by allowing the presence of looser leptons. Additionally, at least three jets are required, of which one is tagged with the 85 % efficiency b-tagging working point.

Events with $t\bar{t}$-like final states, without an OSSF pair, where the loose non-tight lepton is part of the same-sign lepton pair, are used to obtain regions targeting fake leptons from heavy-flavour sources. Two regions are defined based on the lepton flavour of the loose non-tight lepton: $CR\text{-}t\bar{t}\text{-}e$ and $CR\text{-}t\bar{t}\text{-}\mu$. In these regions, the loose lepton is an electron ($CR\text{-}t\bar{t}\text{-}e$) or a muon ($CR\text{-}t\bar{t}\text{-}\mu$). To further target $t\bar{t}$-like final states, events with OSSF pairs are vetoed.

Table 6.1: Definition of the fake-enriched control regions. The same preselection as presented in Chapter 4 is applied.

Variable	**Selection**		
N_ℓ $(\ell = e, \mu)$	$= 3$ (of which $= 1$ loose non-tight)		
p_{T} (ℓ_1, ℓ_2, ℓ_3)	$> 27,\ 20,\ 15$ GeV		
Sum of lepton charges	± 1		
N_{jets} $(p_{\mathrm{T}} > 25$ GeV)	≥ 3		
$N_{b-\mathrm{jets}}$	$\geq$ 1@85%		
	Event classification (cut-based)		
	CR-$t\bar{t}$-e	*CR-$t\bar{t}$-μ*	*CR-Z-e*
Lepton flavours	no OSSF pair (loose lepton is an electron)	no OSSF pair (loose lepton is a muon)	OSSF pair (exactly 3 electrons)
$E_{\mathrm{T}}^{\mathrm{miss}}$	—	—	< 80 GeV

Table 6.2: Event yields in the three fake-enriched regions. All prompt background processes apart from the $t\bar{t}Z$ signal process are grouped into *FR Other*. The uncertainty includes statistical and systematic uncertainties.

Process	*CR-$t\bar{t}$-e*	*CR-$t\bar{t}$-μ*	*CR-Z-e*
$t\bar{t}Z$	3 ± 1	1 ± 1	33 ± 2
FR Other	10 ± 2	5 ± 1	50 ± 8
F-e-HF	830 ± 70	$< 10^{-3}$	600 ± 60
F-e-Other	147 ± 9	0 ± 1	214 ± 25
F-μ-HF	0 ± 1	720 ± 60	$< 10^{-3}$
F-Other	2 ± 1	31 ± 16	1 ± 1
Total	990 ± 80	750 ± 60	900 ± 90
Data	949	768	892

Furthermore, a Z-like control region (*CR-Z-e*) requires three electrons, one OSSF pair, and $E_{\mathrm{T}}^{\mathrm{miss}} < 80\,\mathrm{GeV}$. The event selection for the fake lepton control regions is summarised in Table 6.1. The resulting yields in the three regions, based on the preselection criteria discussed in Chapter 4 and the selection presented in Table 6.1 are given in Table 6.2.

Three fake factors ($\mathcal{N}_{e,\mathrm{HF}}$, $\mathcal{N}_{e,\mathrm{Other}}$, and $\mathcal{N}_{\mu,\mathrm{HF}}$) are extracted as free-floating parameters in a profile-likelihood fit of the event yields in the *CR-$t\bar{t}$-e* and *CR-$t\bar{t}$-μ* region and the reconstructed transverse mass of the W boson, $m_{\mathrm{T}}(\mathrm{W})$, in the *CR-Z-e* control region. The choice of $m_{\mathrm{T}}(\mathrm{W})$ originates from its separating power between $t\bar{t}$-based fake processes and other processes, thereby providing a better handle on $\mathcal{N}_{e,\mathrm{HF}}$ and $\mathcal{N}_{e,\mathrm{Other}}$. The technical components of the fit will be explained in detail in Section 7.2 as the fit at this point is only meant to validate that the three ex-

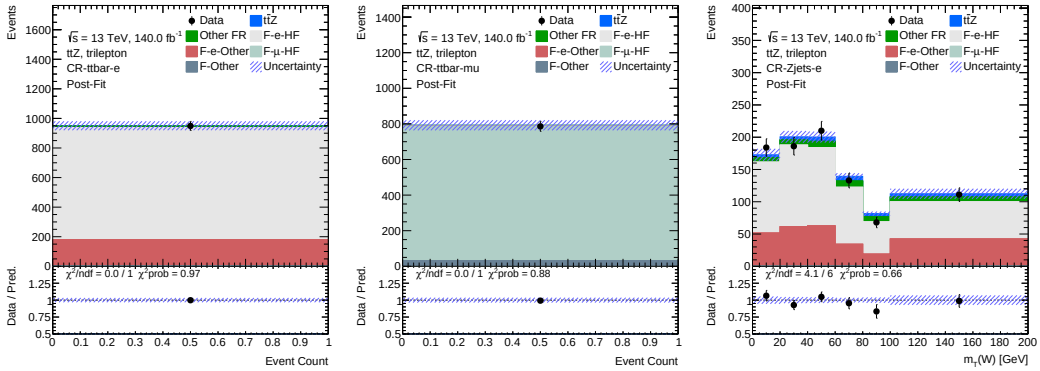

Figure 6.1: Post-fit distributions of the three fake regions: $CR\text{-}t\bar{t}\text{-}e$ (left), $CR\text{-}t\bar{t}\text{-}\mu$ (center), and $CR\text{-}Z\text{-}e$ (right). The different fake contributions, as well as other SM backgrounds, are shown. The uncertainty is shown in blue and includes statistical and systematic uncertainties.

tracted fake factors show good agreement with the SM prediction. While they are not expected to precisely follow the SM prediction due to the modelling challenges highlighted above, they should not differ significantly from it either. In the final fit procedure, these three regions are included as control regions in the fit.

The post-fit distributions of fitting the three regions independently are shown in Figure 6.1.

Pre-fit distributions and a ranking of relevant systematic uncertainties of the fit are shown in Figures E.3 to E.5 and Figure E.2, in the appendix. The fit yields the following fake factors:

$$\mathcal{N}_{e,\mathrm{HF}} = 0.873^{+0.098}_{-0.091}, \tag{6.1}$$

$$\mathcal{N}_{e,\mathrm{Other}} = 1.171^{+0.406}_{-0.361}, \tag{6.2}$$

$$\mathcal{N}_{\mu,\mathrm{HF}} = 1.000^{+0.088}_{-0.081}. \tag{6.3}$$

All three extracted parameters agree with the SM within less than 1.3σ. To evaluate the agreement between data and simulation, the post-fit distributions of the leading, sub-leading and trailing lepton p_{T} and the respective η distributions are shown in Figures 6.2 and 6.3. Based on the amount of observed non-closure visible in the distributions of Figures 6.2 and 6.3, an additional normalisation uncertainties of 20 % on fake electrons and 10 % on fake muons is assigned.

The extracted fake factors are further validated by applying them on all selected events following the description in Chapter 4, with the difference that one lepton is required to be loose[1], denoted $VR\text{-}3\ell\text{-}Z1b3j$. The distributions of the p_{T} and η of the three leptons in $VR\text{-}3\ell\text{-}Z1b3j$ are shown in Figure 6.4. A good agreement between data and MC is observed.

[1]It should be noted here that this region is not entirely orthogonal to the regions used to extract the three norm factors.

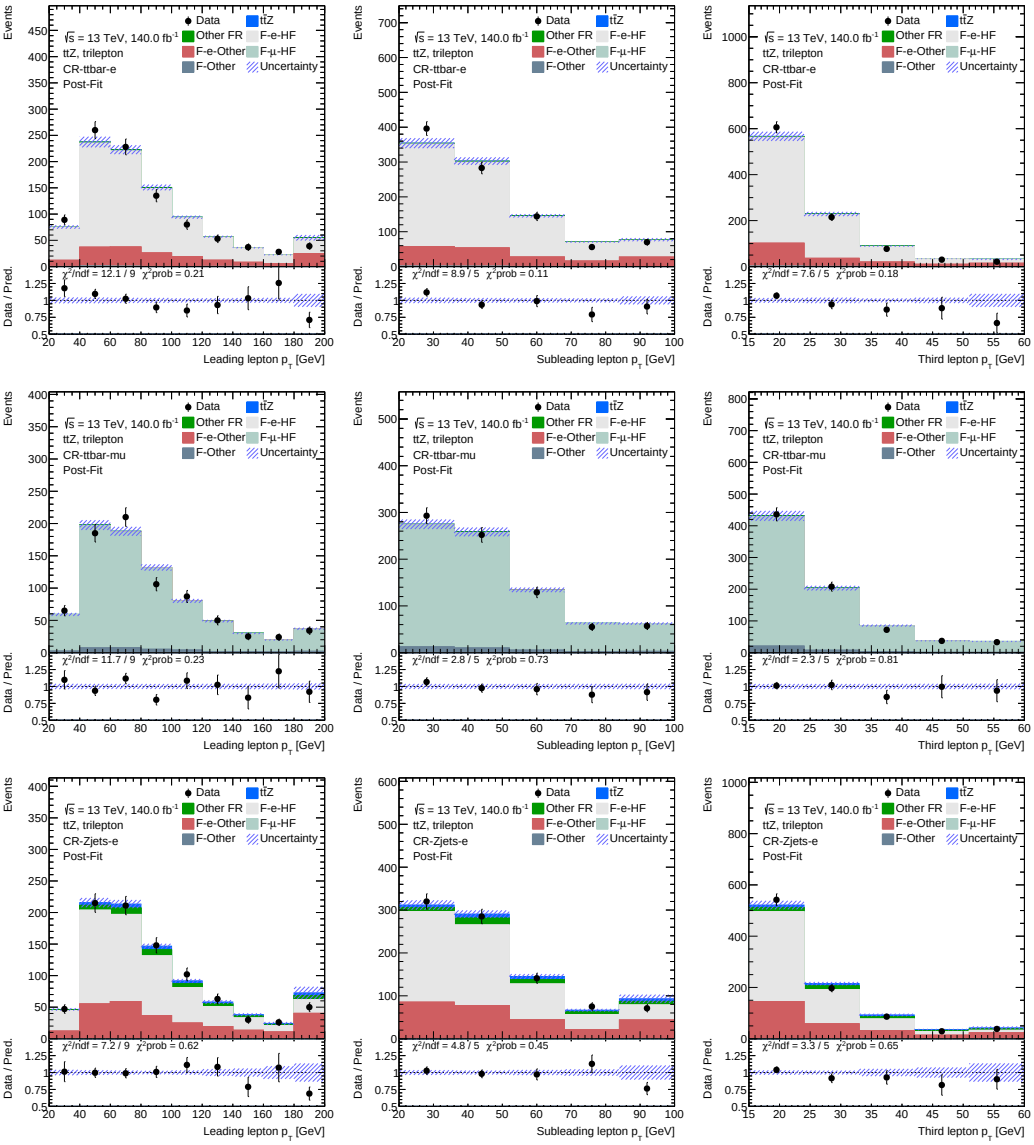

Figure 6.2: Post-fit distributions of the leading, sub-leading and trailing lepton p_{T} in the three fake regions: *CR-$t\bar{t}$-e* (top), *CR-$t\bar{t}$-μ* (middle), and *CR-Z-e* (bottom). The different fake contributions, as well as other SM backgrounds, are shown. All prompt background processes apart from the $t\bar{t}Z$ signal process are grouped into *FR Other*. Data are shown as black dots. The uncertainty is shown in blue and includes statistical and systematic uncertainties.

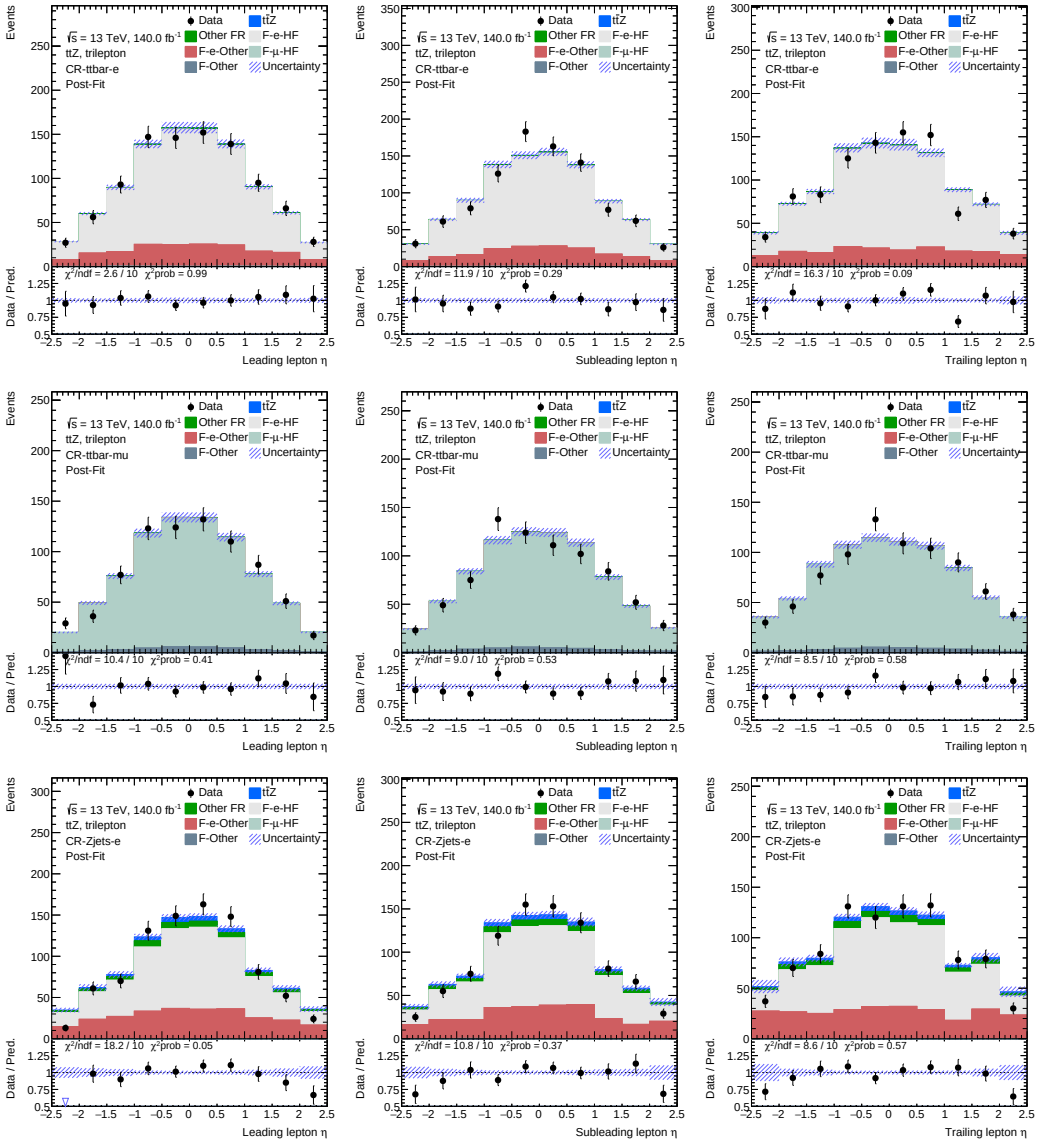

Figure 6.3: Post-fit distributions of the leading, sub-leading and trailing lepton η in the three fake regions: *CR-$t\bar{t}$-e* (top), *CR-$t\bar{t}$-μ* (middle), and *CR-Z-e* (bottom). The different fake contributions, as well as other SM backgrounds, are shown. All prompt background processes apart from the $t\bar{t}Z$ signal process are grouped into *FR Other*. Data are shown as black dots. The uncertainty is shown in blue and includes statistical and systematic uncertainties.

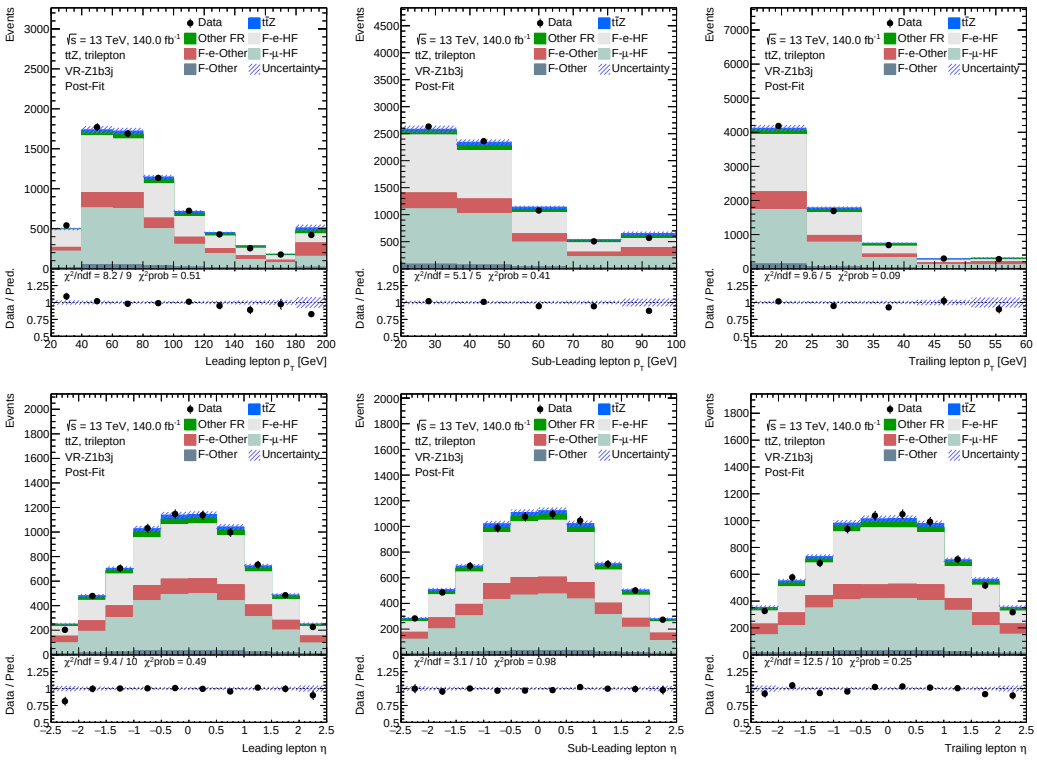

Figure 6.4: Post-fit distributions of the leading, sub-leading and trailing lepton p_{T} and η in VR-3ℓ-Z1b3j. The different fake contributions, as well as other SM backgrounds, are shown. All prompt background processes apart from the $t\bar{t}Z$ signal process are grouped into *FR Other*. Data are shown as black dots. The uncertainty is shown in blue and includes statistical and systematic uncertainties.

CHAPTER 7

Analysis strategy

The dataset used in this thesis is described in Chapter 4. The event signatures targeted here are $t\bar{t}Z$ final states where the $t\bar{t}$ pair and Z boson decay into final states with three leptons as follows:

$$
\begin{aligned}
t\bar{t} &\to W^+bW^-\bar{b} \to q\bar{q}'b + \bar{\nu}_\ell\ell^-\bar{b} \\
t\bar{t} &\to W^+bW^-\bar{b} \to \nu_\ell\ell^+b + q\bar{q}'\bar{b} \\
Z &\to \ell^+\ell^-
\end{aligned}
$$

Only decays into electrons or muons are considered for all leptonic decays. Additionally, events with four prompt leptons, such as

$$
\begin{aligned}
t\bar{t} &\to W^+bW^-\bar{b} \to \nu_\ell\ell^+\bar{\nu}_\ell\ell^- \\
Z &\to \ell^+\ell^-
\end{aligned}
$$

can be selected by the trileptonic event selection presented in Chapter 4 if one of the leptons is not reconstructed or lost in the detector. Decays with

$$
Z \to \tau^+\tau^- \to e^+e^-/\mu^+\mu^-
$$

are heavily suppressed in the event selection due to the $|m_{\ell\ell} - m_Z| < 10\,\text{GeV}$ requirement. Their impact on the event yields is negligible.

Figure 7.1 shows the $t\bar{t}$ and Z boson branching ratios. The phase spaces probed by the 3ℓ-channel, discussed in this thesis, are highlighted. This channel covers 30.2 % of the SM $t\bar{t}$ decays. The complete analysis, comprised of the 2ℓ, 3ℓ, and 4ℓ channel, further addresses dileptonic and fully hadronic $t\bar{t}$ decays comprising $\sim 85.7\,\%$ of the SM $t\bar{t}$ branching ratio. Similarly $\sim 6.7\,\%$ of the SM Z boson decays are covered, thereby probing a significant portion of the $t\bar{t}Z$ phase space[1].

[1] The phase space probed is naturally smaller than the values quoted here due to selection cuts and limitations in acceptance. The numbers, however, provide an overview of the reach of the full analysis.

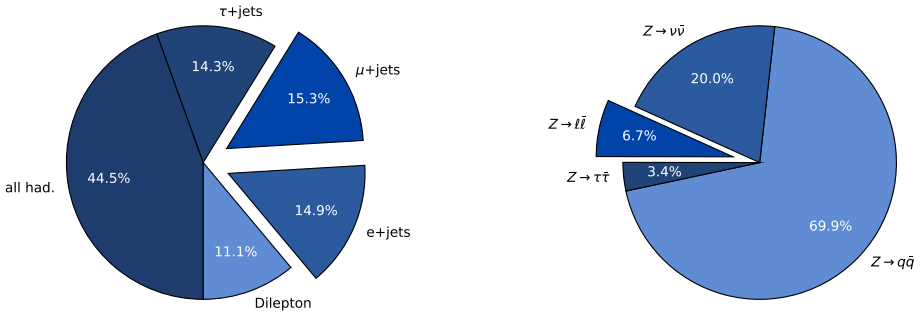

Figure 7.1: Graphical representation of the $t\bar{t}$ and Z boson branching ratios [42].

In the following, the focus will lie on the 3ℓ channel. Preselected 3ℓ-events are classified using a neural network to define signal regions with high purity and differing backgrounds as described in Chapter 4. To reduce the impact of WZ+l, WZ+c and WZ+b events on the precision of the measurement and to specifically reduce extrapolation uncertainties on the WZ+b contribution, which was estimated to be approximately 50 % in the previous ATLAS measurement of the $t\bar{t}Z$ production process [147], signal regions are designed with negligible contributions of WZ+l and WZ+c. A dedicated region is constructed from which the WZ+b normalisation and its uncertainty are directly estimated from the fit. To estimate the contribution of events with fake leptons, fake-enriched control regions are defined, and data-driven fake factors for different fake lepton sources are extracted as highlighted in Chapter 6.

As summarised in Chapter 3, this measurement uses a NLO simulation of the $t\bar{t}Z$ signal process using the MadGraph5_aMC@NLO 2.8.1 generator as well as the NNPDF3.0NLO PDF set. All events passing the selection cuts and originating from these signal samples are considered signal events except those with at least one fake lepton in the final state.

7.1 Parton and particle level fiducial phase-spaces

A fiducial phase-space volume must be defined at the parton and particle level to determine the cross-section from a measurement based on reconstructed objects. These particle level and parton level fiducial phase-space definitions are summarised in Table 7.1 and explained in detail in the following paragraphs.

At the particle level, objects with a lifetime greater than 30 ps in the MC simulation are treated as stable particles. No simulation of the interaction of these objects with the detector volume or other pp interaction is performed. At this level, the fiducial volume in the trileptonic channel is defined using objects defined in Section 2.3, featuring the hadronisation of quarks. Events must have exactly three leptons with p_{T} of at least 27, 20, and 15 GeV, originating from a Z boson or top quark decays.

Table 7.1: Summary of particle and parton level fiducial volume definitions.

	Variable	Selection
Particle level	Lepton multiplicity	$= 3$
	Jet multiplicity	≥ 3 (anti-k_t, $R = 0.4$)
	b-jet multiplicity	≥ 1 (ghost matched)
	Lepton p_{T}	27, 20, 15 GeV
	Jet p_{T}	25, 25, 25 GeV
	OSSF lepton pair	$= 1$
	Z candidate requirements	$\lvert m_{\ell\ell} - m_Z \rvert < 10\,\mathrm{GeV}$
Parton level	Z boson decay	$Z \to e^+e^-$, $Z \to \mu^+\mu^-$
	Z-window mass requirement	$\lvert m_{\ell\ell} - m_Z \rvert \leq 15\,\mathrm{GeV}$

Leptons are combined with photons within a cone of $\Delta R = 0.1$ about their direction, excluding photons from hadron decays. Leptons originating from a hadron or quark (u, d, s, c, b) are discarded. Additionally, one OSSF lepton pair must fulfil the Z-candidate requirements. Furthermore, events must have at least three jets with a minimum p_{T} of 25 GeV. These jets are reconstructed with the anti-k_t jet clustering algorithm with a radius parameter of $R = 0.4$ based on all stable particles. Contributions from electrons, muons, and photons used in the definition of the leptons as mentioned above and neutrinos originating from the Z boson or the top quark decay are excluded in the clustering. Energies of b-hadrons with $p_{\mathrm{T}} > 5\,\mathrm{GeV}$ in the simulated MC decay chain are set to 0. They are clustered in the stable-particle jets. Jets containing one or more b-hadrons fulfilling this criterion are considered to originate from a b quark. This procedure is referred to as *ghost matching*. Missing transverse energy is defined through the vector sum of the transverse momenta of all neutrinos found in the MC simulation history of the event. Neutrinos originating from hadron decays are excluded.

At parton-level objects are obtained from the MC generation history of the $t\bar{t}Z$ system, referred to as the *parton-level history*. Here, the fiducial volume is defined by considering a semileptonic decay of the $t\bar{t}$ system into electrons and muons and the corresponding neutrinos. The top and anti-top quark and the Z boson are taken as the last instances in the parton-level history, just before their respective $t \to Wb$ and $Z \to \ell\ell$ decay occurs. The Z boson decays leptonically into a pair of electrons ($Z \to e^+e^-$) or a pair of muons ($Z \to \mu^+\mu^-$). The first instances of the leptons originating from the Z and W bosons, immediately after the $Z \to \ell\ell$ and $W \to \ell\nu$ decay, are considered as the leptons, respectively.

Events with τ leptons originating from a leptonically decaying Z boson or the decay of a W in the top quark decay chain are removed. This choice is independent of the decay products of the τ leptons themselves. The decay $Z \to \tau^+\tau^-$ is suppressed by applying the Z-window mass requirement so that the majority of remaining τ

leptons originate from leptonically decaying top quarks. The invariant mass of the lepton pairs originating from the Z boson must be within $\pm 15\,\text{GeV}$ around the pole mass of the Z boson [42].

7.2 Fitting procedure

The following sections discuss the profile likelihood fit alongside the application of systematics. As previously discussed, the analysis strategy is based on separating signal and background using a DNN-based multi-class classifier. The signal strength, $\mu_{t\bar{t}Z}$, and the normalisation of the WZ+b SM background are extracted in the three signal regions defined by the classifier's output. In addition, the normalisation of the F-e-HF, F-e-Other, and F-μ-HF SM backgrounds are mainly extracted from dedicated fake-enriched control regions[2]. Control and signal regions are represented by multiple bins or a distribution consisting of a single bin, namely the event count.

Determining the cross-section value from these signal and control regions is an involved process, as the number of parameters in the fitting procedure is significant.

For the estimation of the cross-section value, an estimator $\hat{\theta}$ is required. This estimator should ideally be *unbiased*, i.e. the estimator's expectation value equals the estimated parameter's actual value. It should be *consistent*, i.e. it should approach the parameter's actual value as the sample size increases, and it should be *efficient*, i.e. having the smallest variance among all unbiased estimators for a given parameter.

The fit strategy pursued here to extract the $t\bar{t}Z$ inclusive cross-section is based on simultaneously determining the fitting model parameters, $\vec{\theta}$, through a profile-likelihood fit using the maximum-likelihood estimator. The technical implementation is done through the HISTFACTORY [249] software tool for creating statistical models with the ROOFIT [250] and ROOSTATS [251] libraries within the ROOT software framework [252].

The distributions in the individual regions mentioned above are used as inputs to the profile-likelihood fit to extract the signal strength of the $t\bar{t}Z$ process. The likelihood that is maximised is defined as:

$$L\left(\vec{n}|\mu,\vec{\theta},\vec{k}\right) = \prod_{r\in\text{regions}}\prod_{i\in\text{bins}} \text{Pois}\left(n_{i,r}|\mu S_{i,r}(\vec{\theta}) + B_{i,r}(\vec{\theta},\vec{k})\right) \tag{7.1}$$

$$\times \prod_{j\in\text{NP}} \text{Gaus}(\theta_j^0|\theta_j,\Delta\theta_j), \tag{7.2}$$

where $\vec{n}$ and $n_{i,r}$ represents the data vector and the data yields in bin i in region r. Other parameters, the *nuisance parameters* (NPs), affecting the number of signal (background) events in bin i in the region r, $S_{i,r}$ ($B_{i,r}$), are denoted by $\vec{\theta}$. The normalisation parameters affecting the number of background events in the fit are denoted by $\vec{k}$. The parameter of interest (POI), i.e. the signal strength is described

[2]These three parameters are technically treated as free parameters in the fit of the signal regions. However, their values are mainly determined by the fake-enriched control regions.

by μ. It is defined as the ratio of measured signal events to the SM prediction. The terms *Pois* and *Gaus* represent the Poisson and Gaussian distributions, respectively. The Gaussian term in the likelihood represents a bell curve centred at $\theta_j^0 = 0$ with a standard deviation of $\Delta\theta_j = 1$ that acts as a *penalty term*. Through the term, significant deviations of θ_j from θ_j^0 are disfavoured in the fit, thereby imposing implicit constraints on the NPs. Free-floating parameters, denoted as *normalisation factors*, remain unconstrained.

The concept of nuisance parameters introduced above within the frequentist approach is non-trivial as any particle physics experiment outcome can be treated as the estimation of a *random variable*, i.e. the fact that the measured data is a repeatable random sample, the random variable, with a specific probability. Variations of this random variable are understood as the variable's variability, not its underlying probability distribution, which is assumed to be fixed by nature.

Systematic uncertainties in the form of nuisance parameters can be described as a priori unknown variations in a measurement that do not vary when comparing one subset of data to another taken using an identical setup. As these fluctuations are often not random, they are not simply fluctuations of the measurement. An example of such a systematic uncertainty would be a systematic bias introduced by an imperfect measurement apparatus.

The description of systematic uncertainties in the frequentist approach is solved by the fact that systematic uncertainties have to be estimated rigorously, and at least partially, the idea of a reproducible experimental setup is given up. The fit setup and its implementation are described in detail in the following paragraphs before the individual systematic uncertainties relevant to the measurement of the inclusive $t\bar{t}Z$ cross-section are introduced in Chapter 8.

In general, two fit setups will be discussed throughout this thesis. The first setup uses data taken by the ATLAS detector to perform the fit. It extracts the POI and the corresponding $t\bar{t}Z$ inclusive and differential cross-sections.

The second setup uses a dataset where the maximum likelihood best-fit value of the set of free-floating parameters and the NPs equals their initial values, i.e. $\hat{\mu} = \mu_0$ and $\hat{\theta} = \theta_0$. It is used to evaluate the impact of systematic uncertainties on the fit without unblinding the POI.

In the following, this dataset is referred to as *Asimov pseudo-dataset*, or *Asimov data* and the fit using the dataset is referred to as *Asimov fit*.

In the case of the Asimov fit, all NPs are expected to fulfil $(\hat{\theta} - \theta_0) = 0$, where $\hat{\theta}$ is the maximum likelihood estimator of a given NP[3] with a nominal pre-fit value, θ_0. Constraining the central value of a NP to zero only holds for an Asimov fit. When fitted to real data, $(\hat{\theta} - \theta_0)$ can take non-zero values. These cases are colloquially referred to as *pulls*, as the NP is *pulled away* from its central value, potentially compensating for a mismatch between data and MC in the fit.

As the fit can constrain nuisance parameters, the post-fit impact can be smaller than the pre-fit impact. Normalised by the pre-fit uncertainty ($\Delta\Theta$), all NPs are

[3]In the following this will be referred to as the *post-fit value* of the NP.

then expected to fulfil $|(\hat{\theta} - \theta_0)| \leq 1.0$ in the Asimov fit. In the Asimov fit, the NPs are initially uncorrelated, with post-fit correlations arising from the fit itself through improved knowledge of the parameters.

Systematic uncertainties can affect different samples and regions in the fit. Uncertainties with an identical effect in all regions, such as a cross-section uncertainty for a given process, are referred to as *normalisation uncertainties*. They are either treated as free parameters in the fit, such as the aforementioned free parameters, namely $\mathcal{N}_{WZb}$, $\mathcal{N}_{\text{F-e-HF}}$, $\mathcal{N}_{\text{F-e-Other}}$, $\mathcal{N}_{\text{F-m-HF}}$ or are constrained through the Gaussian term in the likelihood. Most systematic uncertainties are assessed region by region and sample by sample, and the impact may vary between regions and samples. These effects can be generally grouped into effects on the normalisation or shape of the nominal distribution or a combination of both. Suppose a NP affects both the shape and the normalisation. In that case, it is split into a pure shape and normalisation component, where the shape component uses a bin-by-bin linear interpolation strategy; the normalisation component uses an exponential interpolation strategy to prevent the normalisation from taking nonphysical negative values. Even though these components can be split, they share the same Gaussian penalty term.

Several procedures are applied to ensure a converging fit behaviour while at the same time preserving the meaningful behaviour of systematic uncertainties. These procedures, namely *smoothing*, *symmetrisation*, and *pruning*, are described in the following paragraphs.

Smoothing of uncertainties

Like nominal distributions, distributions representing systematic uncertainties suffer from statistical fluctuations. These statistical fluctuations can introduce constraints on individual NPs in the fit as the distribution is described by a single NP, not individual bins. To avoid constraints originating from statistical fluctuations, distributions are averaged across bins. This procedure is referred to as *smoothing*. The smoothing algorithm 353QH TWICE [253] is applied to the distribution to smoothen the transition between the individual bins. First the algorithm considers different medians, namely *medians of three* ($z_i^{(3)}$) and *medians of five* ($z_i^{(5)}$) which are calculated using adjacent values $(y_{i-2}, ..., y_{i+2})$:

$$z_i^{(3)} = \text{median}(y_{i-1}, y_i, y_{i+1}),$$
$$z_i^{(5)} = \text{median}(y_{i-2}, y_i, y_{i+2}).$$

For the smoothing, the algorithm calculates running medians of three, followed by running medians of five and again three, referred to as *353* smoothing. Due to clipping and flattening of *peaks* and *valleys*, the procedure can result in valleys three values long, which is remedied by quadratic interpolation (Q step). Monotonic

discontinuity problems are resolved by Hanning or running means (H step):

$$z_i = \frac{1}{4} z_{i-1} + \frac{1}{2} z_i + \frac{1}{4} z_{i+1}.$$

To prevent the over-smoothing of real peaks and valleys, the smoothed distribution is calculated as the sum of the original sequence and the smoothened residuals, $r_i = y_i - z_i$,

$$z = \text{smooth}(y) + \text{smooth}(r)$$
$$z = \text{smooth}(y) + \text{smooth}(y - \text{smooth}(y)).$$

This procedure is referred to as *twicing*.

Symmetrisation of uncertainties

Most systematic uncertainties discussed here have an up and down variation about a nominal value. Therefore, for each uncertainty, three templates are available, including a nominal prediction and two variations. In cases where the up and down variations differ significantly, the systematic uncertainty becomes asymmetric. Uncertainties for which a significant asymmetry is observed[4] are symmetrised. Two symmetrisation scenarios are used: *one-sided* symmetrisation and *two-sided* symmetrisation. While the two-sided symmetrisation is used for uncertainties with up and down variations (v_{up} and v_{down}), the one-sided symmetrisation is used for uncertainties with either up or down variations.

In cases where a significant asymmetry is observed between the up and down variation, a one-sided symmetrisation using the more significant variation is used to conserve the more considerable uncertainties and provide a conservative uncertainty estimate. In the case of one-sided symmetrisation, the present variation is mirrored to produce symmetric uncertainty variations. In the case of the two-sided symmetrisation strategy, the symmetrised variations, $v_{\text{up}}^{\text{sym}}$ and $v_{\text{down}}^{\text{sym}}$, are determined per bin using

$$v_{\text{up, down}}^{\text{sym}} = \pm \left| \frac{|v_{\text{up}}| - |v_{\text{down}}|}{2 \cdot v_{\text{nominal}}} \right|, \tag{7.3}$$

where $|v_{\text{up}}|$ and $|v_{\text{down}}|$ denote the absolute up and down variations. The central nominal distribution is described by v_{nominal}. Both symmetrisation schemes have no effect if the up and down variations are symmetric around the central value.

Pruning of uncertainties

In total, over 300 systematic uncertainties are considered to describe a wide range of experimental and theoretical uncertainties. However, only some of these uncertainties have a sizable impact on the fit. To reduce the complexity of the likelihood

[4] This includes uncertainties that only have either an up or a down variation and are by construction fully asymmetric.

maximisation, systematic uncertainties with negligible effects are removed from the fit, which would otherwise produce a large number of local minima in the multidimensional likelihood.

Removing uncertainties from the fit is called *pruning*. Each systematic, in each region and for each sample, is split into a shape and normalisation component. If the impact of the normalisation from a given systematic uncertainty is smaller than 0.01 %, the normalisation impact of that uncertainty is removed from consideration for the given systematic uncertainty for the given region and the given sample. The shape impact is evaluated by normalising the systematically varied histogram to the same integral as the nominal distribution. If the bin-wise impact of this normalised systematic variation is smaller than 0.01 % for all bins of the distribution, the shape impact is dropped.

A set of different pruning thresholds was tested by evaluating the achieved uncertainties in the Asimov fit. The 0.01 % threshold provided a stable fit without omitting a significant number of NPs.

7.3 Determination of differential cross-sections

The measurement of *differential* cross-sections extends the inclusive cross-section measurement by considering cross-sections relative to a variable of interest (typically at truth level) such as p_{T}^{Z} resulting in $\mathrm{d}\sigma/\mathrm{d}p_{\mathrm{T}}^{Z}$. However, the effects of the detector response function, such as its resolution, efficiency, and acceptance, distort the true underlying differential cross-section. Removing all detector effects is necessary as only this underlying, detector-independent cross-section can generally be compared to theoretical predictions. These effects are removed in a procedure colloquially referred to as *unfolding*.

In the $t\bar{t}Z$ analysis, an extensive list of observables with sensitivity to possible EFT effects is unfolded in the 3ℓ and 4ℓ channels as these two channels contribute purer $t\bar{t}Z$ regions compared to the 2ℓ channel, which suffers from considerable background contamination.

The strategy to unfold the differential distributions to particle and parton level relies on a *Profile Likelihood Unfolding* (PLU) approach based on the standard profile likelihood approach presented above. Using the profile-likelihood machinery, this approach converts the unfolding task into a common problem of fitting the normalisation in each bin of different binned distributions.

To extend it to the unfolding problem, consider an arbitrary truth distribution, T_N, on parton or particle level with N bins and a corresponding *response matrix*, $R_{N\times M}$, with dimensions $N \times M$, where M describes the number of bins on detector level. This matrix combines the selection efficiency, migration effects and acceptance into one matrix. While the selection efficiency and the acceptance describe the probability of an event being selected on the reconstruction level and lying within the detector acceptance, the elements of the migration matrix represent the probability of an event entering bin i in a given parton or particle level distribution to be observed

in bin j at reconstruction level.

The binned distribution on the detector level, D_M, is obtained through a matrix multiplication,

$$D_M = R_{N\times M} T_{N\times 1}, \tag{7.4}$$

yielding one distribution with M bins for each *truth bin* on the detector level, here referred to as the *folded* distribution. The normalisation (signal strength) of these folded distributions on the detector level equals the truth distribution's normalisation. Performing a standard profile-likelihood fit then yields the normalisation of each folded distribution on the detector level, thereby providing a measurement of the normalisation on the truth level, i.e. yielding the target information of the unfolding procedure.

For this procedure, the Gaussian term in the likelihood used for the inclusive cross-section measurement as presented in Equation 7.2 is adapted to read

$$\prod_{j\in \mathrm{NP}} \mathrm{Gaus}(\theta_j^0|\theta_j, \Delta\theta_j) \times R(\vec{\mu}), \tag{7.5}$$

where $R(\vec{\mu})$ represents a penalty term as a function of the normalisation factors for each truth bin. If the regularisation term equals unity, the PLU is equivalent to unfolding via the inversion of the response matrix, R.

Additionally, the scalar signal strength μ is replaced by the normalisation vector, $\vec{\mu}$, in the Poisson term, reflecting the fact that only one free parameter ($\mu_{t\bar{t}Z}$) is needed for the profile-likelihood fit, but a vector of normalisation parameters is needed in the PLU. The likelihood for the differential cross-section measurement hence reads:

$$L\left(\vec{n}|\vec{\mu},\vec{\theta},\vec{k}\right) = \prod_{r\in \mathrm{regions}} \prod_{i\in \mathrm{bins}} \mathrm{Pois}\left(n_{i,r}|\vec{\mu}S_{i,r}(\vec{\theta}) + B_{i,r}(\vec{\theta},\vec{k})\right) \tag{7.6}$$

$$\times \prod_{j\in \mathrm{NP}} \mathrm{Gaus}(\theta_j^0|\theta_j, \Delta\theta_j) \times R(\vec{\mu}). \tag{7.7}$$

The advantage of the PLU technique over other techniques such as *iterative-bayesian unfolding* [254] is that it provides a common statistical framework for the inclusive and differential cross-section measurements. Additionally, background contributions can be treated as free-floating parameters, similar to those in the inclusive measurement and control regions, and NPs constraint can be considered. Furthermore, combinations with other differential measurements utilising the PLU approach are straightforward as the likelihoods can be readily combined by simply multiplying the likelihoods for different measurements. Since the full $t\bar{t}Z$ analysis was designed with combination opportunities with other ATLAS or CMS measurements in mind, PLU is a logical choice.

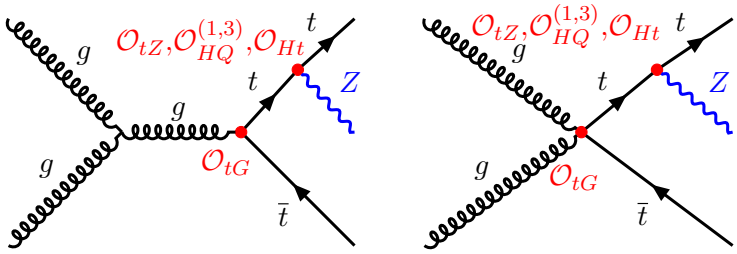

Figure 7.2: Examples of Feynman diagrams showing the top-Z coupling in the $t\bar{t}Z$ production process with the Z marked in blue in the SM gluon-gluon fusion production mode (left) and the newly introduced $ggt\bar{t}$-four-point interaction introduced through SMEFT (right). The vertices affected by EFT top-boson operators are marked in red.

7.4 Interpretation within the SM EFT

In total, 29 dimension-6 operators corresponding to 42 Wilson coefficients are considered in interpreting the results. They are loosely grouped into three categories: *top-boson* operators modifying the vertices between the top quark and the gauge bosons, *four-quark* operators introducing four-quark couplings of the type $q\bar{q}t\bar{t}$, and *top-lepton* operators corresponding to $t\bar{t}l\bar{l}$ and $b\bar{b}l\bar{l}$ vertices. The top-boson operators are of particular interest as they provide a handle on the top-Z interaction and probe the neutral current weak interaction in the SMEFT framework. In contrast to Section 1.1 the complex Higgs-doublet will be reffered to as H in the context of the SMEFT framework here. The top-boson operators relevant here are the $\mathcal{O}_{tW}$, $\mathcal{O}_{tB}$, $\mathcal{O}_{tG}$, $\mathcal{O}_{HQ}^{(1)}$, $\mathcal{O}_{HQ}^{(3)}$, and $\mathcal{O}_{Ht}$ operators. The $\mathcal{O}_{tG}$ operator modifies the $gt\bar{t}$ vertex and introduces a new $ggt\bar{t}$ vertex[5]. The linear combination of C_{tB} and C_{tW}, for which the Wilson coefficient is defined through

$$C_{tZ} = -\sin(\theta_W)C_{tB} + \cos(\theta_W)C_{tW}, \tag{7.8}$$

where C_{tB} and C_{tW} are the Wilson coefficients corresponding to the $\mathcal{O}_{tB}$ and $\mathcal{O}_{tW}$ operator, respectively, modifies the $t\bar{t}Z$ vertex and introduces a new $Ht\bar{t}Z$ vertex. The $\mathcal{O}_{HQ}^{(1)}$, $\mathcal{O}_{HQ}^{(3)}$, and $\mathcal{O}_{Ht}$ vertex all (among others) modify the $t\bar{t}Z$ vertex and also introduce a new $Ht\bar{t}Z$ vertex.

Figure 7.2 provides examples of Feynman diagrams highlighting the SM $t\bar{t}Z$ vertices affected by the top-boson operators listed above and an example of a newly introduced SMEFT $ggt\bar{t}$-four-point interaction vertex[6]. A complete list of all operators studied is provided in Table 7.2. From Figure 7.2, it can be readily understood that the fiducial cross-section measurement for which the measurement strategy is highlighted in the section above as well as differential distribution of observables

[5]Which is not shown in the figure.

[6]In this figure the Z is radiated from the top quark. Similar diagrams can be drawn with the Z originating from the anti-top quark.

such as p_{T}^{Z}, p_{T}^{t}, $p_{\mathrm{T}}^{t\bar{t}}$, or $m_{t\bar{t}Z}$ are sensitive to changes introduced by the operators as mentioned earlier.

The interpretation within the SMEFT framework pursued here follows the assumptions and SMEFT definitions highlighted in Section 1.2. All SMEFT fits are performed in a Bayesian statistical framework using a multimodal Gaussian likelihood function of the form:

$$-2\ln L(\vec{x}|\vec{y}) = \sum_{i=1}^{n}\sum_{j=1}^{n}(\vec{x}-\vec{y})_i^T \mathcal{M}_{ij}^{-1}(\vec{x}-\vec{y})_j, \tag{7.9}$$

where $\vec{x}$ describes a vector of n measurements with corresponding EFT predictions denoted by $\vec{y}$. These measurements consist of the fiducial cross-section and the normalised differential distributions of all observables unfolded in the measurement of the SM inclusive and differential cross-sections where, deviating from the SM measurement, the tZq normalisation is considered an additional free-floating normalisation factor in the unfolding. This procedure allows for the tZq contribution to be sensitive to possible EFT effects instead of fixing it to the SM prediction.

The matrix $\mathcal{M}_{ij}$ describes the total covariance matrix. The EFT predictions are described using Bayes's theorem using a prior probability $\pi(\vec{C})$ and the underlying Wilson coefficients:

$$p(\vec{C}|\vec{x}) = \frac{L(\vec{x}|\vec{y})\cdot\pi(\vec{C})}{p(\vec{x})}, \quad p(\vec{x}) = \int \mathrm{d}\vec{C} L(\vec{x}|\vec{y})\cdot\pi(\vec{c}). \tag{7.10}$$

The observables $\vec{x}$ in Equations 7.9 and 7.10 consist of the fiducial cross-section measurement for which the measurement strategy is highlighted in the section above. The usage of normalised differential distributions, however, differs from the description above in that in addition to the $t\bar{t}Z$ signal strength, the tZq signal strength, μ_{tZq}, is also treated as a free-floating parameter. This change originates from the fact that both the $t\bar{t}Z$ and tZq processes are affected by the same relevant EFT effects.

The predictions, $\vec{y}$, in Equations 7.9 and 7.10 are based on reweighted EFT MC samples. The reweighting approach is explained in detail in Ref. [1].

As all differential distributions are unfolded independently, correlation matrices are built between different bins of each observable. Subsequently, $\mathcal{M}$ is built with these correlation matrices forming the diagonal. The off-diagonal correlations, i.e. correlations between bins of different observables, are the statistical correlation obtained through a bootstrap method. For these off-diagonal elements, systematic uncertainties are small compared to the statistical uncertainties and hence neglected.

Overall several self-consistent parametrisation[7] scenarios are considered for the SMEFT interpretation. The first scenario considers linear and quadratic terms in Equation 1.13, providing a full SMEFT picture. Secondly, full quadratic parametrisations are performed for each operator, ignoring the effects of all other operators, by

[7] To avoid confusion with the terminology used in the inclusive measurement, the term *parametrisation* is chosen here over the term *fit*.

setting them to their SM value. This scenario provides a way to compare constraints obtained here with those obtained in other analyses that relied on these restricted EFT parametrisation. In the third scenario, only the linear terms of Equation 1.13 are considered instead to probe the SM-SMEFT interference. Lastly, the quadratic term in Equation 1.13 is used as a proxy for missing higher-order terms and a diagonal covariance matrix,

$$D_{ii} = 1 + \sqrt{N_8} \cdot \frac{g_{\text{SM}}^2}{C} \cdot \sqrt{1 + C^{-2}}, \tag{7.11}$$

is added to $\mathcal{M}$ in the quadratic equation, where $N_8 = 100$ describes a conservative choice of the estimated number of relevant dimension-8 operators, $g_{\text{SM}} = \alpha_s(M_Z) = 0.118$ is the relevant SM coupling, and C is a Wilson coefficient.

Table 7.2: Definitions of the relevant dimension-6 SMEFT operators. For the three top-boson operators indicated with a $(\star)$, a distinguishment is made between the real and imaginary parts of the corresponding Wilson coefficients. Three Wilson coefficients correspond to each of the five top-lepton operators, denoted, e.g. $C^{(1)}_{lQ,i}$ with $i = 1, 2, 3$ an index running over the lepton generations.

	Operator	Definition		Comment
top-boson	$\mathcal{O}_{tW}$	$(\bar{Q}\sigma^{\mu\nu}t)\sigma^i\tilde{H}W^i_{\mu\nu}$	$(\star)$	modifies the tWb, $t\bar{t}\gamma$ and $t\bar{t}Z$ vertices, induces new $Ht\bar{t}Z$ vertex
	$\mathcal{O}_{tB}$	$(\bar{Q}\sigma^{\mu\nu}t)\tilde{H}B_{\mu\nu}$	$(\star)$	modifies the tWb, $t\bar{t}\gamma$ and $t\bar{t}Z$ vertices, induces new $Ht\bar{t}Z$ vertex
	$\mathcal{O}_{tG}$	$(\bar{Q}\sigma^{\mu\nu}T^at)\tilde{H}G^a_{\mu\nu}$	$(\star)$	modifies the $gt\bar{t}$ vertex, induces new $ggt\bar{t}$ vertex
	$\mathcal{O}^{(1)}_{HQ}$	$(H^\dagger i\overleftrightarrow{D}_\mu H)(\bar{Q}\gamma^\mu Q)$		modifies the $b\bar{b}Z$ and $t\bar{t}Z$ vertices, induces new $Hb\bar{b}Z$ and $Ht\bar{t}Z$ vertices
	$\mathcal{O}^{(3)}_{HQ}$	$(H^\dagger i\overleftrightarrow{D}^i_\mu H)(\bar{Q}\sigma^i\gamma^\mu Q)$		modifies the tWb, $b\bar{b}Z$ and $t\bar{t}Z$ vertices, induces new $Hb\bar{b}Z$ and $Ht\bar{t}Z$ vertices
	$\mathcal{O}_{Ht}$	$(H^\dagger i\overleftrightarrow{D}_\mu H)(\bar{t}\gamma^\mu t)$		modifies the $t\bar{t}Z$ vertex, induces new $Ht\bar{t}Z$ vertex
four-quark	$\mathcal{O}^{(1)}_{tu}$	$(\bar{t}\gamma_\mu t)(\bar{u}\gamma^\mu u)$		right-handed $u\bar{u}/c\bar{c}$ to right-handed $t\bar{t}$, colour-singlet
	$\mathcal{O}^{(8)}_{tu}$	$(\bar{t}T^a\gamma_\mu t)(\bar{u}T^a\gamma^\mu u)$		right-handed $u\bar{u}/c\bar{c}$ to right-handed $t\bar{t}$, colour-octet
	$\mathcal{O}^{(1)}_{td}$	$(\bar{t}\gamma_\mu t)(\bar{d}\gamma^\mu d)$		right-handed $d\bar{d}/s\bar{s}$ to right-handed $t\bar{t}$, colour-singlet
	$\mathcal{O}^{(8)}_{td}$	$(\bar{t}T^a\gamma_\mu t)(\bar{d}T^a\gamma^\mu d)$		right-handed $d\bar{d}/s\bar{s}$ to right-handed $t\bar{t}$, colour-octet
	$\mathcal{O}^{(1)}_{qt}$	$(\bar{q}\gamma_\mu q)(\bar{t}\gamma^\mu t)$		left-handed $q\bar{q}$ to right-handed $t\bar{t}$, colour-singlet
	$\mathcal{O}^{(8)}_{qt}$	$(\bar{q}T^a\gamma_\mu q)(\bar{t}T^a\gamma^\mu t)$		left-handed $q\bar{q}$ to right-handed $t\bar{t}$, colour-octet
	$\mathcal{O}^{(1)}_{Qt}$	$(\bar{Q}\gamma_\mu Q)(\bar{t}\gamma^\mu t)$		left-handed $b\bar{b}$ to right-handed $t\bar{t}$, colour-singlet
	$\mathcal{O}^{(8)}_{Qt}$	$(\bar{Q}T^a\gamma_\mu Q)(\bar{t}T^a\gamma^\mu t)$		left-handed $b\bar{b}$ to right-handed $t\bar{t}$, colour-octet
	$\mathcal{O}^{(1)}_{Qu}$	$(\bar{Q}\gamma_\mu Q)(\bar{u}\gamma^\mu u)$		right-handed $u\bar{u}/c\bar{c}$ to left-handed $t\bar{t}$, colour-singlet
	$\mathcal{O}^{(8)}_{Qu}$	$(\bar{Q}T^a\gamma_\mu Q)(\bar{u}T^a\gamma^\mu u)$		right-handed $u\bar{u}/c\bar{c}$ to left-handed $t\bar{t}$, colour-octet
	$\mathcal{O}^{(1)}_{Qd}$	$(\bar{Q}\gamma_\mu Q)(\bar{d}\gamma^\mu d)$		right-handed $d\bar{d}/s\bar{s}$ to left-handed $t\bar{t}$, colour-singlet
	$\mathcal{O}^{(8)}_{Qd}$	$(\bar{Q}T^a\gamma_\mu Q)(\bar{d}T^a\gamma^\mu d)$		right-handed $d\bar{d}/s\bar{s}$ to left-handed $t\bar{t}$, colour-octet
	$\mathcal{O}^{(1)}_{QQ}$	$(\bar{Q}\gamma_\mu Q)(\bar{Q}\gamma^\mu Q)$		left-handed $b\bar{b}$ to left-handed $t\bar{t}$, colour-singlet
	$\mathcal{O}^{(8)}_{QQ}$	$(\bar{Q}T^a\gamma_\mu Q)(\bar{Q}T^a\gamma^\mu Q)$		left-handed $b\bar{b}$ to left-handed $t\bar{t}$, colour-octet
	$\mathcal{O}^{(1,1)}_{Qq}$	$(\bar{Q}\gamma_\mu Q)(\bar{q}\gamma^\mu q)$		left-handed $q\bar{q}$ to left-handed $t\bar{t}$, weak-singlet, colour-singlet
	$\mathcal{O}^{(3,1)}_{Qq}$	$(\bar{Q}\sigma^i\gamma_\mu Q)(\bar{q}\sigma^i\gamma^\mu q)$		left-handed $q\bar{q}$ to left-handed $t\bar{t}$, weak-triplet, colour-singlet
	$\mathcal{O}^{(1,8)}_{Qq}$	$(\bar{Q}T^a\gamma_\mu Q)(\bar{q}T^a\gamma^\mu q)$		left-handed $q\bar{q}$ to left-handed $t\bar{t}$, weak-singlet, colour-octet
	$\mathcal{O}^{(3,8)}_{Qq}$	$(\bar{Q}\sigma^iT^a\gamma_\mu Q)(\bar{q}\sigma^iT^a\gamma^\mu q)$		left-handed $q\bar{q}$ to left-handed $t\bar{t}$, weak-triplet, colour-octet
top-lepton	$\mathcal{O}_{et}$	$(\bar{e}_p\gamma_\mu e_r)(\bar{t}\gamma^\mu t)$		right-handed leptons and right-handed quarks in the $t\bar{t}l\bar{l}$ vertex
	$\mathcal{O}_{Qe}$	$(\bar{Q}\gamma_\mu Q)(\bar{e}_p\gamma^\mu e_r)$		right-handed leptons and left-handed quarks in the $t\bar{t}l\bar{l}$ and $b\bar{b}\ell\bar{\ell}$ vertices
	$\mathcal{O}_{lt}$	$(\bar{l}_p\gamma_\mu l_r)(\bar{t}\gamma^\mu t)$		left-handed leptons and right-handed quarks in the $t\bar{t}l\bar{l}$ vertex
	$\mathcal{O}^{(1)}_{lQ}$	$(\bar{l}_p\gamma_\mu l_r)(\bar{Q}\gamma^\mu Q)$		left-handed leptons and left-handed quarks in the $t\bar{t}l\bar{l}$ and $b\bar{b}\ell\bar{\ell}$ vertices, weak-singlet
	$\mathcal{O}^{(3)}_{lQ}$	$(\bar{l}_p\sigma^i\gamma_\mu l_r)(\bar{Q}\sigma^i\gamma^\mu Q)$		left-handed leptons and left-handed quarks in the $t\bar{t}l\bar{l}$ and $b\bar{b}\ell\bar{\ell}$ vertices, weak-triplet

CHAPTER 8

Systematic Uncertainties

The following sections present the systematic uncertainties appropriate to this analysis. They can be divided into two categories: experimental uncertainties related to an imperfect reconstruction of physics objects in the detector and theoretical uncertainties related to incomplete knowledge of the underlying physics processes.

8.1 Experimental uncertainties

The ATLAS detector is a complicated and delicate instrument. The reconstruction and identification of objects in the detector come with systematic uncertainties associated with an imperfect knowledge of the detector and imperfect reconstruction and identification algorithms. These experimental uncertainties generally come with up and down variation. They enter the fit as a two-point uncertainty and are smoothened, symmetrised, and pruned according to the abovementioned procedure. All systematic variations are summarised in Table 8.1. In the following paragraphs, systematic uncertainties originating from experimental sources are highlighted.

Jet-related uncertainties

Jets occur in abundance in events at hadron colliders like the LHC. They are particularly relevant in semi-leptonic top quark decays, as at least four jets are expected for such an event signature. Since jets consist of collimated showers of particles, their modelling and calibration are intrinsically challenging.

Jet uncertainties mainly originate from the jet energy scale (JES) calibration and the jet energy resolution (JER). As described in Section 2.3, the JES calibration is a multi-step procedure, during which the energy scale of jets is step-wise corrected to match the energy scale of well-measured reference objects. The uncertainties for these steps are derived using dedicated *in-situ* techniques described in Ref. [255]. The set of uncertainties for the JES consists of 125 individual components. This set of components is reduced to 30 parameters employing eigenvector decomposition,

Table 8.1: Summary of symmetrisation procedures applied for the systematic uncertainties in the analysis.

Type	Systematics	Symmetrisation
Signal uncertainties	$t\bar{t}Z$ μ_F+μ_R	one-sided
	$t\bar{t}Z$ parton shower	one-sided
	$t\bar{t}Z$ A14	one-sided
	$t\bar{t}Z$ PDF	one-sided
Background uncertainties	All, except:	one-sided
	tWZ, tZq μ_F+μ_R	two-sided
	tZq A14	two-sided
	WZ & ZZ PDF scale	two-sided
	WZ & ZZ PDF α_s	two-sided
Experimental uncertainties	All	two-sided

combining p_{T}-dependent in-situ uncertainty components into separate groups depending on their origin. Sub-components which have a large impact on this analysis are the JES pile-up ρ topology, i.e. the pile-up contribution to the JES estimated from the median p_{T}-density of jets in the η-ϕ-plane, and the components describing the uncertainty originating from the response to jets of different flavours. Figure 8.1 provides an overview of the major JES components for particle-flow jets at different p_{T} and η values. While for jets with p_{T} up to approximately 30 GeV pile-up components are dominant, the predominant JES component for jets with $30\,\mathrm{GeV} < p_{\mathrm{T}} < 400\,\mathrm{GeV}$, originates from the difference in response between quark-initiated and gluon-initiated jets. The analysis presented here contains an insignificant number of higher-p_{T} jets.

Additionally, Figure 8.1 highlights the effect of the two main JES uncertainties the analysis is sensitive to: the JES pile-up ρ topology and the JES flavour composition. The region most sensitive to variations introduced by these uncertainties is that with high $t\bar{t}Z$ output values as predicted by the $t\bar{t}Z$ output of the used multi-class classifier.

The uncertainty and its major components are reflected in the highest-ranked jet-related uncertainties in this analysis.

Uncertainties related to the JER are estimated using theoretically well-understood dijet events for a *balance method* as described in Ref. [255]. In this procedure, already utilised in Run 1 [256, 257], the momentum of a jet is measured with respect to a recoiling reference object. An imperfect modelling of jets and the JES uncertainties at these momenta dominates the uncertainty on the JER at low transverse momentum. At transverse momenta above 200 GeV non-closure uncertainties between the jet energy scale measured in MC and data dominate. At large transverse momenta, not probed by this analysis, the increased JES uncertainties, previously highlighted in Figure 8.1 dominate again. The relative JER and the composition of its uncertainty are shown in detail in Figure 8.2. The complete set of uncertainties results in 117

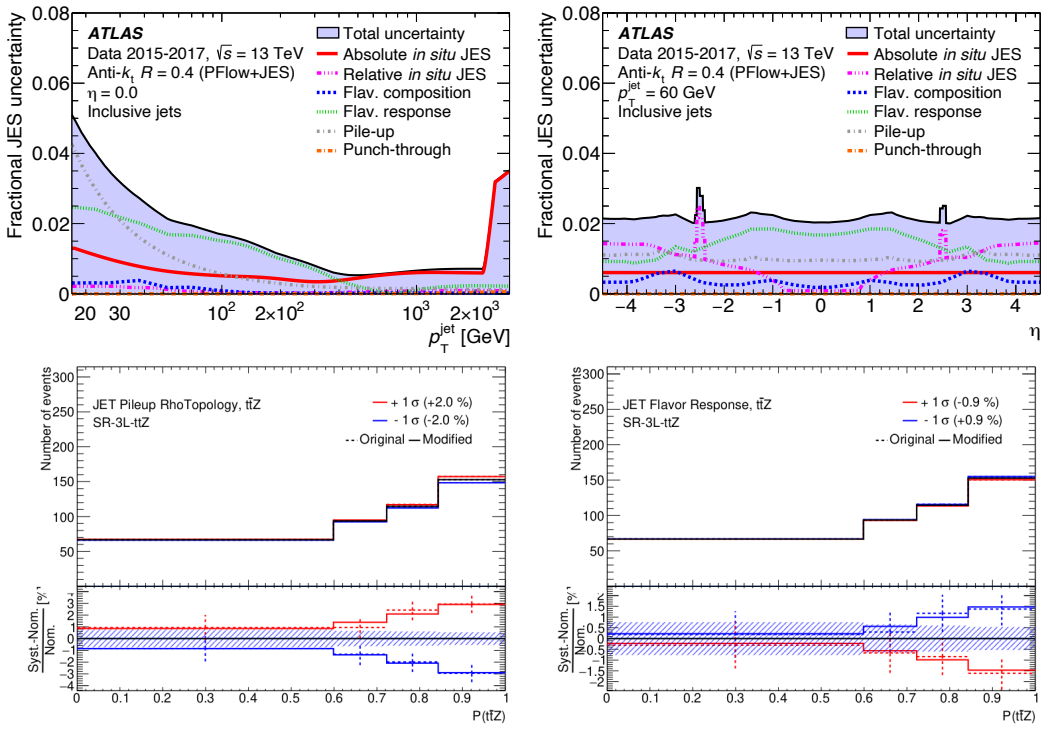

Figure 8.1: Overview of major JES uncertainty components represented by dotted lines for anti-k_t particle-flow jets at $\eta = 0$ as a function of p_{T} (top left) and as a function of η (top right) at a typical jet p_{T} of 60 GeV [255]. The total uncertainty is shown as a blue area. The effects of the two dominating jet uncertainties, JES pile-up ρ topology (bottom left) and JES flavour composition (bottom right) on SR-3ℓ-$t\bar{t}Z$, are shown.

NPs. Their number is again reduced through eigenvector decomposition as done for the JES. The reduced set of JER NPs used in this analysis consists of 13 NPs, corresponding to a description of the JER uncertainties with $\sim 5\,\%$ loss in correlation with respect to the complete list of NPs.

Uncertainties related to the JVT efficiency are evaluated in $Z(\rightarrow \mu\mu)$+jets data and MC events using a tag-and-probe procedure, where the probe jet is recoiling against the Z boson, satisfying $|\Delta\phi(Z, \text{jet})| > 2.8$ [205]. Pile-up contributions are estimated through a pile-up-dominated control region. The systematic uncertainty on the obtained simulation-to-data scale factors is comprised of an uncertainty representing a potential mismodelling of the $|\Delta\phi(Z, \text{jet})|$-distribution for hard-scatter jets and an uncertainty arising from non-negligible MC-to-MC differences of the hard-scatter jet efficiency between events generated with SHERPA and POWHEG.

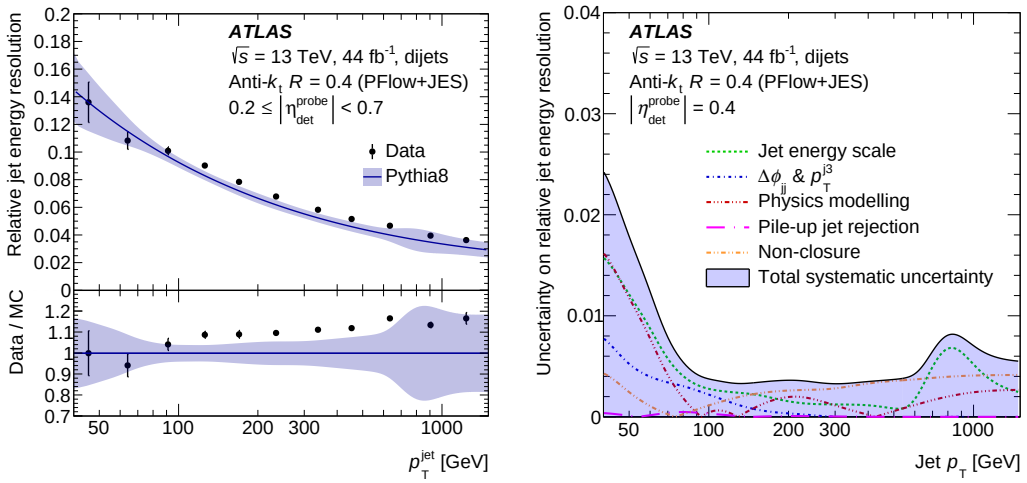

Figure 8.2: The relative JER as a function of p_{T} (left) and the overview of major JER uncertainty components for anti-k_t particle-flow jets (right). The black dots represent the resolution in data, and the solid blue line is the resolution in MC. The uncertainty is split into the major components, represented by a set of dotted lines, with the full uncertainty shown as a blue area. Figure is taken from Ref. [255].

Flavour tagging uncertainties

Jets tagged as b-jets play a significant role in top-quark physics due to the dominance of the $t \to b(W \to f\bar{f})$ decay channel over the $t \to d(W \to f\bar{f})$ and $t \to s(W \to f\bar{f})$ decay channels, where $f\bar{f}$ can be a pair of quarks or a pair of leptons. The b-jet tagging and the c-jet mistagging efficiencies for the DL1r flavour-tagging algorithm used in this analysis are measured using dileptonic and single-leptonic $t\bar{t}$ events, respectively [258, 259]. Corrections are applied to simulated jets in bins of p_{T} to match the efficiency observed in the data. Jet flavour-dependent data-to-simulation scale factors are close to unity. The uncertainties originate from various sources, such as modelling differences between generators and experimental uncertainties of the $t\bar{t}$ analysis mentioned above. The flavour tagging uncertainties are then described by varying the correlated scale factors within their intrinsic uncertainties. Decorrelation of these variations via eigenvector decomposition results in 45 NPs, describing the b-tagging scale factor variations and 20 NPs describing c-jet and l-jet mistagging variations. All NPs depend on the p_{T} of the jet. The NPs associated with the l-jet mistagging also depend on the η of the jet.

Charged lepton uncertainties

Experimental uncertainties associated with muons and electrons are grouped into two categories: the first category summarises uncertainties from trigger, identification, isolation and reconstruction efficiencies, and the second category comprises lepton

momentum resolution and scale uncertainties.

Electron efficiencies measured in MC, i.e. efficiencies of the first category, are matched to efficiencies observed in data through scale factors. Two different systematic models with varying description power are used for the electron identification and isolation uncertainties on the one hand and the trigger and reconstruction efficiencies on the other.

The scale factor measurements for the identification and isolation efficiencies are conducted in statistically independent bins of p_{T} and η. Systematic uncertainties are correlated between the bins. For this measurement, the *full* uncertainty model comprised of 218 uncorrelated NPs is broken down to a *simplified* set of 15 uncorrelated and 10 correlated NPs across $\eta \times p_{\mathrm{T}}$, where $|\eta| = [0, 1.37, 4.9]$ and $p_{\mathrm{T}} = [7, 10, 15, 20, 25, 30, 60, 80, \infty]\,\mathrm{GeV}$ is choosen.

Electron reconstruction and trigger uncertainties are described using a simplified systematic uncertainty model consisting of a single variation for the corresponding scale factors, as trigger and reconstruction uncertainties are observed to be largely sub-dominant for this analysis.

The electron momentum scale and resolution efficiency are checked by comparing them to the scale and resolution efficiency observed in $Z \to \ell^+\ell^-$ and $J/\psi \to \ell^+\ell^-$ events, utilising the well-known masses of the mother particles involved in the two processes [260, 261][1]. The corresponding *full* uncertainty model consisting of more than 60 systematic variations is broken down to a *simplified* model where all systematic effects are considered correlated across the full η range and summed up in quadrature. The simplified model yields two systematic up-and-down variations, one for the electron momentum scale and one for the resolution. A detailed description of the momentum scale and resolution efficiency measurements can be found in Ref. [260, 261].

Similar to the treatment of electrons, scale factors are determined and applied to address differences in the muon identification, isolation and trigger efficiency between MC and data. Additionally, scale factors are applied to correct for differences in the track-to-vertex association (TTVA) between reconstructed muons in MC and data.

The efficiencies of the categories mentioned above are measured using a tag-and-probe method in $Z \to \mu\mu$ and $J/\Psi \to \mu\mu$ efficiency measurements. Detailed information on the procedures of these measurements can be found in Ref. [262].

The uncertainties of the muon trigger scale factors are determined using a systematic uncertainty model resulting in one up/down variation. The identification, isolation and TTVA scale factor uncertainties are broken down by source of the systematic uncertainty. This results in 14, 10 and 6 systematic variations for the identification, isolation and TTVA scale factors, respectively. These variations include variations for muons with low transverse momenta, i.e. $p_{\mathrm{T}} < 15\,\mathrm{GeV}$.

Muon momentum scale and resolution uncertainties arise from corrections applied to muons in the MC simulation to match the momentum scale and resolution seen in the data. For these systematic uncertainties, the scale and resolution measured

[1] In addition studies of the ratio E/p in $W \to e\nu$ events are also used.

in the MS and the ID are considered and varied independently. Furthermore, charge-dependent scale corrections are taken into account. A detailed description of the extraction of the scale factor mentioned above can be found in Refs. [262, 263].

Missing transverse momentum

As highlighted in Section 2.3, the missing transverse momentum, $p_{\mathrm{T}}^{\mathrm{miss}}$, colloquially referred to as missing transverse energy, $E_{\mathrm{T}}^{\mathrm{miss}}$, is constructed as the negative vector sum of all transverse momenta of all objects in an event. Additionally, a *soft term* is subtracted to account for *soft activity* within the detector, such as contributions from jets with $p_{\mathrm{T}} < 20\,\mathrm{GeV}$, and clusters in the calorimeters not associated with any other objects. The uncertainty on the reconstructed $E_{\mathrm{T}}^{\mathrm{miss}}$ is based on comparing the individual hard terms with the soft term as highlighted in Equation 2.7. For the estimation, the $E_{\mathrm{T}}^{\mathrm{miss}}$-related systematic uncertainties, scale and resolution uncertainties of analysis-dependent hard-term physics objects are propagated. Correlations for objects of the same type are taken into account. Additionally, the scale and resolution uncertainty of the soft term is evaluated in $Z \to \mu\mu$ events with no genuine $E_{\mathrm{T}}^{\mathrm{miss}}$ contribution, i.e. $E_{\mathrm{T}}^{\mathrm{miss}} = -(p_{\mathrm{T}}^{\mathrm{hard}} + p_{\mathrm{T}}^{\mathrm{soft}}) = 0$.

For events without jets, $p_{\mathrm{T}}^{\mathrm{soft}}$ is expected to point in the opposite direction of $p_{\mathrm{T}}^{\mathrm{hard}}$ in the transverse plane. Derivations from this expectation are expressed in two projections of $p_{\mathrm{T}}^{\mathrm{soft}}$ onto $p_{\mathrm{T}}^{\mathrm{hard}}$, one parallel ($\mathcal{P}_{\parallel}$) and one perpendicular ($\mathcal{P}_{\perp}$). The systematic uncertainties of the soft term are then determined based on data-to-MC comparisons of $\langle \mathcal{P}_{\parallel} \rangle (p_{\mathrm{T}}^{\mathrm{hard}})$, $\mathrm{RMS}_{\parallel}^{2}(p_{\mathrm{T}}^{\mathrm{hard}})$ and $\mathrm{RMS}_{\perp}^{2}(p_{\mathrm{T}}^{\mathrm{hard}})$, where the first describes the response and the latter two the resolution, which lead to three NPs [209]. Varying the NPs up and down by one standard deviation represents the $E_{\mathrm{T}}^{\mathrm{miss}}$-related systematic uncertainties.

Luminosity and Pile-up

The integrated luminosity recorded by ATLAS during Run 2 is based on luminosity-sensitive sub-detectors calibrated during low-luminosity runs with dedicated LHC run conditions using van der Meer scans [264,265]. A detailed description of the measurements is given in Ref. [190]. During Run 2, the primary bunch-to-bunch luminosity measurement was performed by the ATLAS LUCID 2 Cherenkov detector [189]. The systematic uncertainty on the integrated luminosity is 0.83 %. It is applied to all processes determined from MC simulations.

Systematic uncertainties related to the pile-up distribution described in Section 2.1 are obtained by symmetrically rescaling the mean number of interactions, $\langle \mu \rangle$, by 1/0.99 and 1/1.07 around the central scale factor of 1/1.03.

8.2 Theoretical uncertainties

In the $t\bar{t}Z$ analysis, a wide range of theoretical uncertainties is considered for signal and background processes. The set of theoretical uncertainties is comprised of various

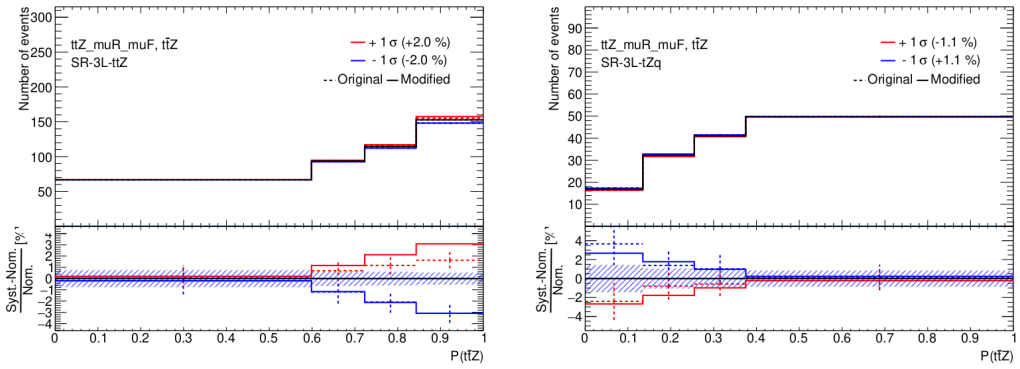

Figure 8.3: effect of the joint variation of the factorisation and renormalisation scale for the $t\bar{t}Z$ process in the SR-3ℓ-$t\bar{t}Z$ region (left) and the SR-3ℓ-tZq (right).

components. Global theoretical uncertainties are, for example, used to describe normalisation uncertainties of several background processes. In some cases, the used MC generators or shower algorithms or inputs to them are varied to estimate the uncertainty originating from the choice of generators and shower algorithms. The variations of the renormalisation and factorisation scales with respect to the nominal prediction are also considered.

The following sections describe the theoretical uncertainties for the signal and background processes.

$t\bar{t}Z$ signal uncertainties

For the $t\bar{t}Z$ signal process, several sources of systematic uncertainties are considered. The renormalisation and factorisation scale uncertainty is obtained by simultaneously varying the scales up and down by a factor of 2 and comparing it to the nominal prediction. Both independent and joint variations are tested, with the latter providing an accurate envelope of both effects. Therefore only the joint variation is used in this analysis. The effect of this simultaneous variation of the renormalisation and factorisation scale on the $t\bar{t}Z$ signal process in the two most sensitive signal regions, SR-3ℓ-$t\bar{t}Z$ and SR-3ℓ-tZq, is shown in Figure 8.3. The uncertainty is symmetrised to account for a slightly asymmetric shape.

Uncertainties on the PDF set follow the prescription in Ref. [266]. These uncertainties include uncertainties on functional forms and experimental uncertainties entering in fits used to determine the PDF sets. They take estimates of missing higher-order uncertainties in the DGLAP equation into account through scale variations and probe several other theoretical uncertainties, such as the choice of the flavour scheme.

Parton shower uncertainties[2] are evaluated by comparing the distributions of

[2]I.e. the uncertainties associated with the parton shower algorithm and the underlying event model.

interest obtained with MadGraph5_aMC@NLO interfaced to Pythia 8 to distributions obtained using MadGraph5_aMC@NLO interfaced to Herwig 7. Uncertainties related to modelling the initial-state radiation are obtained by varying the var3c parameter of the Pythia a14 tune using dedicated alternative samples.

The Sherpa generator is used to model the $t\bar{t}Z$ process at different levels of precision as described in Section 3.1. These variations only enter the differential measurements to provide a cross-check with respect to the nominal predictions. They do not enter as an additional systematic uncertainty.

Uncertainties on background processes

Theoretical uncertainties of the $WZ \to \ell\ell\ell\nu$ (WZ) and $ZZ \to \ell\ell\ell\ell$ (ZZ) processes[3] are evaluated using alternative truth-level samples. The ckkw matching scale in these samples is varied from its nominal value of 20 GeV to 15 GeV and 30 GeV, respectively. The qsf parameter, i.e. the resummation scale, is varied by a factor of two up and down. Lastly, an alternative recoiling scheme variation is used.

For the evaluation of the renormalisation and factorisation scale uncertainties, the same procedure as that presented for the $t\bar{t}Z$ samples is pursued: the joint variation of both scales is found to cover both individual variations. It is subsequently varied up and down by a factor of two. Uncertainties arising from the choice of the pdf set are evaluated by comparing the nominal values of the ct14 [267] and mmht14 [268] pdf sets, also including variations of α_s.

Flat normalisation uncertainties of 30 % are applied to the WZ+l and WZ+c processes. Additionally, normalisation uncertainties are applied to the ZZ+l (15 %) and ZZ+c (30 %) processes, motivated by the uncertainties used in the previously performed $t\bar{t}Z$ measurement by atlas [147], where these uncertainties were determined through dedicated control regions in data and extrapolated to the WZ+b (50 %) and ZZ+b (50 %) processes.

In this analysis, the ZZ+b and the WZ+b normalisation and its uncertainty are determined in the fit. They are implemented as individual nps.

For the normalisation of the tZq background, a 14 % normalisation uncertainty is used, based on the dedicated atlas measurement presented in Ref. [269]. An alternative sample generated with MadGraph5_aMC@NLO interfaced to Herwig 7 instead of Pythia 8 describes uncertainties due to the choice of parton shower. Following the procedure used for the $t\bar{t}Z$ signal samples, variations of the var3c parameter of the Pythia a14 tune and variations of the renormalisation and factorisation scales are considered. Systematic uncertainties originating from the choice of the pdf set follow the prescriptions in Ref. [266].

For the tWZ background, the difference between samples generated with the dr1 and dr2 diagram removal schemes, as described in Refs. [270–272], is used as a

[3] ZZ events end up in the signal region through $Z \to \tau\tau$ with one τ decaying leptonically and the other decaying hadronically or through $ZZ \to 4\ell$ where one lepton falls out of the acceptance of the detector.

modelling uncertainty. As for the tZq, and $t\bar{t}Z$ processes PDF and renormalisation and factorisation scale uncertainties are considered.

A normalisation uncertainty is considered for the $t\bar{t}H$ background process, based on the NLO QCD + EWK calculation in Ref. [165]. This leads to a scale uncertainty of $^{+5.5}_{-9.2}$ % and a PDF+α_s uncertainty of ± 3.6 %.

The remaining background processes, such as HV, VVV, $t\bar{t}W$, $t\bar{t}WW$, $tt\bar{t}$ and $t\bar{t}t\bar{t}$, contribute less than 1 % to the total event yields in the relevant analysis regions. Hence a conservative normalisation uncertainty of 50 % is considered. In the case of the $t\bar{t}t\bar{t}$ background process, an additional shower uncertainty is considered, exchanging the nominal shower algorithm, PYTHIA 8, for HERWIG 7.

The fake contribution due to fakes from other sources, which is not extracted from an independent data-driven estimation, is assigned a conservative 50 % normalisation uncertainty. Non-closure uncertainties covering a possible mismodelling between data and MC observed in the fake-enriched control regions are also derived for this fake component and applied in the signal regions.

CHAPTER 9

Results

The results of the measurement[1] addressed in this thesis are split into three different categories: An inclusive cross-section measurement in the trilepton channels, the combination with the dilepton and tetralepton channel, differential cross-section measurements in the trilepton and tetralepton channels, and subsequent interpretations in the SMEFT framework.

While the author's main focus was the inclusive measurement of the $t\bar{t}Z$ cross-section in the trilepton channel, the inclusive and differential measurements in the dilepton and tetralepton channels and the subsequent interpretation in the SMEFT framework provide complementary results.

Dominik Babal and Lucia Keszeghova primarily handled the measurements in the dilepton and tetralepton channels. Lucia Keszeghova and Harriet Watson were responsible for the differential $t\bar{t}Z$ cross-section measurements in the trilepton and tetralepton channels, respectively. These measurements are discussed in depth in their theses. Baptiste Ravina interpreted the results within the SM EFT framework. The author summarises the analysis here, including the differential measurements and the results of the SM EFT interpretation, to give an overview of the study's implications and conclusions.

9.1 Measurement of the inclusive $t\bar{t}Z$ cross-section

Before presenting the results of the inclusive and differential cross-section measurements, a study of the inclusive fit setup is shown.

This study of the fit setup is based on an *Asimov* fit in the trilepton channel to test the behaviour of the fit on a pseudo-dataset. On the other hand, the fit is performed using observed data in all scenarios for the fake-enriched control regions.

[1] The results and the corresponding conclusions presented in the following were undergoing final review by the ATLAS collaboration when this thesis was submitted. Where appropriate results were updated to reflect those in Ref. [1].

Table 9.1: Ratios of $t\bar{t}Z$, tZq, and WZ+b events with respect to all other events. The first row describes the signal purity in the individual signal regions. The second and third rows describe the tZq, and WZ+b contributions in the SR-3ℓ-tZq and SR-3ℓ-WZ signal regions, respectively.

	SR-3ℓ-$t\bar{t}Z$	SR-3ℓ-tZq	SR-3ℓ-WZ
$t\bar{t}Z$/Rest	3.12	0.62	0.37
tZq/Rest	0.04	0.33	0.08
WZ+b/Rest	0.04	0.09	0.43

For the trileptonic fit results, the signal regions introduced in Chapter 4 and the fake-enriched control regions described in Chapter 6 are used. All events originating from signal samples, summarised in detail in Chapter A, are considered signal events except for those with at least one fake lepton. The signal purity, S/B, where S denotes signal events and B denotes background events is 3.12 for SR-3ℓ-$t\bar{t}Z$, 0.62 for SR-3ℓ-tZq, and 0.37 for SR-3ℓ-WZ. While SR-3ℓ-$t\bar{t}Z$ provides the most prominent handle on $\mu_{t\bar{t}Z}$, SR-3ℓ-tZq allows to evaluate and reduce the impact of the tZq normalisation uncertainty on the measurement. The third region, SR-3ℓ-WZ, helps to constrain the WZ+b background in the fit by allowing $\mathcal{N}_{WZb}$ to float freely.

Table 9.1 summarises the individual signal purities and the tZq and WZ+b background contributions in the three signal regions. The predicted event yields and those obtained using ATLAS proton-proton collision data, in the following referred to as ATLAS data, are shown in Table 9.2 for the three signal regions. As explained in Section 7.2, the Asimov data is set to match exactly the predicted event yields. In this case

$$\mu_{t\bar{t}Z} = \mathcal{N}_{\text{WZb}} = \mathcal{N}_{\text{F-e-HF}} = \mathcal{N}_{\text{F-e-Other}} = \mathcal{N}_{\text{F-m-HF}} = 1.0 \tag{9.1}$$

holds. This means that the Asimov dataset matches exactly the SM model prediction embodied by the MC simulation.

In order to provide a fiducial cross-section measurement, a cut on the mass of the fermion pair, $m_{\ell\ell}$, originating from the Z boson is introduced, constraining $m_{\ell\ell}$ into the window of $70-110\,\text{GeV}$ in order to exclude off-shell Z boson decay contributions and the interference with $t\bar{t}\gamma$.

This mass window cut matches the cut chosen by the CMS collaboration in their fiducial $t\bar{t}Z$ measurement [148] and the previously performed Run 2 measurement of the $t\bar{t}Z$ process by the ATLAS collaboration [147] allowing for a comparison with these results.

To determine the fiducial cross-section, the fraction of the parton-level events within the Z-mass window is determined to be 94.5% using truth information. The

Table 9.2: Expected and observed event yields in the trilepton signal regions, obtained for an integrated luminosity of $140\,\text{fb}^{-1}$. The indicated errors include the Monte Carlo statistical uncertainty and all other systematic uncertainties discussed in Chapter 8. Rounding to significant digits is applied.

	SR-3ℓ-$t\bar{t}Z$		*SR*-3ℓ-WZ		*SR*-3ℓ-tZq	
	Fit to Asimov data	Fit to ATLAS data	Fit to Asimov data	Fit to ATLAS data	Fit to Asimov data	Fit to ATLAS data
$t\bar{t}Z$	424.0 ± 20.0	432.0 ± 26.0	45.8 ± 2.3	47.0 ± 4.0	139.0 ± 9.0	142.0 ± 13.0
$t\bar{t}W$	4.2 ± 2.2	4.4 ± 2.1	2.1 ± 1.1	2.2 ± 1.1	5.2 ± 2.6	5.5 ± 2.7
$t\bar{t}H$	11.7 ± 1.2	11.8 ± 1.1	1.4 ± 0.2	1.4 ± 0.2	6.5 ± 0.6	6.6 ± 0.6
WZ+b	23.0 ± 6.0	24.0 ± 8.0	51.0 ± 14.0	52.0 ± 17.0	30.0 ± 8.0	30.0 ± 10.0
WZ+c	9.0 ± 4.0	9.0 ± 4.0	13.0 ± 5.0	12.0 ± 5.0	12.0 ± 5.0	11.0 ± 5.0
WZ+l	1.2 ± 0.6	1.2 ± 0.6	1.7 ± 0.8	1.7 ± 0.8	1.8 ± 0.8	1.8 ± 0.8
ZZ+b	4.4 ± 2.6	4.3 ± 2.6	7.0 ± 4.0	7.0 ± 4.0	7.0 ± 4.0	7.0 ± 4.0
ZZ+c	1.0 ± 0.5	1.0 ± 0.5	1.0 ± 0.5	1.0 ± 0.5	1.3 ± 0.6	1.3 ± 0.6
ZZ+l	0.4 ± 0.2	0.4 ± 0.2	0.3 ± 0.2	0.2 ± 0.1	0.5 ± 0.2	0.5 ± 0.2
tZq	20.0 ± 4.0	22.0 ± 4.0	12.1 ± 2.9	13.7 ± 2.4	90.0 ± 22.0	103.0 ± 17.0
tWZ	37.0 ± 8.0	37.0 ± 8.0	16.0 ± 4.0	16.0 ± 4.0	22.7 ± 3.0	22.8 ± 3.0
$t\bar{t}t\bar{t}$	1.6 ± 0.1	1.6 ± 0.1	0.1 ± 0.1	0.1 ± 0.1	0.3 ± 0.2	0.3 ± 0.2
Other	1.2 ± 0.7	1.2 ± 0.6	1.3 ± 0.9	1.3 ± 0.6	0.4 ± 0.3	0.3 ± 0.2
F-e-HF	5.0 ± 1.1	4.4 ± 1.1	4.2 ± 1.0	3.8 ± 0.9	13.0 ± 2.7	11.6 ± 2.6
F-e-Other	6.3 ± 1.4	7.8 ± 2.9	6.0 ± 1.6	7.4 ± 2.7	12.2 ± 2.7	15.0 ± 6.0
F-μ-HF	6.7 ± 0.8	6.8 ± 0.9	5.0 ± 1.4	5.1 ± 0.7	17.5 ± 2.0	17.7 ± 2.3
F-Other	2.4 ± 1.3	2.5 ± 1.2	2.3 ± 1.3	2.4 ± 1.2	3.8 ± 2.0	3.9 ± 1.9
Total	560 ± 28	572 ± 22	171 ± 17	176 ± 13	363 ± 28	381 ± 15
Data	-	560	-	171	-	363

result of the product of the signal strength, $\mu_{t\bar{t}Z}$, and the sum of all signal MC cross-sections are then multiplied by this fraction to obtain the measured cross-section value to be quoted.

The smoothing, symmetrisation and pruning procedures are applied as explained in Section 7.2, i.e. all systematic uncertainties are symmetrised as alternative studies of a fit setup with unsymmetrised systematic uncertainties yielded a negligible difference in uncertainties, but strongly asymmetric rankings of some of the uncertainties. Detailed summaries on the pruning of the NPs in the three signal regions of the analysis can be found in Figures B.1 to B.3 in the appendix for all signal regions.

A profile likelihood fit is performed using the likelihood presented in Equation 7.1 in Section 7.2. The impact of the NPs on the Asimov fit result is evaluated by investigating their constraints and relative importance.

Figure 9.1 shows the fitted distributions in the three signal regions (*SR*-3ℓ-$t\bar{t}Z$, *SR*-3ℓ-tZq, *SR*-3ℓ-WZ) and the three fake-enriched control regions (*CR*-$t\bar{t}$-e, *CR*-$t\bar{t}$-μ, *CR*-*Z*-e). The blue uncertainty band denotes the combined statistical and systematic uncertainties post-fit. In the *SR*-3ℓ-$t\bar{t}Z$ and *SR*-3ℓ-tZq signal regions, the $t\bar{t}Z$ output of the multi-class classifier is fitted as it provides good background rejection power in these regions. In *SR*-3ℓ-WZ, the number of expected events is fitted. The impact of this region on $\mu_{t\bar{t}Z}$ is small due to the minor signal contribution.

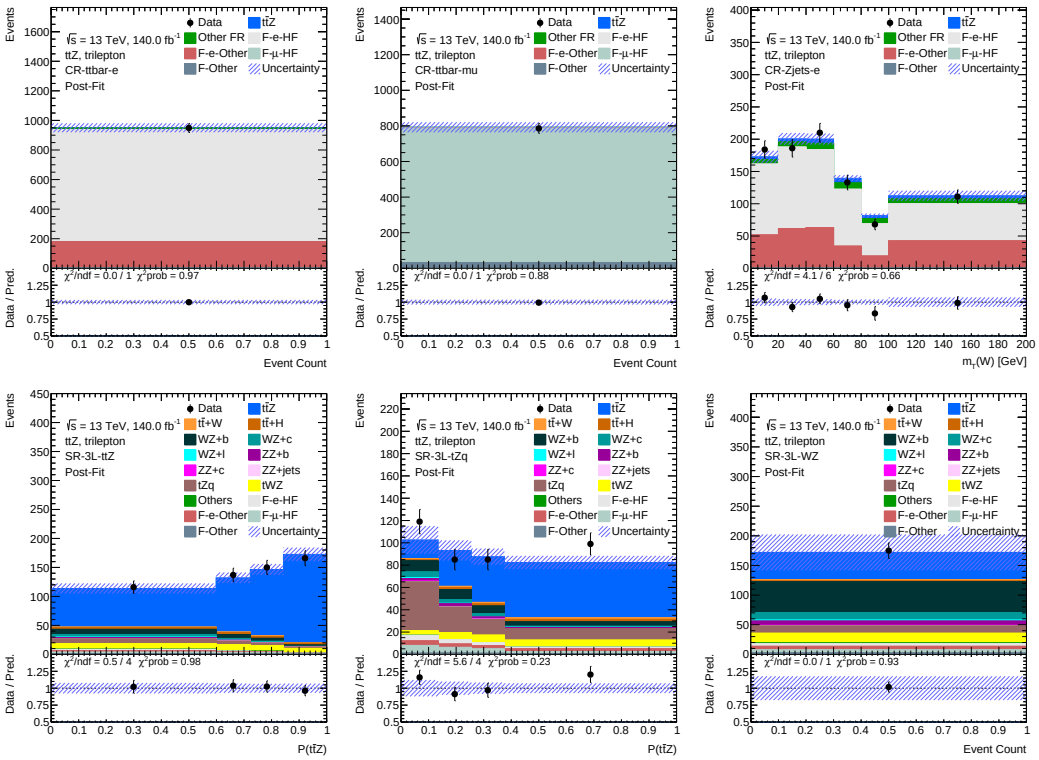

Figure 9.1: Distributions used in the fit to extract the inclusive cross-section. A fit is performed using the three signal regions (SR-3ℓ-$t\bar{t}Z$, SR-3ℓ-tZq, SR-3ℓ-WZ) and the three fake-enriched control regions (CR-$t\bar{t}$-e, CR-$t\bar{t}$-μ, CR-Z-e). The shaded error bands represent the combined statistical and systematic uncertainties. The shown observables, starting from the top left, are the event yield for CR-$t\bar{t}$-e and CR-$t\bar{t}$-μ, the reconstructed transverse mass of the W ($m_T(W)$) for CR-Z-e, $t\bar{t}Z$ probability ($P(t\bar{t}Z)$) for SR-3ℓ-$t\bar{t}Z$ and SR-3ℓ-tZq, and the *Event Count* for SR-3ℓ-WZ.

Nevertheless, it provides a handle on $\mathcal{N}_{WZb}$.

In addition, data is overlayed; however, it does not affect the Asimov fit presented here. Instead, the data shown are used to calculate the MC-data agreement using a χ^2 test. The χ^2 probabilities in the fake-enriched regions are 0.89 for CR-$t\bar{t}$-e, 1.00 for CR-$t\bar{t}$-μ, and 0.67 for CR-Z-e. The fit yields a post-fit χ^2 probability of 0.98 (SR-3ℓ-$t\bar{t}Z$), 0.32 (SR-3ℓ-tZq), and 0.97 (SR-3ℓ-WZ) in the three signal regions, indicating a good agreement between the expected and observed distributions in the signal regions but with some slight tension in SR-3ℓ-tZq.

Alternative fit configurations were also tested. In these configurations, the number of signal regions, free-floating parameters and input distributions were varied to study their impact on the measurement. The fit configuration discussed here represents the best fit configuration concerning the achieved precision on $\mu_{t\bar{t}Z}$ found in

Table 9.3: List of NPs constrained by $(\hat{\theta} - \theta_0)/\Delta\theta = \Delta\hat{\theta}/\Delta\theta < 0.95$ in the Asimov fit. The largest constraints are observed for the NP corresponding to the tZq cross-section uncertainty and the associated parton shower uncertainty.

Nuisance parameter	constraint $\Delta\hat{\theta}/\Delta\theta$ [%]
tZq parton shower	81.1
tZq cross-section	90.8
Jet JER effective NP 4	94.4
$t\bar{t}Z$ A14 variation	95.0

these studies.

The fit considers the WZ+b normalisation, $\mathcal{N}_{WZb}$, as an additional free parameter in this final configuration. After performing the profile likelihood fit, the following results are obtained:

$$\mu_{t\bar{t}Z} = 1.00 \pm 0.08 = 1.000 \pm 0.06(\text{stat.}) \pm 0.06(\text{syst.}),$$
$$\mathcal{N}_{WZb} = 1.00 \pm 0.42.$$

To put this result into perspective, an alternative fit scenario featuring a classical cut-and-count-based approach relying on jet and b-jet multiplicities for the definition of signal regions instead of neural-network-based cuts, documented in Chapter F, is tested, yielding:

$$\mu_{t\bar{t}Z}^{\text{cut and count}} = 1.00 \pm 0.11 = 1.00 \pm 0.06(\text{stat.}) \pm 0.09(\text{syst.}).$$

No WZ+b normalisation is extracted in this alternative scenario as no dedicated WZ+b signal region with comparable separation power can be easily constructed. Apart from this difference, the fit procedure equals the neural-network-based fit. Concerning this alternative scenario, the neural-network-based fitting strategy improves the precision of $\sim 18\,\%$, mainly originating from improved systematical uncertainty in the neural-network-based fitting strategy. Furthermore, the usage of the information on shapes of the individual fitted distributions contributes.

In the following, all NPs of the Asimov fit configuration that are pulled or constrained by $(\hat{\theta} - \theta_0)/\Delta\theta = \Delta\hat{\theta}/\Delta\theta < \theta_{\text{threshold}} = 0.95$ are further investigated. The threshold value, $\theta_{\text{threshold}}$, is arbitrarily chosen to include a reasonable number of NPs for study. All other NPs remain above this given threshold. Table 9.3 summarises the NP defined as *constrained* following the definition from above. Four NPs fulfil the above criteria: the $t\bar{t}Z$ A14 variation, the tZq cross-section, the tZq parton shower, and one jet energy resolution effective NP. All NPs are found to be insignificantly constrained and pulled by the fit.

As these results originate from a combination of the Asimov fit in the signal regions and the fit to ATLAS data in the fake-enriched regions, the NP constraints can be

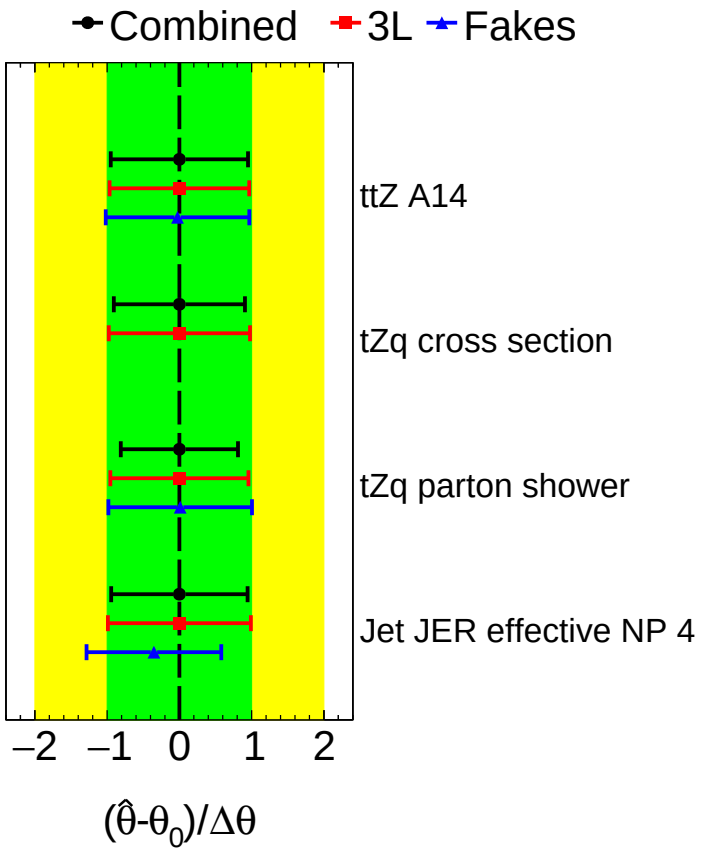

Figure 9.2: NPs that are pulled (constrained) in the Asimov fit by $(\hat{\theta} - \theta_0)/\Delta_\theta > 0.10$ (0.025). The different markers denote the three fits. The coloured bands indicate the 1σ and 2σ uncertainty bands.

split further into the constraints introduced by the individual fits. The results of the fits to the signal and control regions are presented separately in Figure 9.2, labelled as *3L* and *Fakes*, respectively. Blue triangle markers represent the fit to the control regions, while red square markers represent the signal regions. The combined fit is shown with black circles, and the coloured bands indicate the 1σ and 2σ uncertainty. The tZq normalisation NP is not displayed for the fit in the fake-enriched regions since the NP is pruned in this fit following a negligible impact on the extracted fake factors. It can be readily understood that any pulls mentioned above can only be introduced by combining the fit to ATLAS data in the fake-enriched control regions, as for all NPs in the signal region $\hat{\theta} = \theta_0$ holds by construction. The most extensive pull is observed for the JER-related NP. This pull can be comprehended by examining the fit of the fake-enriched control regions, where a high correlation arises from the independent fit of the three fake factors. As uncertainties related to JES and JER are NPs originating from the eigenvector decomposition of the complete set of uncer-

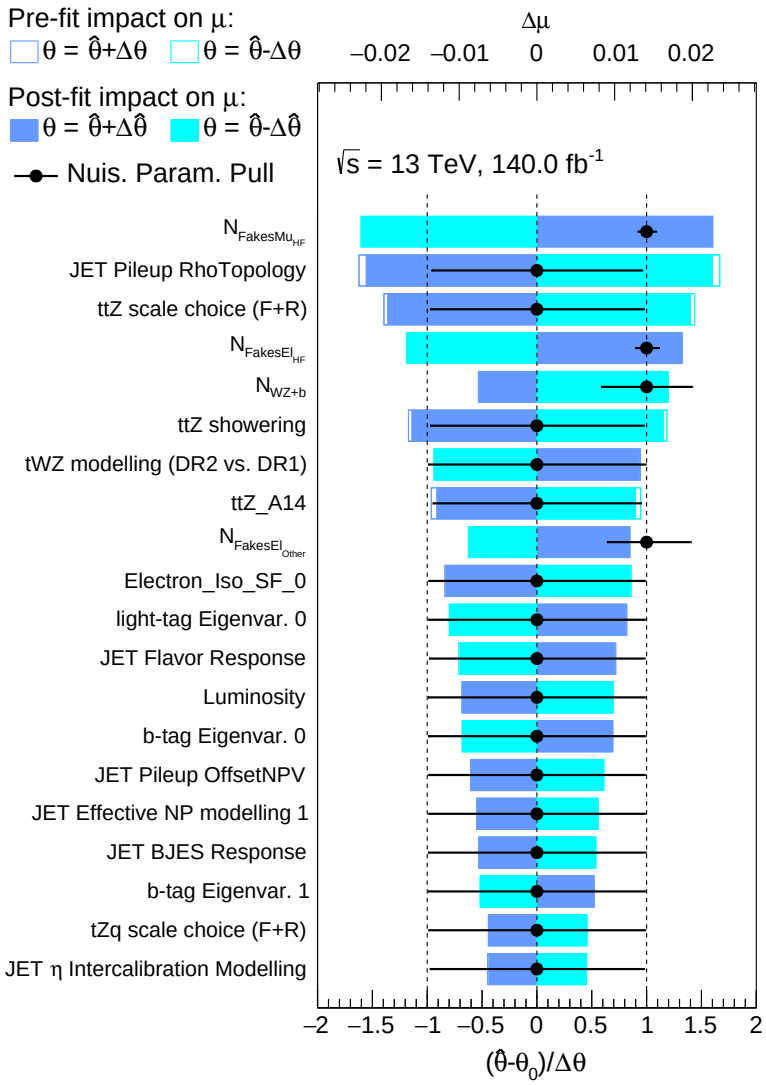

Figure 9.3: uncertainty ranking plot for Asimov fit in the trilepton channel. The uncertainties are ranked by their post-fit impact on $\mu_{t\bar{t}Z}$. The blue and turquoise-filled (unfilled) rectangles indicate the post-fit (pre-fit) uncertainty. NPs pulls are shown as black dots. The impact on the uncertainty on the POI is shown at the top x-axis.

tainties, the physics meaning of individual NPs is non-trivial. The small number of constrained and pulled NPs highlights a remarkably stable fit behaviour.

Figure 9.3 shows the 15 highest ranked NPs in the Asimov fit. Four independent fits are performed for each nuisance parameter where the NP is set to its pre-fit and post-fit value. In addition, this value is varied up and down by the pre-fit and post-fit uncertainty, respectively, yielding four different results for the signal strength,

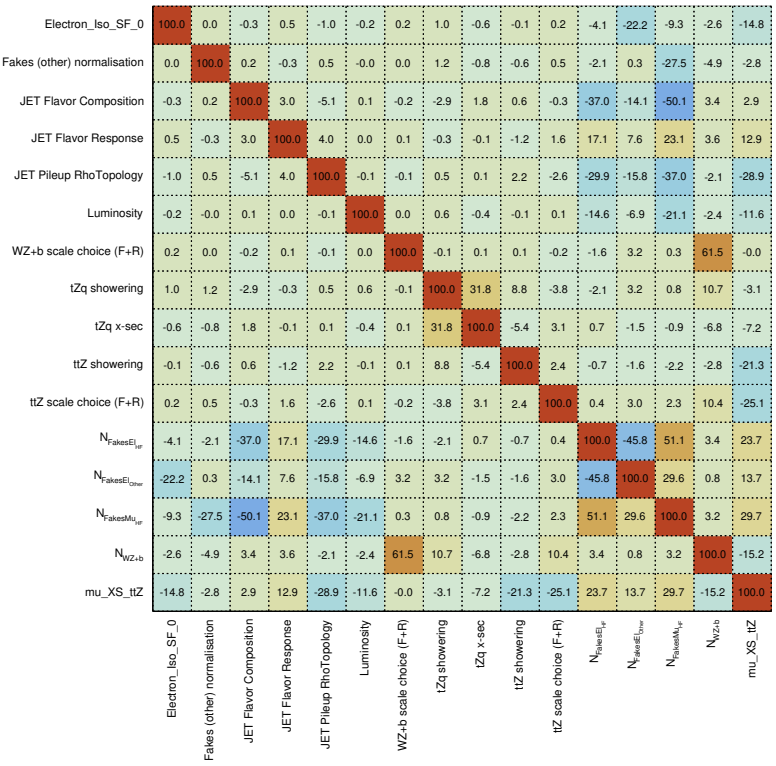

Figure 9.4: Correlation matrix for all NPs with an absolute correlation of $\geq 20\,\%$ with other NPs or with the signal strength, $\mu_{t\bar{t}Z}$.

$\mu_{t\bar{t}Z,i}$ $(i = 1, 2, 3, 4)$. The impact on $\mu_{t\bar{t}Z}$ is calculated as the difference between $\mu_{t\bar{t}Z,i}$ and the nominal signal strength, $\mu_{t\bar{t}Z}$. The highest-ranked systematic is the $\mathcal{N}_{\text{F-m-HF}}$ normalisation uncertainty which arises from a sizable correlation with the signal strength, $\mu_{t\bar{t}Z}$. The highest-ranked experimental uncertainty is the pileup ρ topology (previously highlighted Figure 8.1 in Chapter 8). This uncertainty is also (insignificantly) constrained by the fit. The high ranking of this uncertainty arises from its particularly large impact on the most sensitive bins of the fitted distribution with significant $t\bar{t}Z$ contributions, which was previously shown in Figure 8.1 in Chapter 8.

Other large uncertainties arise from the $t\bar{t}Z$ scale choice (previously discussed Figure 8.3 in Chapter 8), $\mathcal{N}_{e,\text{HF}}$, and $\mathcal{N}_{WZb}$. Similar to the pileup ρ topology, the $t\bar{t}Z$ scale choice significantly influences sensitive bins of the fitted distribution in SR-3ℓ-$t\bar{t}Z$. The impact of $\mathcal{N}_{e,\text{HF}}$ and $\mathcal{N}_{WZb}$ on $\mu_{t\bar{t}Z}$ arises from non-negligible correlations with $\mu_{t\bar{t}Z}$ shown in Figure 9.4.

Other significant correlations are also presented for all NPs with an absolute correlation of 20 % or higher with other NPs or with the signal strength, $\mu_{t\bar{t}Z}$.

Table 9.4: List of NPs constrained by $(\hat{\theta} - \theta_0)/\Delta\theta = \Delta\hat{\theta}/\Delta\theta < 0.95$ or pulled by $(\hat{\theta} - \theta_0) > 0.10$ in the fit to ATLAS data.

Nuisance parameter	constraint $\Delta\hat{\theta}/\Delta\theta$ [%]		
tZq parton shower	-0.42	0.81	0.81
tZq cross-section	0.34	0.89	0.89
Jet JER effective NP 4	-0.38	0.93	0.93

Observed results

The following section presents the fit results in the trilepton channel performed on ATLAS data. The data is selected using the same event selection as those applied on MC events, following the description in Chapter 4.

To assign neural network output scores to the data events, the k-folding procedure presented in Section 5.2 is again followed, i.e. the data events are split by their event numbers, and neural network output scores are determined using the corresponding neural network.

The fit setup is identical to that used for the Asimov fit. The following results are obtained:

$$\mu_{t\bar{t}Z} = 1.02 \pm 0.08 = 1.02 \pm 0.06(\text{stat.}) \pm 0.06(\text{syst.}),$$
$$\mathcal{N}_{WZb} = 1.03 \pm 0.43.$$

The fit constrains nuisance parameters, and the post-fit impact can be smaller than the pre-fit impact. Correlations between individual NPs and the signal strength are taken into account. Additionally, $(\hat{\theta} - \theta_0)$ can take non-zero values, i.e. differ from the nominal prior value. Table 9.4 lists all NPs that are either constrained by $(\hat{\theta} - \theta_0)/\Delta\theta = \Delta\hat{\theta}/\Delta\theta < 0.95$ or pulled by $(\hat{\theta} - \theta_0) > 0.10$ in the fit to ATLAS data. Small pulls are observed for the tZq parton shower NP (-0.42σ), tZq cross-section NP (-0.34σ) and the fourth effective JER NP (-0.382σ). The observed constraints are similar to those observed in the Asimov fit. A complete list of all pulls and constraints is given in Figure 9.5. In addition to the pulled NPs listed above, several jet-related NPs show small pulls. As already highlighted for the Asimov fit, these pulls originate from the fit to data in the fake-enriched control regions, which, due to their $t\bar{t}$ nature, are sensitive to JER and JES NPs such as the JER-related effective NPs from the eigenvalue decomposition and the JES-related specific nuisance parameter for the jet flavour composition and the η inter-calibration uncertainties.

Figure 9.6 shows the correlation matrix for all NPs with an absolute correlation of 20 % or higher with other NPs or the signal strength, $\mu_{t\bar{t}Z}$, in the fit to ATLAS data. The differences between the correlation matrix in the Asimov fit and the fit to data are negligible. Similarly, as for the Asimov fit, the fitted $\mathcal{N}_{\text{F-m-HF}}$ factor is correlated with the signal strength, $\mu_{t\bar{t}Z}$.

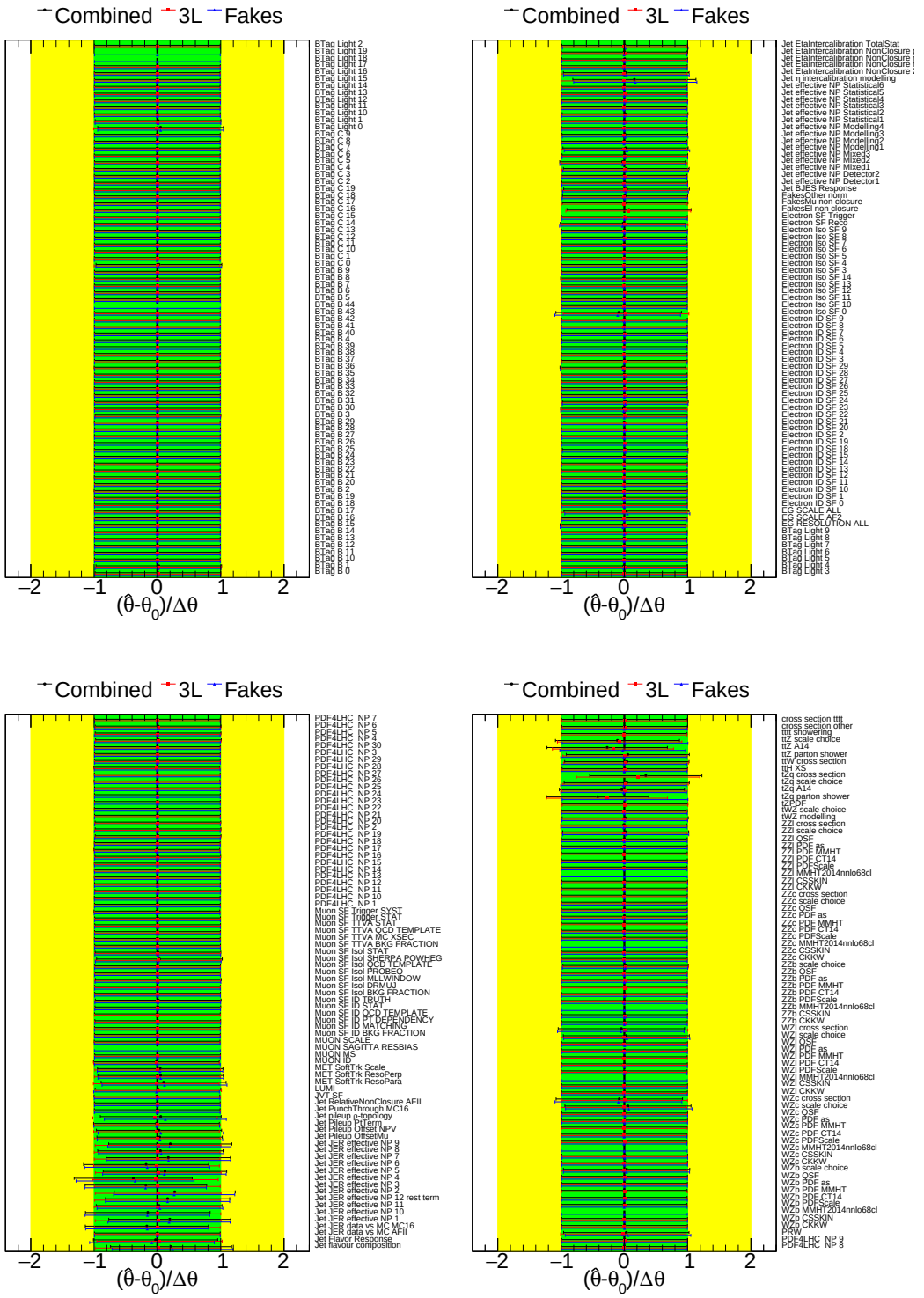

Figure 9.5: Complete list of NP pulls in the fit to ATLAS data. For readability, the plot is cut into four pieces. The post-fit estimates $\hat{\theta}$ are slightly shifted away from the central prior value θ. The shift is visualised as a fraction of $\Delta\theta$.

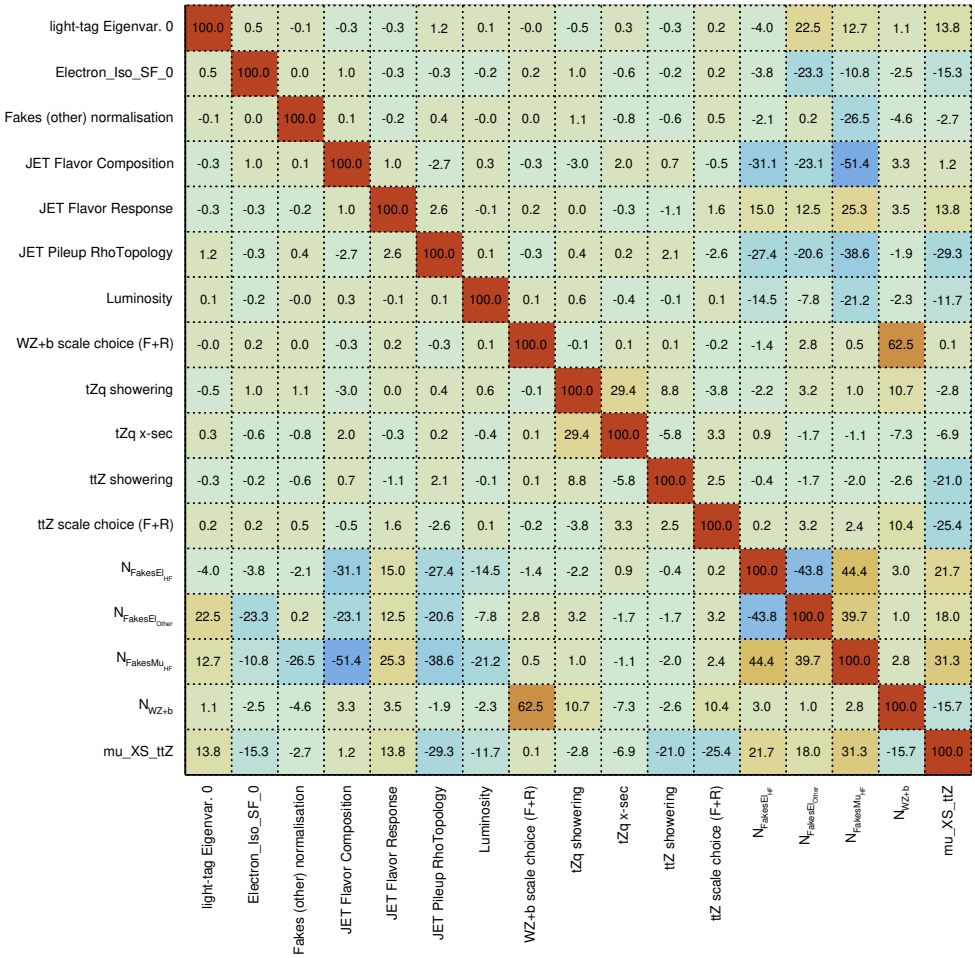

Figure 9.6: Correlation matrix for all NPs with an absolute correlation of $\geq 20\,\%$ with other NPs or the signal strength, $\mu_{t\bar{t}Z}$, in the fit to ATLAS data.

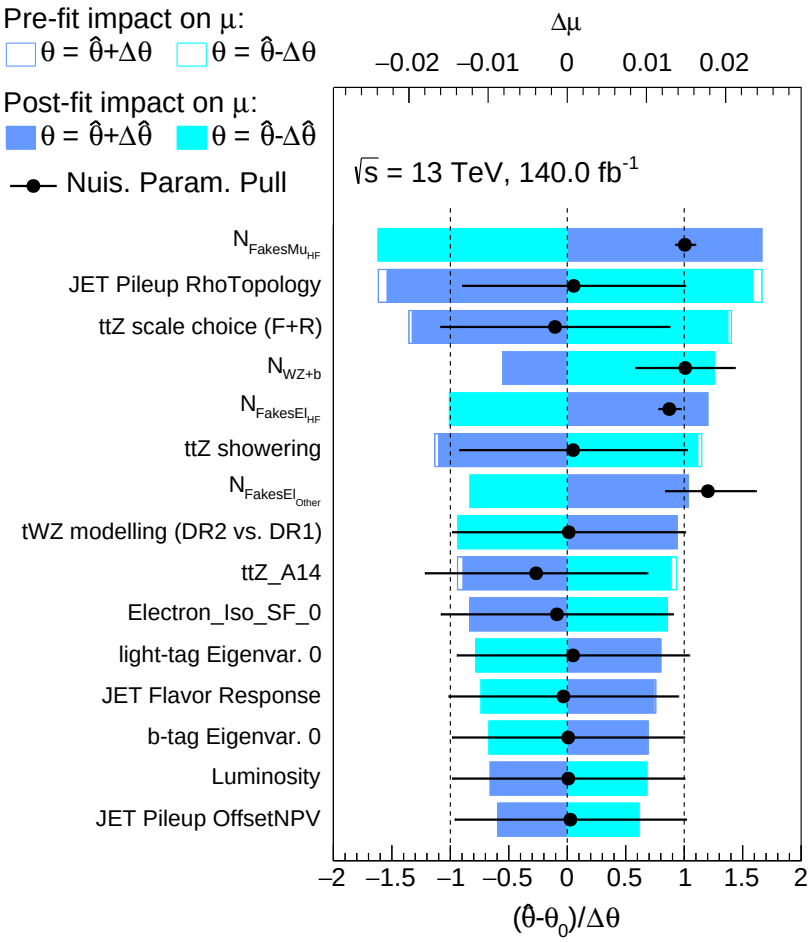

Figure 9.7: uncertainty ranking plot for the fit to ATLAS data in the trilepton channel. The uncertainties are ranked by their post-fit impact on the fit. The blue and turquoise-filled (unfilled) rectangles indicate the post-fit (pre-fit) uncertainty. NPs pulls are shown as black dots.

Figure 9.7 shows the 15 highest ranked NPs in the fit to ATLAS data. The highest-ranked uncertainty arises again from the $\mathcal{N}_{\text{F-m-HF}}$ factor and the pileup ρ topology, just like in the Asimov fit results presented above. Further substantial uncertainties are the scale choice for the $t\bar{t}Z$ signal sample, the $\mathcal{N}_{\text{F-e-HF}}$ factor, and the $\mathcal{N}_{WZb}$ factor. As the differences between the ranking obtained in the Asimov fit and the one resulting from the fit on ATLAS data are small, the same conclusions as presented above apply concerning the discussion of leading systematic uncertainties. A complementary overview of the effect of the systematic uncertainties on $\mu_{t\bar{t}Z}$ is given in Table 9.5 by grouping several NPs into easy-to-understand superordinate categories. To evaluate the impact of a group of systematic uncertainties, they are removed from the fit, leading to a reduced uncertainty on the signal strength, $\Delta'\mu_{t\bar{t}Z}$, with

Table 9.5: Grouped impact of systematic uncertainties in the trilepton inclusive fit to ATLAS data.

Category	Uncertainty
Background normalisations	3.1 %
Jets and MET	3.1 %
$t\bar{t}Z$ fact. and renorm. scale	2.0 %
b-tagging	1.8 %
$t\bar{t}Z$ Showering	1.7 %
Leptons	1.5 %
tWZ Modelling	1.4 %
$t\bar{t}Z$ A14	1.3 %
tZq Modelling	1.1 %
Luminosity	1.0 %
Other Backgrounds	0.7 %
MC stat.	0.6 %
PDF	0.6 %
Fakes	0.5 %
Diboson	0.4 %
Theory	0.4 %
Pile-up	0.2 %

respect to the nominal POI uncertainty, $\Delta\mu_{t\bar{t}Z}$. The impact is then defined through quadrature subtraction of the POI uncertainties, $\sqrt{\Delta\mu^2_{t\bar{t}Z} - \Delta\mu'^2_{t\bar{t}Z}}$. Due to correlations between groups of NPs, their quadrature sum will generally not add up to the total POI uncertainty. The largest impact of systematic uncertainties arises from background normalisations and uncertainties related to jet and $E_{\mathrm{T}}^{\mathrm{miss}}$ uncertainties.

Combination of the three analysis channels

The trilepton channel results can be compared with those obtained in the dilepton and tetralepton channels. As in the Trilepton channel to measure $\mu_{t\bar{t}Z}$, a profile-likelihood fit is performed in the Dilepton and tetralepton channels. In the Dilepton channel, three signal regions are defined based on the jet and b-jet multiplicity. The $t\bar{t}Z$ signal strength and the Z+b and Z+c normalisations are taken as free parameters in the fit. In the tetralepton channel, two signal regions are defined based on the flavour of the leptons not originating from the Z boson. The $t\bar{t}Z$ signal strength and the ZZ+b normalisation are free parameters in the fit. Further details on the used regions and fit strategies for these two analysis channels can be found in Ref. [1] and Dominik Babal's and Lucia Keszeghova's respective theses.

The result from the Trilepton channel is then combined with the results of these two analysis channels to determine the final inclusive cross-section measurement. A simultaneous fit of all three channels is performed to obtain this value, including all distributions used in the individual fits.

Eight signal distributions, three distributions in the fake-enriched control regions, and an additional tetraleptonic control region to determine the ZZ+b contribution are fitted. The combined fit has eight free parameters:

$\mathcal{N}_{WZb}$	WZ+b normalisation (Only in 3ℓ channel),
$\mathcal{N}_{Z+b}$	Z+b normalisation (Only in 2ℓ channel),
$\mathcal{N}_{Z+c}$	Z+c normalisation (Only in 2ℓ channel),
$\mathcal{N}_{ZZ+b}$	ZZ+b normalisation (Only in 4ℓ channel),
$\mathcal{N}_{e,\mathrm{HF}}$	F-e-HF normalisation,
$\mathcal{N}_{\mu,\mathrm{HF}}$	F-μ-HF normalisation,
$\mathcal{N}_{e,\mathrm{Other}}$	F-e-Other normalisation,
$\mu_{t\bar{t}Z}$	$t\bar{t}Z$ signal strength,

where the WZ+b normalisation and ZZ+b normalisation are applicable to the 3ℓ and 4ℓ channel, respectively. The Z+b and Z+c normalisation parameters are exclusive to the 2ℓ channel.

The stability of the combination is tested by performing a scan of the profiled likelihood in the individual channels and the combined fit using Asimov data. The likelihood is scanned for $\mu_{t\bar{t}Z} \in [0.5, 1.5]$ using an equidistant step size of 0.02, meaning that a set of 51 individual fits are performed with varying values of $\mu_{t\bar{t}Z}$. For each fit, the resulting log-likelihood value is compared to the log-likelihood value from the nominal fit. The difference is denoted with $\Delta \ln(L)$.

Figure 9.8 shows the calculated likelihood differences, $\Delta \ln(L)$, in the form of likelihood curves for the three individual fits in the three analysis channels and the combined fit. Additionally, a dotted red line indicates the 1σ uncertainty interval for the combined results, and a dashed black line indicates the central value of the theory prediction [141]. All three individual measurements agree with one another and the combined result within the 1σ uncertainty band. The impact of the three individual measurements on the combined result can be seen from the width of the likelihood parabolas, underlining the precision achieved with the trileptonic channel alone. The resulting likelihood curves are smooth in all individual and combined fits. No instabilities, such as local minima or other artefacts, are observed.

When fitted to ATLAS data, the following results are obtained in the individual channels:

$$\mu^{2\ell}_{t\bar{t}Z} = 1.02 \pm 0.13 = 1.02 \pm 0.07(\mathrm{stat.})^{+0.11}_{-0.10}(\mathrm{syst.}), \qquad (2\ell \text{ channel})$$
$$\mu^{3\ell}_{t\bar{t}Z} = 1.02 \pm 0.08 = 1.02 \pm 0.06(\mathrm{stat.}) \pm 0.06(\mathrm{syst.}), \qquad (3\ell \text{ channel})$$
$$\mu^{4\ell}_{t\bar{t}Z} = 1.17^{+0.15}_{-0.14} = 1.17^{+0.13}_{-0.13}(\mathrm{stat.})^{+0.07}_{-0.06}(\mathrm{syst.}), \qquad (4\ell \text{ channel})$$

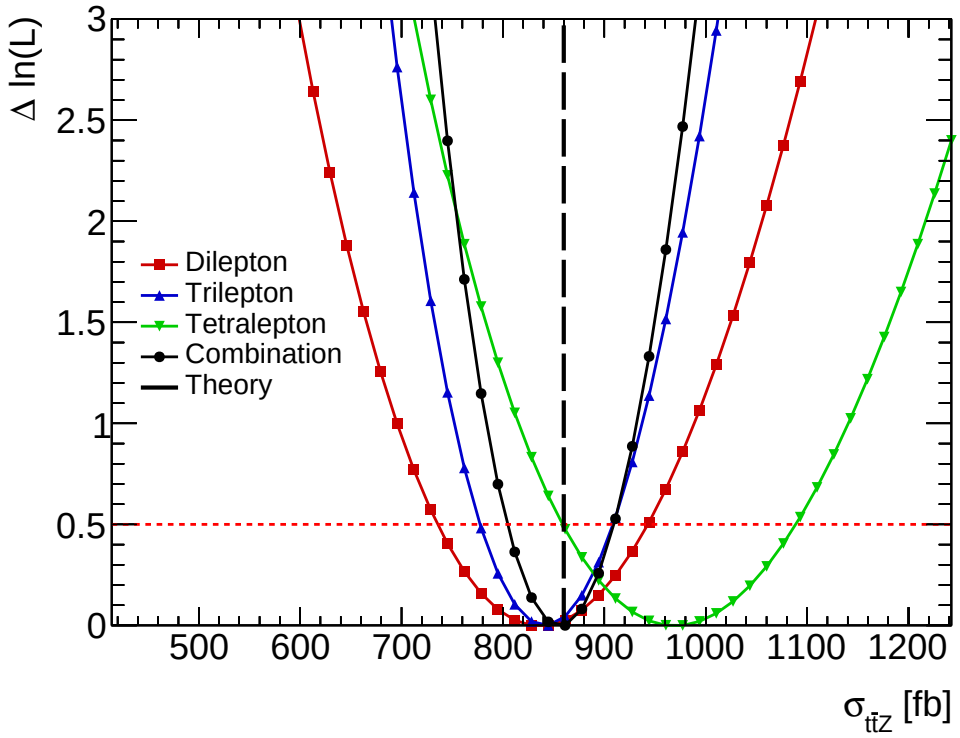

Figure 9.8: Likelihood scans from the fits to ATLAS data in the 2ℓ (red), 3ℓ (blue), and 4ℓ (green) channels and their combination (black). The 1σ uncertainty interval for the combined results is also indicated as the intersection between the individual lines and the horizontal dotted red line. A dashed black line indicates the central value of the theory prediction [141].

and in the combination yielding the quoted inclusive $t\bar{t}Z$ signal strength:

$$\mu_{t\bar{t}Z}^{\text{comb.}} = 1.04 \pm 0.07 = 1.04 \pm 0.05(\text{stat.}) \pm 0.05(\text{syst.}), \qquad \text{(combination)}$$

where the first and second uncertainty represents the statistical and systematic uncertainty, respectively. The statistical uncertainties are evaluated by performing a *stat-only* fit, where all NPs are set to their best-fit values. The systematic uncertainties are calculated as the quadratic difference between the statistical and total uncertainties. The measurement corresponds to an inclusive cross-section of[2]:

$$\sigma_{t\bar{t}Z}^{\text{comb.}} = 0.86 \pm 0.06\,\text{pb} = 0.86 \pm 0.04(\text{stat.}) \pm 0.04(\text{syst.})\,\text{pb}$$

The measurement in the 3ℓ channel alone corresponds to a total relative uncertainty of $^{+7.9\,\%}_{-7.9\,\%}$. The total relative uncertainty of the combination of the three

[2]Note here that this result takes the fraction of the parton-level events within the Z-mass window (94.5%) into account.

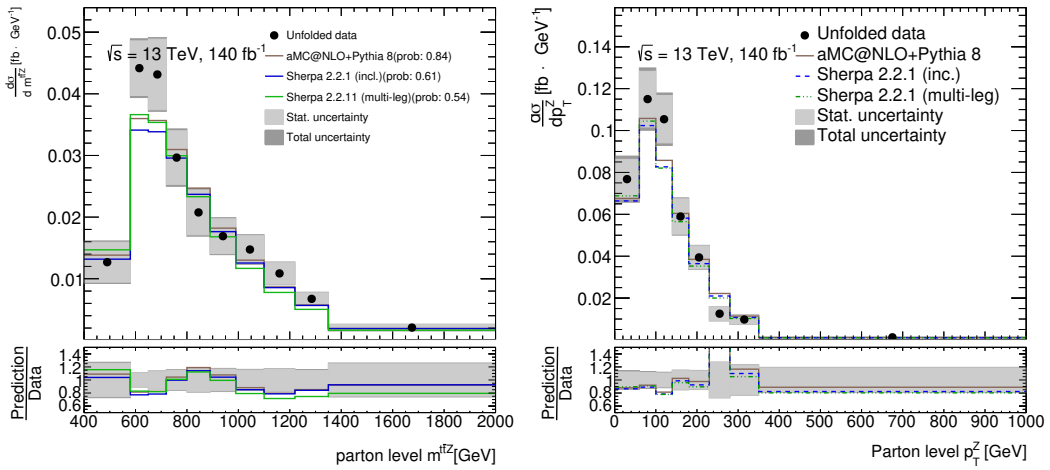

Figure 9.9: Differential cross-sections for $m_{t\bar{t}Z}$ (left) and p_{T}^{Z} (right) obtained by unfolding ATLAS data and compared to theoretical predictions. Grey bands represent statistical and total uncertainties, while coloured lines show theoretical predictions from different generators. Figure taken from Ref. [1].

analysis channels corresponds to a total relative uncertainty of $^{+6.2\,\%}_{-6.0\,\%}$. This result represents the most precise measurement of the $t\bar{t}Z$ production process to date.

9.2 Measurement of the differential $t\bar{t}Z$ cross-section

The following section briefly summarises the results of the differential cross-section measurements in Ref. [1]. Here two particular measurements performed with respect to two observables, namely $m_{t\bar{t}Z}$ and p_{T}^{Z}, are presented since the theory calculations discussed in Section 1.3 provide theoretical predictions for these distributions. Further unfolded ATLAS data is shown in Ref. [1]. The differential cross-sections are again measured following the procedure highlighted in Section 7.3, including the systematic uncertainties discussed in Chapter 8. Figure 9.9 shows the measured differential distributions unfolded to the parton level as a function of the invariant mass of the $t\bar{t}Z$ system, $m_{t\bar{t}Z}$, and the transverse momentum of the reconstructed Z boson, p_{T}^{Z}. The uncertainties are divided into statistical and total uncertainty, shown as grey uncertainty bands. Theoretical predictions following the prescription in Section 3.1 are shown as coloured lines. The observed distributions show small differences with these spectra. The agreement between the theoretical predictions and the observed data is calculated using a Pearson χ^2 test. The resulting probabilities are shown in the figure and together with the reduced χ^2 values in Table 9.6. While good agreement is observed between the unfolded ATLAS data and the NLO theory predictions for $m_{t\bar{t}Z}$, reflected by p-values of 0.54 (SHERPA 2.2.11), 0.61 (SHERPA 2.2.1) and 0.84 (MADGRAPH5_aMC@NLO+PYTHIA 8), minor tensions are observed

Table 9.6: Pearson χ^2 test results comparing theoretical predictions to observed differential distributions, shown as reduced χ^2 values and corresponding p-values. Results from Ref. [1].

	MadGraph5_aMC@NLO +Pythia 8		Sherpa 2.2.1 (incl.)		Sherpa 2.2.11 (multi-leg)	
Observable	χ^2/NDF	p-value	χ^2/NDF	p-value	χ^2/NDF	p-value
$m_{t\bar{t}Z}$	5.69/10	0.84	8.20/10	0.61	8.88/10	0.54
p_{T}^{Z}	13.48/8	0.10	12.5/8	0.13	10.80/8	0.21

Table 9.7: Pearson χ^2 test results comparing theoretical predictions to observed normalised differential distributions, shown as reduced χ^2 values and corresponding p-values. Results from Ref. [1].

	MadGraph5_aMC@NLO +Pythia 8		Sherpa 2.2.1 (incl.)		Sherpa 2.2.11 (multi-leg)	
Observable	χ^2/NDF	p-value	χ^2/NDF	p-value	χ^2/NDF	p-value
$m_{t\bar{t}Z}$	4.95/9	0.84	5.41/9	0.80	5.21/9	0.82
p_{T}^{Z}	14.33/7	0.07	12.85/7	0.12	10.72/7	0.22

in the p_{T}^{Z} distribution when comparing unfolded ATLAS data to the predictions. The unfolded ATLAS data and the predictions agree well for both observables and all considered theoretical predictions, reflected by p-values of 0.21 (Sherpa 2.2.11), 0.13 (Sherpa 2.2.1) and 0.10 (MadGraph5_aMC@NLO+Pythia 8).

Furthermore, normalised differential distributions where the total cross-section is used to normalise each bin of the two distributions are shown in Figure 9.10. Again the distributions of the invariant mass of the $t\bar{t}Z$ system and the transverse momentum of the reconstructed Z boson are shown. The agreement between the theoretical predictions and the normalised spectra is summarised in Table 9.7 using a χ^2 test. In general, slightly smaller p-values are observed compared to those for the absolute spectra. Qualitative comparisons between the observed spectra and the theory calculations presented in Figure 1.6 can be drawn. Tensions between the data and the predictions by the investigated generators mainly manifest in the bulk of the spectra. In the regions sensitive to differences between the NLO and the NLO+NNLL calculations, that is at high values of $m_{t\bar{t}Z}$ and p_{T}^{Z} no significant deviations between the observation and the predictions of the generators is found, indicating a good agreement of the NLO+NNLL calculations in these extreme phase spaces. However, it should be noted here that the theoretical calculations extend beyond the $m_{t\bar{t}Z}$ range probed here.

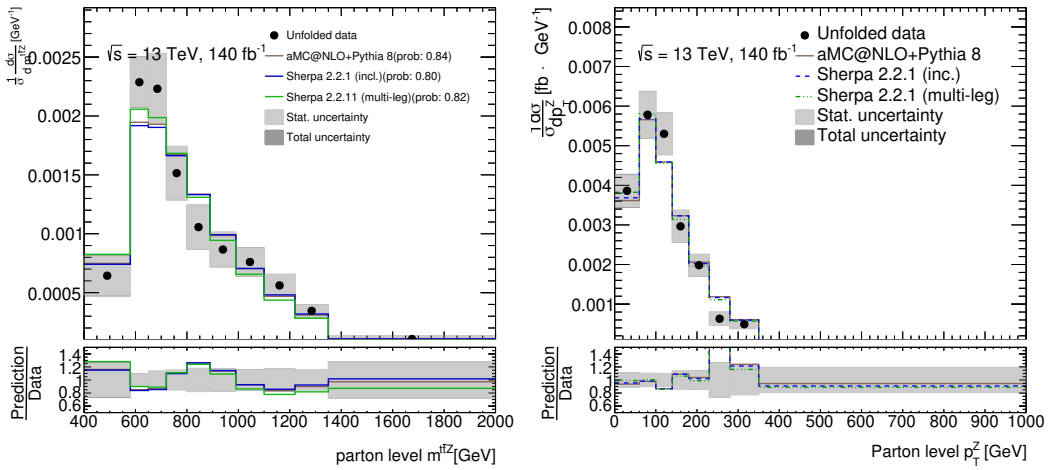

Figure 9.10: Differential cross-sections for $m_{t\bar{t}Z}$ (left) and p_{T}^{Z} (right) obtained by unfolding ATLAS data and compared to theoretical predictions. Each bin of the two distributions is normalised by the total cross-section. Grey bands represent statistical and total uncertainties, while coloured lines show theoretical predictions from different generators. Figure taken from Ref. [1].

9.3 Interpretation in the SMEFT framework

Extracting limits on Wilson coefficients follows the procedure highlighted in Section 7.4. Based on the measured fiducial cross-section and the normalised differential cross-sections presented in the previous sections, various EFT fits are performed. The resulting constraints for the relevant top-boson operators are presented here to provide complementary information to the abovementioned measurements further. Constraints on all top-boson operators are summarised in Table 9.8. Further constraints on four-quark-related operators can be found in Ref. [1].

In all cases, the tightest constraints are achieved in fits, where all Wilson coefficients, except the one considered, are set to zero. In these cases constraints of the order $C/\Lambda^2 \leq \mathcal{O}(0.2)\,\mathrm{TeV}^{-2}$ are achieved at 95 % confidence limit.

In the quadratic fits competitive limits of the order $C/\Lambda^2 \leq \mathcal{O}(0.5) - \mathcal{O}(1)\,\mathrm{TeV}^{-2}$ are achieved at 95 % confidence limit. These fits provide a complete picture of operators at dimension six. Here and in the linearised global fit, some global modes are insignificantly shifted from zero. This observation originates from the correlations arising between different operators as not all of them represent directions in EFT space which can be individually probed through the set of measurements presented above. For operators with negligible SM-EFT interference effects (e.g. for $\mathcal{C}_{tG}$, $\mathcal{C}_{tW}$ and $\mathcal{C}_{tB}$) no results are quoted here.

Introducing theory uncertainties due to missing dimension-8 EFT effects on the linear fit shows a degradation of the results presented above, which is most visible for the real part of $\mathcal{C}_{tW}$ and $\mathcal{C}_{tB}$. Competitive constraints are achieved for $\mathcal{C}_{tZ}$,

i.e. the linear combination of $\mathcal{C}_{tW}$ and $\mathcal{C}_{tB}$. For a more detailed interpretation and comparison of the measurement, see Ref. [1]

Table 9.8: Summary of observed and expected 68% and 95% credible intervals for the studied top-boson operators. The results obtained from the four fit scenarios are shown for each operator. The best-fit values (global mode) are shown in the last column for each operator and fit scenario. The results are taken from [1].

Wilson coefficient		68% CI (exp.)	95% CI (exp.)	68% CI (obs.)	95% CI (obs.)	Best-fit
$C_{HQ}^{(1)}$	$\mathcal{O}(\Lambda^{-2})$ (marg.)	$[-5.1, 5.4]$	$[-8.9, 8.7]$	$[-9.0, -1.7]$	$[-10, 2.3]$	-8.
	$\mathcal{O}(\Lambda^{-2})$ (marg, σ_{d8})	$[-6.0, 6.0]$	$[-9.3, 9.3]$	$[-9.9, -2.6]$	$[-10, 2.4]$	-1.e+01
	$\mathcal{O}(\Lambda^{-4})$ (marg.)	$[-1.2, 1.8]$	$[-3.1, 4.7]$	$[-1.5, 1.7]$	$[-6.0, 3.5]$	-0.4
	$\mathcal{O}(\Lambda^{-4})$ (indp.)	$[-0.58, 0.56]$	$[-1.1, 1.1]$	$[-0.86, 0.26]$	$[-1.4, 0.84]$	-0.3
$C_{HQ}^{(3)}$	$\mathcal{O}(\Lambda^{-2})$ (marg.)	$[-4.7, 4.7]$	$[-8.5, 8.4]$	$[-0.90, 7.1]$	$[-3.5, 9.9]$	0.5
	$\mathcal{O}(\Lambda^{-2})$ (marg, σ_{d8})	$[-5.4, 5.6]$	$[-9.1, 9.0]$	$[-0.80, 7.9]$	$[-3.8, 9.9]$	-2.
	$\mathcal{O}(\Lambda^{-4})$ (marg.)	$[-1.1, 2.6]$	$[-2.8, 4.4]$	$[1.9, 5.7]$	$[-5.6e-17, 7.7]$	4.
	$\mathcal{O}(\Lambda^{-4})$ (indp.)	$[-0.85, 0.75]$	$[-1.6, 1.4]$	$[-0.15, 1.3]$	$[-0.95, 2.0]$	0.7
C_{Ht}	$\mathcal{O}(\Lambda^{-2})$ (marg.)	$[-4.3, 4.2]$	$[-7.9, 8.1]$	$[-10, -5.2]$	$[-10, -0.80]$	-1.e+01
	$\mathcal{O}(\Lambda^{-2})$ (marg, σ_{d8})	$[-4.8, 4.8]$	$[-8.6, 8.5]$	$[-10, -6.0]$	$[-10, -1.4]$	-1.e+01
	$\mathcal{O}(\Lambda^{-4})$ (marg.)	$[-4.0, 0.90]$	$[-6.1, 3.5]$	$[-9.5, -6.0]$	$[-10, -4.0]$	-9.
	$\mathcal{O}(\Lambda^{-4})$ (indp.)	$[-1.0, 0.95]$	$[-2.0, 1.7]$	$[-1.2, 0.95]$	$[-2.2, 1.6]$	-0.06
$\Im[C_{tB}]$	$\mathcal{O}(\Lambda^{-2})$ (marg.)	—	—	—	—	—
	$\mathcal{O}(\Lambda^{-2})$ (marg, σ_{d8})	—	—	—	—	—
	$\mathcal{O}(\Lambda^{-4})$ (marg.)	$[-0.84, 1.0]$	$[-1.6, 1.7]$	$[-0.80, 1.0]$	$[-2.0, 2.0]$	-0.9
	$\mathcal{O}(\Lambda^{-4})$ (indp.)	$[-1.0, 1.0]$	$[-1.6, 1.6]$	$[-1.4, 1.5]$	$[-1.9, 1.9]$	1.
$\Re[C_{tB}]$	$\mathcal{O}(\Lambda^{-2})$ (marg.)	$[-6.7, 6.7]$	$[-9.3, 9.7]$	$[-6.2, 6.5]$	$[-9.5, 9.3]$	1.
	$\mathcal{O}(\Lambda^{-2})$ (marg, σ_{d8})	$[-9.9, 8.0]$	$[-10, 9.8]$	$[-8.8, 8.8]$	$[-10, 9.9]$	1.e+01
	$\mathcal{O}(\Lambda^{-4})$ (marg.)	$[-1.3, 0.90]$	$[-2.3, 2.0]$	$[-1.7, 0.90]$	$[-2.5, 2.3]$	0.7
	$\mathcal{O}(\Lambda^{-4})$ (indp.)	$[-1.0, 0.92]$	$[-1.6, 1.6]$	$[-1.3, 0.82]$	$[-1.7, 1.6]$	-0.8
$\Im[C_{tG}]$	$\mathcal{O}(\Lambda^{-2})$ (marg.)	—	—	—	—	—
	$\mathcal{O}(\Lambda^{-2})$ (marg, σ_{d8})	—	—	—	—	—
	$\mathcal{O}(\Lambda^{-4})$ (marg.)	$[-0.19, 0.17]$	$[-0.32, 0.32]$	$[-0.16, 0.16]$	$[-0.30, 0.31]$	-0.01
	$\mathcal{O}(\Lambda^{-4})$ (indp.)	$[-0.22, 0.22]$	$[-0.36, 0.36]$	$[-0.19, 0.18]$	$[-0.32, 0.33]$	-0.
$\Re[C_{tG}]$	$\mathcal{O}(\Lambda^{-2})$ (marg.)	$[-0.70, 0.70]$	$[-1.4, 1.3]$	$[0.25, 1.6]$	$[-0.35, 2.2]$	1.
	$\mathcal{O}(\Lambda^{-2})$ (marg, σ_{d8})	$[-0.75, 0.75]$	$[-1.4, 1.5]$	$[0.20, 1.7]$	$[-0.50, 2.4]$	1.
	$\mathcal{O}(\Lambda^{-4})$ (marg.)	$[-0.11, 0.23]$	$[-0.27, 0.38]$	$[-0.015, 0.32]$	$[-0.18, 0.43]$	0.2
	$\mathcal{O}(\Lambda^{-4})$ (indp.)	$[-0.14, 0.21]$	$[-0.26, 0.36]$	$[-0.11, 0.20]$	$[-0.23, 0.34]$	0.03
$\Im[C_{tW}]$	$\mathcal{O}(\Lambda^{-2})$ (marg.)	—	—	—	—	—
	$\mathcal{O}(\Lambda^{-2})$ (marg, σ_{d8})	—	—	—	—	—
	$\mathcal{O}(\Lambda^{-4})$ (marg.)	$[-0.56, 0.56]$	$[-1.1, 1.1]$	$[-0.48, 0.62]$	$[-0.98, 1.2]$	0.5
	$\mathcal{O}(\Lambda^{-4})$ (indp.)	$[-0.56, 0.56]$	$[-0.92, 0.92]$	$[-0.72, 0.74]$	$[-1.0, 1.0]$	0.5
$\Re[C_{tW}]$	$\mathcal{O}(\Lambda^{-2})$ (marg.)	$[-5.8, 5.9]$	$[-9.4, 9.7]$	$[-3.0, 8.1]$	$[-8.0, 9.9]$	2.
	$\mathcal{O}(\Lambda^{-2})$ (marg, σ_{d8})	$[-7.0, 6.8]$	$[-9.9, 9.7]$	$[-1.7, 9.9]$	$[-8.4, 9.9]$	9.
	$\mathcal{O}(\Lambda^{-4})$ (marg.)	$[-0.72, 0.60]$	$[-1.3, 1.3]$	$[-0.82, 0.66]$	$[-1.3, 1.5]$	0.4
	$\mathcal{O}(\Lambda^{-4})$ (indp.)	$[-0.52, 0.60]$	$[-0.88, 0.92]$	$[-0.38, 0.80]$	$[-0.84, 1.0]$	0.5

CHAPTER 10

Summary and conclusions

The neutral current electroweak coupling between the top quark and the Z boson can be probed through studies of the $t\bar{t}Z$ production process, where a Z boson is radiated from one of two top quarks in the final state. In the case of deviations from the SM hypothesis in the form of an alternative coupling structure and strength, deviations would arise in the $t\bar{t}Z$ production cross-section and differential distributions, indicating the presence of physics beyond the SM. Model-independent constraints on new physics can be established through interpretations within the SM effective field theory.

This thesis presents results of a $t\bar{t}Z$ cross-section measurement based on $140\,\text{fb}^{-1}$ of proton-proton collision data taken by the ATLAS experiment between 2015 and 2018 during the Run 2 of the LHC at a centre-of-mass energy of 13 TeV. Its focus lies in measuring the inclusive cross-section in the Trilepton channel. Events with precisely three leptons (electrons or muons), one opposite sign, same flavour lepton pair, and at least three jets are selected, of which one must be b-tagged.

Three signal regions are defined using the output of a three-class multi-class neural network, separating the $t\bar{t}Z$ signal events and the background processes, especially diboson and tZq events. The rate of fake lepton events is estimated through a fake-factor method using dedicated control regions.

In the trilepton channel, ATLAS data are compared to predictions using the $t\bar{t}Z$ probability distributions of the multi-class classifier in two signal regions enriched in $t\bar{t}Z$ and tZq, respectively. The event yields are used in the third signal region enriched in WZ+b events. The signal strength, $\mu_{t\bar{t}Z}$, of the $t\bar{t}Z$ production process is extracted following a profile-likelihood approach by a simultaneous fit of three signal-enriched regions and three fake-enriched control regions.

The complete analysis consists of similar measurements performed in three analysis channels: the dilepton opposite sign, trilepton, and tetralepton channel. The

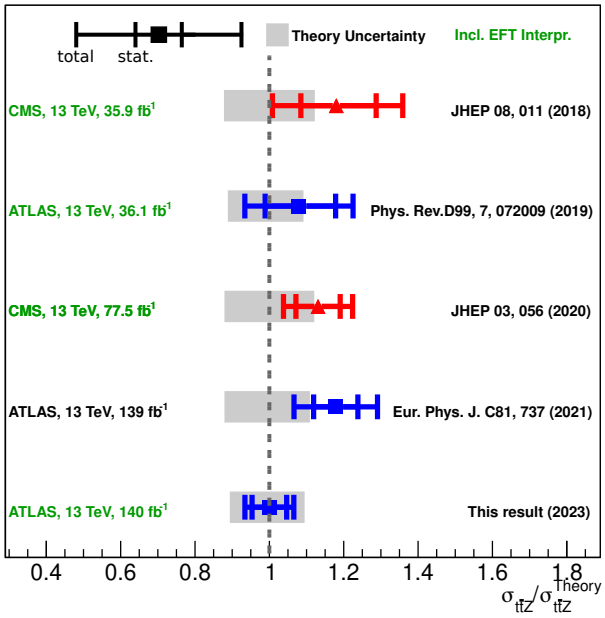

Figure 10.1: Measurements of the $t\bar{t}Z$ production at the LHC [147, 148, 159–163] including the measurement presented in this thesis and all reference cross-sections [141, 142, 145, 164–166], presented as the ratio of the measured cross-section with respect to the theory predictions. Different markers indicate the collaborations. Measurements with a corresponding EFT interpretation are marked in green.

,

determined inclusive $t\bar{t}Z$ cross-section, $\sigma_{t\bar{t}Z}$, corresponds to the production of a top quark pair in association with an on-shell Z for dilepton masses, $m_{\ell\ell} \in (70, 110)\,\text{GeV}$. The cross-section is measured to be $\sigma_{t\bar{t}Z} = 0.86 \pm 0.06\,\text{pb}$, in agreement with the SM prediction $\sigma_{t\bar{t}Z}^{\text{NLO+NNLL}} = 0.86^{+0.08}_{-0.09}\,\text{pb}$ [141] and other calculations performed at NLO QCD and electroweak accuracy [142, 164, 165]. Results are limited by systematic uncertainties associated with $t\bar{t}Z$ MC scale choices and background-process modelling. The total uncertainty of the combined result on the $t\bar{t}Z$ cross-section is improved by $\sim 50\,\%$ compared to the previous $t\bar{t}Z$ measurement performed by ATLAS [147] and by $\sim 15\,\%$ compared to the most recent $t\bar{t}Z$ measurement performed by CMS [148][1]. Figure 10.1 depicts a summary of measurements performed by the ATLAS and CMS collaborations and contextualises the result presented in this thesis. The inclusive cross-section measurement in the trilepton channel alone provides a result with a relative uncertainty of $\sim 7.9\,\%$ providing a more precise result than the previous ATLAS measurement and a competitive result compared to the most recent CMS measurement. The improvement of these results originates mainly from the

[1]Performed with at partial Run 2 dataset corresponding to $77\,\text{fb}^{-1}$.

introduction of potent machine learning approaches, which significantly enhance the separation between signal and background processes. Combining all three analysis channels surpasses both measurements for precision and represents the most precise measurement of the $t\bar{t}Z$ production process to date.

Measurements of differential cross-sections are presented and compared to state-of-the-art MC calculations. All distributions agree well with the SM prediction.

Based on the inclusive and differential measurements, an interpretation within the SM effective field theory is performed. Several fitting scenarios are considered to provide a complete picture of possible EFT effects in $t\bar{t}Z$ production. An extensive set of operators affecting the top-Z coupling, $t\bar{t}$ production, and new four-quark interactions is considered in these fits. This interpretation constrains potential BSM effects such as neutral current electroweak coupling variations in the form of constraints on the Wilson coefficients corresponding to variations of the top-Z-coupling structure and strength. In the absence of significant deviations from the SM prediction, competitive exclusion limits are computed for several top-electroweak SMEFT operators. From a SMEFT perspective, the top-Z coupling continues to stand the test of time, showing no significant indications for physics beyond the SM.

The measurement of the $t\bar{t}Z$ process presented here portrays a remarkable improvement from the previous measurement performed with the same dataset. In the presently ongoing Run 3 of the LHC, the centre-of-mass-energy increases to 13.6 TeV, marginally raising the $t\bar{t}Z$ production cross-section. Following the current long-term schedule of the LHC, an indicative integrated luminosity target of $250\,\text{fb}^{-1}$ after four planned years of data-taking is set, exceeding the currently available dataset by $\sim 80\,\%$. Using this dataset, an improvement of the statistical uncertainty of $\sim 25\,\%$ can be expected compared to the measurement based on the Run 2 dataset. However, as the measurement is dominated by systematic uncertainties, which can typically be only improved on longer time scales, it is unlikely that measurements of the $t\bar{t}Z$ process will provide further significant improvements in the immediate future. Improvements can only be expected through the reduction of systematic uncertainties and a more extensive dataset which are reasonable to expect by the end of Run 3 in 2025. A more extensive dataset will also provide a further reach of the differential cross-section measurements into regions of phase space with larger Z boson transverse momenta, p_{T}^{Z}. Due to the current limitations of the available datasets, this measurement will stand for some time as the $t\bar{t}Z$ inclusive cross-section benchmark measurement.

Over the past decade, machine learning approaches have become increasingly prevalent in ATLAS analyses, and the experience gained can be applied to future studies during the remainder of Run 3 and beyond it. Novel algorithms with improved performance have been developed for tasks such as jet clustering and particle tagging [206,259,273], and the reconstruction and unfolding of entire events [274,275], some of which are already in use today. These algorithms, in combination with the new possibilities described earlier, will enable even more precise measurements of the $t\bar{t}Z$ production process in the near future.

Moreover, yet unexplored Z boson decay modes like $t\bar{t}(Z \to \tau^+\tau^-)$ and $t\bar{t}(Z \to$

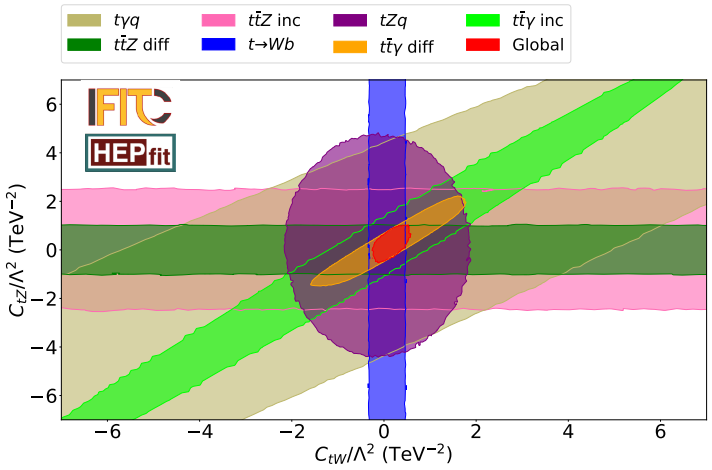

Figure 10.2: Example of two-dimensional bounds on $\mathcal{C}_{tZ}$ and $\mathcal{C}_{tW}$ originating from fits taking the most constraining measurements into account. A clear orthogonality between different analyses can be seen. The figure is taken from Ref. [278].

$\nu\bar{\nu}$) offer opportunities to expand knowledge of the $t\bar{t}Z$ process and search for physics beyond the SM, but pose challenges due to difficulties in reconstructing hadronically decaying τ leptons and neutrinos in the ATLAS detector. Reconstruction of the $t\bar{t}Z$ system will require sophisticated techniques due to the significant amount of missing transverse momentum introduced by both $Z \to \tau^+\tau^-$ and $Z \to \nu\bar{\nu}$ decay modes, necessitating improved identification and reconstruction algorithms such as novel τ reconstruction techniques [276, 277].

The $t\bar{t}Z$ production cross-section measurement outside the on-shell *mass window* of $m_{\ell\ell} \notin (70, 110)$, GeV, referred to as the *off-shell* $t\bar{t}Z$ production cross-section, remains to be probed by ATLAS and CMS. The off-shell phase space region is well suited to probe EFT effects further because events with high Z boson masses are susceptible to possible deviations of the top-Z electroweak coupling from its SM prediction. To achieve a good Z reconstruction and separation from dominant backgrounds like $t\bar{t}W$ and events with non-prompt leptons, reconstruction of the Z boson and powerful separation algorithms are required for studying these challenging final states. Performing an in-depth probe of the entire electroweak sector and the electroweak symmetry-breaking process requires a complete $t\bar{t}X$-based approach, including considering top-Z couplings and other top-boson couplings from processes like $t\bar{t}\gamma$. Recent measurements at the LHC provide a recipe for future global combinations of $t\bar{t}X$ processes in global fits, as shown in Figure 10.2, highlighting the potential for better constraints with a more complete $t\bar{t}X$ picture. Improved measurements of the $t\bar{t}\gamma$ production in conjunction with the results presented in this thesis will contribute to better constraints in the near future.

Bibliography

[1] ATLAS Collaboration, *Inclusive and differential cross-section measurements of $t\bar{t}Z$ production in pp collisions at $\sqrt{s} = 13$ TeV with the ATLAS detector, including EFT and spin-correlation interpretations*, `arXiv:2312.04450 [hep-ex]`, submitted to JHEP.

[2] J. J. Thomson, *Cathode rays*, Lond. Edinb. Dublin philos. mag. **44** (1897) 293–316.

[3] J. J. Thomson, *On the structure of the atom: an investigation of the stability and periods of oscillation of a number of corpuscles arranged at equal intervals around the circumference of a circle; with application of the results to the theory of atomic structure*, Lond. Edinb. Dublin philos. mag. **7** (1904) 237–265.

[4] E. Rutherford, *The scattering of α and β particles by matter and the structure of the atom*, Lond. Edinb. Dublin philos. mag. **21** (1911) 669–688.

[5] Geiger, H. and Marsden, E., *On a Diffuse Reflection of the α -Particles*, Proc. R. Soc. Lond. A **82** (1909) 495–500.

[6] Dr. H. Geiger and E. Marsden , *The laws of deflexion of α particles through large angles*, Lond. Edinb. Dublin philos. mag. **25** (1913) 604–623.

[7] E. Rutherford, *Collision of α particles with light atoms I. Hydrogen*, Lond. Edinb. Dublin philos. mag. **37** (1919) 537–561.

[8] E. Rutherford, *Collision of α particles with light atoms II. Velocity of the hydrogen atom*, Lond. Edinb. Dublin philos. mag. **37** (1919) 562–571.

[9] E. Rutherford, *Collision of α particles with light atoms III. Nitrogen and oxygen atoms*, Lond. Edinb. Dublin philos. mag. **37** (1919) 571–580.

[10] E. Rutherford, *Collision of α particles with light atoms. IV. An anomalous effect in nitrogen*, Lond. Edinb. Dublin philos. mag. **37** (1919) 581–587.

[11] J. Chadwick, *Possible Existence of a Neutron*, Nature **129** (1932) 312.

[12] C. D. Anderson, *The Positive Electron*, Phys. Rev. **43** (1933) 491–494.

[13] C. M. G. Lattes, G. P. S. Occhialini, and C. F. Powell, *Observations on the Tracks of Slow Mesons in Photographic Emulsions. 1*, Nature **160** (1947) 453–456.

[14] C. M. G. Lattes, G. P. S. Occhialini, and C. F. Powell, *Observations on the Tracks of Slow Mesons in Photographic Emulsions. 2*, Nature **160** (1947) 486–492.

[15] J. C. Street and E. C. Stevenson, *New Evidence for the Existence of a Particle of Mass Intermediate Between the Proton and Electron*, Phys. Rev. **52** (1937) 1003–1004.

[16] P. A. M. Dirac, *The quantum theory of the electron*, Proc. R. Soc. Lond. A **117** (1928) 610–624.

[17] Y. Ne'eman, *Derivation of strong interactions from a gauge invariance*, Nucl. Phys. **26** (1961) 222–229.

[18] M. Gell-Mann, *Symmetries of baryons and mesons*, Phys. Rev. **125** (1962) 1067–1084.

[19] M. Gell-Mann, *A Schematic Model of Baryons and Mesons*, Phys. Lett. **8** (1964) 214–215.

[20] V. E. e. a. Barnes, *Observation of a Hyperon with Strangeness Minus Three*, Phys. Rev. Lett. **12** (1964) 204–206.

[21] W. Albrecht, et al., *Inelastic electron proton scattering at high momentum transfers*, Phys. Lett. B **28** (1968) 225–228.

[22] E. D. Bloom et al., *High-Energy Inelastic e p Scattering at 6-Degrees and 10-Degrees*, Phys. Rev. Lett. **23** (1969) 930–934.

[23] M. Breidenbach, et al., *Observed behavior of highly inelastic electron-proton scattering*, Phys. Rev. Lett. **23** (1969) 935–939.

[24] DONUT Collaboration, *Observation of tau neutrino interactions*, Phys. Lett. B **504** (2001) 218–224.

[25] ATLAS Collaboration, *Observation of a new particle in the search for the Standard Model Higgs boson with the ATLAS detector at the LHC*, Phys. Lett. B **716** (2012) 1–29.

[26] CMS Collaboration, *Observation of a New Boson at a Mass of 125 GeV with the CMS Experiment at the LHC*, Phys. Lett. B **716** (2012) 30–61.

[27] S. L. Glashow, *Partial Symmetries of Weak Interactions*, Nucl. Phys. **22** (1961) 579–588.

[28] S. Weinberg, *A Model of Leptons*, Phys. Rev. Lett. **19** (1967) 1264–1266.

[29] A. Salam, *Weak and Electromagnetic Interactions*, Conf. Proc. C **680519** (1968) 367–377.

[30] S. L. Glashow, J. Iliopoulos, and L. Maiani, *Weak Interactions with Lepton-Hadron Symmetry*, Phys. Rev. D **2** (1970) 1285–1292.

[31] G. 't Hooft, *Renormalization of Massless Yang-Mills Fields*, Nucl. Phys. B **33** (1971) 173–199.

[32] G. 't Hooft, *Renormalizable Lagrangians for Massive Yang-Mills Fields*, Nucl. Phys. B **35** (1971) 167–188.

[33] G. 't Hooft and M. J. G. Veltman, *Regularization and Renormalization of Gauge Fields*, Nucl. Phys. B **44** (1972) 189–213.

[34] G. 't Hooft and M. J. G. Veltman, *Combinatorics of gauge fields*, Nucl. Phys. B **50** (1972) 318–353.

[35] H. Georgi and S. L. Glashow, *Unified weak and electromagnetic interactions without neutral currents*, Phys. Rev. Lett. **28** (1972) 1494.

[36] H. D. Politzer, *Reliable Perturbative Results for Strong Interactions?*, Phys. Rev. Lett. **30** (1973) 1346–1349.

[37] D. J. Gross and F. Wilczek, *Ultraviolet Behavior of Nonabelian Gauge Theories*, Phys. Rev. Lett. **30** (1973) 1343–1346.

[38] H. D. Politzer, *Asymptotic Freedom: An Approach to Strong Interactions*, Phys. Rept. **14** (1974) 129–180.

[39] P. W. Higgs, *Broken symmetries, massless particles and gauge fields*, Phys. Lett. **12** (1964) 132–133.

[40] F. Englert and R. Brout, *Broken Symmetry and the Mass of Gauge Vector Mesons*, Phys. Rev. Lett. **13** (1964) 321–323.

[41] Poincaré, Henri, *Sur la dynamique de l'électron*, Compt. Rend. Hebd. Seances Acad. Sci. **140** (1905) 1504–1508.

[42] Particle Data Group Collaboration, R. L. Workman and Others, *Review of Particle Physics*, PTEP **2022** (2022) 083C01.

[43] D. J. Gross and F. Wilczek, *Asymptotically Free Gauge Theories - I*, Phys. Rev. D **8** (1973) 3633–3652.

[44] D. J. Gross and F. Wilczek, *Asymptotically Free Gauge Theories - II.*, Phys. Rev. D **9** (1974) 980–993.

[45] H. Fritzsch, M. Gell-Mann, and H. Leutwyler, *Advantages of the Color Octet Gluon Picture*, Phys. Lett. B **47** (1973) 365–368.

[46] S. Weinberg, *Nonabelian Gauge Theories of the Strong Interactions*, Phys. Rev. Lett. **31** (1973) 494–497.

[47] BESIII Collaboration, *Observation of a Charged Charmoniumlike Structure in $e^+e^- \to \pi^+\pi^- J/\psi$ at $\sqrt{s}$ =4.26 GeV*, Phys. Rev. Lett. **110** (2013) 252001.

[48] Belle Collaboration, *Study of e^+e^-ßπ$^+\pi^- J/\psi$ and Observation of a Charged Charmoniumlike State at Belle*, Phys. Rev. Lett. **110** (2013) 252002, [Erratum: Phys.Rev.Lett. 111, 019901 (2013)].

[49] LHCb Collaboration, LHCb Collaboration, *Observation of the resonant character of the $Z(4430)^-$ state*, Phys. Rev. Lett. **112** (2014) 222002.

[50] LHCb Collaboration, *Observation of $J/\psi p$ Resonances Consistent with Pentaquark States in $\Lambda_b^0 \to J/\psi K^- p$ Decays*, Phys. Rev. Lett. **115** (2015) 072001.

[51] CDF Collaboration, *Measurement of the Strong Coupling Constant from Inclusive Jet Production at the Tevatron $\bar{p}p$ Collider*, Phys. Rev. Lett. **88** (2002) 042001.

[52] ZEUS Collaboration, *Multijet production in neutral current deep inelastic scattering at HERA and determination of alpha(s)*, Eur. Phys. J. C **44** (2005) 183–193.

[53] ZEUS Collaboration, *Jet-radius dependence of inclusive-jet cross-sections in deep inelastic scattering at HERA*, Phys. Lett. B **649** (2007) 12–24.

[54] DØ Collaboration, *Search for anomalous top quark couplings with the* DØ *detector*, Phys. Rev. Lett. **102** (2009) 092002.

[55] H1 Collaboration, *Measurement of multijet production in ep collisions at high Q^2 and determination of the strong coupling α_s*, Eur. Phys. J. C **75** (2015) 65.

[56] DØ Collaboration, *Determination of the strong coupling constant from the inclusive jet cross section in $p\bar{p}$ collisions at sqrt(s)=1.96 TeV*, Phys. Rev. D **80** (2009) 111107.

[57] B. Malaescu and P. Starovoitov, *Evaluation of the Strong Coupling Constant α_s Using the ATLAS Inclusive Jet Cross-Section Data*, Eur. Phys. J. C **72** (2012) 2041.

[58] DØ Collaboration, *Measurement of angular correlations of jets at $\sqrt{s} = 1.96$ TeV and determination of the strong coupling at high momentum transfers*, Phys. Lett. B **718** (2012) 56–63.

[59] CMS Collaboration, *Measurement of the Ratio of the Inclusive 3-Jet Cross Section to the Inclusive 2-Jet Cross Section in pp Collisions at $\sqrt{s} = 7$ TeV and First Determination of the Strong Coupling Constant in the TeV Range*, Eur. Phys. J. C **73** (2013) 2604.

[60] CMS Collaboration, *Measurement of the inclusive 3-jet production differential cross section in proton–proton collisions at 7 TeV and determination of the strong coupling constant in the TeV range*, Eur. Phys. J. C **75** (2015) 186.

[61] CMS Collaboration, *Constraints on parton distribution functions and extraction of the strong coupling constant from the inclusive jet cross section in pp collisions at $\sqrt{s} = 7$ TeV*, Eur. Phys. J. C **75** (2015) 288.

[62] ATLAS Collaboration, *Measurement of transverse energy-energy correlations in multi-jet events in pp collisions at $\sqrt{s} = 7$ TeV using the ATLAS detector and determination of the strong coupling constant $\alpha_s(m_Z)$*, Phys. Lett. B **750** (2015) 427–447.

[63] H1 Collaboration, *Measurement of Jet Production Cross Sections in Deep-inelastic ep Scattering at HERA*, Eur. Phys. J. C **77** (2017) 215, [Erratum: Eur.Phys.J.C 81, 739 (2021)].

[64] CMS Collaboration, *Measurement and QCD analysis of double-differential inclusive jet cross sections in pp collisions at $\sqrt{s} = 8$ TeV and cross section ratios to 2.76 and 7 TeV*, JHEP **03** (2017) 156.

[65] CMS Collaboration, *Measurement of the triple-differential dijet cross section in proton-proton collisions at $\sqrt{s} = 8$ TeV and constraints on parton distribution functions*, Eur. Phys. J. C **77** (2017) 746.

[66] ATLAS Collaboration, *Determination of the strong coupling constant α_s from transverse energy–energy correlations in multijet events at $\sqrt{s} = 8$ TeV using the ATLAS detector*, Eur. Phys. J. C **77** (2017) 872.

[67] D. Britzger, et al., *Determination of the strong coupling constant using inclusive jet cross section data from multiple experiments*, Eur. Phys. J. C **79** (2019) 68.

[68] V. N. Gribov and L. N. Lipatov, *Deep inelastic e p scattering in perturbation theory*, Sov. J. Nucl. Phys. **15** (1972) 438–450.

[69] G. Altarelli and G. Parisi, *Asymptotic Freedom in Parton Language*, Nucl. Phys. B **126** (1977) 298–318.

[70] Y. L. Dokshitzer, *Calculation of the Structure Functions for Deep Inelastic Scattering and e+ e- Annihilation by Perturbation Theory in Quantum Chromodynamics.*, Sov. Phys. JETP **46** (1977) 641–653.

[71] NNPDF Collaboration, R. D. Ball et al., *Parton distributions for the LHC Run II*, JHEP **04** (2015) 040.

[72] J. C. Collins, D. E. Soper, and G. F. Sterman, *Factorization of Hard Processes in QCD*, Adv. Ser. Direct. High Energy Phys. **5** (1989) 1–91.

[73] Feynman, R.P. and Zee, A., *QED: The Strange Theory of Light and Matter*. Alix G. Mautner memorial lectures. 2006.

[74] G. Gabrielse, et al., *New Determination of the Fine Structure Constant from the Electron g Value and QED*, Phys. Rev. Lett. **97** (2006) 030802, [Erratum: Phys.Rev.Lett. 99, 039902 (2007)].

[75] B. C. Odom, et al., *New Measurement of the Electron Magnetic Moment Using a One-Electron Quantum Cyclotron*, Phys. Rev. Lett. **97** (2006) 030801.

[76] M. Kobayashi and T. Maskawa, *CP Violation in the Renormalizable Theory of Weak Interaction*, Prog. Theor. Phys. **49** (1973) 652–657.

[77] N. Cabibbo, *Unitary Symmetry and Leptonic Decays*, Phys. Rev. Lett. **10** (1963) 531–533.

[78] C. S. Wu, et al., *Experimental Test of Parity Conservation in β Decay*, Phys. Rev. **105** (1957) 1413–1414.

[79] E. Corbelli and P. Salucci, *The Extended Rotation Curve and the Dark Matter Halo of M33*, Mon. Not. Roy. Astron. Soc. **311** (2000) 441–447.

[80] F. Zwicky, *Die Rotverschiebung von extragalaktischen Nebeln*, Helv. Phys. Acta **6** (1933) 110–127.

[81] F. Zwicky, *On the Masses of Nebulae and of Clusters of Nebulae*, Astrophys. J. **86** (1937) 217–246.

[82] Supernova Search Team Collaboration, A. G. Riess et al., *Observational evidence from supernovae for an accelerating universe and a cosmological constant*, Astron. J. **116** (1998) 1009–1038.

[83] Supernova Cosmology Project Collaboration, S. Perlmutter et al., *Measurements of Ω and Λ from 42 high redshift supernovae*, Astrophys. J. **517** (1999) 565–586.

[84] WMAP Collaboration, G. Hinshaw et al., *Nine-Year Wilkinson Microwave Anisotropy Probe (WMAP) Observations: Cosmological Parameter Results*, Astrophys. J. Suppl. **208** (2013) 19.

[85] Planck Collaboration, N. Aghanim et al., *Planck 2018 results. VI. Cosmological parameters*, Astron. Astrophys. **641** (2020) A6, [Erratum: Astron.Astrophys. 652, C4 (2021)].

[86] Super-Kamiokande Collaboration, Y. Fukuda et al., *Evidence for oscillation of atmospheric neutrinos*, Phys. Rev. Lett. **81** (1998) 1562–1567.

[87] H. P. Nilles, *Supersymmetry, Supergravity and Particle Physics*, Phys. Rept. **110** (1984) 1–162.

[88] J. H. Christenson, et al., *Evidence for the* 2π *Decay of the* K_2^0 *Meson*, Phys. Rev. Lett. **13** (1964) 138–140.

[89] M. L. Perl et al., *Evidence for Anomalous Lepton Production in e+ - e- Annihilation*, Phys. Rev. Lett. **35** (1975) 1489–1492.

[90] E288 Collaboration, *Observation of a Dimuon Resonance at 9.5-GeV in 400-GeV Proton-Nucleus Collisions*, Phys. Rev. Lett. **39** (1977) 252–255.

[91] H. Georgi and M. Machacek, *B Meson Decay and Partial Unification of Strong, Electromagnetic and Weak Interactions*, Phys. Rev. Lett. **43** (1979) 1639.

[92] H. Georgi and S. Glashow, *Making do without the t quark*, Nucl. Phys. B **167** (1980) 173–180.

[93] G. L. Kane and M. E. Peskin, *A Constraint from B Decay on Models with No T Quark*, Nucl. Phys. B **195** (1982) 29–38.

[94] CLEO Collaboration, P. Avery et al., *Upper Limit on Flavor Changing Neutral Current Decays of the b Quark*, Phys. Rev. Lett. **53** (1984) 1309–1313.

[95] CLEO Collaboration, A. Bean et al., *Improved Upper Limit on Flavor Changing Neutral Current Decays of the B Quark*, Phys. Rev. D **35** (1987) 3533.

[96] E. Ma and J. Okada, *How Many Neutrinos?*, Phys. Rev. Lett. **41** (1978) 287, [Erratum: Phys.Rev.Lett. 41, 1759 (1978)].

[97] G. Barbiellini, B. Richter, and J. Siegrist, *Radiative Z0 Production: A Method for Neutrino Counting in e+ e- Collisions*, Phys. Lett. B **106** (1981) 414–418.

[98] K. J. F. Gaemers, R. Gastmans, and F. M. Renard, *Neutrino Counting in e+ e- Collisions*, Phys. Rev. D **19** (1979) 1605.

[99] ALEPH Collaboration, *Determination of the Number of Light Neutrino Species*, Phys. Lett. B **231** (1989) 519–529.

[100] OPAL Collaboration, *A direct measurement of the Z^0 invisible width by single photon counting*, Z. Phys. C **50** (1991) 373–384.

[101] ALEPH Collaboration, ALEPH Collaboration, *A Direct measurement of the invisible width of the Z from single photon counting*, Phys. Lett. B **313** (1993) 520–534.

[102] CDF Collaboration, *Observation of top quark production in $\bar{p}p$ collisions*, Phys. Rev. Lett. **74** (1995) 2626–2631.

[103] DØ Collaboration, *Observation of the top quark*, Phys. Rev. Lett. **74** (1995) 2632–2637.

[104] M. Jeżabek and J. Kühn, *QCD corrections to semileptonic decays of heavy quarks*, Nucl. Phys. B **314** (1989) 1–6.

[105] CMS Collaboration, *Measurement of the Single-Top-Quark t-Channel Cross Section in pp Collisions at $\sqrt{s} = 7$ TeV*, JHEP **12** (2012) 035.

[106] CMS Collaboration, V. Khachatryan et al., *Measurement of the ratio $\mathcal{B}(t \to Wb)/\mathcal{B}(t \to Wq)$ in pp collisions at $\sqrt{s} = 8$ TeV*, Phys. Lett. B **736** (2014) 33–57.

[107] I. I. Y. Bigi, et al., *Production and Decay Properties of Ultraheavy Quarks*, Phys. Lett. B **181** (1986) 157–163.

[108] G. Degrassi, et al., *Higgs mass and vacuum stability in the Standard Model at NNLO*, JHEP **08** (2012) 098.

[109] T. Markkanen, A. Rajantie, and S. Stopyra, *Cosmological Aspects of Higgs Vacuum Metastability*, Front. Astron. Space Sci. **5** (2018) 40.

[110] D. Choudhury, T. M. P. Tait, and C. E. M. Wagner, *Beautiful mirrors and precision electroweak data*, Phys. Rev. D **65** (2002) 053002.

[111] D. Chang, W.-F. Chang, and E. Ma, *Alternative interpretation of the Tevatron top events*, Phys. Rev. D **59** (1999) 091503.

[112] CMS Collaboration, *Constraints on the Top-Quark Charge from Top-Pair Events*,.

[113] CDF Collaboration, *Exclusion of exotic top-like quarks with -4/3 electric charge using jet-charge tagging in single-lepton ttbar events at CDF*, Phys. Rev. D **88** (2013) 032003.

[114] ATLAS Collaboration, *Measurement of the top quark charge in pp collisions at $\sqrt{s} = 7$ TeV with the ATLAS detector*, JHEP **11** (2013) 031.

[115] DØ Collaboration, *Measurement of the Electric Charge of the Top Quark in $t\bar{t}$ Events*, Phys. Rev. D **90** (2014) 051101, [Erratum: Phys.Rev.D 90, 079904 (2014)].

[116] CDF and DØ Collaboration, *Combination of Measurements of the Top-Quark Pair Production Cross Section from the Tevatron Collider*, Phys. Rev. D **89** (2014) 072001.

[117] CDF Collaboration, T. Aaltonen et al., *Measurement of the top-quark pair production cross-section in events with two leptons and bottom-quark jets using the full CDF data set*, Phys. Rev. D **88** (2013) 091103.

[118] CDF Collaboration, *Study of Top-Quark Production and Decays involving a Tau Lepton at CDF and Limits on a Charged-Higgs Boson Contribution*, Phys. Rev. D **89** (2014) 091101.

[119] DØ Collaboration, *Measurement of the Inclusive $t\bar{t}$ Production Cross Section in $p\bar{p}$ Collisions at $\sqrt{s} = 1.96$ TeV and Determination of the Top Quark Pole Mass*, Phys. Rev. D **94** (2016) 092004.

[120] ATLAS and CMS Collaboration, *Combination of ATLAS and CMS top-quark pair cross section measurements using up to 1.1 fb^{-1} of data at 7 TeV*, `https://cds.cern.ch/record/1478422`, ATLAS-CONF-2012-134.

[121] ATLAS and CMS Collaboration, *Combination of ATLAS and CMS top quark pair cross section measurements in the $e\mu$ final state using proton-proton collisions at $\sqrt{s}$= 8 TeV*, `https://cds.cern.ch/record/1951322`, ATLAS-CONF-2014-054.

[122] ATLAS Collaboration, *Simultaneous measurements of the $t\bar{t}$, W^+W^-, and $Z/\gamma^* \to \tau\tau$ production cross-sections in pp collisions at $\sqrt{s} = 7$ TeV with the ATLAS detector*, Phys. Rev. D **91** (2015) 052005.

[123] ATLAS Collaboration, *Measurement of the $t\bar{t}$ production cross-section using $e\mu$ events with b-tagged jets in pp collisions at $\sqrt{s}$ = 7 and 8* TeV *with the ATLAS detector*, Eur. Phys. J. C **74** (2014) 3109, [Addendum: Eur.Phys.J.C 76, 642 (2016)].

[124] CMS Collaboration, *Measurement of the t-tbar production cross section in the e-mu channel in proton-proton collisions at sqrt(s) = 7 and 8 TeV*, JHEP **08** (2016) 029.

[125] CMS Collaboration, *Measurement of the* $\mathrm{t\bar{t}}$ *production cross section, the top quark mass, and the strong coupling constant using dilepton events in pp collisions at $\sqrt{s} = 13$ TeV*, Eur. Phys. J. C **79** (2019) 368.

[126] CMS Collaboration, *Measurement of the top quark pair production cross section in dilepton final states containing one τ lepton in pp collisions at $\sqrt{s} = 13$ TeV*, JHEP **02** (2020) 191.

[127] ATLAS Collaboration, *Measurement of the $t\bar{t}$ production cross-section and lepton differential distributions in $e\mu$ dilepton events from pp collisions at $\sqrt{s} = 13$ TeV with the ATLAS detector*, Eur. Phys. J. C **80** (2020) 528.

[128] ATLAS Collaboration, *Measurement of the $t\bar{t}$ production cross-section in the lepton+jets channel at $\sqrt{s} = 13$ TeV with the ATLAS experiment*, Phys. Lett. B **810** (2020) 135797.

[129] ATLAS Collaboration, *Measurements of top-quark pair single- and double-differential cross-sections in the all-hadronic channel in pp collisions at $\sqrt{s} = 13$ TeV using the ATLAS detector*, JHEP **01** (2021) 033.

[130] CMS Collaboration, *Measurement of differential $t\bar{t}$ production cross sections in the full kinematic range using lepton+jets events from proton-proton collisions at $\sqrt{s} = 13$ TeV*, Phys. Rev. D **104** (2021) 092013.

[131] CMS Collaboration,, *Measurement of the inclusive $\mathrm{t\bar{t}}$ production cross section in pp collisions at $\sqrt{s} = 5.02$ TeV*, `https://cds.cern.ch/record/2758333`, CMS-PAS-TOP-20-004.

[132] ATLAS Collaboration, *Measurement of the $t\bar{t}$ production cross-section using dilepton events in pp collisions at $\sqrt{s} = 5.02$ TeV with the ATLAS detector*, `https://cds.cern.ch/record/2754223`, ATLAS-CONF-2021-003.

[133] CMS Collaboration, *First measurement of the top quark pair production cross section in proton-proton collisions at $\sqrt{s} = 13.6$ TeV*, JHEP **08** (2023) 204.

[134] M. Czakon, P. Fiedler, and A. Mitov, *Total Top-Quark Pair-Production Cross Section at Hadron Colliders Through $O(\alpha_S^4)$*, Phys. Rev. Lett. **110** (2013) 252004.

[135] S. Catani, et al., *Top-quark pair production at the LHC: Fully differential QCD predictions at NNLO*, JHEP **07** (2019) 100.

[136] M. Czakon and A. Mitov, *Top++: A Program for the Calculation of the Top-Pair Cross-Section at Hadron Colliders*, Comput. Phys. Commun. **185** (2014) 2930.

[137] ATLAS Collaboration, *Measurement of the $t\bar{t}$ cross section and its ratio to the Z production cross section using pp collisions at $\sqrt{s}$=13.6 TeV with the ATLAS detector*, Phys. Lett. B **848** (2024) 138376.

[138] ATLAS Collaboration, *LHC Top Working Group $t\bar{t}$ Cross-Section Summary*, `https://twiki.cern.ch/twiki/bin/view/LHCPhysics/LHCTopWGSummaryPlots`. Accessed on Oct. 30, 2022.

[139] A. Lazopoulos, K. Melnikov, and F. J. Petriello, *NLO QCD corrections to the production of $t\bar{t}Z$ in gluon fusion*, Phys. Rev. D **77** (2008) 034021.

[140] A. Lazopoulos, et al., *Next-to-leading order QCD corrections to $t\bar{t}Z$ production at the LHC*, Phys. Lett. B **666** (2008) 62–65.

[141] A. Kulesza, et al., *Associated production of a top quark pair with a heavy electroweak gauge boson at NLO+NNLL accuracy*, Eur. Phys. J. C **79** (2019) 249.

[142] A. Broggio, et al., *Top-quark pair hadroproduction in association with a heavy boson at NLO+NNLL including EW corrections*, JHEP **08** (2019) 039.

[143] A. Kulesza, et al., *Associated $t\bar{t}H$ production at the LHC: Theoretical predictions at NLO+NNLL accuracy*, Phys. Rev. D **97** (2018) 114007.

[144] A. Kardos, Z. Trocsanyi, and C. Papadopoulos, *Top quark pair production in association with a Z-boson at NLO accuracy*, Phys. Rev. D **85** (2012) 054015.

[145] M. V. Garzelli, et al., *$t\,\bar{t}\,W^{+-}$ and $t\,\bar{t}\,Z$ Hadroproduction at NLO accuracy in QCD with Parton Shower and Hadronization effects*, JHEP **11** (2012) 056.

[146] M. V. Garzelli, et al., *Z0 - boson production in association with a top anti-top pair at NLO accuracy with parton shower effects*, Phys. Rev. D **85** (2012) 074022.

[147] ATLAS Collaboration, *Measurements of the inclusive and differential production cross sections of a top-quark–antiquark pair in association with a Z boson at $\sqrt{s} = 13$ TeV with the ATLAS detector*, Eur. Phys. J. C **81** (2021) 737.

[148] CMS Collaboration, *Measurement of top quark pair production in association with a Z boson in proton-proton collisions at $\sqrt{s} = 13$ TeV*, JHEP **03** (2020) 056.

[149] A. Broggio, et al., *Associated production of a top pair and a Higgs boson beyond NLO*, JHEP **03** (2016) 124.

[150] A. Broggio, et al., *Associated production of a top pair and a W boson at next-to-next-to-leading logarithmic accuracy*, JHEP **09** (2016) 089.

[151] A. Broggio, et al., *NNLL resummation for the associated production of a top pair and a Higgs boson at the LHC*, JHEP **02** (2017) 126.

[152] A. Broggio, et al., *Pseudoscalar couplings in $t\bar{t}H$ production at NLO+NLL accuracy*, Phys. Rev. D **96** (2017) 073005.

[153] A. Manohar, et al., *How bright is the proton? A precise determination of the photon parton distribution function*, Phys. Rev. Lett. **117** (2016) 242002.

[154] A. V. Manohar, et al., *The Photon Content of the Proton*, JHEP **12** (2017) 046.

[155] R. Frederix, et al., *Four-lepton production at hadron colliders: aMC@NLO predictions with theoretical uncertainties*, JHEP **02** (2012) 099.

[156] W. Buchmuller and D. Wyler, *Effective Lagrangian Analysis of New Interactions and Flavor Conservation*, Nucl. Phys. B **268** (1986) 621–653.

[157] I. Brivio and M. Trott, *The Standard Model as an Effective Field Theory*, Phys. Rept. **793** (2019) 1–98.

[158] I. Brivio, *SMEFTsim 3.0 — a practical guide*, JHEP **04** (2021) 073.

[159] CMS Collaboration, *Measurement of associated production of vector bosons and top quark-antiquark pairs at sqrt(s) = 7 TeV*, Phys. Rev. Lett. **110** (2013) 172002.

[160] ATLAS Collaboration, *Measurement of the $t\bar{t}W$ and $t\bar{t}Z$ production cross sections in pp collisions at $\sqrt{s} = 8$ TeV with the ATLAS detector*, JHEP **11** (2015) 172.

[161] CMS Collaboration, *Observation of top quark pairs produced in association with a vector boson in pp collisions at $\sqrt{s} = 8$ TeV*, JHEP **01** (2016) 096.

[162] CMS Collaboration, *Measurement of the cross section for top quark pair production in association with a W or Z boson in proton-proton collisions at $\sqrt{s} = 13$ TeV*, JHEP **08** (2018) 011.

[163] ATLAS Collaboration, *Measurement of the $t\bar{t}Z$ and $t\bar{t}W$ cross sections in proton-proton collisions at $\sqrt{s} = 13$ TeV with the ATLAS detector*, Phys. Rev. D **99** (2019) 072009.

[164] S. Frixione, et al., *Electroweak and QCD corrections to top-pair hadroproduction in association with heavy bosons*, JHEP **06** (2015) 184.

[165] LHC Higgs Cross Section Working Group Collaboration, D. de Florian et al., *Handbook of LHC Higgs Cross Sections: 4. Deciphering the Nature of the Higgs Sector*, `arXiv:1610.07922 [hep-ph]`.

[166] R. Frederix, et al., *The automation of next-to-leading order electroweak calculations*, JHEP **07** (2018) 185, [Erratum: JHEP 11, 085 (2021)].

[167] B. Grzadkowski, et al., *Dimension-Six Terms in the Standard Model Lagrangian*, JHEP **10** (2010) 085.

[168] L. Evans and P. Bryant, *LHC Machine*, JINST **3** (2008) S08001.

[169] ATLAS Collaboration, *The ATLAS Experiment at the CERN Large Hadron Collider*, JINST **3** (2008) S08003.

[170] CMS Collaboration, *The CMS Experiment at the CERN LHC*, JINST **3** (2008) S08004.

[171] ALICE Collaboration, *The ALICE experiment at the CERN LHC*, JINST **3** (2008) S08002.

[172] LHCb Collaboration, *The LHCb Detector at the LHC*, JINST **3** (2008) S08005.

[173] LEP Working Group for Higgs boson searches and ALEPH and DELPHI and L3 and OPAL Collaborations, *Search for the standard model Higgs boson at LEP*, Phys. Lett. B **565** (2003) 61.

[174] CDF and DØ Collaborations, *Updated Combination of CDF and* DØ *Searches for Standard Model Higgs Boson Production with up to 10.0 fb^{-1} of Data*, 7, 2012. `arXiv:1207.0449 [hep-ex]`. FERMILAB-CONF-12-318-E, CDF-NOTE-10884, D0-NOTE-6348.

[175] ATLAS Collaboration, *Luminosity Public Results Run 2*, `https://twiki.cern.ch/twiki/bin/view/AtlasPublic/LuminosityPublicResultsRun2`, Accessed on Oct. 18, 2022.

[176] ATLAS Collaboration, *ATLAS Inner Detector: Technical design report. Vol. 1*, `https://cds.cern.ch/record/331063`, CERN-LHCC-97-16, ATLAS-TDR-4.

[177] ATLAS Collaboration, *ATLAS Inner Detector: Technical design report. Vol. 2*, `https://cds.cern.ch/record/331064`, CERN-LHCC-97-17.

[178] ATLAS Collaboration, *ATLAS Central Solenoid: Technical design report*, `https://cds.cern.ch/record/331067`, CERN-LHCC-97-21.

[179] ATLAS Collaboration, *Technical Design Report for the ATLAS Inner Tracker Strip Detector*, `https://cds.cern.ch/record/2257755`, CERN-LHCC-2017-005, ATLAS-TDR-025.

[180] ATLAS Collaboration, *Technical Design Report for the ATLAS Inner Tracker Pixel Detector*, `https://cds.cern.ch/record/2285585`, CERN-LHCC-2017-021, ATLAS-TDR-030.

[181] A. Ahmad et al., *The Silicon microstrip sensors of the ATLAS semiconductor tracker*, Nucl. Instrum. Meth. A **578** (2007) 98.

[182] ATLAS Collaboration, *ATLAS liquid argon calorimeter: Technical design report*, `https://cds.cern.ch/record/331061`, CERN-LHCC-96-41.

[183] ATLAS Collaboration, *ATLAS tile calorimeter: Technical design report*, `https://cds.cern.ch/record/331062`, CERN-LHCC-96-42.

[184] ATLAS Collaboration, *ATLAS barrel toroid: Technical design report*, `https://cds.cern.ch/record/331065`, CERN-LHCC-97-19.

[185] ATLAS Collaboration, *ATLAS endcap toroids: Technical design report*, https://cds.cern.ch/record/331066, CERN-LHCC-97-20.

[186] ATLAS Collaboration, *Technical Design Report for the Phase-I Upgrade of the ATLAS TDAQ System*, https://cds.cern.ch/record/1602235, CERN-LHCC-2013-018, ATLAS-TDR-023.

[187] ATLAS Collaboration, *Performance of electron and photon triggers in ATLAS during LHC Run 2*, Eur. Phys. J. C **80** (2020) 47.

[188] ATLAS Collaboration, *Performance of the ATLAS muon triggers in Run 2*, JINST **15** (2020) P09015.

[189] G. Avoni et al., *The new LUCID-2 detector for luminosity measurement and monitoring in ATLAS*, JINST **13** (2018) P07017.

[190] ATLAS Collaboration, *Luminosity determination in pp collisions at* $\sqrt{s} = 13$ *TeV using the ATLAS detector at the LHC*, arXiv:2212.09379 [hep-ex].

[191] ATLAS Collaboration, *Topological cell clustering in the ATLAS calorimeters and its performance in LHC Run 1*, Eur. Phys. J. C **77** (2017) 490.

[192] T. G. Cornelissen, et al., *The global chi**2 track fitter in ATLAS*, J. Phys. Conf. Ser. **119** (2008) 032013.

[193] ATLAS Collaboration, *Improved electron reconstruction in ATLAS using the Gaussian Sum Filter-based model for bremsstrahlung*, https://cds.cern.ch/record/1449796, ATLAS-CONF-2012-047.

[194] W. Lampl, et al., *Calorimeter clustering algorithms: Description and performance*, https://cds.cern.ch/record/1099735, ATL-LARG-PUB-2008-002.

[195] ATLAS Collaboration, *Electron and photon energy calibration with the ATLAS detector using LHC Run 1 data*, Eur. Phys. J. C **74** (2014) 3071.

[196] ATLAS Collaboration, *Electron and photon energy calibration with the ATLAS detector using 2015–2016 LHC proton-proton collision data*, JINST **14** (2019) P03017.

[197] M. Cacciari, G. P. Salam, and G. Soyez, *The anti-*k_t *jet clustering algorithm*, JHEP **04** (2008) 063.

[198] M. Cacciari, G. P. Salam, and G. Soyez, *FastJet User Manual*, Eur. Phys. J. C **72** (2012) 1896.

[199] ATLAS Collaboration, *Jet reconstruction and performance using particle flow with the ATLAS Detector*, Eur. Phys. J. C **77** (2017) 466.

[200] ATLAS Collaboration, *Performance of algorithms that reconstruct missing transverse momentum in $\sqrt{s} = 8$ TeV proton-proton collisions in the ATLAS detector*, Eur. Phys. J. C **77** (2017) 241.

[201] M. Cacciari and G. P. Salam, *Pileup subtraction using jet areas*, Phys. Lett. B **659** (2008) 119–126.

[202] M. Cacciari, G. P. Salam, and G. Soyez, *The Catchment Area of Jets*, JHEP **04** (2008) 005.

[203] ATLAS Collaboration, *Jet energy measurement with the ATLAS detector in proton-proton collisions at $\sqrt{s} = 7$ TeV*, Eur. Phys. J. C **73** (2013) 2304.

[204] ATLAS Collaboration, *Jet energy scale measurements and their systematic uncertainties in proton-proton collisions at $\sqrt{s} = 13$ TeV with the ATLAS detector*, Phys. Rev. D **96** (2017) 072002.

[205] ATLAS Collaboration, *Tagging and suppression of pileup jets*, `https://cds.cern.ch/record/1700870`, ATLAS-CONF-2014-018.

[206] ATLAS Collaboration, *ATLAS b-jet identification performance and efficiency measurement with $t\bar{t}$ events in pp collisions at $\sqrt{s} = 13$ TeV*, Eur. Phys. J. C **79** (2019) 970.

[207] ATLAS Collaboration, *Performance of b-Jet Identification in the ATLAS Experiment*, JINST **11** (2016) P04008.

[208] ATLAS Collaboration, *Optimisation and performance studies of the ATLAS b-tagging algorithms for the 2017-18 LHC run*, `https://cds.cern.ch/record/2273281`, ATL-PHYS-PUB-2017-013.

[209] ATLAS Collaboration, *Performance of missing transverse momentum reconstruction with the ATLAS detector using proton-proton collisions at $\sqrt{s}$ = 13 TeV*, Eur. Phys. J. C **78** (2018) 903.

[210] ATLAS Collaboration, *The ATLAS Simulation Infrastructure*, Eur. Phys. J. C **70** (2010) 823–874.

[211] GEANT4 Collaboration, S. Agostinelli et al., *GEANT4–a simulation toolkit*, Nucl. Instrum. Meth. A **506** (2003) 250–303.

[212] T. Sjostrand, S. Mrenna, and P. Z. Skands, *PYTHIA 6.4 Physics and Manual*, JHEP **05** (2006) 026.

[213] T. Sjostrand, S. Mrenna, and P. Z. Skands, *A Brief Introduction to PYTHIA 8.1*, Comput. Phys. Commun. **178** (2008) 852–867.

[214] T. Sjöstrand, et al., *An introduction to PYTHIA 8.2*, Comput. Phys. Commun. **191** (2015) 159–177.

[215] J. Alwall, et al., *The automated computation of tree-level and next-to-leading order differential cross sections, and their matching to parton shower simulations*, JHEP **07** (2014) 079.

[216] ATLAS Collaboration, *Modelling of the $t\bar{t}H$ and $t\bar{t}V$ $(V = W, Z)$ processes for $\sqrt{s} = 13$ TeV ATLAS analyses*, `https://cds.cern.ch/record/2120826`, ATL-PHYS-PUB-2016-005.

[217] S. Frixione, et al., *Angular correlations of lepton pairs from vector boson and top quark decays in Monte Carlo simulations*, JHEP **04** (2007) 081.

[218] P. Artoisenet, et al., *Automatic spin-entangled decays of heavy resonances in Monte Carlo simulations*, JHEP **03** (2013) 015.

[219] R. D. Ball et al., *Parton distributions with LHC data*, Nucl. Phys. B **867** (2013) 244–289.

[220] ATLAS Collaboration, *ATLAS Pythia 8 tunes to 7 TeV data*, `https://cds.cern.ch/record/1966419`, ATL-PHYS-PUB-2014-021.

[221] D. J. Lange, *The EvtGen particle decay simulation package*, Nucl. Instrum. Meth. A **462** (2001) 152–155.

[222] M. Bahr et al., *Herwig++ Physics and Manual*, Eur. Phys. J. C **58** (2008) 639–707.

[223] J. Bellm et al., *Herwig 7.0/Herwig++ 3.0 release note*, Eur. Phys. J. C **76** (2016) 196.

[224] Sherpa Collaboration, E. Bothmann et al., *Event Generation with Sherpa 2.2*, SciPost Phys. **7** (2019) 034.

[225] S. Alioli, et al., *A general framework for implementing NLO calculations in shower Monte Carlo programs: the POWHEG BOX*, JHEP **06** (2010) 043.

[226] S. Catani, et al., *QCD matrix elements + parton showers*, JHEP **11** (2001) 063.

[227] S. Hoeche, et al., *QCD matrix elements and truncated showers*, JHEP **05** (2009) 053.

[228] S. Hoeche, et al., *A critical appraisal of NLO+PS matching methods*, JHEP **09** (2012) 049.

[229] S. Hoeche, et al., *QCD matrix elements + parton showers: The NLO case*, JHEP **04** (2013) 027.

[230] F. Cascioli, P. Maierhofer, and S. Pozzorini, *Scattering Amplitudes with Open Loops*, Phys. Rev. Lett. **108** (2012) 111601.

[231] A. Denner, S. Dittmaier, and L. Hofer, *Collier: a fortran-based Complex One-Loop LIbrary in Extended Regularizations*, Comput. Phys. Commun. **212** (2017) 220–238.

[232] ATLAS Collaboration, *ATLAS data quality operations and performance for 2015–2018 data-taking*, JINST **15** (2020) P04003.

[233] ATLAS Collaboration, *Selection of jets produced in 13TeV proton-proton collisions with the ATLAS detector*, `https://cds.cern.ch/record/2037702`, ATLAS-CONF-2015-029.

[234] A. M. Turing, *On Computable Numbers, with an Application to the Entscheidungsproblem*, Proceedings of the London Mathematical Society **2** (1936) 230–265.

[235] David Hilbert, *Mathematische Probleme*, Nachrichten von der Gesellschaft der Wissenschaften zu Göttingen, Mathematisch-Physikalische Klasse **1900** (1900) 253–297.

[236] W. Mcculloch and W. Pitts, *A Logical Calculus of Ideas Immanent in Nervous Activity*, Bulletin of Mathematical Biophysics **5** (1943) 127–147.

[237] F. Rosenblatt, *The perceptron - A perceiving and recognizing automaton*, Tech. Rep. 85-460-1, Cornell Aeronautical Laboratory, Ithaca, New York, January, 1957.

[238] Rosenblatt, F., *The perceptron: A probabilistic model for information storage and organization in the brain.*, Psychological Review **65** (1958) 386–408.

[239] D. E. Rumelhart, G. E. Hinton, and R. J. Williams, *Learning Internal Representations by Error Propagation*, pp. , 318–362. MIT Press, 1986.

[240] D. P. Kingma and J. Ba, *Adam: A Method for Stochastic Optimization*, 2014. `http://arxiv.org/abs/1412.6980`. Published as a conference paper at the 3rd International Conference for Learning Representations, San Diego, 2015.

[241] Tibshirani, R., *Regression Shrinkage and Selection via the Lasso*, Journal of the Royal Statistical Society (Series B) **58** (1996) 267–288.

[242] Hoerl, A. E. and Kennard, R. W., *Ridge Regression: Biased Estimation for Nonorthogonal Problems*, Technometrics **12** (1970) 55–67.

[243] Nitish, Srivastava and others, *Dropout: A Simple Way to Prevent Neural Networks from Overfitting*, Journal of Machine Learning Research **15** (2014) 1929–1958.

[244] Massey, F. J., *The Kolmogorov-Smirnov test for goodness of fit*, Journal of the American Statistical Association **46** (1951) 68–78.

[245] F. Chollet et al., *Keras*, `https://keras.io`, 2015. Accessed on Oct. 10, 2022.

[246] M. Abadi, et al., *TensorFlow: Large-Scale Machine Learning on Heterogeneous Systems*, 2015. `https://www.tensorflow.org/`. Software available from tensorflow.org.

[247] X. Glorot and Y. Bengio, *Understanding the difficulty of training deep feedforward neural networks*, in *Proceedings of the Thirteenth International Conference on Artificial Intelligence and Statistics*, Y. W. Teh and M. Titterington, eds., pp. , 249–256. PMLR, Chia Laguna Resort, Sardinia, Italy, 13–15 may, 2010. `https://proceedings.mlr.press/v9/glorot10a.html`.

[248] Nesterov, Yurii, *A method of accelerating the convergence of iterative methods*, Soviet Mathematics Doklady **27** (1983) 372–376.

[249] ROOT Collaboration, K. Cranmer, et al., *HistFactory: A tool for creating statistical models for use with RooFit and RooStats*, `https://cds.cern.ch/record/1456844`, CERN-OPEN-2012-016.

[250] W. Verkerke and D. P. Kirkby, *The RooFit toolkit for data modeling*, eConf **C0303241** (2003) MOLT007.

[251] L. Moneta, et al., *The RooStats Project*, PoS **ACAT2010** (2010) 057.

[252] R. Brun and F. Rademakers, *ROOT: An object oriented data analysis framework*, Nucl. Instrum. Meth. A **389** (1997) 81–86.

[253] *1974 CERN School of Computing, Godoysund, Norway, 11-24 Aug 1974: Proceedings*, CERN Yellow Reports: School Proceedings. 11, 1974.

[254] G. D'Agostini, *Improved iterative Bayesian unfolding*, in *Alliance Workshop on Unfolding and Data Correction*. 10, 2010. `arXiv:1010.0632 [physics.data-an]`.

[255] ATLAS Collaboration, *Jet energy scale and resolution measured in proton–proton collisions at $\sqrt{s} = 13$ TeV with the ATLAS detector*, Eur. Phys. J. C **81** (2021) 689.

[256] ATLAS Collaboration, *Jet energy measurement and its systematic uncertainty in proton-proton collisions at $\sqrt{s} = 7$ TeV with the ATLAS detector*, Eur. Phys. J. C **75** (2015) 17.

[257] ATLAS Collaboration, *Determination of jet calibration and energy resolution in proton-proton collisions at $\sqrt{s} = 8$ TeV using the ATLAS detector*, Eur. Phys. J. C **80** (2020) 1104.

[258] ATLAS Collaboration, *Measurements of b-jet tagging efficiency with the ATLAS detector using $t\bar{t}$ events at $\sqrt{s} = 13$ TeV*, JHEP **08** (2018) 089.

[259] ATLAS Collaboration, *Measurement of the c-jet mistagging efficiency in $t\bar{t}$ events using pp collision data at $\sqrt{s} = 13$ TeV collected with the ATLAS detector*, Eur. Phys. J. C **82** (2022) 95.

[260] ATLAS Collaboration, *Electron and photon performance measurements with the ATLAS detector using the 2015–2017 LHC proton-proton collision data*, JINST **14** (2019) P12006.

[261] ATLAS Collaboration, *Electron reconstruction and identification in the ATLAS experiment using the 2015 and 2016 LHC proton-proton collision data at $\sqrt{s}$ = 13 TeV*, Eur. Phys. J. C **79** (2019) 639.

[262] ATLAS Collaboration, *Muon reconstruction and identification efficiency in ATLAS using the full Run 2 pp collision data set at $\sqrt{s} = 13$ TeV*, Eur. Phys. J. C **81** (2021) 578.

[263] ATLAS Collaboration, *Muon reconstruction performance of the ATLAS detector in proton–proton collision data at $\sqrt{s}$ =13 TeV*, Eur. Phys. J. C **76** (2016) 292.

[264] S. van der Meer, *Calibration of the effective beam height in the ISR*, `https://cds.cern.ch/record/296752`, CERN-ISR-PO-68-31.

[265] P. Grafström and W. Kozanecki, *Luminosity determination at proton colliders*, Prog. Part. Nucl. Phys. **81** (2015) 97–148.

[266] J. Butterworth et al., *PDF4LHC recommendations for LHC Run II*, J. Phys. G **43** (2016) 023001.

[267] S. Dulat, et al., *New parton distribution functions from a global analysis of quantum chromodynamics*, Phys. Rev. D **93** (2016) 033006.

[268] L. A. Harland-Lang, et al., *Parton distributions in the LHC era: MMHT 2014 PDFs*, Eur. Phys. J. C **75** (2015) 204.

[269] ATLAS Collaboration, *Observation of the associated production of a top quark and a Z boson in pp collisions at $\sqrt{s} = 13$ TeV with the ATLAS detector*, JHEP **07** (2020) 124.

[270] S. Frixione, et al., *Single-top hadroproduction in association with a W boson*, JHEP **07** (2008) 029.

[271] W. Hollik, J. M. Lindert, and D. Pagani, *NLO corrections to squark-squark production and decay at the LHC*, JHEP **03** (2013) 139.

[272] F. Demartin, et al., *tWH associated production at the LHC*, Eur. Phys. J. C **77** (2017) 34.

[273] ATLAS Collaboration, *Performance of top-quark and W-boson tagging with ATLAS in Run 2 of the LHC*, Eur. Phys. J. C **79** (2019) 375.

[274] A. Shmakov, et al., *SPANet: Generalized permutationless set assignment for particle physics using symmetry preserving attention*, SciPost Phys. **12** (2022) 178.

[275] A. Andreassen, et al., *OmniFold: A Method to Simultaneously Unfold All Observables*, Phys. Rev. Lett. **124** (2020) 182001.

[276] ATLAS Collaboration, *Identification of hadronic tau lepton decays using neural networks in the ATLAS experiment*, `https://cds.cern.ch/record/2688062`, ATL-PHYS-PUB-2019-033.

[277] ATLAS Collaboration,, *Reconstruction, Identification, and Calibration of hadronically decaying tau leptons with the ATLAS detector for the LHC Run 3 and reprocessed Run 2 data*, `https://cds.cern.ch/record/2827111`, ATL-PHYS-PUB-2022-044.

[278] V. Miralles, et al., *The top quark electro-weak couplings after LHC Run 2*, JHEP **02** (2022) 032.

APPENDIX A

List of MC samples

A complete list of all data and simulated MC samples used in the analysis is shown in Tables A.1 to A.3. Only processes with 3 prompt leptons are considered Alternative signal and background samples which are used for the evaluation of theoretical uncertainties are also listed. The r-tag number depends on the MC campaign (*r9364* for `mc16a`, *r10201* for `mc16d` and *r10726* for `mc16e`).For simplicity only the samples corresponding to the `mc16d` MC campaign are shown. The *p-tag* number depends on the ATLAS software release used for the derivation production. The data and MC samples are skimmed into *TOPQ1* derivations with the following ATLAS software caches. The derivation software used corresponds always to a p-tag $\geq$ 3629, and includes the pile-up robust isolation variables. Data: ATLAS derivation cache 21.2.123.0 (p-tag 4513). MC: Derivation cache 21.2.111.0 (p-tag 4346). The majority of the listed MC samples correspond to full-simulation samples. Exceptions based on AtlFast II, such as the MadGraph5_aMC@NLO $t\bar{t}H$, the tZq and tWZ samples, are indicated with a $(\star)$[1].

Table A.1: Summary of the data containers describing the proton-proton collision data taken between 2015 and 2018.

Year	Container name	Luminosity [pb^{-1}]
2015	`data15_13TeV.AllYear.physics_Main.PhysCont.DAOD_TOPQ1.grp15_v01_p4513`	3244.54
2016	`data16_13TeV.AllYear.physics_Main.PhysCont.DAOD_TOPQ1.grp16_v01_p4513`	33402.2
2017	`data17_13TeV.AllYear.physics_Main.PhysCont.DAOD_TOPQ1.grp17_v01_p4513`	44630.6
2018	`data18_13TeV.AllYear.physics_Main.PhysCont.DAOD_TOPQ1.grp18_v01_p4513`	58791.6
Run 2		140068.94

[1]Some of the alternative samples, including the Sherpa [2.2.1] NLO signal $t\bar{t}Z$ samples are also produced with AtlFast II.

Table A.2: Descriptive list of MC signal samples used in this analysis: The r-tag number describes the MC campaign (r9364 for `mc16a`, r10201 for `mc16d` and r10724 for `mc16e`). This table only shows `mc16d` samples. The usage of the other two campaigns is implied. The p-tag number defines the ATLAS software release used for the derivation production. The samples marked with ($\star$) correspond to fast-simulation samples.

Description	Signal MC sample name	
nominal $t\bar{t}(Z \to e^+e^-)$	504330.aMCPy8EG_NNPDF30NLO_A14N23LO_ttee.deriv.DAOD_TOPQ1.e8255_s3126_r10201_p4346	
nominal $t\bar{t}(Z \to \mu^+\mu^-)$	504334.aMCPy8EG_NNPDF30NLO_A14N23LO_ttmumu.deriv.DAOD_TOPQ1.e8255_s3126_r10201_p4346	
nominal $t\bar{t}(Z \to \tau^+\tau^-)$	504342.aMCPy8EG_NNPDF30NLO_A14N23LO_tttautau.deriv.DAOD_TOPQ1.e8255_s3126_r10201_p4346	
Alt. shower variation	504329.aMCH7EG_NNPDF30NLO_H721UE_ttee.deriv.DAOD_TOPQ1.e8255_a875_r10201_p4346	($\star$)
	504333.aMCH7EG_NNPDF30NLO_H721UE_ttmumu.deriv.DAOD_TOPQ1.e8255_a875_r10201_p4346	($\star$)
	504341.aMCH7EG_NNPDF30NLO_H721UE_tttautau.deriv.DAOD_TOPQ1.e8255_a875_r10201_p4346	($\star$)
A14 up variation	504332.aMCPy8EG_NNPDF30NLO_A14N23LO_ttee_A14Var3cUp.deriv.DAOD_TOPQ1.e8255_a875_r10201_p4346	($\star$)
	504336.aMCPy8EG_NNPDF30NLO_A14N23LO_ttmumu_A14Var3cUp.deriv.DAOD_TOPQ1.e8255_a875_r10201_p4346	($\star$)
	504344.aMCPy8EG_NNPDF30NLO_A14N23LO_tttautau_A14Var3cUp.deriv.DAOD_TOPQ1.e8255_a875_r10201_p4346	($\star$)
A14 down variation	504331.aMCPy8EG_NNPDF30NLO_A14N23LO_ttee_A14Var3cDown.deriv.DAOD_TOPQ1.e8255_a875_r10201_p4346	($\star$)
	504335.aMCPy8EG_NNPDF30NLO_A14N23LO_ttmumu_A14Var3cDown.deriv.DAOD_TOPQ1.e8255_a875_r10201_p4346	($\star$)
	504343.aMCPy8EG_NNPDF30NLO_A14N23LO_tttautau_A14Var3cDown.deriv.DAOD_TOPQ1.e8255_a875_r10201_p4346	($\star$)
Sherpa 2.2.1. for cross-check	413022.Sherpa_221_ttll_NLO_inc.deriv.DAOD_TOPQ1.e7504_a875_r10201_p4514	
	413023.Sherpa_221_ttll_multileg_NLO.deriv.DAOD_TOPQ1.e7504_e5984_s3126_r10201_r10210_p4166	
Sherpa 2.2.11. for cross-check	700309.Sh_2211_ttll.deriv.DAOD_TOPQ1.e8312_s3126_r10201_p4174	
SMEFT sample (LO)	508772.MGPy8_ttll_SMEFTsim_reweighted.DAOD_TOPQ1.e8379_a875_r10201_p4514	($\star$)
	508773.MGPy8_ttll_SMEFTsim_reweighted_prop.DAOD_TOPQ1.e8379_a875_r10201_p4514	($\star$)
	508985.MGPy8_tllq_SMEFTsim_reweighted.DAOD_TOPQ1.e8379_a875_r10201_p4514	($\star$)
	508986.MGPy8_tllq_SMEFTsim_reweighted_prop.DAOD_TOPQ1.e8379_a875_r10201_p4514	($\star$)

Table A.3: List of MC background samples used in this analysis. The structure of the table is the same as Table A.2.

Description	Signal MC sample name	
$t\bar{t}t\bar{t}$	304014.MadGraphPythia8EvtGen_A14NNPDF23_3top_SM.deriv.DAOD_TOPQ1.e4324_s3126_r10201_p4514	
WH	342284.Pythia8EvtGen_A14NNPDF23LO_WH125_inc.deriv.DAOD_TOPQ1.e4246_s3126_r10201_p4512	
ZH	342285.Pythia8EvtGen_A14NNPDF23LO_ZH125_inc.deriv.DAOD_TOPQ1.e4246_s3126_r10201_p4512	
$t\bar{t}H$ ($t\bar{t} \to 2\ell$)	346443.aMcAtNloPythia8EvtGen_ttH_noShWe_dilep.deriv.DAOD_TOPQ1.e7310_a875_r10201_p4346	($\star$)
$t\bar{t}H$ ($t\bar{t} \to 1\ell$)	346444.aMcAtNloPythia8EvtGen_ttH_noShWe_semilep.deriv.DAOD_TOPQ1.e7310_a875_r10201_p4346	($\star$)
$t\bar{t}H$ ($t\bar{t} \to 0\ell$)	346445.aMcAtNloPythia8EvtGen_ttH_noShWe_allhad.deriv.DAOD_TOPQ1.e7310_a875_r10201_p4346	($\star$)
WZ	363358.Sherpa_221_NNPDF30NNLO_WqqZll.deriv.DAOD_TOPQ1.e5525_s3126_r10201_p4344	
WW	363359.Sherpa_221_NNPDF30NNLO_WpqqWmlv.deriv.DAOD_TOPQ1.e5583_s3126_r10201_p4344	
	363360.Sherpa_221_NNPDF30NNLO_WplvWmqq.deriv.DAOD_TOPQ1.e5983_s3126_r10201_p4344	
Z + jets (+fake leptons)	364100...364141.Sherpa_221_NNPDF30NNLO_Zmumu_MAXHTPTV0_70...1000_CVetoBVeto.DAOD_TOPQ1.e5271_s3126_r10201_p4344	
	364100...364127.Sherpa_221_NNPDF30NNLO_Zee_MAXHTPTV0_70...1000_CVetoBVeto.DAOD_TOPQ1.e5271_s3126_r10201_p4344	
	364128...364141.Sherpa_221_NNPDF30NNLO_Ztautau_MAXHTPTV0_70...1000_CVetoBVeto.DAOD_TOPQ1.e5271_s3126_r10201_p4344	
$WWW \to 3\ell 3\nu$	364242.Sherpa_222_NNPDF30NNLO_WWW_3l3v_EW6.deriv.DAOD_TOPQ1.e5887_s3126_r10201_p4344	
$WWZ \to 4\ell 2\nu$	364243.Sherpa_222_NNPDF30NNLO_WWZ_4l2v_EW6.deriv.DAOD_TOPQ1.e5887_s3126_r10201_p4344	
$WWZ \to 2\ell 4\nu$	364244.Sherpa_222_NNPDF30NNLO_WWZ_2l4v_EW6.deriv.DAOD_TOPQ1.e5887_s3126_r10201_p4344	
$WZZ \to 3\ell 3\nu$	364246.Sherpa_222_NNPDF30NNLO_WZZ_3l3v_EW6.deriv.DAOD_TOPQ1.e5887_s3126_r10201_p4344	
$ZZZ \to 4\ell 2\nu$	364248.Sherpa_222_NNPDF30NNLO_ZZZ_4l2v_EW6.deriv.DAOD_TOPQ1.e5887_s3126_r10201_p4344	
$ZZZ \to 2\ell 4\nu$	364249.Sherpa_222_NNPDF30NNLO_ZZZ_2l4v_EW6.deriv.DAOD_TOPQ1.e5887_s3126_r10201_p4344	
$ZZ \to 4\ell$	345705.Sherpa_222_NNPDF30NNLO_gglllll_0M4l130.DAOD_TOPQ1.e6213_s3126_r10201_p4344	
	345706.Sherpa_222_NNPDF30NNLO_gglllll_130M4l.DAOD_TOPQ1.e6213_s3126_r10201_p4344	
	364250.Sherpa_222_NNPDF30NNLO_llll.DAOD_TOPQ1.e5894_s3126_r10201_p4344	
	364288.Sherpa_222_NNPDF30NNLO_llll_lowMllPtComplement.DAOD_TOPQ1.e6096_s3126_r10201_p4344	
$WZ \to 3\ell 1\nu$	364253.Sherpa_222_NNPDF30NNLO_lllv.DAOD_TOPQ1.e5916_s3126_r10201_p4344	
Z + jets + photon	364284.Sherpa_222_NNPDF30NNLO_lllvjj_EW6.DAOD_TOPQ1.e6055_s3126_r10201_p4344	
	366140...366144.Sh_224_NN30NNLO_eegamma_LO_pty_7...140_15...E.deriv.DAOD_TOPQ1.e7006_s3126_r10201_p4344	
	366145...366149.Sh_224_NN30NNLO_mumugamma_LO_pty_7...140_15...E.deriv.DAOD_TOPQ1.e7006_s3126_r10201_p4344	
	366150...366154.Sh_224_NN30NNLO_tautaugamma_LO_pty_7...140_15...E.deriv.DAOD_TOPQ1.e7006_s3126_r10201_p4344	
$t\bar{t}WW$	410081.MadGraphPythia8EvtGen_A14NNPDF23_ttbarWW.DAOD_TOPQ1.e4111_s3126_r10201_p4514	
$t\bar{t}\gamma$	410389.MadGraphPythia8EvtGen_A14NNPDF23_ttgamma_nonallhadronic.deriv.DAOD_TOPQ1.e6155_s3126_r10201_p4346	
$t\bar{t}$ (+fake leptons)	410470.PhPy8EG_A14_ttbar_hdamp258p75_nonallhad.deriv.DAOD_TOPQ1.e6337_s3126_r10201_p4346	
	410471.PhPy8EG_A14_ttbar_hdamp258p75_allhad.deriv.DAOD_TOPQ1.e6337_s3126_r10201_p4346	
	410472.PhPy8EG_A14_ttbar_hdamp258p75_dil.DAOD_TOPQ1.e6348_s3126_r10201_p4514	
$t\bar{t}t\bar{t}$	412043.aMcAtNloPythia8EvtGen_A14NNPDF31_SM4topsNLO.DAOD_TOPQ1.e7101_a875_r10201_p4346	
$t\bar{t}t\bar{t}$ alt. shower	412044.aMcAtNloHerwig7EvtGen_H7UE_SM4topsNLO.DAOD_TOPQ1.e7102_a875_r10201_p4346	
tWZ	412118.aMcAtNloPythia8EvtGen_tWZ_Ztoll_DR1.deriv.DAOD_TOPQ1.e7518_s3126_r10201_p4346	
tWZ modelling	412119.aMcAtNloPythia8EvtGen_tWZ_Ztoll_DR2.deriv.DAOD_TOPQ1.e7518_s3126_r10201_p4346	
$t\bar{t}(Z \to qq)$	504338.aMCPy8EG_NNPDF30NLO_A14N23LO_ttZqq.deriv.DAOD_TOPQ1.e8255_s3126_r10201_p4346	
$t\bar{t}(Z \to \nu\nu)$	504346.aMCPy8EG_NNPDF30NLO_A14N23LO_ttZnunu.deriv.DAOD_TOPQ1.e8255_s3126_r10201_p4346	
tZq	512059.aMCPy8EG_NNPDF30NLO_A14N23LO_tllq_4FS.DAOD_TOPQ1.e8400_s3126_r10201_p4514	
tZq alt. shower variation	512130.aMCH7EG_NNPDF30NLO_H716UE_tllq_4FS.DAOD_TOPQ1.e8418_a875_r10201_p4514	($\star$)
tZq A14 up variation	512168.aMCPy8EG_NNPDF30NLO_A14N23LO_tllq_4FS_A14Var3cDown.DAOD_TOPQ1.e8418_a875_r10201_p4514	($\star$)
tZq A14 down variation	512169.aMCPy8EG_NNPDF30NLO_A14N23LO_tllq_4FS_A14Var3cUp.DAOD_TOPQ1.e8418_a875_r10201_p4514	($\star$)
$t\bar{t}W$	700168.Sh_2210_ttW.deriv.DAOD_TOPQ1.e8273_s3126_r10201_p4346	
	700205.Sh_2210_ttW_EWK.deriv.DAOD_TOPQ1.e8307_s3126_r10201_p4174	

APPENDIX B

Pruning results in the signal regions

In the figure, the NPs for the individual samples are shown in dedicated columns. As the fake-related contributions are estimated through a dedicated data-driven method, no NPs are associated with them. NPs marked in red are dropped from the fit. NPs which are kept are marked green. If the normalisation component is dropped, the NP is marked orange. If the shape component is dropped, the NP is marked yellow. NPs marked in grey denote cases where the NP does not exist for the sample or region.

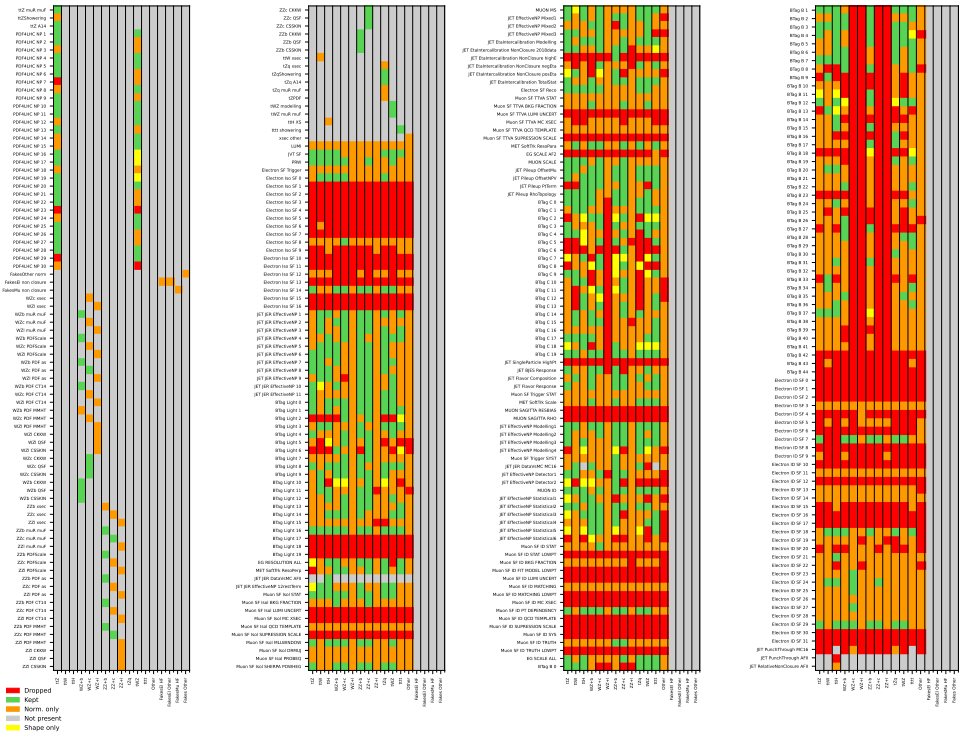

Figure B.1: Summary of pruned NPs in the SR-3ℓ-$t\bar{t}Z$ region.

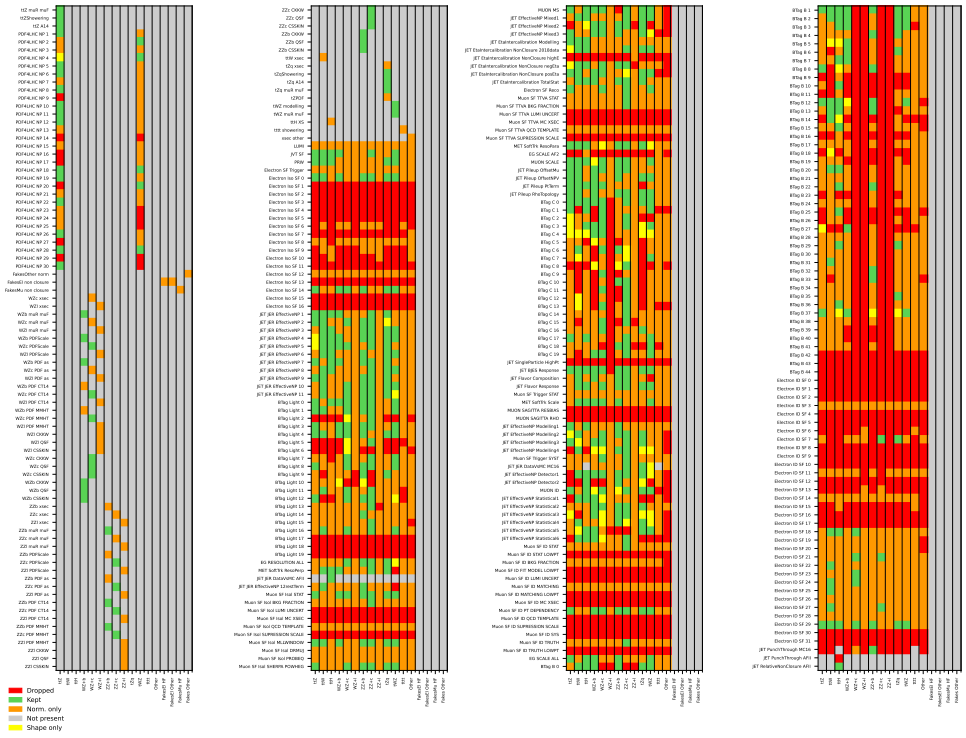

Figure B.2: Summary of pruned NPs in the *SR-3ℓ-tZq* region.

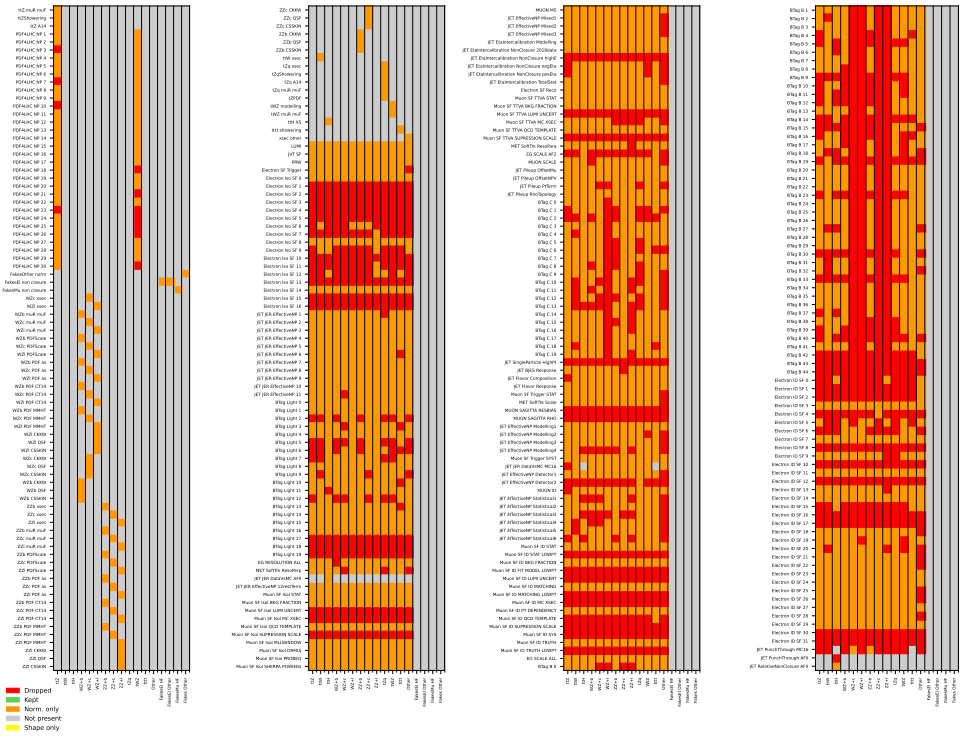

Figure B.3: Summary of pruned NPs in the $SR\text{-}3\ell\text{-}WZ$ region.

APPENDIX C

Study of impact of negative weights

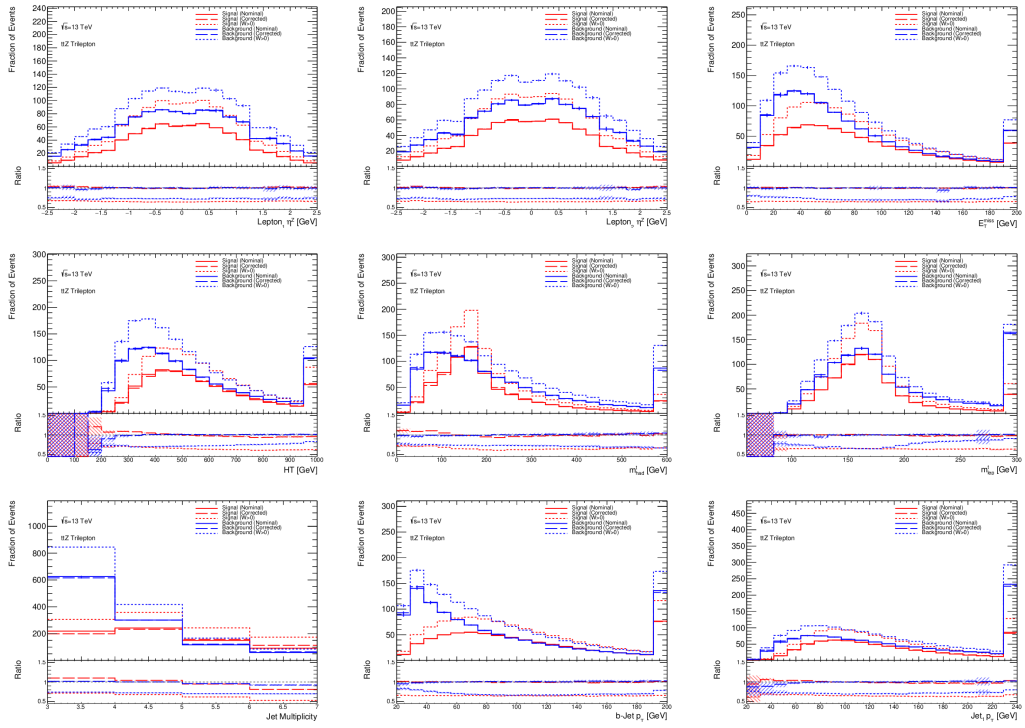

Figure C.1: Summary plots highlighting the impact of negative weights for the different neural network input variables.

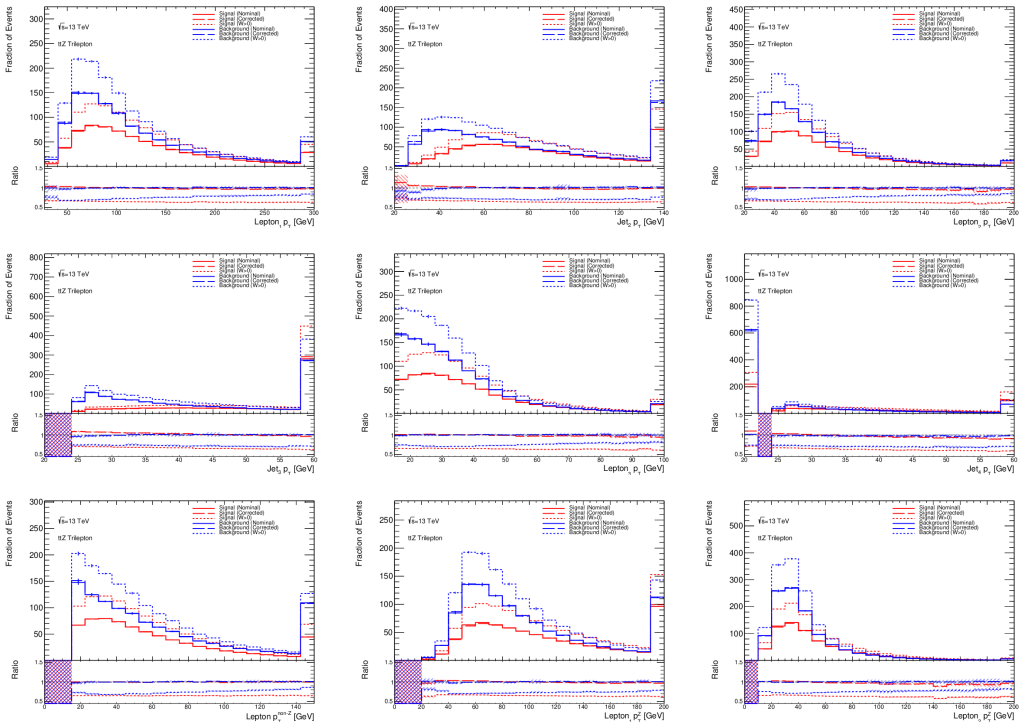

Figure C.2: Summary plots highlighting the impact of negative weights for the different neural network input variables.

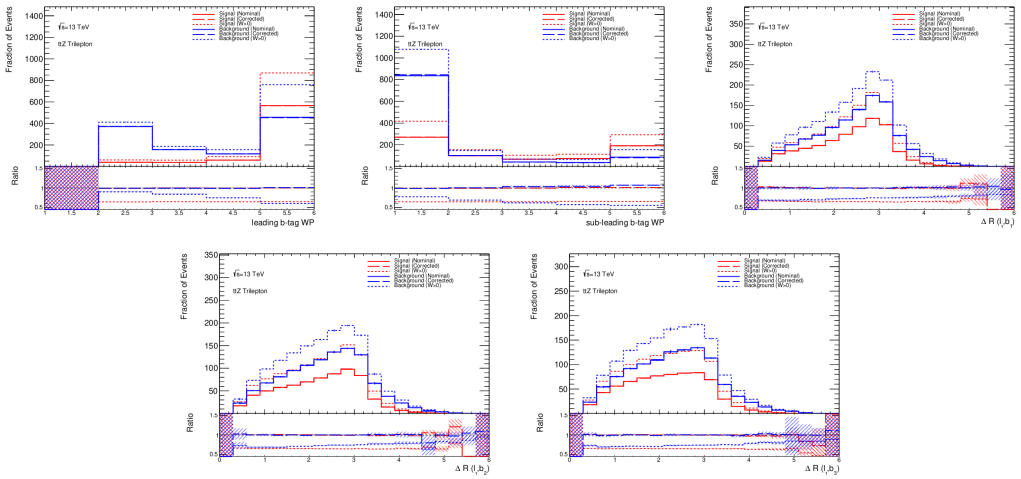

Figure C.3: Summary plots highlighting the impact of negative weights for the different neural network input variables.

APPENDIX D

Additional Kolmogorov-Smirnov tests

Figure D.1 provides an overview of the remaining Kolmogorov-Smirnov test for the $t\bar{t}Z$, tZq, and diboson output nodes not previously shown in the main body.

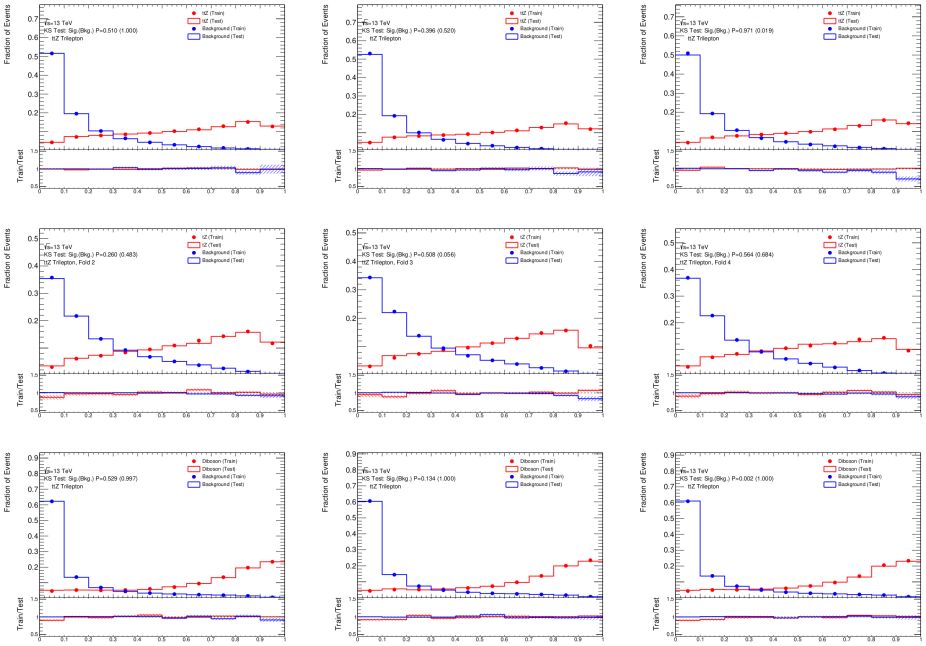

Figure D.1: Kolmogorov-Smirnov test for the $t\bar{t}Z$ (top), tZq (middle), and diboson (bottom) output nodes for the second, third, and fourth fold. No significant deviation between training and testing distribution is observed indicating good generalisation performance of the model.

APPENDIX E

Estimation of the fake lepton background

The following chapter provides a further details on the independent fit performed in the fake-enriched control regions, namely $CR\text{-}t\bar{t}\text{-}e$, $CR\text{-}t\bar{t}\text{-}\mu$, $CR\text{-}Z\text{-}e$ to extract the three normfactors:

$\mathcal{N}_{e,\mathrm{HF}}$	- Electron fakes from heavy flavour sources,
$\mathcal{N}_{e,\mathrm{Other}}$	- Electron fakes from other sources,
$\mathcal{N}_{\mu,\mathrm{HF}}$	- Muon fakes from heavy flavour sources.

The normfactors are estimated through a profile-likelihood fit. The pre-fit agreement of the individual regions is shown in Figure E.1. Good pre-fit agreement between MC and data is observed in all three regions.

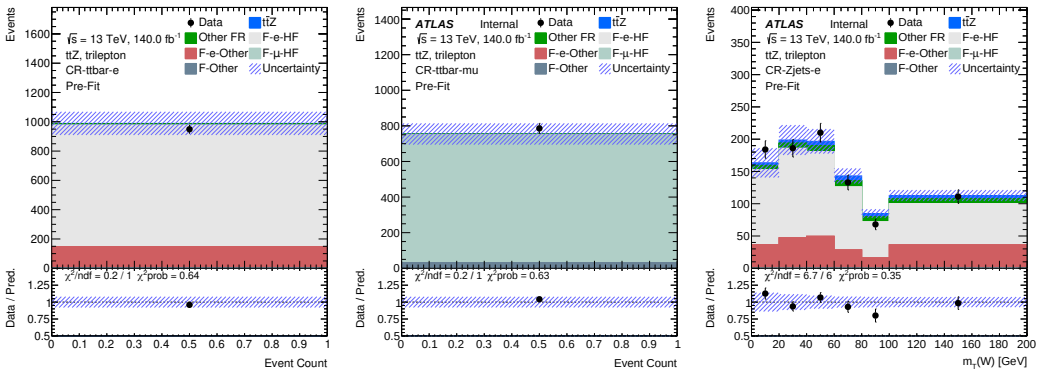

Figure E.1: Post-fit distributions of the three fake regions: $CR\text{-}t\bar{t}\text{-}e$ (left), $CR\text{-}t\bar{t}\text{-}\mu$ (center), and $CR\text{-}Z\text{-}e$ (right). The three fake factors, $\mathcal{N}_{e,\mathrm{HF}}$, $\mathcal{N}_{e,\mathrm{Other}}$, and $\mathcal{N}_{\mu,\mathrm{HF}}$, are extracted from a simultaneous profile-likelihood fit of all three distributions.

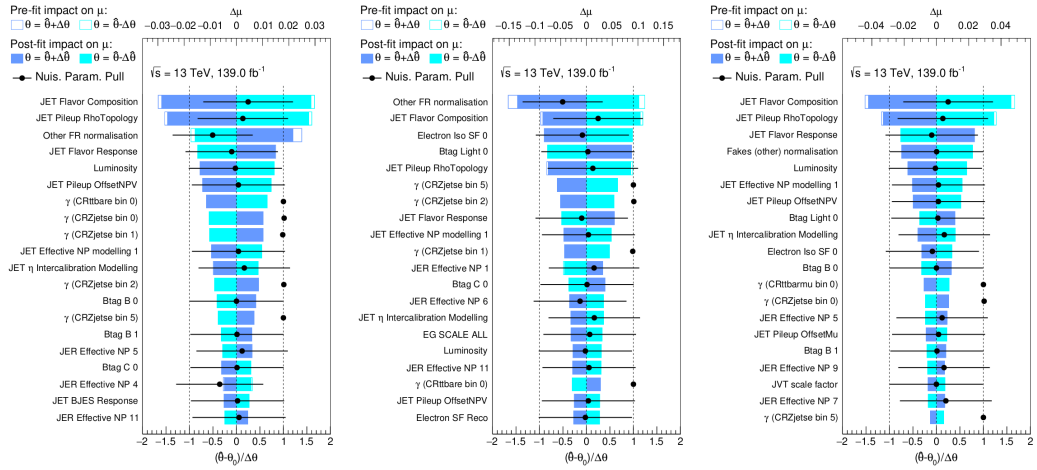

Figure E.2: Ranking plots of the leading systematic uncertainties for the exctraction of the fake factors in the fake factor fit for the extraction of $\mathcal{N}_{e,\mathrm{HF}}$ (left), $\mathcal{N}_{e,\mathrm{Other}}$ (center), and $\mathcal{N}_{\mu,\mathrm{HF}}$ (right).

In the *CR-$t\bar{t}$-e* and *CR-$t\bar{t}$-μ* regions the observed event yields are fitted. In the *CR-Z-e* region the transverse mass of the W boson is fitted, as it provides some separation power between the different processes. Alternative fit scenarios using different observables and binnings were tested, yielding negligible differences with respect to the obtained values for the normfactors and their uncertainties. The following results are obtained for the normfactors:

$$\mathcal{N}_{e,\mathrm{HF}} = 0.873^{+0.098}_{-0.091}, \tag{E.1}$$

$$\mathcal{N}_{e,\mathrm{Other}} = 1.171^{+0.406}_{-0.361}, \tag{E.2}$$

$$\mathcal{N}_{\mu,\mathrm{HF}} = 1.000^{+0.088}_{-0.081}. \tag{E.3}$$

Figure E.2 shows the leading 20 systematic uncertainties for the determination of the three normalisation factors. No NP is significantly constrained. The leading systematic uncertainties are related to the jet flavour composition, the jet ρ topology and the jet flavour response. Further leading systematic uncertainties are the b-tagging efficiency, specifically the rejection of light-flavour jets *Btag Light 0*, the leading electron isolation scale factor (*Electron Iso SF 0*), and the normalisation of fakes from other sources (*Other FR normalisation).* Control plots of the leading, sub-leading, and trailing lepton's kinematics are shown in Figures E.3 to E.5 to validate the quality of the extracted normfactors. From the observed amount of non-closure a conservative normalisation uncertainty of 20 % on fake electrons and 10 % on fake muons is derived and applied in the $t\bar{t}Z$ signal regions.

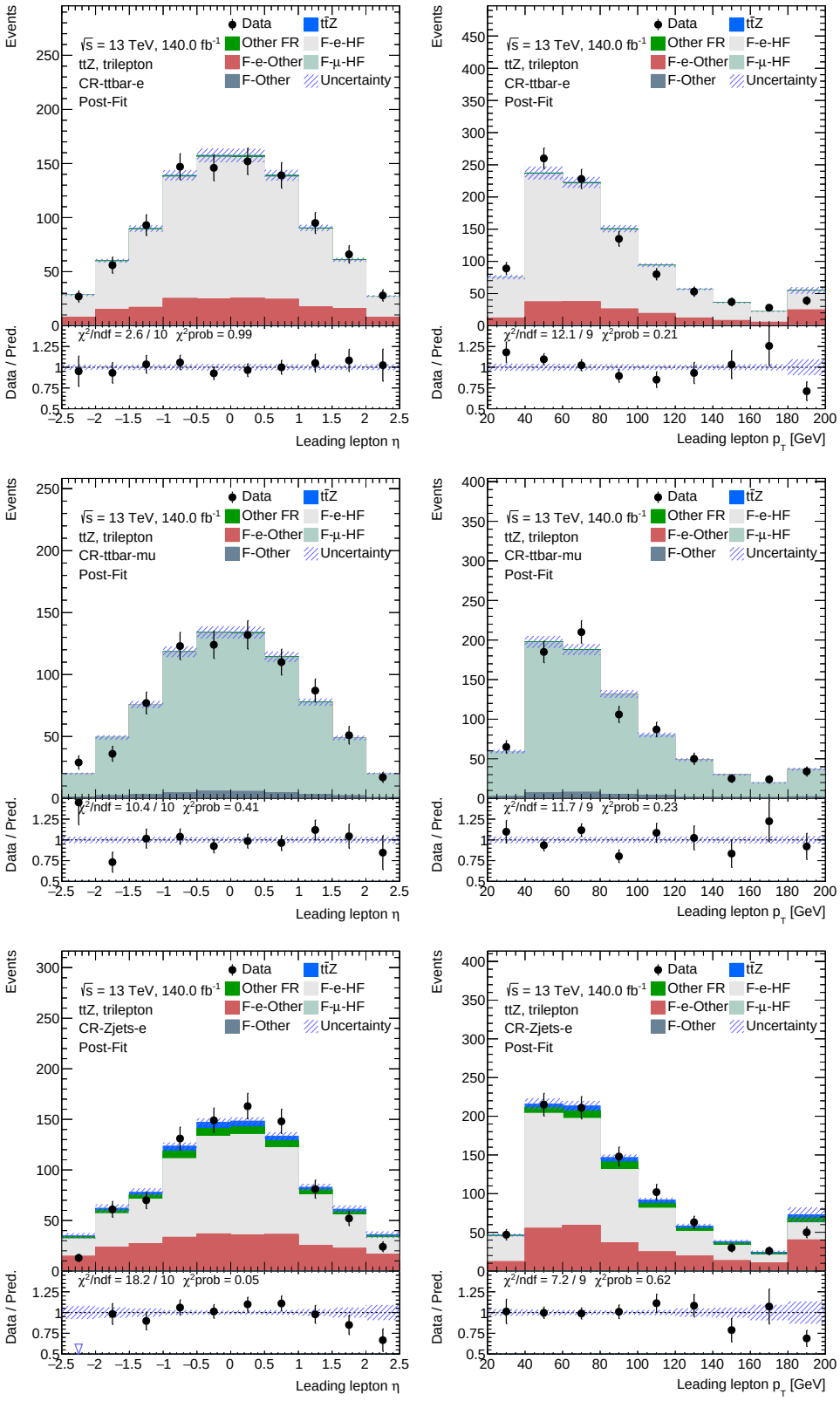

Figure E.3: Control plots showing the η and p_{T} distributions of the leading lepton in the three fake-enriched regions.

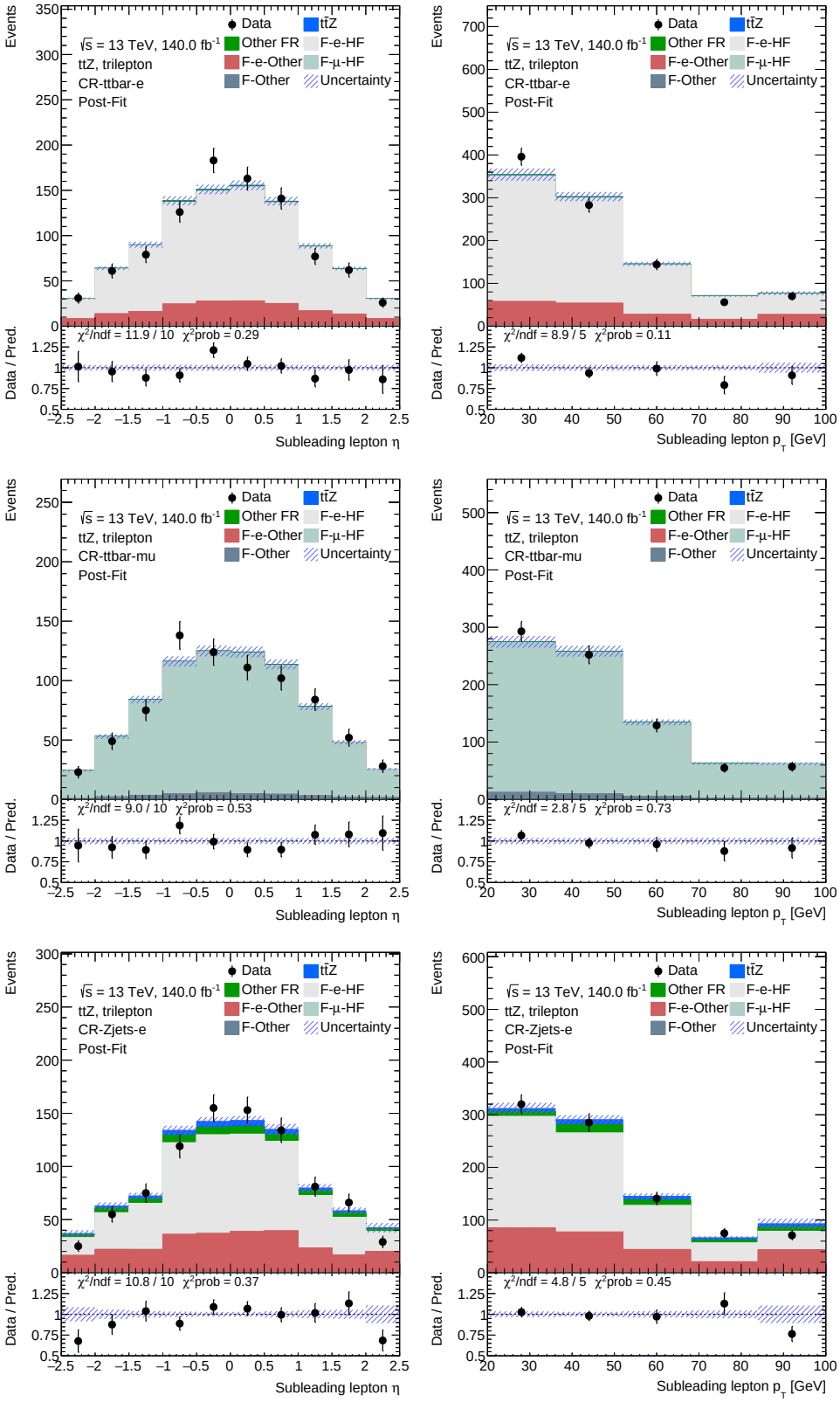

Figure E.4: Control plots showing the η and p_{T} distributions of the sub-leading lepton in the three fake-enriched regions.

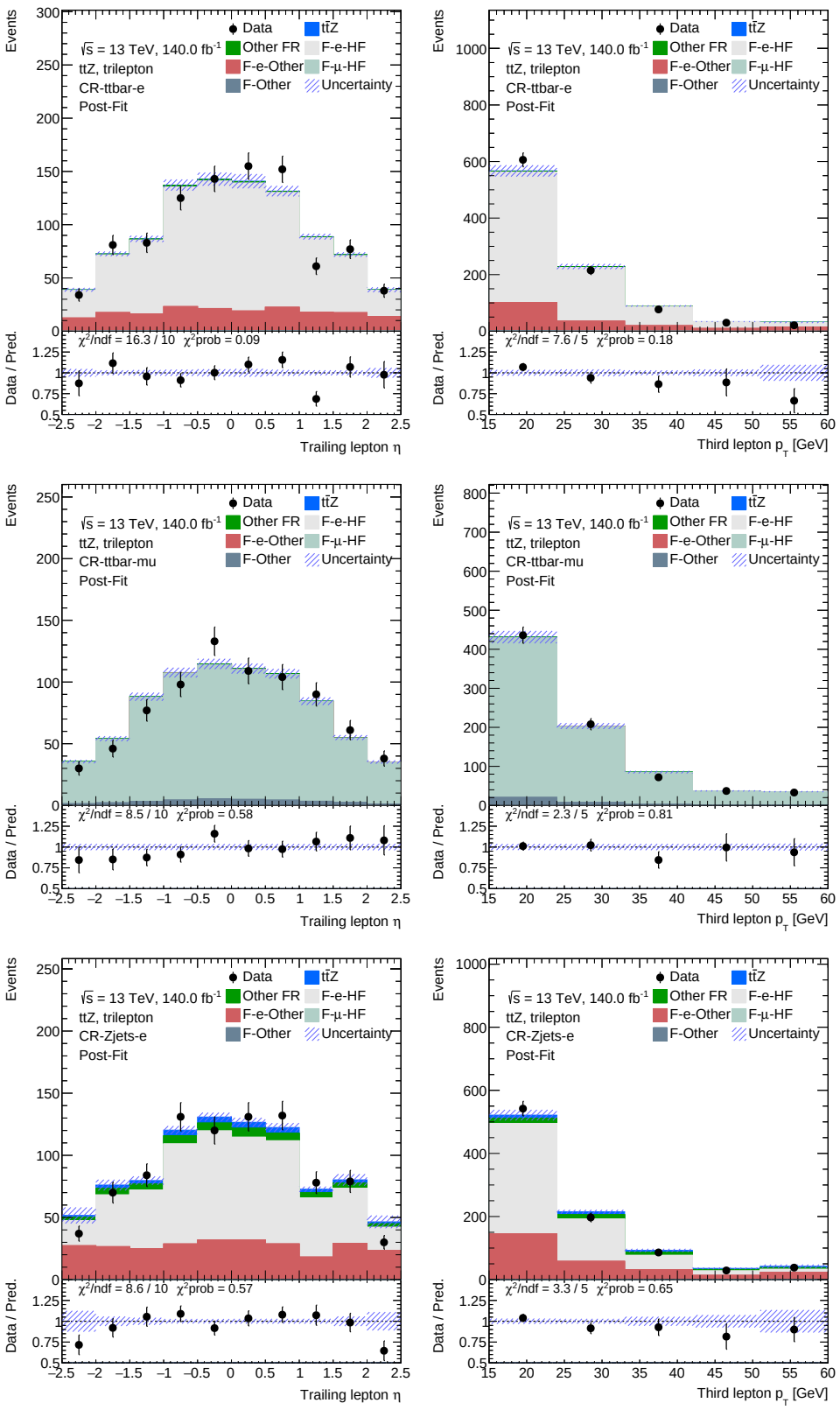

Figure E.5: Control plots showing the η and p_{T} distributions of the trailing lepton in the three fake-enriched regions.

APPENDIX F

Alternative cut and count fit

Table F.1: Definition of the alternative trilepton signal regions and the WZ control region.

Variable	**Preselection**		
N_ℓ $(\ell = e, \mu)$	$= 3$ ≥ 1 OSSF lepton pair with $\lvert m_{\ell\ell} - m_Z \rvert < 10$ GeV for all OSSF combinations: $m_{\text{OSSF}} > 10$ GeV		
p_{T} (ℓ_1, ℓ_2, ℓ_3)	$> 27,\ 20,\ 15$ GeV		
N_{jets} $(p_{\text{T}} > 25$ GeV)	≥ 3		
$N_{b-\text{jets}}$	≥ 1@85%		
	SR-1b-4j	**SR-2b-3j**	**WZCR**
n_{Jets}	≥ 4	≥ 3	≥ 3
$N_{b-\text{jets}}$	== 1@60%, veto add. @70%	≥ 2@70%	veto all@77% and tighter

To emulate a cut-and-count based alternative fit scenario in the trilepton channel of the analysis signal regions and a dedicated WZ control region are defined as presented in Table F.1. The cuts presented here are inspired by the cut-and-count-based cuts used in the previous ATLAS analysis [147]. In addition to the nominal fit setup, the three fake-enriched control regions are used in the fit. The three fake-enriched control regions, the two signal regions presented above and the WZ control region are fitted simultaneously. In the fit, the $t\bar{t}Z$ signal strength and the three fake normalisation parameters are free-floating. As no dedicated WZ+b region can be defined, the free-floating normalisation of WZb is replaced by its SM value. A conservative 50% normalisation uncertainty is assigned. An Asimov fit is performed following the nominal fitting procedure. The following results are obtained:

$$\mu_{t\bar{t}Z} = 1.000^{+0.1025}_{-0.1025} = 1.000^{+0.0583}_{-0.0583}(\text{stat.}) \pm^{+0.0843}_{-0.0843} (\text{syst.}). \tag{F.1}$$

These results should be compared to the nominal fit results:

$$\mu_{t\bar{t}Z} = 1.000^{+0.0773}_{-0.0773} = 1.000^{+0.0561}_{-0.0561}(\text{stat.}) \pm^{+0.0532}_{-0.0532} (\text{syst.}), \tag{F.2}$$

$$\mathcal{N}_{WZb} = 1.000^{+0.4149}_{-0.4149}. \tag{F.3}$$

An improvement of $\sim$ 18%for $\mu_{t\bar{t}Z}$ is observed when comparing the nominal fit to this alternative fit scenario. Additionally, the nominal fit scenario can better constrain the WZ+b normalisation than the conservative 50% uncertainty, which had to be used for the cut-and-count-based scenario. As this fit is performed with the same object definitions and definitions of systematics as the nominal fit, these improvements can be attributed to the machine learning approach in the nominal fit and its improved separation power.